

ABSTRACT

Title of dissertation: BETTII: A PATHFINDER FOR HIGH ANGULAR RESOLUTION OBSERVATIONS OF STAR-FORMING REGIONS IN THE FAR-INFRARED

Maxime J. Rizzo, Doctor of Philosophy, 2016

Dissertation directed by: Professor Lee Mundy, Department of Astronomy
and Dr. Stephen Rinehart, NASA GSFC

In this thesis, we study clustered star formation in nearby star clusters and discuss how high angular resolution observations in the far-infrared regime could help us understand these important regions of stellar birth. We use the increased angular resolution from the FORCAST instrument on the SOFIA airborne observatory to study 10 nearby star-forming regions, and discuss the physical properties of sources in these regions that we can infer from radiative transfer modeling using these new observations. We discuss the design of BETTII, a pathfinder balloon-borne interferometer which will provide significantly better angular resolution in the far-infrared regime, and pave the way for future space-borne observatories. We elaborate on the details of BETTII's core technique, called Double-Fourier interferometry, and how to accurately compute the sensitivity of instruments which use this technique. Finally, we show our design and implementation results of the control and attitude estimation system for the BETTII payload, which poses unique challenges as an interferometer on a balloon platform.

BETTII: A pathfinder for high angular resolution observations of star-forming
regions in the far-infrared

by

Maxime J. Rizzo

Dissertation submitted to the Faculty of the Graduate School of the
University of Maryland, College Park in partial fulfillment
of the requirements for the degree of
Doctor of Philosophy
2016

Advisory Committee:

Professor Lee G. Mundy, Chair/Advisor (UMD)
Dr. Stephen A. Rinehart, Co-Advisor (NASA GSFC)
Professor Andrew Harris (UMD)
Dr. Alison Nordt (Lockheed Martin)
Dr. Mark Wolfire (UMD)
Professor Eun-Suk Seo, Graduate Dean's representative (UMD)

To Michelle, my parents, and my brother.

Acknowledgements

First and foremost, I would like to thank my advisors Lee Mundy and Stephen Rinehart for continuously supporting me during this thesis. Their guidance, knowledge and the trust they have put in me have been essential to the success of this work. Thanks for allowing me to do my first steps as a young instrument scientist, and giving me the opportunity to work on the BETTII project since day one. Special thanks to Aki Roberge for her continued mentorship, and to Richard Lyon, who originally inspired into getting my Ph.D. during my first internship at Goddard in 2008. I would also like to thank Andrew Harris, Alison Nordt, Eun-Suk Seo, and Mark Wolfire for accepting to serve on my thesis committee.

Much of what is written in this thesis is a result of discussions and reflections with members of the BETTII team, who have been supporting me during my entire graduate work. On the technical side, Dale Fixsen and Dominic Benford have inspired me tremendously with their all-around knowledge of physics and engineering and how they apply to astronomical instrumentation. I thank the rest of the team for the respect and trust they have given me: David Leisawitz, Stephen Maher, Eric Mentzell, Elmer Sharp, Robert Silverberg, Johannes Staguhn; but also Arnab Dhabal, Jordi Vila, Todd Veach and Roser Juanola-Parramon who, as graduate students and postdocs, have shared this wonderful experience with me. This extends to the entire Goddard community which has always been a friendly and welcoming group to work with.

Working on BETTII would not have been the same without the community of the UMD Department of Astronomy. I shared my experience with wonderful classmates, who always provided friendship, technical assistance, and support when needed. I especially want to thank Vicki Toy and John Capone for being my Goddard crew, and of course my

office mate Taro Shimizu for his patience and assistance with some aspects of my work. In addition, I wanted to thank my professors for always having their door open for my questions, in particular Richard Mushotzky, and Alberto Bolatto. Finally, I have had a fantastic experience with the research scientists and staff of the department. In particular I wanted to thank Peter Teuben and Adrienne Newman for their patience in assisting me all the time.

I am grateful for my friends and family in France, in the U.S., and elsewhere who have continually provided encouragements and support, despite the long distances that often separate us in this world that still doesn't seem connected enough. I want to thank especially my parents and my brother, who have been strong supporters of this endeavor. Thanks to Pauline Simonet, Jean-Baptiste Vallart, and the rest of my SUPAERO crew with who I learned so much. Thanks to Simon Oudin and Adrien Pavageau for those special moments together. Thanks to my old friends in Alsace, Cédric & Noémie, Thibaut & Jen, Adrien & Auré, and Adé, for holding the fort and never missing an occasion to get together when I come home.

Last, but not least, no one deserves more gratitude than my wife Michelle, who has given me her unconditional support, relentless encouragements, and has always been here for me since the day I met her. Michelle, this work would have been impossible without you.

Contents

Acknowledgements	iii
Contents	v
List of Tables	ix
List of Figures	xi
I Star Formation in Clustered Environments	5
I.1 Molecular Clouds	5
I.2 Star formation	7
I.2.1 Standard models	7
I.2.1.1 Gravitational collapse	7
I.2.1.2 YSO classification and characteristics	11
I.2.2 Mass accretion in clusters	16
I.3 Dust as a tracer of star formation	17
I.3.1 Dust populations and properties	19
I.3.2 Basics of dust extinction	20
I.3.3 Radiative transfer modeling	23
I.3.4 Observing star formation	25
II Star Formation in Clustered environments with SOFIA FORCAST	27
II.1 Introduction	27
II.2 Sample description and scientific goals	29
II.3 Observations	30
II.4 SOFIA FORCAST characterization	33
II.4.1 PSF size	33
II.4.2 Aperture correction factor	35
II.4.3 Instrument response and overall uncertainty	37
II.5 Data reduction and photometry	39
II.5.1 Pre-treatment	39
II.5.2 Source flux extraction	39
II.5.3 Image sensitivity	42
II.5.4 Other photometry	43
II.6 Data products	45
II.6.1 Mosaics	45
II.6.2 Photometry catalog	47
II.6.3 Fitted physical parameters	51

II.7 SED fitting	52
II.7.1 A custom grid of models	54
II.7.2 Fitting method	59
II.7.3 Overview of derived parameters	61
II.7.4 Estimating parameter uncertainty	66
II.7.5 Discussion	67
II.8 A close look at IRAS 20050+2720	69
II.8.1 Overview	71
II.8.2 Observations and discussion	72
II.8.2.1 A clustered region with an outflow	72
II.8.2.2 SEDs and fitted parameters	77
II.8.2.3 Diffuse emission	79
II.8.2.4 Conclusions on IRAS 20050+2720	82
II.9 Conclusion and future work	83
III The Balloon Experimental Twin Telescope for Infrared Interferometry	87
III.1 Towards higher angular resolution in the far-IR	87
III.2 BETTII description	88
III.3 Basics of interferometry	89
III.3.1 Fourier transform spectroscopy	90
III.3.2 Aperture synthesis	92
III.3.3 Double-Fourier interferometry	96
III.4 BETTII Instrument design	97
III.4.1 Stratospheric balloon environment	98
III.4.2 Mechanical design	100
III.4.3 Warm optical system	102
III.4.3.1 Optics layout	103
III.4.3.2 Optics manufacturing	105
III.4.4 Cryogenic instrument	107
III.4.5 Data products & analysis	110
III.5 Sensitivity analysis	112
III.5.1 Instrument and observing parameters	112
III.5.2 Far-IR background noise estimation	112
III.5.3 Interferometric visibility budget	117
III.5.4 Science channel estimated sensitivity	118
III.5.5 Tracking channel estimated sensitivity	121
III.6 Targets	123
III.6.1 Calibrators	124
III.6.2 Science targets	125
IV Far-IR double-Fourier interferometers and their spectral sensitivity	127
IV.1 Introduction	127
IV.1.1 Spatio-spectral interferometry	128
IV.1.2 The case study: BETTII	131
IV.2 Mathematical formalism	133
IV.2.1 Interferograms for a single baseline	134
IV.2.2 Measured interferograms	137
IV.3 Noise sources	140

IV.3.1	Intensity noise	141
IV.3.2	OPD noise	142
IV.4	Spectral signal-to-noise ratio	143
IV.4.1	Effects of Gaussian intensity noise	143
IV.4.2	Effects of Gaussian OPD noise	147
IV.4.3	Co-adding interferograms	149
IV.4.4	Implications for spectroscopy	150
IV.5	Spectral sensitivity analysis for BETTII	152
IV.5.1	Noise sources and control system	153
IV.5.2	Derived sensitivity and faintest detectable targets	156
IV.6	Conclusion	158
V	Attitude estimation and control for BETTII	161
V.1	Control system architecture	162
V.1.1	Overall strategy	162
V.1.1.1	Requirements	162
V.1.1.2	BETTII Coordinate systems	164
V.1.1.3	Control architecture and operating modes	167
V.1.2	Subsystems	173
V.1.2.1	Gyroscopes	173
V.1.2.2	Star cameras	179
V.1.2.3	Azimuth control	182
V.1.2.4	Momentum dump mechanism	186
V.1.2.5	Elevation control	189
V.1.2.6	Delay lines	191
V.1.2.7	Tip/tilt	192
V.1.2.8	Fine guidance sensor	193
V.1.2.9	Clocks and timing	194
V.1.2.10	Computers	196
V.1.3	Software architecture	198
V.1.4	Controls architecture summary	199
V.2	3D attitude estimation and sensor fusion	200
V.2.1	Sensor models	202
V.2.1.1	Gyroscope model	202
V.2.1.2	Star camera model	204
V.2.2	Continuous state equation and error	205
V.2.3	Integration of continuous equations	208
V.2.4	Discrete covariance matrices	208
V.2.5	Discrete Kalman filter setup	209
V.2.6	Kalman filter: prediction	211
V.2.7	Kalman filter: update	212
V.2.8	Delayed star camera solution	213
V.2.9	Enhancing the Kalman filter models	213
V.2.9.1	Estimating angular error between reference frames	215
V.2.9.2	Estimating the orthogonalization error and scale factor error	216
V.2.10	Conclusions on sensor fusion	217

VI Implementation and on-sky testing	219
VI.1 Key pre-flight procedures	220
VI.1.1 Inertia measurement	220
VI.1.2 Sensor alignment and calibration	221
VI.1.2.1 Gyroscope spectral analysis in flight configuration	221
VI.1.2.2 Orthogonalization of gyroscope mount	224
VI.1.2.3 Alignment of gyroscope mount to star camera mounts	226
VI.1.3 Star camera	226
VI.1.3.1 Tuning tests	226
VI.1.3.2 Live star camera diagnostic software	229
VI.2 Estimator implementation	230
VI.2.1 Test setup and limitations	230
VI.2.2 Autofocus implementation	231
VI.2.3 Gyro attitude estimator	232
VI.2.4 Telescope attitude estimator	236
VI.2.5 Phase estimator	237
VI.3 Pointing tests and performance results	238
VI.3.1 Control system in practice	238
VI.3.2 Gondola pointing stability with high bay doors closed	240
VI.3.3 On-sky pointing control	244
VI.3.4 What's left: Fine guiding sensor loop implementation	248
VII Concluding remarks	251
A Far-IR double-Fourier interferometers and their spectral sensitivity	255
A.1 Deriving the Interferogram Equation in a Double Fourier System	255
A.2 Spectral noise in presence of gaussian phase noise	258
A.3 Fringe tracking in the science channels	260
B Attitude representation in three dimensions	263
B.1 Tait-Bryan/Euler angles	264
B.2 Rotation matrices	265
B.3 Quaternions	270
B.3.1 Quaternion multiplication	272
B.3.2 Relationship with matrices and elementary quaternions	273
B.4 Quaternion derivative and integration	274
B.5 Covariance matrices in different reference frames	276
B.5.1 Small angle approximation	277
C The PID control loop	279
D FORCAST fit results	283

List of Tables

II.1	List of desired sensitivities for different distances	31
II.3	List of targets	32
II.5	SOFIA photometry comparison	41
II.7	FORCAST Sensitivities	42
II.9	Spitzer photometry comparison	44
II.11	NGC1333 photometry	48
II.13	SED model grid	57
II.15	Hyperion simulation parameters	58
II.17	Fitted parameters	65
II.19	Source fluxes in IRAS 20050+2720’s dense core	74
II.21	Fitted parameters in IRAS 20050+2720	77
II.23	Clustered sources in IRAS 20050+2720’s dense core	79
III.1	Instrument parameters	113
III.3	Thermal noise contributors	115
III.5	Power and NEP contributors	116
III.7	Interferometric visibility budget	118
III.9	BETTII sensitivity estimates	120
III.11	BETTII Targets	126
IV.1	BETTII sensitivity estimates	156
V.2	Operating modes	172
V.3	Gyroscope properties	178
V.4	Star camera properties	181
V.5	BETTII embedded computers	196
VI.1	Star camera tests	227
D.1	Fitted parameters	284

List of Figures

I.1	Protostar	11
I.2	Early evolution of YSOs	14
I.3	Late evolution of YSOs	15
I.4	Scenarios of clustered star formation	18
II.1	Saturation and confusion	28
II.2	PSF size	34
II.3	PSF size of calibrators	36
II.4	aperture correction	37
II.5	Instrumental response	38
II.6	RGB images of select sample of sources	46
II.7	NGC1333 SEDs	50
II.8	Confusion in NGC1333	51
II.9	Ophiuchus SEDs	52
II.10	Spectral Index distribution of point sources	53
II.11	Fitted envelope mass and luminosity distribution	61
II.12	Distribution of R	62
II.13	IRAS 20050+2720	70
II.14	IRAS 20050+2720 core	73
II.15	Multi-wavelength view of the IRAS 20050+2720 core	75
II.16	IRAS20050+2720 extended emission SED	76
II.17	IRAS20050+2720 SEDs	80
III.1	Michelson interferometer	90
III.2	Simple interferogram	91
III.3	Michelson Stellar interferometer	93
III.4	Aperture synthesis	95
III.5	FTS vs Double-Fourier	97
III.6	Balloon launch	99
III.7	BETTII Rendering	101
III.8	Payload in high bay	102
III.9	Telescope assembly layout	104
III.10	Small optical assemblies	104
III.11	Optics layout	105
III.12	Telescope assemblies	106
III.13	Cryostat crossection	108

III.14	Cold bench	109
III.15	Cryostat top plate	110
III.16	Data processing	111
III.17	BETTII Transmission curves	114
III.18	Model atmospheric transmission, from Rizzo et al., 2012.	122
III.19	Visibilities of calibrators	125
III.20	Targets	126
IV.1	WideField	131
IV.2	Optics layout of Double-Fourier interferometers	133
IV.3	interfero	139
IV.4	BETTII Spectral SNR	158
V.1	BETTII coordinate systems	164
V.2	The celestial sphere	166
V.3	The star camera reference frame	168
V.4	Azimuth and elevation of a target	169
V.5	Fiber optic gyro 3-axes mount	174
V.6	100s of gyroscope data	175
V.7	Power spectral density	176
V.8	Normality analysis	178
V.9	Allan deviation plots	179
V.10	Star camera assembly	180
V.11	Quantum efficiency of star camera sensor	182
V.12	CCMG schematics	185
V.13	CCMG testing	186
V.14	Momentum dump assembly	187
V.15	Momentum dump mechanism and pin	188
V.16	Momentum dump PID	189
V.17	Rotation stages	190
V.18	Kmirror	193
V.19	Clocks	195
V.20	Flow diagram	197
V.21	Software diagram	198
V.22	Control System Design	199
V.23	Kalman filter steps	218
VI.1	Gyroscope noise	222
VI.2	Star camera example WISE	228
VI.3	Attitude estimation while on the ground	233
VI.4	Zoom on attitude estimate plot	234
VI.5	Bias estimation while on the ground	234
VI.6	Error between measured position and estimated position	235
VI.7	The star camera reference frame	236
VI.8	Integrated gyro time series while hanging	240
VI.9	Noise while hanging	242
VI.10	Cross-elevation error indoors	243
VI.11	Slew and point on the sky	245

VI.12	Cross-elevation error	247
VI.13	Elevation and cross-elevation error	248
B.1	Rotation of 30 degrees about K	267
B.2	Rotation of -30 degrees about K	268
B.3	Two consecutive elementary rotations	269
B.4	Three consecutive elementary rotations	269
C.1	PID loop	280

Introduction

In order to improve the mind, we ought less to learn, than to contemplate.

R. Descartes

The work presented in this thesis is centered around the design, development, and testing of an astronomical balloon-borne telescope called BETTII: the Balloon Experimental Twin Telescope for Infrared Interferometry. Developed at NASA Goddard Space Flight Center, this instrument is exploring a relatively new observation technique called "Double-Fourier" interferometry, which could lead to future space-borne telescopes with high angular resolution in the far-infrared regime. Various fields in astronomy would benefit from such enhanced capability, as demonstrated by the success of far-infrared single-aperture telescopes such as *WISE*, *Spitzer* and *Herschel*.

More than just a pathfinder, BETTII is a scientific instrument in its own right. For its first flights, it will study regions of clustered star formation in unprecedented details, providing almost an order of magnitude better spatial resolution than any existing or past far-IR facility.

The following chapters describe aspects of my involvement with BETTII as well as my contributions to the scientific field of clustered star formation using another far-IR facility, the Stratospheric Observatory for Infrared Astronomy (SOFIA). The thesis is organized as follows:

- Chapter I describes the framework and current understanding of how stars are forming in clusters, and lays out the tools that we use to study these regions at far infrared wavelengths.
- Chapter II is a study of nearby star-forming clusters using new data that we obtained with the SOFIA observatory. SOFIA offers moderately high angular resolution, which we use to improve the study of the brightest, densest regions of star formation. This work is to be submitted for publication shortly after the conclusion of this dissertation.
- Chapter III describes the physical principles of interferometry which drive the design of the balloon instrument. We predict the sensitivity of the BETTII instrument and identify scientific targets and calibrators that are suitable for our first flights.
- Chapter IV is a standalone, refereed paper that was published in 2015 on the spectral sensitivity of double-Fourier interferometers in general. It proposes a mathematical framework to analyze the sensitivity of such instruments to various types of noise sources. We apply those findings to the case of BETTII.
- Chapter V discusses the design of the control system for BETTII, which presents unique challenges compared to any other balloon-borne instrument. We also discuss the controls algorithm that is used in flight to properly estimate the orientation of the payload, a key requirement to achieve successful interferometry.
- Chapter VI shows results of the implementation of the control system on BETTII. This consists of laboratory and on-sky testing of BETTII at GSFC.

- Chapter VII summarizes our findings and discusses the path forward for the BETTII project.

BETTII will be shipping out to Fort Sumner, New Mexico, for its first balloon flight in early August. The flight window is from mid to late September. The technical work in chapters III to VI plays a key role in the success of this first flight.

Chapter I

Star Formation in Clustered Environments

This chapter is an introduction to some of the concepts which play a role in the formation of stars. First, we discuss properties of the molecular clouds which are the sites of star formation. Second, we elaborate on the physics of the star-forming processes and the evolutionary stages in star formation. Third, we discuss the properties of the dust, which is the main observable of relevance for the rest of this thesis. This chapter is not meant to be an exhaustive review of the field, but instead explains the aspects of the star formation phenomenon which are important to understand when designing an observatory to study it.

I.1 Molecular Clouds

Molecular clouds are dense regions of the interstellar medium (ISM) where stars are forming. They contain about half the mass of the ISM in $< 2\%$ of its volume (see Kennicutt et al., 2012, and references therein). High densities ($n \gtrsim 1000 \text{ cm}^{-3}$) of mostly molecular hydrogen and low temperatures ($< 20 \text{ K}$) distinguish molecular clouds from the other

major components of the ISM in galaxies: the Hot Ionized Medium, the Warm Neutral Medium, the Warm Ionized Medium, and the other cold phase of the ISM, the Cold Neutral Medium, which is thought to be the parent medium from which molecular clouds are formed. In addition to molecular hydrogen, molecular clouds contain Helium (cosmic abundance of 10% by number), dust ($\sim 1\%$ by mass), CO ($\sim 1 \times 10^{-4}$ by number), and traces of many other molecules.

Observations reveal that molecular clouds are highly structured often with filamentary structure on a range of spatial scales (Heyer et al., 2015; André et al., 2010; André et al., 2014; Williams et al., 2000). We are particularly interested in the star formation process in these regions so our focus is on the youngest systems, $\lesssim 2$ Myr, where stars are often still embedded and may not yet have accreted the majority of their final mass.

Approximately 60% of all stars are thought to form in embedded, young stellar clusters with 100 or more stars (Porras et al., 2003; Allen et al., 2007). These >100 star clusters have characteristic sizes of 2-4 parsecs (pc) with peak surface densities of >10 stars per square parsec and a typical median distance between nearest neighbor young stellar objects (YSOs) <0.06 pc (Gutermuth et al., 2009).

Because star-forming clusters are surrounded by interstellar matter from the parent molecular cloud, they usually cannot be studied at optical wavelengths, due to the large obscuration from dust grains along the line of sight. Infrared observations can be used to probe these structures since the dust can acquire sufficient temperature to emit thermally from the mid-infrared through millimeter wavelengths.

The high density of YSOs within clusters, combined with their typical separations of few hundredths of parsecs requires a high angular resolution in order to capture the relevant spatial scales to identify individual sources and probe their physical characteristics.

I.2 Star formation

I.2.1 Standard models

A considerable literature exists on the theory of star formation and the various physical processes involved in forming stars (e.g. Evans, 1999; McKee et al., 2007; Portegies Zwart et al., 2010; Kennicutt et al., 2012; Hennebelle et al., 2012, and references therein). In this section, we review some of the most standard views that describe how stars are born and grow to acquire their final masses.

I.2.1.1 Gravitational collapse

The simplest way to derive characteristic quantities related to the formation of stars is to consider a pre-stellar core as a spherical clump of uniform, isothermal gas in hydrostatic equilibrium (no magnetic field or turbulence). For such a system, the Virial theorem applies, which describes the balance between the gravitational potential and the kinetic thermal energy within the gas. In other words, in hydrostatic equilibrium, the core's self-gravity is compensated by the internal pressure caused by the temperature of the gas. If the temperature decreases, or if the core mass increases, the core will contract and can become unstable to further contraction. While simplistic, this treatment leads to a handy derivation of critical timescales, sizes, and masses that form a good starting point for more elaborate theories.

First, it is important to determine what are the characteristic timescales of star formation. In the core with a uniform density, the simplest timescale to define is called the free-fall time t_{ff} : this is the time it takes for the total gravitational collapse of a spherically-symmetric clump of uniform density ρ if only the force of gravity is considered

(no pressure):

$$t_{\text{ff}} \sim \left(\frac{3\pi}{32G\rho} \right)^{1/2} \sim 1 \times 10^6 \text{ yr} \left(\frac{n}{1000 \text{ cm}^{-3}} \right)^{-1/2} = 1 \times 10^6 \text{ yr} \left(\frac{\rho}{4 \times 10^{-21} \text{ g cm}^{-3}} \right)^{-1/2}, \quad (\text{I.1})$$

where we have substituted a typical value for the particle density in molecular clouds $n \equiv n_{H_2} \approx 1000 \text{ cm}^{-3}$, and also converted it into a mass density, using a mean molecular weight $\mu = 2.33$ (corresponding to a Helium abundance of 10% in number as in McKee et al. (2007)). The free-fall time is usually a lower limit on the collapse timescale, since there can always be some physical mechanisms such as thermal and turbulent pressure or magnetic fields that oppose gravity and slow down the infall of gas into the potential well.

The other relevant quantity that involves time is the sound speed in the cloud, $c_s = (kT/(\mu m_H))^{1/2}$, where $\mu \approx 2.33$ is the mean molecular weight of the gas and m_H the mass of hydrogen. For a given spatial scale R , the sound-crossing time is defined as $t_s = R/c_s = 4.9 \times 10^5 \text{ yr} \left(\frac{R}{0.1 \text{ pc}} \right) \left(\frac{c_s}{0.2 \text{ km s}^{-1}} \right)^{-1}$. This is the time it takes for a wave to cross the scale R while traveling at the sound speed. Intuitively, if the core has a size R such that $t_{\text{ff}} < t_s$, it tends to collapse faster than the gas on larger scales in the cloud can react. This corresponds to a size scale that is called the Jeans' length, and corresponds to the characteristic size scale of gravitational instability within a cloud (McKee et al., 2007):

$$\lambda_J = c_s \times t_{\text{ff}} = 0.2 \text{ pc} \left(\frac{c_s}{0.2 \text{ km s}^{-1}} \right) \left(\frac{n}{1000 \text{ cm}^{-3}} \right)^{-1/2}. \quad (\text{I.2})$$

The Jeans mass is the amount of mass within a sphere of diameter λ_J , and corresponds intuitively to the characteristic mass of a core that can undergo gravitational

collapse:

$$M_J = \frac{4\pi}{3} \rho \left(\frac{\lambda_J}{2} \right)^3, \quad (I.3)$$

$$= 0.3 M_{\odot} \left(\frac{c_s}{0.2 \text{ km s}^{-1}} \right)^3 \left(\frac{n}{1000 \text{ cm}^{-3}} \right)^{-1/2}. \quad (I.4)$$

Note that this formalism ignores the material that surrounds the core while it collapses. In practice, the cloud exerts an external pressure on the core that needs to be taken into account when calculating the critical masses. This case of a clump of self-gravitating gas that is immersed in a medium of external pressure P_{ext} is called a Bonnor-Ebert sphere. It can be shown (McKee et al., 2007) that the sizescale for a critical Bonnor-Ebert sphere is similar to the Jeans' length, and the mass scale is:

$$M_{\text{BE}} = 1.18 \frac{c_s^4}{G^{3/2} P_{\text{ext}}^{1/2}}, \quad (I.5)$$

$$= 0.85 M_{\odot} \left(\frac{c_s}{0.2 \text{ km s}^{-1}} \right)^4 \left(\frac{P_{\text{ext}}}{3 \times 10^5 k_B \text{ cm}^{-3}} \right)^{-1/2}, \quad (I.6)$$

$$\sim 2.73 M_J. \quad (I.7)$$

where we have used the characteristic turbulent pressure in molecular clouds, $P_{\text{ext},0} = 3 \times 10^5 k_B \text{ cm}^{-3} \text{ K}$, for the external pressure term (McKee et al., 2007) (k_B is the Boltzmann constant). The turbulent pressure is dominant over thermal temperature on the large scale in molecular clouds because the observed turbulent velocities are supersonic (by factors of 5-10) compared to the sound speed in gas at 10 K temperature .

This turbulent nature of cloud can drive local overdensities which reach and exceed the Jean's or Bonnor-Ebert masses in regions where turbulent cells collide. The overdense region can then fragment into multiple centers of collapse, each of which will lead to a

star. Accretion from the turbulent surrounding core material may occur throughout this process. Within these centers of collapse, gravity is dominating the evolution and it is still useful to refer back to simple, symmetric accretion model for overall guidance.

In the simple model, the collapse from a Bonner-Ebert sphere results in an infalling envelope with density profile which follow power laws from $r_{\text{env}}^{-1.5}$ to r_{env}^{-2} , an important observable that can be useful to testing models. Some models of slowly-rotating infalling clouds suggest more complex density profiles for the envelopes (e.g. Ulrich, 1976; Terebey et al., 1984) than simple power laws, but differences from the traditional power-law envelope have been observationally difficult to constrain due the scales at which those differences become significant, 100-1000 astronomical units (au).

Nevertheless, it is expected that collapsing cores will have some amount of angular momentum and that angular momentum becomes significant with the material is falling from 1,000's of AU to stellar scales, roughly 6 orders of magnitude. Due to conservation of angular momentum all of the material cannot fall directly onto the star and some creates a circumstellar disk. Observationally, we know that the process by which this disk material accretes onto the star is associated with outflows of material along the rotation axis, which are called bipolar outflows, and these outflows carve out a cavity in the envelope along the axis of rotation of the star.

The object now has three characteristic components: the star itself; the flattened circumstellar disk; and a diffuse envelope with an open cavity, which constitutes a mass reservoir for future accretion onto the star. A cartoon of the protostar is shown in Fig. I.1.

Although most of the mass is contained in the H₂ gas, there is a small fraction of material in the form of dust grains of various sizes and populations. Despite their low mass, these grains play a very important role in determining the observable properties

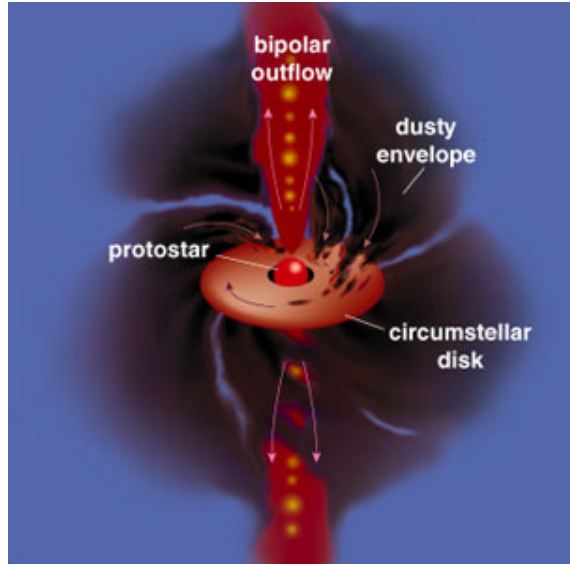


FIGURE I.1: Cartoon of a protostar (Greene, 2001) with the envelope, a flattened circumstellar disk, the bipolar outflow/cavity, and the protostar at the center. A typical scale for the envelope of a young object is $\sim 10\,000$ au.

of YSOs, because they absorb short wavelengths and radiate in the thermal infrared (see Section I.3).

I.2.1.2 YSO classification and characteristics

The observational characteristics of YSOs are dominated by emission from the star, disk, and envelope, and the evolution of these components is reflected in the evolution of these observable characteristics. The star is fairly well understood as an object in rough hydrostatic equilibrium that is accreting material on its way to the main sequence. The luminosity of a YSO is a combination of internal stellar luminosity which is due to Kelvin-Helmholtz contraction and/or hydrogen burning in the core, and accretion luminosity; in all cases, the dominant luminosity is created within 1 to several stellar radii. The spatial distribution of gas in the disk and the envelope changes as the YSO evolves and is primarily responsible for the observable emission at infrared through millimeter wavelengths. Simple models assume that the material distribution is axially symmetric, but in all likelihood it

is more complex. For clarity, we will discuss here the simple models that can be used to describe the YSOs in the primary stages of their evolution.

In the most common model of the evolution of young stars, there are four stages in the lifetime of a YSO. The first stage consists of a dense core right after the YSO is born. The disk is almost non-existent, the envelope still is dense and circularly symmetric. This is called Class 0. As the system evolves, the YSO grows in mass, an outflow forms and increases the opening angle creating a bipolar cavity in the envelope, the density of the envelope decreases, and the size of the disk increases.

The classes of YSO, from 0 to III, are defined by their broad emission spectra, called Spectral Energy Distributions (SEDs), although the actual observed SED of a specific YSO is dependent on our viewing angle. In practice, since it is generally difficult to obtain full SEDs from optical to millimeter wavelength for large numbers of YSOs, the most commonly used tool to classify YSOs based on the spectral index of the emission, which is defined as the near-IR to mid-IR wavelength slope of the emission, α , in the log-log plots, with $\alpha = d(\log \lambda F_\lambda)/d(\log \lambda)$ between 2 to 20 μm (McKee et al., 2007). Various authors propose different different boundaries for α corresponding to each class. The four classes of YSOs are:

- Class 0: Most the of short-wavelength ($< 10 \mu\text{m}$) light is highly obscured by the dust in the massive envelope. Most of the emission is around $100 \mu\text{m}$ and into the submillimeter/radio regimes. If there is a disk, it is very small. Some authors (Dunham et al., 2010) classify a source as Class 0 as long as the amount of the mass in the envelope is at least half the total mass. The typical spectral index is a positive number typically > 1.5 .

- Class I: Light scatters at short wavelength off the dust grains to give us a hint at the embedded object, but it is still very obscured. The envelope's mass is lower, and the disk extends to larger distances. The typical spectral index α is $0 < \alpha < 1.5$.
- Class II: The YSO is now a pre-main sequence star, with a spectral index $-1.5 < \alpha < 0$ and a significant circumstellar disk. This is traditionally referred to as a classical T-Tauri star.
- Class III: Still a pre-main sequence star, but most of the accretion has stopped, and $\alpha < -1.5$. The envelope has almost completely disappeared, and so has most or all of the disk, as traced by infrared excess emission.

An illustration of canonical SED and density structure is shown in Figs. I.2 and I.3 for the four main classes, with parameters taken in Whitney et al. (2003b)¹. On the left of each picture, the SED is the measurable quantity when the YSO is unresolved at all wavelengths. The challenge is to estimate the density structure (to the right) by measuring the SED. The different lines plotted in the SEDs are different inclination angles, highlighting the enormous impact of the viewing angle on the potential interpretation of these SEDs. The dashed line corresponds to the Planck function from the central source. These models were run using the Hyperion software (Robitaille, 2011) with "OH5" dust (Ossenkopf et al., 1994), as discussed in more details in Section I.3.

These SEDs can also be characterized and classified with a numerical observational metric such as the bolometric luminosity (Myers et al., 1993; Dunham et al., 2010):

$$L_{\text{bol}} = 4\pi d^2 \int_0^{\infty} S_{\nu} d\nu, \quad (\text{I.8})$$

¹except for the Class III model, for which we reduced the envelope mass by 3 orders of magnitude, as we think it is more representative of these objects

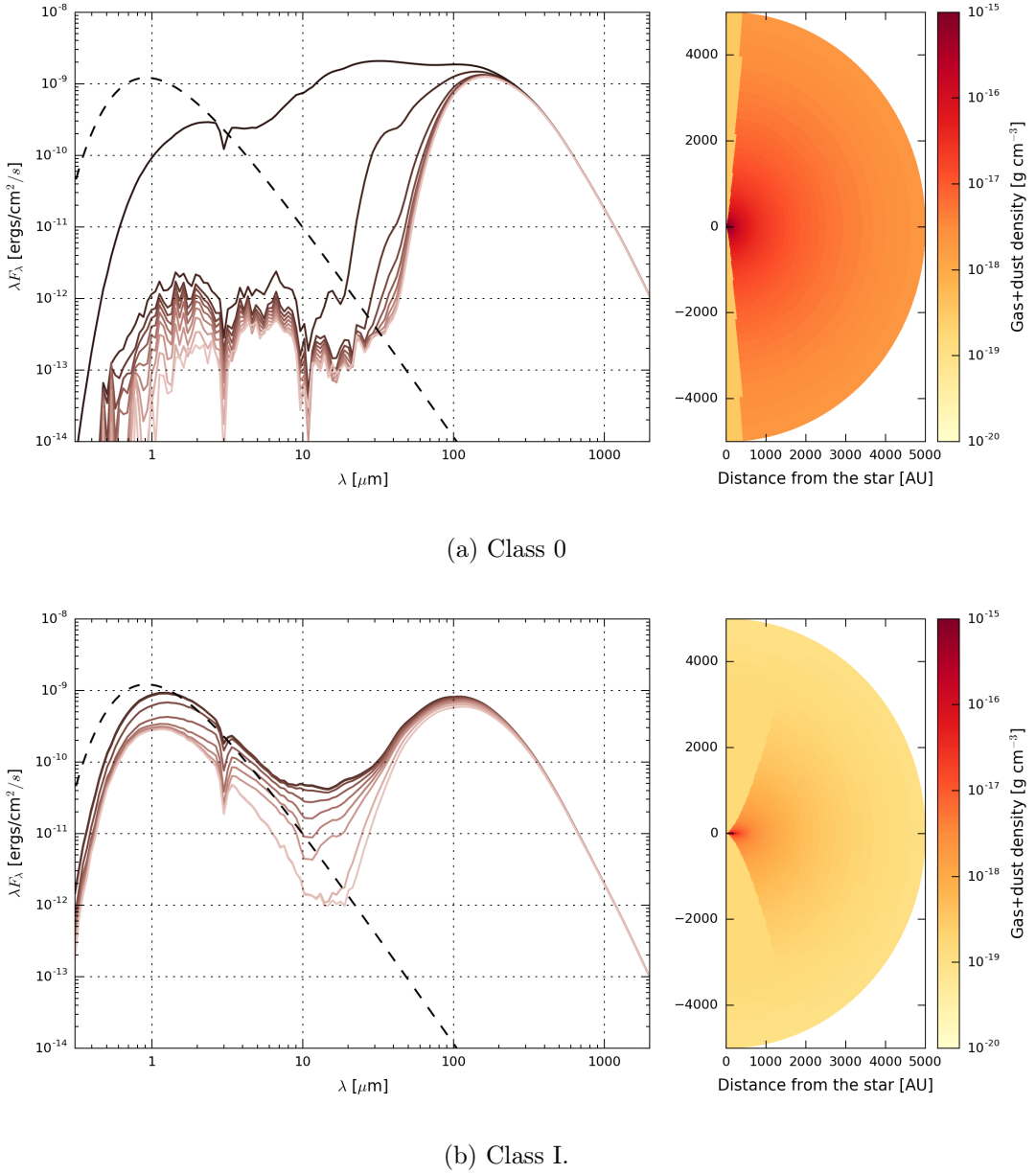


FIGURE I.2: Early evolution of YSOs. The left panel shows the spectral energy distribution (SED) of the object. Lines of different colors show different inclination angles. The dashed line corresponds to the SED of the central object only. The right panel shows a cross-section of the mass density (including both gas and dust) profile used in the modeling. Darker colors indicate higher densities. In this model, the cavity is in the up/down direction, coaligned with the circumstellar disk axis. The circumstellar disk is present in those models, although difficult to distinguish in the density maps because of its small scale.

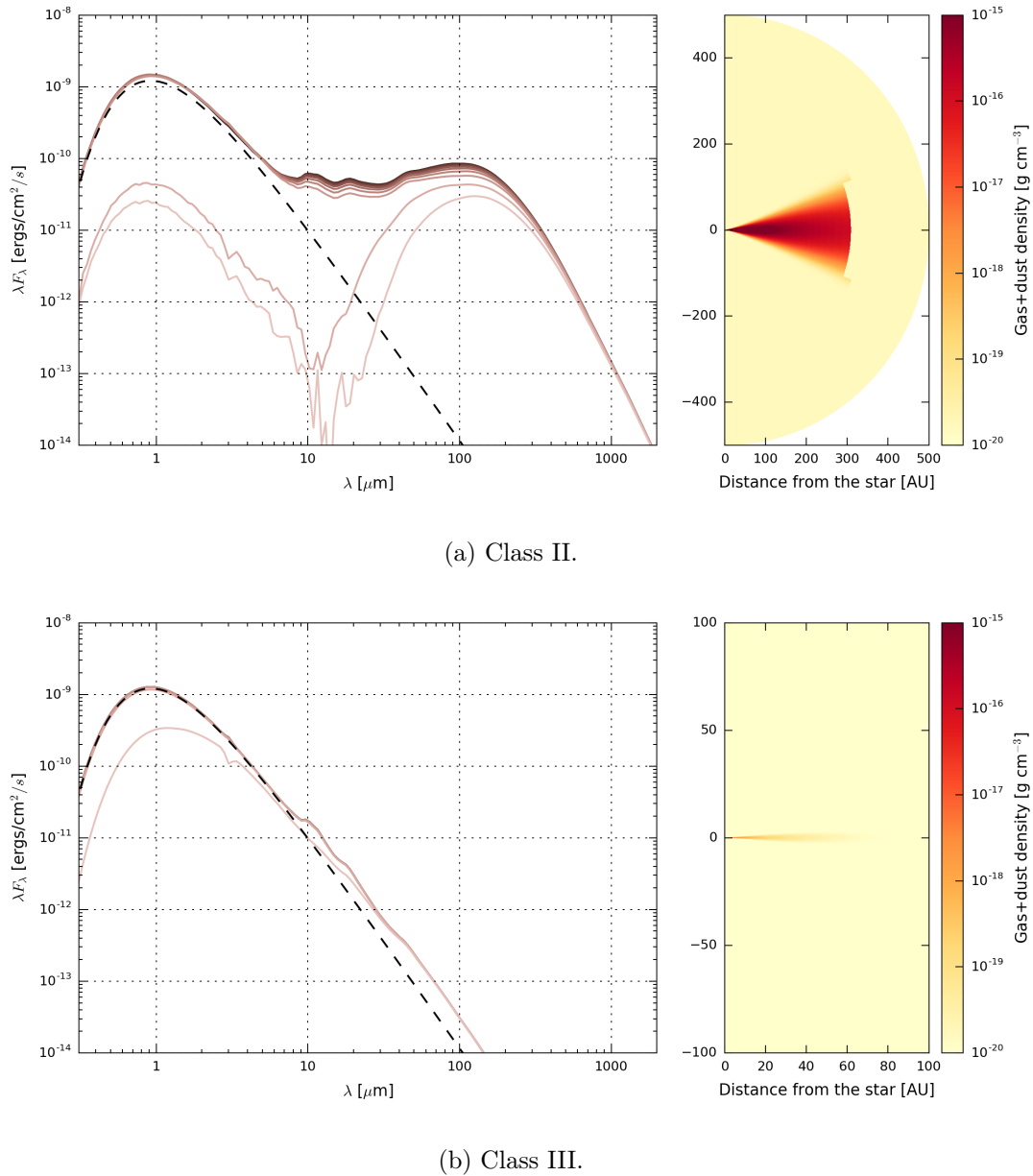


FIGURE I.3: Late evolution of YSOs.

where S_ν is the flux density in $\text{W m}^{-2} \text{Hz}^{-1}$. We will use the bolometric luminosity later in our analysis of our SOFIA FORCAST data as it is a direct observable, whereas the "true" luminosity of most YSO system can only be derived from modeling, and the derived answer is model dependent.

I.2.2 Mass accretion in clusters

The discussion in the previous section represents a simplified view of how a single core collapses and forms a star. While it is convenient to assume that the original core forms from a fixed reservoir of gas that will determine the star's final mass, it is likely too simplistic, since YSOs are preferentially forming in cluster environments with multiple other YSOs nearby and sharing a dense, often turbulent environment (Porras et al., 2003; Allen et al., 2007; Gutermuth et al., 2009).

The answer to how stars acquire their final mass is a key issue in star formation. Does dense gas fragment into isolated centers of collapse? Do young stars competitively accrete material from a surrounding common reservoir? Do gravitational interactions between forming young objects play a significant role in setting the final stellar mass function? Better observational understanding of these clusters is necessary to address these questions and to discriminate between the different models, as noted by Bonnell et al. (2006), Offner et al. (2011) and Myers (2011).

Given the typical stellar separations in clusters with fully formed YSOs and the typical densities of gas in these cores, several 1000s of au ($1 \text{ pc} = 206\,265 \text{ au}$) is the size scale over which forming stars must draw material to become $0.5\text{-}10 M_\odot$. Once the material is inside a few 100's of au, it is strongly bound to the forming stellar system (which may be one or more stars) and its fate is determined. To give an idea of the possibilities for accreting

material, Fig. I.4 sketches three scenarios for how stars could capture mass in the cluster environment: (a) core collapse, (b) competitive accretion, and (c) collisional merging. In core collapse (CC) (Fig. I.4a, McKee et al., 2003; Myers, 2011), the cluster's gas fragments into cores which collapse individually to form single, binary, or small multiple star systems; the available mass is defined by the original fragment. In competitive accretion (CA) (Fig. I.4b, Bonnell et al., 1997), the initial core collapses but contains a small fraction of the star's final mass; additional mass is captured competitively with other forming stars from the surrounding dense core gas. In collisional merging (CM) (Fig. I.4c, Bonnell et al., 2002), the initial fragments interact gravitationally and form larger mass cores before and during the formation process.

Are all these processes observed at once in star forming clusters? Only one? What conditions favor one versus the other, and why? Do different processes dominate at different stages in the cluster's history?

Recent studies by Offner et al. (2011) and Myers (2011) compared protostar luminosity distributions with predictions of models based on these ideas. Offner et al. (2011) suggest that both CC and CA could work if the star formation rate in the cluster increases with time; (Myers, 2011) finds that a CA-type model with additional Bondi accretion to produce massive stars works best. As highlighted at the end of the Offner et al. (2011) paper, larger cluster samples and better data on massive stars are needed to improve the observational constraints on models.

I.3 Dust as a tracer of star formation

Despite being a small component by mass, interstellar dust is an important tracer of star formation activity and its absorption and emission of radiation is an important factor in

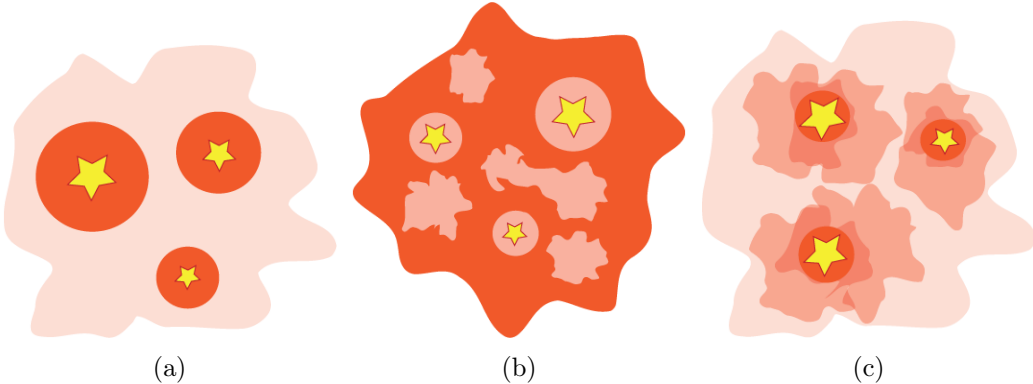


FIGURE I.4: Three scenarios of clustered star formation: (a) core collapse, (b) competitive accretion, and (c) collisional merging. Darker colors indicate higher densities.

the evolution and outcome of the star formation process. Dust grains are heated up by absorbing the short wavelength emission from stars and re-radiate in the thermal infrared, accounting for $\sim 30\%$ of the total luminosity of the galaxy (Mathis, 1990).

Observationally, dust plays perhaps the most important role when it comes to studying star formation. It usually is assumed that dust is well mixed with the gas, which makes it an excellent tracer of the gravitational well and mass distribution in YSOs. Because H₂ and He molecules have very few spectral signatures at temperatures below 100 K, they are difficult to observe and study directly. Dust grains block UV and visible star light and emit continuum far-IR radiation, opening a large region of the electromagnetic spectrum for astronomers to study the properties of star formation. Alternative tools to study star formation are dedicated to observing spectral lines of the molecular species of the ISM such as CO and other dense gas tracers, which reveal information about the dynamics of the gas in these regions.

I.3.1 Dust populations and properties

One of the best early studies of the composition of dust grains in the ISM was done by Mathis et al. (1977), where they studied the absorption spectrum of the diffuse ISM, and found that the measurements were appropriately fitted with a dust grain composition of silicates and small graphite particles (Stecher et al., 1965). They were able to fit the observed extinction curve with a grain-size distribution, typically $n(a) \propto a^{-3.5}$, where a is the grain size (assuming spherical grains) and $n(a)$ corresponds to the number of grains of size a . This distribution requires low and high cutoffs for the grain sizes, typically 50 Å and 0.25 μm, respectively (Weingartner et al., 2001).

This grain size distribution model was later enhanced by Cardelli et al. (1989) to account for the difference in interstellar extinctions (hence grain size distributions) across different galactic lines of sight. These authors were able to successfully parameterize the grain size distribution using a single parameter, R_V , which is the ratio of the total extinction $A(V)$ to selective extinction² (or color) $E(B - V) = A(B) - A(V)$. The distributions of sizes of graphite and silicate grains vary between the low density regions of the ISM, where $R_V = 3.1$, and the high density regions, where $R_V = 5.3$ (Kim et al., 1994).

Observations in the thermal infrared from space telescopes have detected strong absorption lines at 9.7 μm and 18 μm which are attributed to stretching mode of Si-O and bending mode of O-Si-O, confirming the presence of silicates in dust compositions (Weingartner et al., 2001). Other emission features at 3.3, 6.2, 7.7, 8.6, and 11.3 μm (Sellgren, 1994) are attributed to bending and stretching modes of polycyclic aromatic hydrocarbons (PAH, see Gillett et al., 1973; Allamandola et al., 1985), which are complex, planar organic molecules.

²Extinction and colors are expressed in magnitudes

A consolidated model matching all-sky measurements by the COBE, IRAS and *Planck* missions confirms the composition of amorphous silicates and carbonaceous grains with sizes ranging from large grains ($\approx 1 \mu\text{m}$) down to tens of atoms (*Planck* Collaboration et al., 2016), where the larger carbonaceous grains have graphitic properties and the smaller population have PAH-like properties.

In the very cold and dense regions surrounding a YSO, where the dust temperature typically never exceeds a few tens of K, it is expected that these dust grains are covered by a mantel of ices which can dramatically change their radiative properties, especially at short wavelengths (e.g. Ossenkopf et al., 1994). It is also expected that the grain size distribution will shift to larger sizes due to coagulation of grains.

Knowledge of the dust composition and size distribution of grains is important to properly characterize its observational characteristics and relate its measured emission to the physical quantities of interest in astronomical objects. Unfortunately, the properties of dust grains, especially in the range of circumstellar environments of direct interest to modeling the infrared emission from YSOs, are not yet well known. Calculated dust models can provide the quantities that are needed in radiative transfer modeling (see Section I.3.3), such as the albedo, the scattering function, and the opacity, but knowledge of the calculated properties should not be mistaken for accurate knowledge of the true grain properties in a YSO's environment.

I.3.2 Basics of dust extinction

Dust grains are responsible for the extinction within molecular clouds, inside of clusters, and in the environment each YSO; in principle, each region, and even different regions

within the YSO environment could have significantly different grain populations. The typical representation of the extinction along a line of sight uses the ratio of observed flux over the expected flux, measured in V-band: $A_V \equiv A(V) = 2.5 \log(F_\nu^{\text{obs}}/F_\nu)$; this definition puts the visual extinction in the astronomical units of magnitudes. The extinction as a function of wavelength, $A(\lambda)$, then expresses the light absorption property of dust in magnitudes for different wavelengths. An alternative representation is to consider the extinction as being caused by an optical depth τ_{ext} such that $\exp(-\tau_{\text{ext}}) \equiv F_\nu^{\text{obs}}/F_\nu$. The two definitions have the equivalence $A(\lambda) = 1.086\tau_{\text{ext}}(\lambda)$.

At sufficiently long wavelength, dust opacity models can usually be represented by a simple power-law, $\kappa_\nu = \kappa_0(\nu/\nu_0)^\beta$, with the index β depending on the specifics of the dust model (Draine, 2011). The opacity κ_ν is expressed in $\text{cm}^2 \text{g}^{-1}$, and can be interpreted as a extinction cross-section per unit mass. Most dust models assume a 1:100 dust-to-gas ratio, and derive opacities per unit gas+dust mass, instead of just dust mass. From a radiative transfer perspective, the observed specific intensity from a thermal source $B_\nu(T)$ at temperature T in the optically thin regime is $I_\nu = \int B_\nu(T)d\tau_\nu$, where the optical depth is $\tau_\nu = \int \kappa_\nu \rho_{\text{dust}} dl$. In this expression all quantities depend on the location l along the line of sight. If T , κ_ν , and ρ_{dust} are constant along the line of sight, this simplifies to:

$$I_\nu = \tau_\nu B_\nu(T) = \kappa_\nu \rho_{\text{dust}} L B_\nu(T) = \kappa_\nu \sigma_{\text{dust}} B_\nu(T), \quad (\text{I.9})$$

where we define σ_{dust} as the mass surface density.

A measure of the intensity from a source can thus lead to an approximation of the total mass within a primary beam of the observation, for a given dust grain model. For a source with a measured sub-millimeter flux density S_ν , in the optically thin regime we can

write $S_\nu = \kappa_\nu \sigma_{\text{dust}} B_\nu(T) \Omega$, where Ω is the solid angle of the source. At a distance d , the mass is $M \approx \sigma_{\text{dust}} \Omega d^2$, which leads to (e.g. Shirley et al., 2000):

$$M = \frac{S_\nu d^2}{B_\nu(T_{\text{dust}}) \kappa_\nu}, \quad (\text{I.10})$$

with a dust temperature usually taken to be between 10 to 20 K for general regions of molecular clouds.

With only near- to mid-IR wavelengths observations (2-60 μm), however, it is more difficult to estimate the dust mass, because the system is usually not in the optically thin regime and cool dust at these temperatures emits weakly or not at all at 2-60 μm wavelengths. To use near- to mid-IR observations, which are interesting because they naturally sample material closer to YSOs, detailed radiative transfer models are usually required (see Section I.3.3).

The modeling requirements are especially important at short wavelengths where dust grains both scatter or absorb photons, and each process has its own frequency-dependent efficiency. Scattering mechanisms are more complicated to represent, as they usually involve a scattering phase function, describing the deflection angle of incident photons (which also depends on wavelength). Most models show that dust grains are preferentially forward-scattering (Draine, 2011). The emission at shorter wavelengths can also be affected by stochastic heating of small grains ($< 50 \text{ \AA}$), where single photons can heat up the grains to much higher temperatures for short amounts of time, resulting in a statistical distribution of dust temperatures for a single dust grain size.

I.3.3 Radiative transfer modeling

Several radiative transfer codes exist in the literature, and we have explored a few of them (DIRT, by Wolfire et al. (1986), HOCHUNK by Whitney et al. (2003a) and HOCHUNK3d by Whitney et al. (2013)). We opted for an open-source package called Hyperion (Robitaille, 2011), which has the advantage of having a Python interface and enjoys a relatively large community support. The code can accept different dust models and can generate various types of geometries and density grids. It contains the essential geometrical elements of a YSO: stars, disks, envelopes with cavities, which all have numerous parameters to describe their density structures. It can also accept user-generated, arbitrary density grids.

The radiative transfer code uses a Monte-Carlo technique to propagate packets through the density grid. The code uses an iterative process to follow the absorption and emission of radiation throughout the grid until an equilibrium solution is achieved. The code implements multiple techniques and proxies to improve the computation speed and the accuracy of the simulation, as explained in detail in Robitaille (2011). Beyond the traditional benchmarks used in that paper, we validate our specific usage of the Hyperion code by reproducing SED's from other authors (see Fig. I.2 and I.3 as examples of simulations using this code, which match the calculations in Whitney et al. (2003b)).

The Hyperion models (Robitaille, 2011) have a large number of parameters which describe a physical model for the star-disk-envelope system. As will be discussed in the next chapter, a number of these parameters are degenerate in terms of the calculated SED. At a broader level, SEDs models in general present a significant amount of degeneracy in terms of the derived physical properties of the systems, especially when the entire range of

wavelengths is not covered, as often is the case for observed sources. The reasons for the ambiguity are a combination of limitations of astronomical instrumentation and limitations on our knowledge of the physics in these regions. On the instrumentation side, observations are always associated with measurement errors; systematic calibration uncertainties are typically 5-20% at infrared wavelengths. Ideally, we would want information at scales from 1 au to 10's of au, but this is not achievable at infrared wavelengths for any star-forming region; instead, lower resolution observations can provide at best 100's to 1000's of au linear scales, which integrates over the spatial distribution of the emission and loses information about the source. On the physics side, the detailed distributions of grain sizes, compositions, and structures are not known, and may vary significantly between different parts of the YSO environment. In addition, geometrical effects such as viewing angles can dramatically change the SED shape, as it is illustrated in Fig. I.2 and I.3. Fundamentally, the SED alone can yield only limited information about the properties of the YSO system.

Other authors (e.g., Robitaille et al., 2006) have used similar codes to produce standardized grids of pre-computed models which randomly sample a very large number of source geometry parameters. These grids of models are routinely used by the community to fit a set of unresolved SED measurements at discrete wavelengths. However, most often the scatter in the parameters for the few best fit models prevents the authors from drawing meaningful conclusions on the observations. In Chapter II, we discuss this problem and offer an alternative method to determine the best-fitting models and the range in fitted model parameters.

One of the key challenges of using this code is to determine which dust models to use. For this work, we choose to use exclusively OH5 dust (Ossenkopf et al., 1994), which represents grains with an ice mantle which are the result of a coagulation phase of an

initial distribution of grain sizes following $n \propto a^{-3/2}$. This model was found to accurately represent some grain distribution in star-forming clusters (see e.g. Dunham et al., 2010).

I.3.4 Observing star formation

In the past decade, space-based infrared observatories such as *Spitzer* and *Herschel* have allowed the beginning of the detailed study of dust around forming stars, by sampling the SEDs in key spectral regions, such as the extended near-infrared (3-8 μm with the IRAC instrument on *Spitzer*), the mid-infrared (with the MIPS instrument on *Spitzer*, especially its 24 μm channel), and the far-IR (with the PACS and SPIRE instruments on *Herschel*). These single-aperture observatories have lead to major advances in our understanding of star formation on its largest scale.

However, these observatories lack the angular resolution required to observe the key physics of star formation in dense clusters in the key wavelength region between 30 μm and 400 μm . For a diffraction-limited single aperture telescope, the angular resolution and spatial resolutions (taken as full width half max or FWHM) are FWHM_θ and $\text{FWHM}_{\text{linear}}$ are:

$$\text{FWHM}_\theta \sim 15'' \left(\frac{\lambda}{70 \mu\text{m}} \right) \left(\frac{D}{1 \text{m}} \right)^{-1}, \quad (\text{I.11})$$

$$\text{FWHM}_{\text{linear}} = 0.04 \text{ pc} \left(\frac{d}{500 \text{ pc}} \right) \left(\frac{\lambda}{70 \mu\text{m}} \right) \left(\frac{D}{1 \text{m}} \right)^{-1}, \quad (\text{I.12})$$

which shows that even *Herschel* with its 3.5 m primary mirror and its 70 μm channel can barely resolve clustered YSOs (typical projected separations of a few hundredths of pc) for the closest star-forming clusters, let alone study the structure of a single YSO system in detail.

To further complicate the problem, most space observatories are designed to make very sensitive observations, so the brightest regions of clusters often saturate the detectors. This reduces the effective angular resolution and confuses the emission in regions of clustered bright YSOs with imaging artifacts. These two issues prevent scientists from gathering a good picture of the physics in these dense and important regions of stellar birth.

In the following chapter, we discuss SOFIA FORCAST imaging from 11 to 37 μm wavelength towards a number of dense star-forming regions which improve on *Spitzer* and *Herschel* in resolution. This is a first step towards a better understanding of these regions. In Chapter 3, we discuss BETTII’s design to provide even higher resolution SEDs from 30 to 100 μm wavelength.

Chapter II

Star Formation in Clustered environments with SOFIA FORCAST

II.1 Introduction

Most stars in the Galaxy form in cluster environments of sizes 2-4 pc, often containing more than 100 young stellar objects (YSOs), with typical separations of <0.05 pc between stars near their centers (Porras et al., 2003; Allen et al., 2007; Gutermuth et al., 2009). Previous studies have been effective in elucidating the young stellar content and distribution in clouds on large scales (parsec down to 0.05 pc) (Kennicutt et al., 2012), but young cluster cores, born in dense portions of molecular clouds, are more difficult to observe. They are obscured at optical through near-IR wavelengths. At mid-IR through far-IR wavelengths, the material surrounding YSOs and involved in the stellar birth process emits due to heating by the young stars, but the resolution to date has not been sufficient to isolate individual stars in the cores of most nearby young clusters.

Spitzer has tremendously advanced our understanding of star formation, by providing sensitive observations in continuum bands from $3.6\text{ }\mu\text{m}$ to $160\text{ }\mu\text{m}$. In particular, the IRAC instrument (with 4 bands from 3.6 to $8.4\text{ }\mu\text{m}$) and MIPS $24\text{ }\mu\text{m}$ channel provided a robust way to determine the spectral index of YSOs, hence leading to dramatic improvement of understanding of the YSO population in molecular clouds (e.g., Gutermuth et al., 2009; Gutermuth et al., 2011).

However, the most dense regions of clusters presented a challenge for the MIPS instrument, as the YSOs are too bright and/or in too close proximity, which led to saturation and confusion, as exhibited in Fig. II.1. In this figure, we show the same region seen by the IRAC $3.6\text{ }\mu\text{m}$ band, the MIPS $24\text{ }\mu\text{m}$ band, and the *Herschel* PACS $70\text{ }\mu\text{m}$, from left to right. While the IRAC instrument can clearly distinguish multiple objects within the region, the MIPS image is completely saturated, while the PACS image is confused and cannot properly resolve the individual objects due to the lower resolution of the *Herschel* telescope at $70\text{ }\mu\text{m}$. Note that these YSOs are much closer to each other than it is typical in clusters (0.01 pc instead of a typical value of 0.04 pc), however this scale of projected separation is not unusual at the centers of clusters.

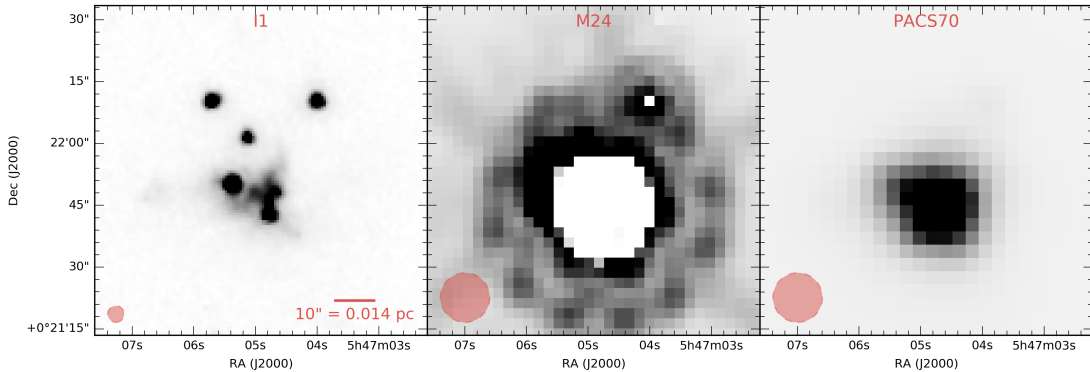


FIGURE II.1: Saturation and confusion in NGC2071.

Future instruments like BETTII will be able to tackle the confusion problem at

wavelengths from 30 to 100 μm , and be complementary to *Herschel* observations of star-forming regions. In the meantime SOFIA, the Stratospheric Observatory For Infrared Astronomy, can already start studying these dense regions, providing 2-3.5'' resolution between 10 and 37 μm , without the saturation problems present in the *Spitzer* data. This corresponds to a factor of 2-3 improvement in angular resolution over *Spitzer* at 24 μm .

II.2 Sample description and scientific goals

This chapter reports the results of a survey of nearby star-forming cluster cores with the SOFIA FORCAST instrument (Herter et al., 2012). The clusters were selected from a list of dense young clusters within 1 kpc of the Sun derived from works by Porras et al. (2003) and Gutermuth et al. (2009). From their lists we selected clusters that were: (1) north of -25° declination so that they could be observed from a northern hemisphere SOFIA flight; (2) included membership of >50 YSOs; and (3) included bright 8-24 μm sources within the dense cores based on *Spitzer* and/or WISE data.

We observed in four FORCAST science continuum bands: 11.1, 19.7, 31.5 and 37.1 μm , which covered the wavelength range available to the instrument at the time of proposal (2012). This wavelength coverage is complementary to archival data from *Spitzer* and *Herschel*. Our selection of bright regions spread all across the sky is convenient for SOFIA, as our project could be observed as a gap-filler between the primary science flight legs of other projects.

The main objectives of the survey are to gather statistics on the YSO content of the *Spitzer* saturated regions, and fill the SED gap between *Spitzer*'s bands and *Herschel*'s bands, when the latter are available. While most of our targets have valid *Spitzer* IRAC

data, often the data from the MIPS instrument is unavailable due to saturation or confusion. *Herschel* photometry usually is not published in the literature for our sources, but maps of our regions are sometimes available so we can retrieve the far-infrared fluxes for some sources. For the targets without MIPS or *Herschel* data, these SOFIA observations are the best information available between the longest IRAC band at 8 μm and the shortest submillimeter bands from ground-based telescopes. Thus our data provide important constraints the SED of very clustered YSOs in these regions to infer their physical properties.

The data analysis and scientific interpretation are presented in the next few sections. First, we describe our observations, as well as the archival datasets that we use to complement them. Second, we characterize the systematics of the FORCAST instrument and their variations over multiple science flights spanning multiple years. Third, the data reduction process is explained, followed by a snapshot of the data products themselves. Fourth, we discuss our SED fitting strategy, and fit the SEDs of some of our clusters to derive the physical properties of their embedded YSOs. Finally, we focus on the case of the young stellar cluster IRAS 20050+2720, and discuss of our FORCAST data helps us understand the physics of such embedded regions.

II.3 Observations

The FORCAST camera (Herter et al., 2012) has two separate 256×256 pixel infrared arrays that can image multiple bands in the wavelength range from 5.5-37 μm with $0.768'' \times 0.768''$ pixels. The two arrays can observe simultaneously through a dichroic beam splitter that divides the wavelength range shortward and longward of 26 μm . Alternatively, the long wavelength array can be used by itself with the dichroic removed from the light path,

gaining a sensitivity factor of ~ 2.5 . We observe the 11.1 and 37.1 μm together (hereafter "mode 1") and the 19.7 and 31.5 μm together (hereafter "mode 2") . We set the 1σ sensitivity threshold of the observations such that a a $1.5 L_{\odot}$ source with a moderately rising SED would be detected at all wavelengths. The integration times were scaled appropriately for the distance to the cluster (see Table II.1). This allows is to probe the same luminosity limit at all distances and obtain a consistent sample of YSOs.

TABLE II.1: List of desired sensitivities for different distances

Distance (pc)	1 σ minimum detectable flux (Jy)				Corresponding minimum L_{\odot}
	11 μm	19 μm	31 μm	37 μm	
200.0	0.1	0.1	0.32	0.7	~ 0.5
400.0	0.1	0.1	0.32	0.6	~ 1.5
600.0	0.05	0.04	0.18	0.25	~ 1.5
800.0	0.02	0.02	0.1	0.12	~ 1.5
1,000.00	0.01	0.01	0.06	0.1	~ 1.5

For the most nearby clusters (< 300 pc), the required observing time was so short that the overhead from the observatory was very costly. Hence, we put a lower threshold to the integration time of 30 s. Similarly, the sensitivity of the 37 μm band is such that in order to be consistent with our sensitivity target, this band was heavily driving the observing time in mode 1. Hence, we observe in this mode as long as is required to meet the sensitivity target for the 11 μm band, and obtained additional observations in the 37 μm band with the dichroic removed (hereafter "mode 3"). This allowed us to request less total observing time while achieving our sensitivity goals. A summary of our sensitivities for various distances is shown in Table II.1.

Several observing strategies are available to the FORCAST user to deal with background subtraction. The most robust techniques are very costly in terms of time overhead for the observatory, so we decided to request the cheapest observing mode: the Chop-Nod

mode (C2N), combined with 9 ditherings for each field, which dramatically helps when co-adding images together. Most of our data was processed by the SOFIA automated pipeline that provided calibrated Level 2 images, except for the data from the first few flights, for which we received the help of FORCAST’s Principal Investigator, Dr. Joe Adams, who processed the raw data through his own instrument pipeline.

The data were acquired over 10 SOFIA flights spanning multiple years, with the last batch dating from February 2015. The actual observing times for each band and cluster is shown in Table II.3. In that table, we have estimated the time for the $37\text{ }\mu\text{m}$ band using a composite formula that levels the observing time from mode 3 to that of mode 1, considering their respective sensitivities. We obtained about 10 h total of on-sky data, and 10 out of our 12 original target clusters were observed.

TABLE II.3: List of targets

Cluster	Coordinates (J2000)	SOFIA Flight IDs	N_{Fields}	d (pc)	T_{11} (s)	T_{19} (s)	T_{31} (s)	T_{37} (s)
Cepheus A	22h56m10s +62d03m26s	F132 F109	2	730	206	234	235	490
Cepheus C	23h05m45s +62d30m05s	F132	1	730	150	121	121	286
IRAS20050	20h07m05s +27d28m51s	F166 F131	2	700	321	224	256	266
NGC1333	03h29m00s +31d17m20s	F129 F193 F190	9	240	530	558	467	446
NGC2071	05h47m06s +00d21m45s	F192	2	420	36	25	33	42
NGC2264	06h41m07s +09d33m35s	F156	4	913	495	300	331	587
NGC7129	21h43m07s +66d06m42s	F109	1	1000	383	214	214	709
Ophiuchus	16h27m05s -24d30m29s	F157	11	150	396	468	501	365
S140	22h19m23s +63d18m44s	F129	1	900	322	393	393	568
S171	00h04m01s +68d34m50s	F132	1	850	253	219	219	476

Notes: For each cluster, we list the SOFIA flights on which the data was taken, the number of individual fields within the cluster, the distance, and the total integration time for each of the 4 observation bands, including all fields. The $37\text{ }\mu\text{m}$ time quoted is a composite time calculated by combining the exposure time of mode 1 with that of mode 3, as discussed in the text.

To complement our SOFIA observations, we obtained publicly available *Spitzer*, and

Herschel images. Most of our targets have already published *Spitzer* IRAC and/or MIPS photometry (mostly from Gutermuth et al., 2009; Megeath et al., 2012; Evans et al., 2009), which we use in the relevant cases. In the cases where no IRAC photometry was available, we applied our own photometry algorithms to publicly available archival images. We could not find published photometry for the targets with available *Herschel* images, hence we also used our own photometry pipeline to derive fluxes from archival images. In some cases, we found published submillimeter continuum measurements to help constrain the long-wavelength behavior of the SEDs.

II.4 SOFIA FORCAST characterization

In addition to the science images, a number of calibrators were observed during each flight for different dichroic settings and wavelength bands. These calibrators are usually bright stars which are point sources for SOFIA’s angular resolution, and have known mid-IR fluxes, so they can be used both for flux and PSF calibration. We use them for two purposes: the first is to obtain a robust metric to determine whether sources are extended or not; the second is to determine the aperture correction factor which will be used for aperture photometry of science sources.

II.4.1 PSF size

The size of the PSF can be defined in multiple ways. We adopt the approach of characterizing the PSF using its encircled energy distribution. Fig II.2 shows the average of the normalized encircled energy distribution of the PSF, measured on all the calibrators observed during our flights which use each filter settings. Each curve represents one of the five different combinations of bandpass filter and dichroic setting that we use for our

observations. For each radius, the total energy is the sum of the pixels within the circular aperture of that radius, to which we subtract an estimate of the background in an annulus around the source (see Section II.5.2 for details on the background subtraction methods).

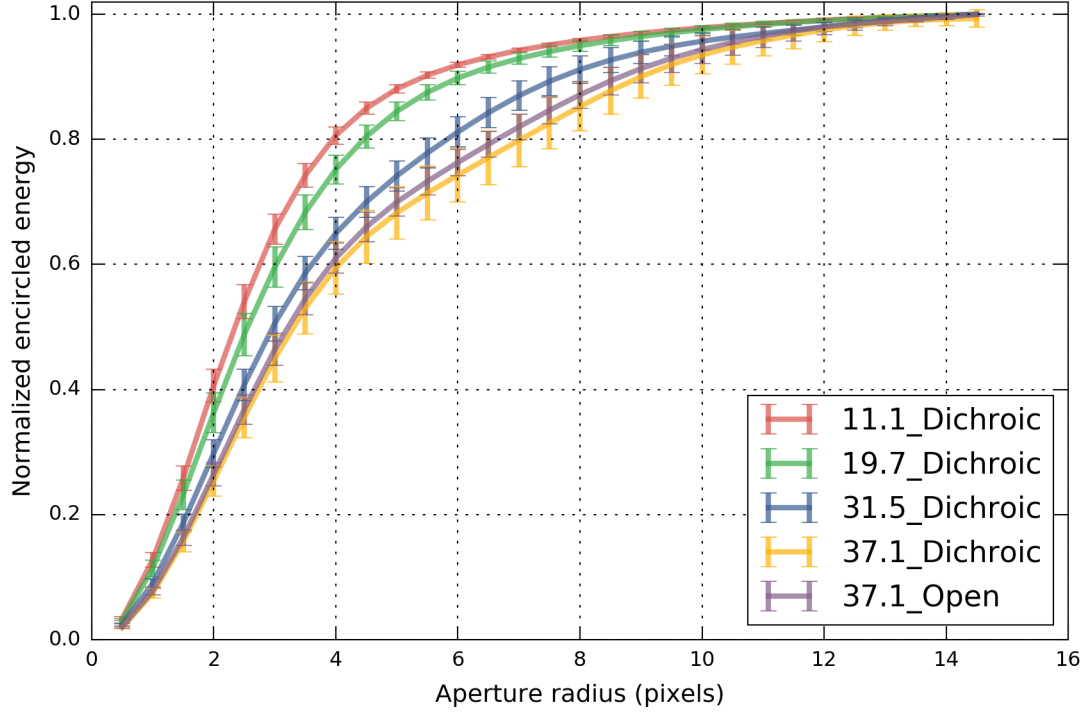


FIGURE II.2: Average PSF encircled energy distribution profile for all calibrator observations.

As expected, the PSF at $37.1\text{ }\mu\text{m}$ is larger than the PSFs at shorter wavelengths, but by less than the traditional diffraction limit rule. This indicates that additional PSF smearing is occurring at short wavelengths, likely due to telescope jitter and pointing errors, which is consistent with what other authors have found (e.g. Herter et al., 2013). Throughout all the flights, point source calibrators have the same encircled energy distribution shape within $\sim 4\%$ rms.

To look at the behavior of the PSF in more detail, we can use the full width at half maximum of the encircled energy distribution, FWHM, as a proxy for PSF size. The

variation of this quantity for the various flights, bandpass/dichroic setting, and calibrators used is showed in Fig. II.3. This shows the flight-to-flight differences and, for some calibrators, the in-flight variability. We find that the latter is usually small, except for the SOFIA flight on 05-02-2014, for which the spread is quite considerable and could have been caused by instrumental malfunction or abnormal levels of water vapor in the atmosphere. The variation from flight to flight is larger than the variation within a given flight, which indicates variability in the observing conditions, systematics, or thermal radiation environment of the observatory between different flights. Even considering the flight-to-flight and calibrator-to-calibrator variations, the overall spread in FWHM for a given observation setting is almost always less then 10%, making this metric a useful reference to compare with scientific data. In our analysis we will compute FWHM for our sources and compare it to the FWHM from the current flight for the same filter setting, if the calibration file exists. If no calibration observation exists for a given setting, we use the mean FWHM for that setting from calibrators observations in other flights. The ratio $\beta_{37} = \text{FWHM}_{\text{source}}/\text{FWHM}_{\text{cal}}$ helps quantify the extension of the source, to within $\sim 10\%$ confidence level.

II.4.2 Aperture correction factor

In Fig. II.2, we observe that the encircled energy does not vary much by an aperture with radius of 12 pixels, so we consider this fiducial aperture as our "total flux" aperture. The goal of aperture photometry is to estimate the amount of flux in this large aperture, which we consider to be the total amount of flux from the source, by only measuring flux within a much smaller aperture. This has the advantage of reducing contamination from other sources, and increases the signal-to-noise ratio of the flux estimate since the pixels near the tail of the PSF usually contain more noise than signal. In Fig II.4, we plot the aperture

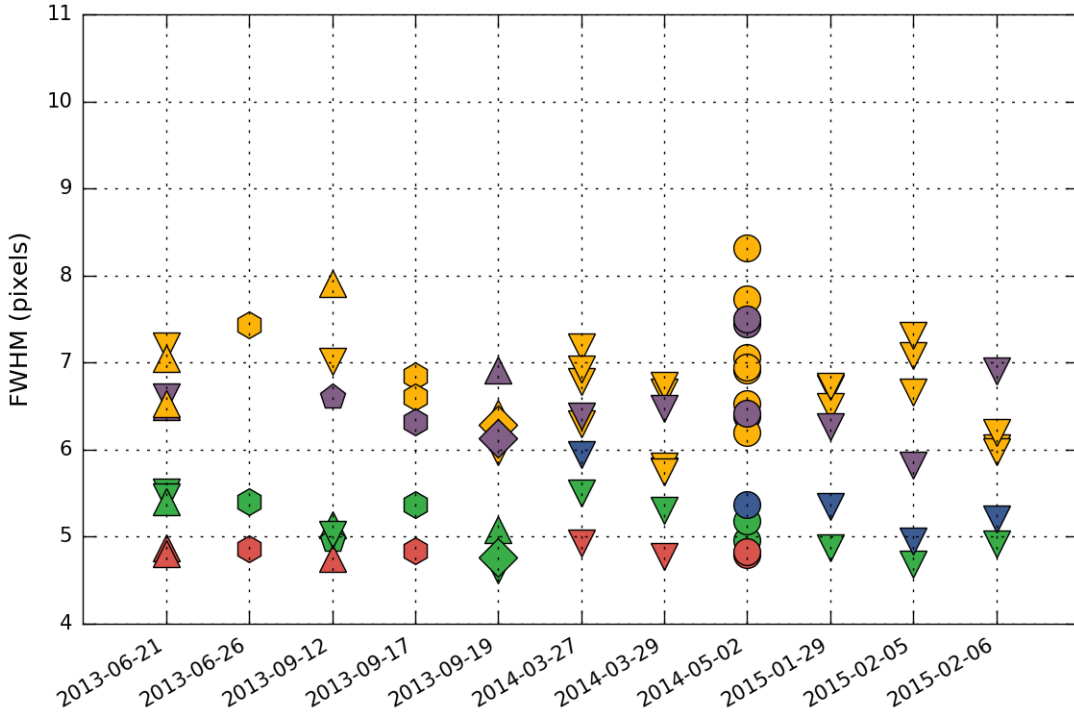


FIGURE II.3: Distribution of the FWHM for all calibrators observations within each bandpass. Lower wavelengths have lower FWHM. In red: 11 μm band, with dichroic; in green: 19 μm band, with dichroic; in blue: 31 μm band, with dichroic; in yellow: 37 μm band, with dichroic; in purple: 37 μm band, no dichroic. Down triangles: α Boo; Pentagons: α Cet; Diamonds: α Tau; Up triangles: β And; Hexagons: β Peg; Circles: β UMi.

correction factor that we compute from the ratio of the flux measured within an aperture of 3 pixels radius and this 12-pixel radius aperture. Not surprisingly, this graph follows very closely the plot of FWHM from Fig II.3, showing the close link between the aperture correction factor and the shape of the calibrator's PSF. We match each observation in our data to the mean of the aperture correction factors for the same observation setting and flight.

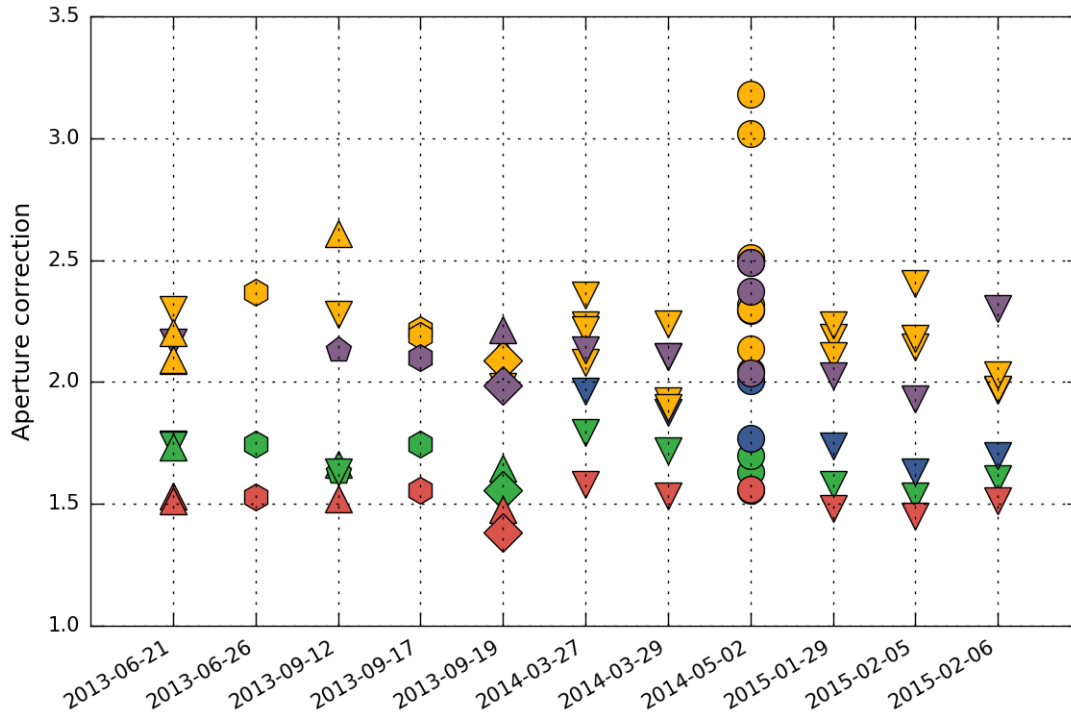


FIGURE II.4: Instrumental response and aperture correction. The color code and marker shape is the same as in Fig. II.3. Lower wavelengths usually have smaller aperture correction.

II.4.3 Instrument response and overall uncertainty

To validate our approach, we take a look at the calibrator fluxes after normalization by the calibration factor, which is provided directly by the FORCAST pipeline. This calibration factors converts the pixel digital value a physical flux density unit, and presumably is determined using the flux from calibrator stars as well. Here we re-measure the flux from each calibrator for each observation setting and each flight, using our standard aperture photometry method and background subtraction. Ideally, we would always obtain the same flux for each setting and calibrator, independently of the flight, an assertion we find true to within $\sim 5\%$ r.m.s (Fig II.5). The in-flight errors are typically lower than this. This validates our aperture photometry method, and we can trust that the instrument's

systematics are well-behaved to within these levels.

This would suggest that we can adopt systematic 1σ uncertainties of $\sim 5\%$, a value which is consistent with the published uncertainties of $3\sigma \approx 20\%$ (De Buizer et al., 2012). In an effort to be conservative, we chose to follow those authors and adopt a $1\sigma \approx 7\%$ systematic measurement uncertainty.

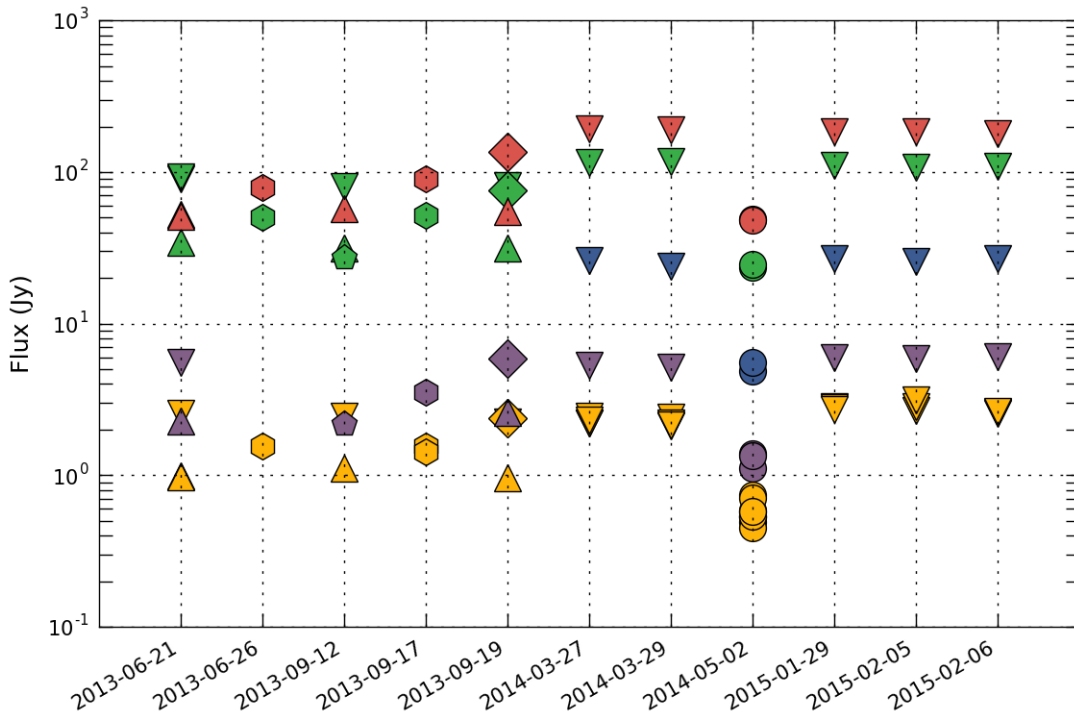


FIGURE II.5: Instrumental response, showing decreased calibrator fluxes with longer wavelengths, which is expected since all calibration targets are evolved stars. The color code and marker shape is the same as in Fig. II.3. In this plot, the variation across multiple flights for a given marker type of a given color is usually less than $\sim 5\%$. Note that for the bottom green triangles (α Boo at 19 μ m), there seems to be a systematic change between flights occurring before and after 2013-09-19.

II.5 Data reduction and photometry

The data were processed through various versions of the online pipeline to yield Level 2 data products available on the archive (Herter et al., 2013). We apply our own reduction procedure and photometry pipeline on those products to derive final images, source positions, fluxes and sensitivities. Our software makes extensive use of the Python *astropy* package (Astropy Collaboration et al., 2013) and its associated modules *photutils* and *APLpy*.

II.5.1 Pre-treatment

Some manual treatment of each image was necessary before it could be analyzed by our software. We followed this procedure: a) visually align the WCS coordinate system, often 10-20" off, using point sources and archival data from other wavelengths and facilities such as IRAC 8 μm ; b) crop the images to clean off the nodded fields, and c) identify the coordinates of each source, both point-like and extended.

After these manual steps, the Level 2 images are multiplied by the calibration factor provided by the online pipeline, which converts them to Jy/pixel. We do not proceed to any systematic color correction, but the effects on the fluxes are very small (Herter et al., 2013).

II.5.2 Source flux extraction

We fed the adjusted files to our photometry pipeline. For each identified source, we determine its flux in all bands using aperture photometry with local background subtraction. The aperture correction factor we used is the one determined from the calibrators observed

for the same observation setting during the same flight as the one when the data was taken. If a calibrator is not available during the flight, we use the average aperture correction factor taken over 9 of our 10 flights (we choose to exclude the flight on 05/02/2014 which seems to have abnormal behavior).

We distinguish between 3 types of sources after manual identification: *isolated*, which are point sources with no nearby objects; *clustered*, which are point sources with nearby objects; and *extended*, which are not consistent with being point sources based on visual inspection.

For point sources that are isolated, we use our standard aperture of 3 pixels at all wavelengths. We consider an annulus surrounding the source extending from 12 to 20 pixels radius (24 to 40 pixels for clustered sources): the local background is determined from the mode of the pixels in the annulus, while the sensitivity is calculated by measuring the standard deviation of the flux values within 3-pixel apertures spread over that annulus (Shimizu et al., 2016). We apply the aperture correction derived from the calibrator observations taken during that flight.

For extended sources, an elliptical aperture is determined manually from the $37\text{ }\mu\text{m}$ images. The local background is determined from the mode of an elliptical annulus, with an inner boundary at the elliptical aperture and an outer boundary corresponding to an ellipse 20% larger. The sensitivity quoted is the point source sensitivity, and is determined following the same method as for point sources, using the standard deviation of apertures spread across the elliptical annulus.

The photometry from sources that were observed in different flights is then combined to increase the signal-to-noise ratio. This combination takes into account the sensitivity of each source by appropriately weighing each image.

The noise level calculated for the observation is added in quadrature to the systematic uncertainty of the instrument, for which we follow the recommendation from (Herter et al., 2012) and adopt a 7%, 1σ uncertainty.

TABLE II.5: SOFIA photometry comparison

SOFIA name	F11	F11L	F19	F31	F31L	F37	F37L
	Jy	Jy	Jy	Jy	Jy	Jy	Jy
S140.3	10.28	9.70	101.49	419.41	401.00	525.90	669.00
S140.4	3.80	4.00	88.95	337.22	368.00	352.07	485.00
S140.5	110.57	110.00	830.97	2065.13	1585.00	2278.61	2176.00
Sum of sources in cluster	124.65	123.70	1021.40	2821.76	2354.00	3156.58	3330.00
Total cluster emission	135.20	145.00	1194.57	4449.46	3780.00	5840.64	6730.00
Ratio	1.08	1.17	1.17	1.58	1.61	1.85	2.02

Notes: Comparison of SOFIA four-band photometry from Harvey et al. (2012) on S140 (columns with 'L'). All fluxes are in Janskies. The authors' "total emission" actually represents the total emission in the entire field of view, whereas our measurement corresponds to a manually-selected source region encompassing only the dense core. The total emission in the entire field of view is less representative, as it could include contribution from other sources as well as areas of negative flux from the chopping and nodding steps. In this cluster, there is a large amount of emission which is not clearly associated to the three identified sources.

To validate our flux extraction method, we compare our results with data from Harvey et al. (2012) who observed one of the sources in our sample, S140. Their photometry (shown in their Table 1) of IRS 1, 2 and 3 (corresponding to our targets S140.5, S140.4, and S140.3, respectively) is compared to our photometry in Table II.5. We find reasonable agreement between our fluxes and theirs, although some differences are larger than expected in the longer wavelength bands. We attribute this to differences in the exact centroid location of the sources, which could be due to a different aperture size. Centroid errors have more impact at longer wavelengths, where the flux is larger and the PSF wings more extended.

II.5.3 Image sensitivity

TABLE II.7: FORCAST Sensitivities

Cluster	F11			F19			F31			F37			Sources
	σ^{man}	σ^{std}	σ^{th}										
CepA	0.07	0.04	0.05	0.11	0.05	0.05	0.19	0.07	0.16	0.26	0.09	0.34	4
CepC	0.03	0.03	0.04	0.10	0.05	0.04	0.19	0.06	0.16	0.16	0.09	0.30	4
IRAS20050	0.04	0.03	0.04	0.08	0.04	0.05	0.13	0.05	0.16	0.30	0.11	0.32	7
NGC1333	0.12	0.04	0.07	0.07	0.07	0.07	0.22	0.08	0.25	0.48	0.13	0.52	11
NGC2071	0.19	0.10	0.12	0.32	0.15	0.15	0.21	0.22	0.49	0.45	0.28	0.81	6
NGC2264	0.07	0.03	0.05	0.19	0.05	0.06	0.28	0.07	0.20	0.21	0.09	0.43	21
NGC7129	0.07	0.03	0.03	0.10	0.04	0.03	0.26	0.09	0.12	0.17	0.08	0.19	5
Ophiuchus	0.11	0.05	0.08	0.16	0.07	0.08	0.31	0.09	0.27	0.41	0.18	0.65	19
S140	0.04	0.03	0.03	0.16	0.03	0.03	0.21	0.07	0.09	0.35	0.11	0.21	7
S171	0.04	0.03	0.03	0.07	0.04	0.03	0.07	0.05	0.12	0.16	0.06	0.23	2

Notes: For each band F11, F19, F31 and F37, we measure the 1σ sensitivity σ^{man} and σ^{std} in each field from the data using two different methods (see text), and present here the median of all fields. The theoretical sensitivity σ^{th} corresponds to the expected sensitivity for the actual integration time, using the SOFIA FORCAST observation planning tools and assuming moderate water vapor content. All sensitivity values are in Janskies.

In order to determine the absolute sensitivity in the image, we use two methods.

First, we manually determine a region near each cluster that visually appears devoid of sources. We calculate the sensitivity as if this background region was a source, by patching apertures in an annulus around this background location and calculating the standard deviation of the obtained fluxes. We call this sensitivity measurement σ^{man} . The main downside of this method is that it requires a manual operation to select the appropriate background field, and hence could have more variation depending on which field we select.

Second, we use a routine that iteratively isolates the pixel values above 2σ of the image, in order to remove the contamination from our actual sources. The standard deviation of the resulting image is then calculated, and is multiplied by the square root of the number of pixels in an aperture of 3 pixel radius. This corresponds to a floor sensitivity σ^{std} . We

present our results in Table II.7, where we also compare this sensitivity with the expected sensitivity σ^{th} obtained using the online calculator with the actual exposure time of our images. We note that usually, the theoretical values are more in agreement with our first method for F31 and F37, while more in agreement with our second method for F11 and F19.

II.5.4 Other photometry

SOFIA provides mid-IR photometry. We looked in the literature for published fluxes on our targets in order to reconstruct more complete SEDs. In addition to our four SOFIA bands, We collected data from 2MASS, *Spitzer*, and other instruments. Photometry from these sources is published in online catalogs, which we programmatically cross-reference with the positions of our targets. The closest target that corresponds to a Vizier location query is selected to be the correct catalog match. For the 2MASS data, the location of the target was required to be less than $2''$ away from our coordinates for point sources, and $5''$ for extended sources. For the *Spitzer* data, the matching radius is $3''$ for point sources and $10''$ for extended sources. In addition to automated online catalog searches, we add values for sources in NGC2071 from Kempen et al. (2012).

For our two most clustered regions, the cores of NGC 2071 and IRAS 20050+2720, the published catalogs do not have all available fluxes. We assume that the sources are so clustered that the source extraction software from the authors do not register them as point sources, due to confusion or saturation effects. Hence we adapt our own photometry routines for these clustered environments and obtain the fluxes directly from the calibrated Level 3 images, which are all available on the archive. In Table II.9, we compare our photometry results with published fluxes from Megeath et al. (2012) and Gutermuth et al.

(2009) for isolated sources elsewhere in these same fields of view. We use the *Spitzer* handbook recommendations for aperture photometry on *Spitzer* archival images ($2.4''$ aperture with and an annulus that extends from 12 to $20''$). We find that our results are within 10% of the other authors' results for isolated sources, which can reflect a simple difference in exact aperture centroiding position.

TABLE II.9: Spitzer photometry comparison

SOFIA name	i1	i2	i3	i4
	Jy	Jy	Jy	Jy
NGC2071.1	0.060	0.056	0.004	-0.021
NGC2071.3	0.018	-0.010	-0.004	-0.047
NGC2071.4	0.090	-0.054	0.036	-0.066
NGC2071.5	-0.130	-0.109	-0.144	-0.139
IRAS20050.1	0.020	0.039	0.017	0.131
IRAS20050.3	0.181	0.122	0.082	0.121
IRAS20050.6	-0.044	-0.046	-0.092	-0.056

Notes: Fractional difference between our own aperture photometry on *Spitzer* archival images and published *Spitzer* photometry from Megeath et al. (2012) for NGC2071, and Gutermuth et al. (2009) for IRAS20050+2720. When values are negative, it means that their photometry is lower than ours.

In some cases, we also found archival Herschel images, although no published photometry was available for most our sources. We then apply our same aperture photometry routines for those calibrated Herschel images, using aperture and background subtraction parameters from Shimizu et al. (2016) for the PACS and SPIRE. We find also very good agreement between our photometry results for the PACS $70\text{ }\mu\text{m}$ band and the published *Spitzer* MIPS $70\text{ }\mu\text{m}$ for some of these sources.

II.6 Data products

We identify 70 point sources and 14 extended sources in our sample. We produced three types of data products: the mosaic images in each band for all the clusters we observed; the photometry catalogs which can be used to make SEDs; and the fitted physical parameters for the point sources, which are determined from our radiative transfer model, explained in Section II.7.

II.6.1 Mosaics

The SOFIA FORCAST images consist of ~ 200 individual images, each representing a field at a given wavelength. Some fields are revisited multiple times when the entire observation could not be completed in a single flight leg. These individual fields are processed and mosaiced together to form one single map for each wavelength and each cluster.

Before mosaicing the fields, we did a 2D background subtraction. This method divides the images into sections of 50×50 pixels, estimates the median in each cell, and fits a 2D function to these median values. This function is used to construct a smooth background, which is then removed from the image. Each background-subtracted image is calibrated (using the calibration factor that is supplied by the FORCAST pipeline), and weighed by its exposure time before it is co-added into a mosaic in the WCS coordinate reference frame. Although these maps are useful for view the source distribution and spot artifacts, the actual photometry described in the previous sections uses each individual raw field, before the mosaicing and without our background subtraction (some level of background subtraction is already done by the SOFIA pipeline on the archive). If a source is present in multiple fields, the photometry from each of these fields is combined to provide

a better flux estimate.

In Fig. II.6 we present four maps from our cluster sample. Each map is a three-color image (red: 37 μm , green: 31 μm and blue: 19 μm), and the scale and stretch of each color is adjusted to balance each color. The three bands have resolutions of 6.4 pixels ($4.9''$), 6 pixels ($4.6''$) and 5 pixel ($3.8''$) FWHM for 37, 31 and 19 μm respectively.

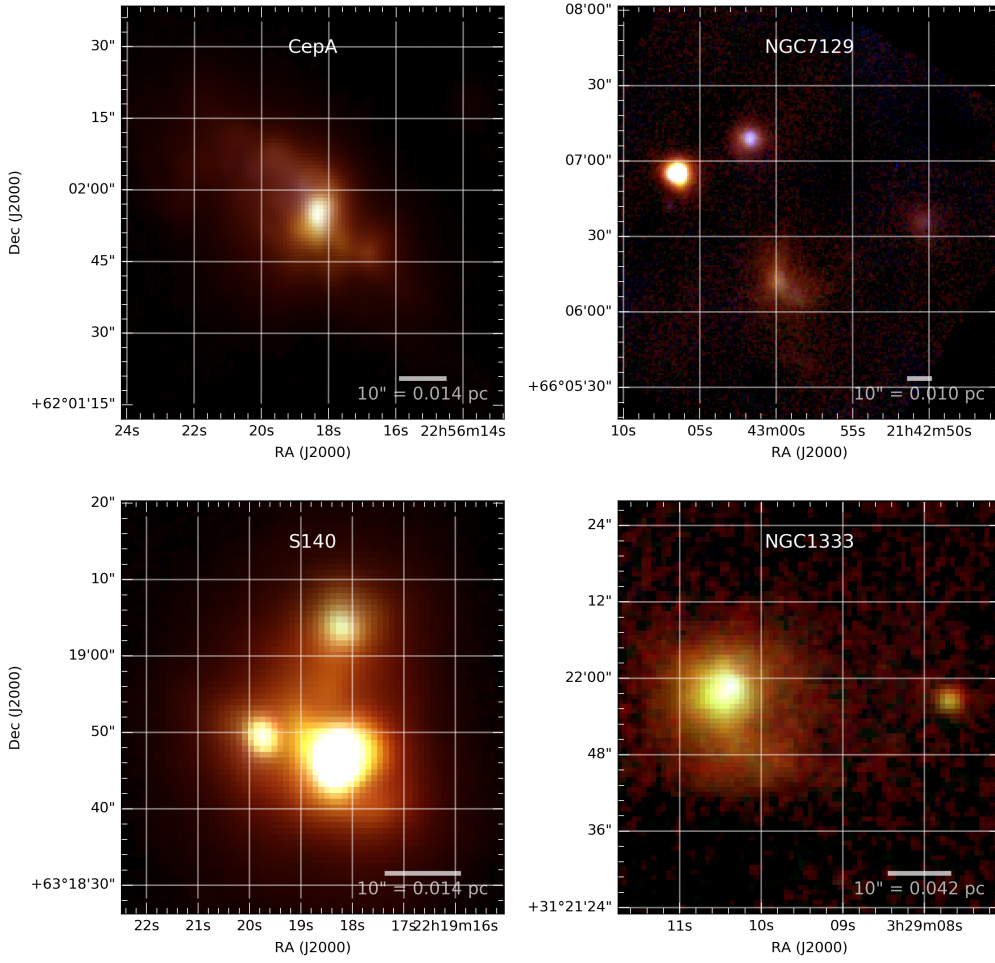


FIGURE II.6: RGB images of selected sample of sources (red: 37 μm , green: 31 μm and blue: 19 μm). In these images, the three bands have 6.4, 6 and 5 pixels FWHM for 37, 31 and 19 μm respectively.

II.6.2 Photometry catalog

TABLE II.11: Extract of NGC1333 photometry used for SED modeling.

SOFIA name	Coordinates	R37	Lbol	j	e_j	h	e_h	ks	e_ks	i1	e_i1	i2	e_i2	
NGC1333.1	03h29m07.7s +31d21m57.0s	0.746	8.385	0.0012	0.0001	0.0031	0.0003	0.0450	0.004	0.696	0.070	1.800	0.180	
NGC1333.2	03h29m10.3s +31d21m55.5s	2.232	27.832	0.2853	0.0285	0.6539	0.0654	0.9010	0.090	0.637	0.064	0.446	0.045	
NGC1333.3	03h29m01.5s +31d20m20.5s	0.904	8.104	0.0008	0.0001	0.0029	0.0003	0.0296	0.003	0.544	0.054	1.090	0.109	
NGC1333.4	03h29m11.1s +31d18m30.8s	1.103	3.056	0.0007	0.0007	0.0009	0.0009	0.0015	0.002	0.001	0.0007	0.004	0.0004	
NGC1333.5	03h29m10.6s +31d18m19.6s	1.623	2.786	0.0007	0.0007	0.0009	0.0009	0.0015	0.002	0.002	0.0002	0.007	0.001	
NGC1333.6	03h29m13.0s +31d18m13.8s	0.951	1.155	0.0007	0.0007	0.0009	0.0009	0.0015	0.0004	0.046	0.005	0.180	0.018	
		i3	e_i3	i4	e_i4	F11	e_F11	F19	e_F19	M24	e_M24	F31	e_F31	F37
NGC1333.1	03h29m07.7s +31d21m57.0s	3.060	0.306	2.550	0.255	0.225	0.169	1.502	0.208	–	0.260	6.886	0.640	10.994
NGC1333.2	03h29m10.3s +31d21m55.5s	0.448	0.080	0.913	0.128	8.414	0.596	36.517	2.562	–	–	106.490	7.457	135.723
NGC1333.3	03h29m01.5s +31d20m20.5s	1.690	0.211	3.060	0.306	1.681	0.131	6.902	0.493	–	0.069	9.256	0.656	9.406
NGC1333.4	03h29m11.1s +31d18m30.8s	0.005	0.001	0.004	0.0004	0.097	0.060	0.076	0.115	0.607	0.061	1.785	0.209	3.040
NGC1333.5	03h29m10.6s +31d18m19.6s	0.010	0.001	0.011	0.001	0.114	0.093	0.150	0.119	0.771	0.077	1.946	0.234	2.166
NGC1333.6	03h29m13.0s +31d18m13.8s	0.274	0.027	0.320	0.032	0.160	0.035	0.570	0.093	0.735	0.074	1.446	0.180	1.806
		e_F37	M70	e_M70	H70	e_H70	H160	e_H160	H70	e_H70	H160	e_H160	H250	e_H250
NGC1333.1	03h29m07.7s +31d21m57.0s	0.948	49.300	4.930	52.724	5.272	66.529	35.197	52.724	5.272	66.529	35.197	71.541	14.258
NGC1333.2	03h29m10.3s +31d21m55.5s	9.507	–	–	70.039	7.004	77.574	20.036	70.039	7.004	77.574	20.036	87.661	15.014
NGC1333.3	03h29m01.5s +31d20m20.5s	0.695	23.400	2.340	20.218	2.022	78.316	7.832	20.218	2.022	78.316	7.832	101.472	18.943
NGC1333.4	03h29m11.1s +31d18m30.8s	0.341	–	–	16.609	1.661	53.689	5.369	16.609	1.661	53.689	5.369	57.215	6.293
NGC1333.5	03h29m10.6s +31d18m19.6s	0.377	20.600	2.060	14.627	1.463	49.868	4.987	14.627	1.463	49.868	4.987	52.536	6.166
NGC1333.6	03h29m13.0s +31d18m13.8s	0.345	4.290	0.429	1.527	3.883	4.702	13.332	1.527	3.883	4.702	13.332	29.105	6.272
		H350	e_H350	H500	e_H500	S850	e_S850	F1100	e_F1100	S1300	e_S1300	α	e_α	
NGC1333.1	03h29m07.7s +31d21m57.0s	45.559	17.857	24.264	16.301	–	–	1.300	0.130	–	–	0.280	0.564	
NGC1333.2	03h29m10.3s +31d21m55.5s	51.506	16.114	24.742	13.062	–	–	–	–	–	–	1.243	–	
NGC1333.3	03h29m01.5s +31d20m20.5s	70.907	17.371	40.867	11.474	–	–	1.500	0.150	–	–	0.714	0.385	
NGC1333.4	03h29m11.1s +31d18m30.8s	38.449	6.033	18.594	4.666	–	–	2.000	0.200	–	–	1.864	0.458	
NGC1333.5	03h29m10.6s +31d18m19.6s	36.232	6.189	18.007	4.878	–	–	2.000	0.200	–	–	1.705	0.273	
NGC1333.6	03h29m13.0s +31d18m13.8s	34.781	8.007	21.255	6.628	–	–	0.630	0.063	–	–	1.001	0.501	

Notes: The table contains the source name, coordinates in J2000, the ratio of R37 = FWHM_{source}/FWHM_{cal}, the bolometric luminosity determined by integrating the data points in log-log space, followed by the photometry and its 1σ error in the 2MASS bands (j, h, k_s at 1.3, 1.6 and 2.2 μm respectively), IRAC bands (i1, i2, i3, i4 at 3.6, 4.5, 5.8 and 8 μm respectively), the FORCAST bands (F11, F19, F31, F37), the *Spitzer* MIPS bands (M24 and M70), the Herschel PACS and SPIRE bands (H70, H160, H250, H350), the SCUBA band (S850), the BOLOCAM band (F1100) and the SMA continuum band (S1300). The number following capital letters in the band denomination indicates the band's central wavelength. Flags are used to designate whether or not a source is considered an upper limit, and are not shown in this table for clarity. The fluxes that are upper limit can be seen in the SED images, Fig. II.7 and Fig II.9. The complete version of this table is made available electronically.

We produced a consolidated list of fluxes for our clusters, where we gather 2MASS, *Spitzer*, FORCAST, *Herschel*, SCUBA, and SMA data, when available, for ~ 90 sources. Most sources are point sources for the SOFIA FORCAST 37 μm band, but some sources present a certain spatial extension which was not known before.

A few other parameters are determined from the FORCAST data and shown in the catalog: the R_{37} ratio, which is the ratio of FWHM for the source and FWHM for the last observed calibrator; the spectral index and its uncertainty, computed from the 2.2 μm - 37 μm fluxes; and the bolometric luminosity for each source. Note that the bolometric luminosity is the integration of the observed emission across the observed wavelength; as such, it is an observed quantity but it is generally not the true luminosity of the source due to extinction (which is not corrected) and viewing angle corrections. An excerpt of the final table containing just the results for a few NGC 1333 sources is shown in Table II.11.

The SEDs for our most complete clusters, NGC1333 and Ophiuchus, are shown in Fig II.7 and Fig II.9. These show the data points in various color codes and marker types, as well as the best fit models for each source, as determined using our custom fitting routine, described in Section II.7. The R-value, indicated for each fit, is a metric that indicates how well the software was able to find a match between the data points and a pre-computed grid of models. Lower values of R generally indicate better fits.

Many SEDs are well fitted. Some of the sources show poor fits ($R > 3$), where it seems difficult to find a model that both satisfies the long-wavelength measurements and the IRAC measurements. This indicated that none of the models in the grid fit well. We think this could be explained either by a mismatch of the spatial resolution for the different measurement bands, in which case the long-wavelength bands sample flux that is not necessarily associated with the protostar, but rather is associated with another, nearby

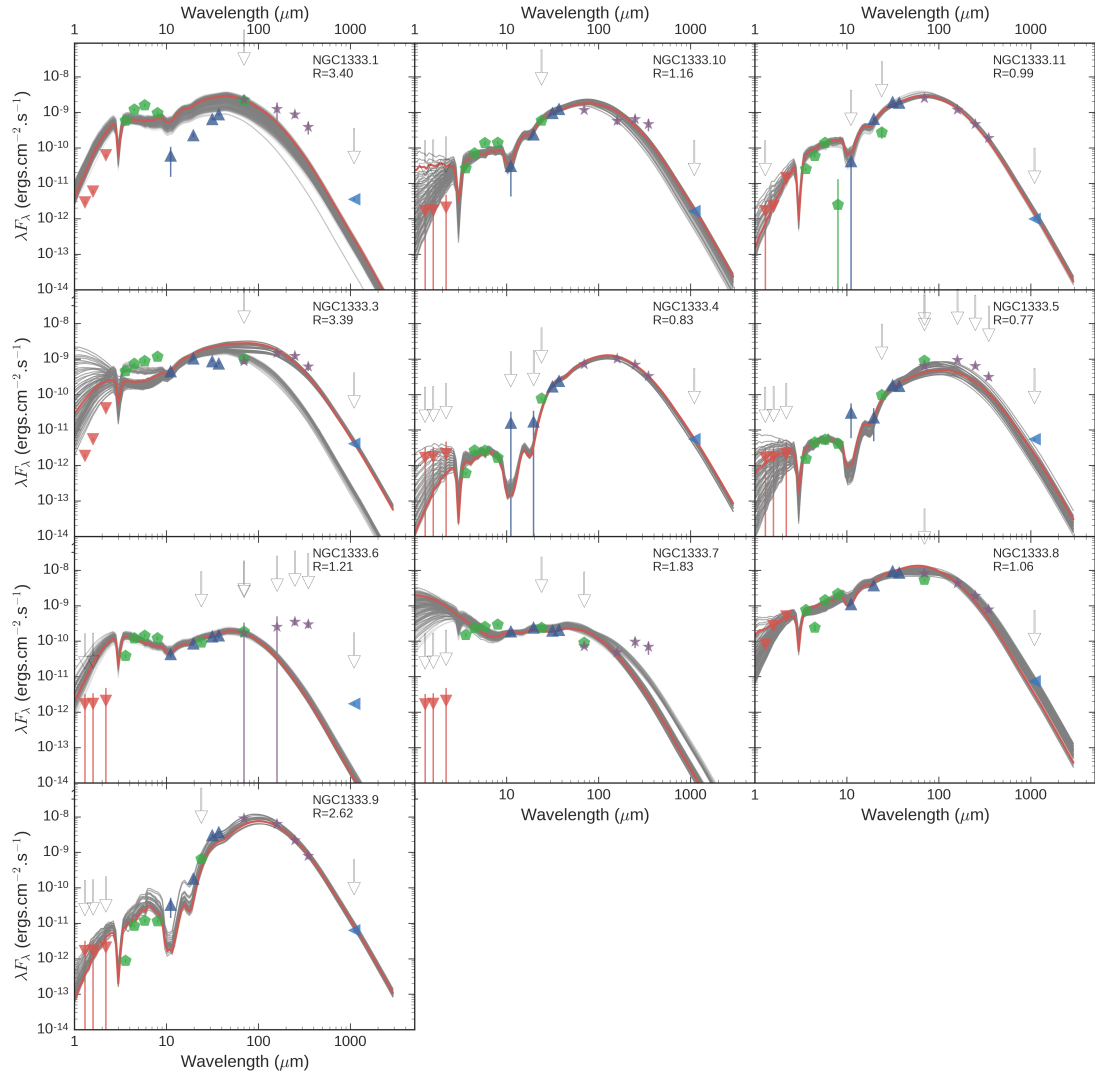


FIGURE II.7: SEDs of the point sources in NGC1333. The red curve represents the best fit. The grey curves represent all the fits with R within 0.5 of the best fit (see Section II.7.2 for details about the fitting process). The white arrows show which data point is considered an upper limit for the fitting routine. Note that 2MASS J- and H-band measurements, as well as *Spitzer* MIPS 24 μm and 70 μm are plotted, but never used for fitting. Red triangles: 2MASS. Green diamonds: *Spitzer* (our photometry or data from existing catalogs). Dark blue triangles: FORCAST (our data). Purple stars: *Herschel* (our photometry). Green triangles: SCUBA 850 μm and SMA 1.3 mm data from (Kempen et al., 2009) and (Kempen et al., 2012). Left-pointing blue triangles: 1.1 mm data from Enoch et al. (2009).

source or extended dense cloud emission; or by an excess flux from the IRAC bands that could be explained by the proximity to an outflow (Noriega-Crespo et al., 2004; Hudgins

et al., 2004). Fig. II.8 shows an example of a poor fit which could be attributed to excess IRAC emission due to a nearby outflow.

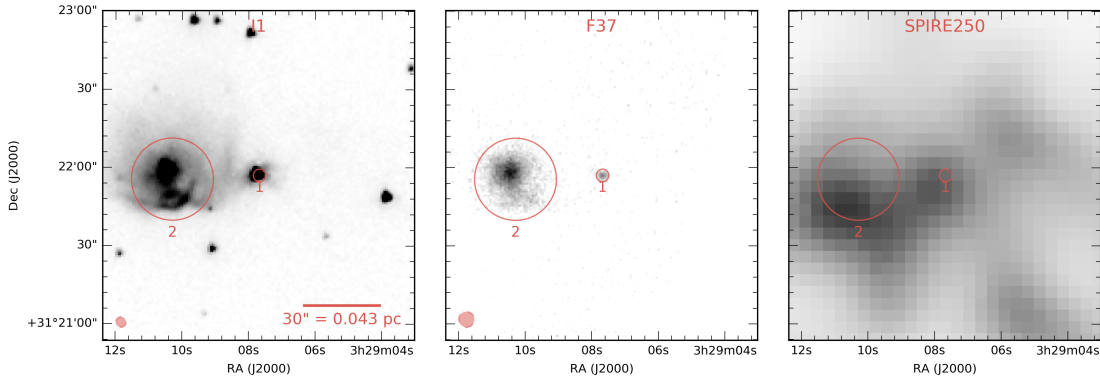


FIGURE II.8: Fields centered on NGC1333.1, a poorly-fitting source that shows a mismatch between the IRAC fluxes and the longer-wavelength fluxes. The *Herschel* SPIRE 250 μm (right) is taken at the same location as the sources identified using *Spitzer* IRAC 3.6 μm (left) and FORCAST 37 μm (middle). The resolution of the SPIRE beam is not shown on the figure, because it has a radius of 22''. In this particular case, it appears that the long-wavelength emission is associated with the source. However, this source is in close proximity to NGC1333.2, an extended source of our sample, which shows a bow shock structure in the southwest of its center seen in IRAC 3.6 μm , as well as diffuse emission that extends all the way to NGC1333.1.

II.6.3 Fitted physical parameters

The spectral index ($\alpha \equiv (d \log(\lambda F_\lambda) / d \log \lambda)$) distribution for the point sources in our sample is shown on the left of Fig. II.10. Most sources have strongly positive spectral indices, indicative of a rise in the SED with increasing wavelength and a significant contribution to the total luminosity by long-wavelength emission. These objects are more embedded, and thought to be younger than objects with negative spectral index. Note however that the emission generally peaks a little shortward of 100 μm . A closer inspection of the distribution of our sources reveals that the targets with negative index mostly lie in the Ophiuchus cluster, and are consistent with late Class I objects which have already cleared a significant fraction of their envelopes (Jørgensen et al., 2008).

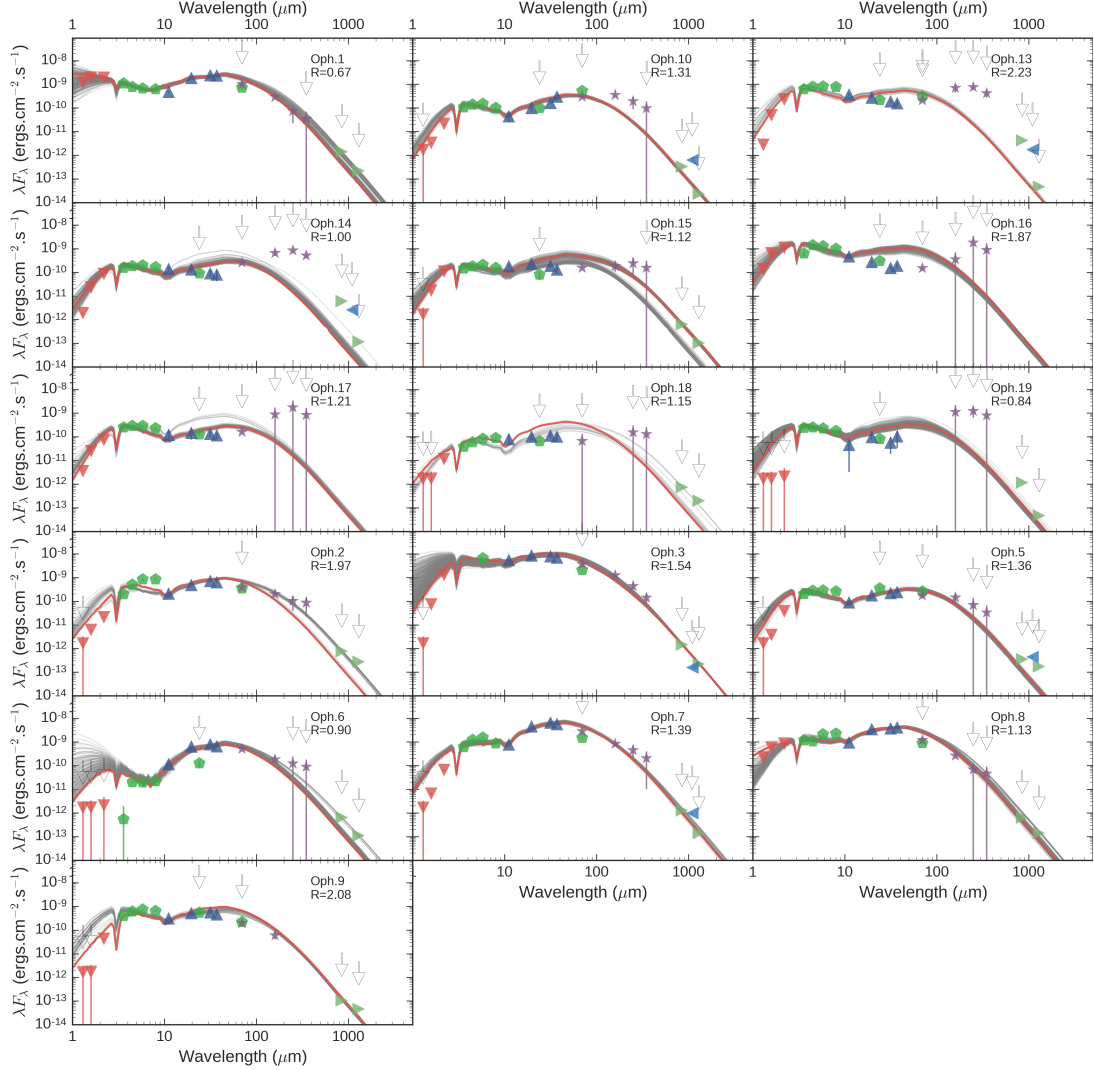


FIGURE II.9: SEDs of the point sources in the Ophiuchus cluster. Same legend as Fig. II.7

The data tables also include all of the physical parameters derived using the technique from Section II.7, as well as their uncertainties.

II.7 SED fitting

This section looks more closely at the SED fitting process: examining its value and its common shortcomings. First, we need to recognize that SED fitting is prone to many

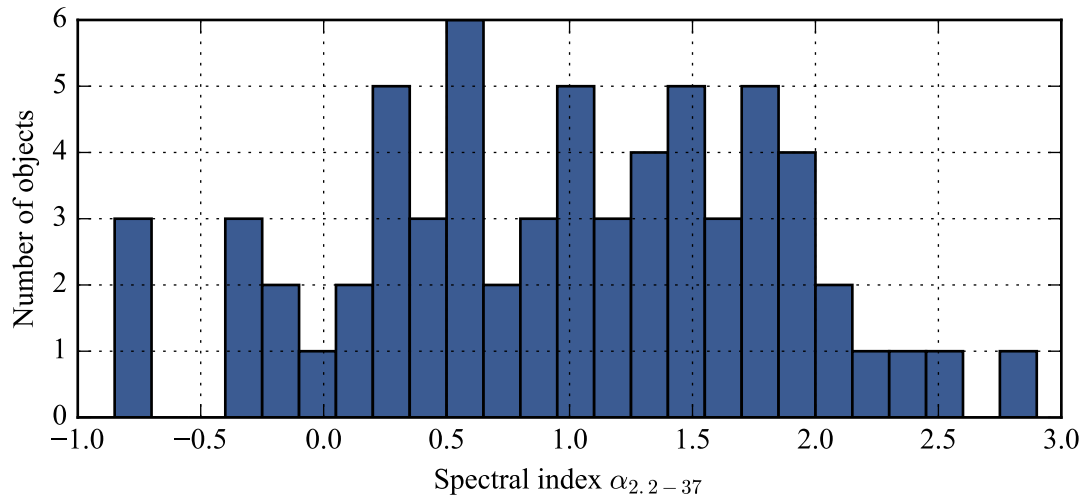


FIGURE II.10: Spectral index distribution of all point sources in our sample. *Left:* standard determination of the spectral index, using 2MASS and *Spitzer* from 2 μm to 24 μm , when data is available. *Right:* Determination of the spectral index using data from 2MASS, *Spitzer* and our FORCAST data up to 37 μm . The distribution changes significantly when you account for the longer fluxes in these clustered regions.

degeneracies (see e.g. Robitaille et al., 2007, for an introduction on the degeneracies of SED fitting) unless one has a great deal of spatial and spectral information about the source, which is usually not the case. In order to make physically plausible models, there are usually many geometrical and physical parameters in detailed radiative transfer models, but only a handful of measurement points are available to fit, leading to a dramatically under-constrained problem. The goals of our fitting procedures are then to reduce the number of parameters to those which have a significant quantitative impact on the SED, to identify the families of model parameters that fit the SED, and to define the "best fit" model and its "uncertainty" which represents the range in the model parameters with "reasonable" fits.

As our starting point of our investigation of fitting SEDs to our sources, we used the *sedfitter* tool from (Robitaille et al., 2006). These authors computed a large grid of tens of thousands of SED models using a radiative transfer code by (Whitney et al., 2003a),

by varying 14 geometrical and physical parameters in the dust density grid such as the size of the disk, the accretion rates, the radius and mass of the envelope, etc. The models are then evaluated in the bands corresponding to our data, and a χ^2 metric is evaluated for each model. By exploring the distribution of χ^2 , we noticed, as expected, the very large correlations between the parameters which is indicative of many local minimas in the 14-dimensional grid. Hence, inferring geometrical and physical parameters from such a grid can be misleading.

II.7.1 A custom grid of models

We use Hyperion (Robitaille, 2011, see also in Section I.3.3) to develop our own capability of calculating SEDs and understand the sensitivity of these parameters on the SED shape of our sources. Based on our investigation, the degeneracy between viewing angle and multiple geometrical parameters is considerable. The sensitivity of our SED to disk properties is small, as most of our YSOs are younger objects with significant envelopes. Since no central star is visible, parameters describing the central source such as the mass, radius and temperature are primarily important when they are combined into one single term, which is the central luminosity. Similarly, the luminosity created by accretion onto the central object can not be distinguished from a more luminous central object and a non-accreting disk. Finally, we find that there is very little difference between Ulrich envelope models (Ulrich, 1976) and standard power-law envelopes (see for example Fig. 14 from Whitney et al. (2013)), except that the latter can more easily be related to physical parameters such as the envelope mass.

From these findings, we created a simplified grid of models by significantly reducing the number of parameters in Hyperion. Table II.13 describes most of the geometric and

physical parameters that are available in Hyperion: divided into the central source, the disk, the envelope and the bipolar cavity. We set most parameters to constants which we determined as average values using literature examples as well as our own investigations for the objects we try to study, which are primarily class 0 and I YSOs. The parameters which we varied in the fits are shown at the bottom of the table: the inclination angle, the central luminosity (irrespective of whether it is caused by the central star or by accretion), the envelope mass, the external extinction and a scaling factor (explained below). The only two physical parameters that we vary are the luminosity and the envelope mass. While others (e.g. Furlan et al., 2016) have also attempted to reduce the number of parameters for their fitting, they still include more parameters such as the disk radius, but generally conclude that they are not able to properly constrain all of their parameters. As will be discussed later, there are a few YSOs which are not well fitted with a heavily reduced set of fitting parameters.

It is an important point to emphasize that we are not know the values of these "fixed" model parameters but rather that fixing them to a typical literature value does not have major impact on the fitted parameters and hence the SED fit. Disk mass and radius are two examples; in the presence of an envelope of comparable or greater mass, the disk emission is a weak function of mass in the wavelengths ($<20 \mu\text{m}$) where it contributes significantly to the SED because it is optically thick at those wavelengths. Similarly, the outer radius of the disk controls its contributions at longer wavelengths ($>50 \mu\text{m}$) where the envelope usually emits effectively; significantly reducing the disk emission at longer wavelengths requires small disk outer radii (10-30 AU) but has little impact on its shorter wavelength emission.

Unlike most authors, who use multiple kinds of dust models for different regions

of the SED which add complexity and number of parameters (Whitney et al., 2003b; Robitaille et al., 2006; Whitney et al., 2013), we choose to use the same dust model (OH5) for both the envelope and the disk, and assume a 1:100 dust-to-gas ratio. By doing so, we tend to overestimate the short-wavelength emission from SEDs, because the OH5 model assumes isotropic scattering whereas most dust grains appear to be forward-scattering (Draine, 2011).

To facilitate the calculation of models, we constructed a wrapper program that can run the Hyperion software for the range of parameters given in Table II.13 to create our model grid.

Because of time and resource limitations, a moderate number of photons was chosen in the Monte Carlo calculation, which can increase the noise at short wavelengths. The details of our modeling parameters, which will be familiar to the Hyperion user, are described in Table II.15. Note that models of more than $1 M_{\odot}$ are actually run with more photons (1×10^6 instead of 2×10^5) for imaging, in order to obtain acceptable SNR at short wavelengths.

The grid is composed of ~ 418 models which are calculated with Hyperion. For models with $M_{\text{env}} > 0.5 M_{\odot}$, we interpolate the grid in mass by increments of 20%, which allows for a finer sampling at higher masses, but increases the number of individual models to 958. The interpolation is done at constant luminosity. Each model is sampled at 10 inclinations, 15 values for external extinction, and five different scaling factors, for a total of 718 500 grid models. Each model is evaluated at all relevant observing bands, from the 2MASS bands all the way to the 1.3 mm SMA bands. Given the sparsity of the grid, and the relatively simple model used, we do not apply color correction to the fluxes, nor do we convolve the model fluxes with the band transmission function: the resulting corrections

TABLE II.13: SED model grid.

Parameter	Description	Values	Units
Constant parameters			
Central source			
M_*	Stellar mass	1	M_\odot
T_*	Stellar temperature	4000	K
Disk			
Type	Flared or alpha disk	Flared	
M_{disk}	Disk mass	0.001	M_\odot
R_{disk}^{\max}	Disk outer radius	100	au
R_{disk}^{\min}	Disk inner radius	sublimation radius	au
β	Flaring parameter	1.25	
p	Disk surface density exponent	-1	
r_0	Reference distance for scale height	R_{disk}^{\min}	au
h_0	Disk scale height at r_0	$0.01 \times R_{\text{disk}}^{\min}$	au
d	Dust	OH5	
Envelope			
Type	Power-law or Ulrich	Power-law	
R_{env}^{\min}	Envelope inner radius	R_{disk}^{\min}	au
R_{env}^{\max}	Envelope outer radius	5000	au
α	Power	-1.5	
r_0^{env}	Reference radius	R_{env}^{\min}	au
d	Dust	OH5	
Cavity			
r_0^{cav}	Cavity outer radius	R_{env}^{\max}	au
θ_0	Opening angle at r_0^{cav}	10	degrees
	Flaring exponent	1.5	
ρ_0	Density at r_0^{cav}	0	g cm^{-3}
α_e	Density profile exponent	0	
Fitted parameters			
i	Inclination angle	0 to 90 in 10 constant increments of $\cos i$	degrees
L_*	Central luminosity	5×1.5^p for $p = -4, -3, \dots, 10$ (from 0.99 to 288)	L_\odot
M_{env}	Envelope mass	0.01×1.5^p for $p = -2, -1, \dots, 19$ (from 0.001 to 22.17)	M_\odot
A_V	External extinction	0, 1, ..., 14	mag
s	Scaling	0.7, 0.85, 1, 1.5, 1.3	

TABLE II.15: Hyperion simulation parameters.

Parameter	Value
Number of photons (initial)	2×10^5
Number of photons (imaging)	2×10^5
Number of photons (raytracing sources)	1×10^6
Number of photons (raytracing dust)	1×10^6
Lucy max iterations	6
Max photon interactions	1×10^5
Geometrical grid parameters (radial, theta and azimuthal)	400, 199, 2
MRW	True

fall within our approximations, and do not affect significantly the outcome of the fitting.

The scaling factor in our fits is used to represent the uncertainty in the distance determination (e.g. Robitaille et al., 2006), but it can also be considered as a scaling to represent modestly different luminosities from the model value (Furlan et al., 2016). Indeed, Furlan et al. (2016) show that, to first order, changing luminosity by a small amount is approximately equivalent to scaling the SED in flux. In their grid, they use a scaling factor that ranges from 0.5 to 2.0, which allows them to have factors of 2.0 in the luminosity of their calculated models. We choose a more conservative approach by actually running the grid at closer luminosity steps (factor of 1.5) and hence have a smaller range of scaling factors.

The extinction parameter is used to represent extinction by material along the line of sight that is *outside* of the core: foreground material which may be extended material within the cluster core or may be additional cloud along the line of sight. This parameter is essential to providing good fits, as most other authors have also found (e.g. Robitaille et al., 2006; Furlan et al., 2016). A discussion of the meaning and importance of this parameter is given in the following sections.

II.7.2 Fitting method

In order to determine which model fits the data best, we adopt a metric defined by Fischer et al. (2012) and Furlan et al. (2016):

$$R = \frac{1}{N} \sum_i w_i |\log[F_{\text{obs}}(\lambda_i)] - \log[F_{\text{mod}}(\lambda_i)]|, \quad (\text{II.1})$$

where i are the indices of the valid data points, the weights w_i correspond to the inverse of the fractional uncertainty of each measurement, F_{obs} and F_{mod} are the observed and model fluxes respectively, and N is the number of valid measurements. For our models, we set the fractional uncertainty to a minimum of 10%, to avoid having a few points completely drive the fit. Early versions of the fitting routines, which used the published 1σ uncertainties would completely skew the results by putting all the weight into a few flux measurements. This was most notable for the *Spitzer* IRAC points, for which published uncertainties are sometimes only have a few percent. We chose to override these uncertainties, in large part because the assumptions of geometry and dust properties that go into a model calculation do not justify that level of confidence in the model output.

Furlan et al. (2016) discuss in more detail the meaning of this R metric, which differs from a standard χ^2 metric such as the one used by Robitaille et al. (2007). R represents a weighted average of the logarithmic deviations between the observations and the model. It is important to note that, although it is normalized, it does not have a statistical interpretation like the standard χ^2 metric. In particular, models with fewer data points or large measurement uncertainties will tend to have smaller values of R , even if the fit is poor. R is only useful as a relative measure of the goodness of fit to the specific observations.

For each source, we calculate R for each model in our grid. The model with the smallest value for R is the best-fitting model by this metric, but given our sparse sampling and the errors of our observations, this is not necessarily the most likely model to best fit the data. We can consider two extremes: in the first case, the best fit has a value of R which is much lower than other models. Then, it is clearly the best fit. In the second case, let's suppose that the 1000 best-fitting models lie very close to the best R . In this case, concluding that the model that best fits our observations (and from which will interpret physical quantities) is the one with the minimum R is too strict and does not account for the uncertainties that are present.

In practice, most of our models fall in the second case. After visual inspection of the fits, we conclude there is very little significant difference between values of R which are separated by ~ 0.5 . They all can be considered equally good (or bad) fits. Hence, for a robust measure of the best-fitting model parameters, we choose the mode (the most likely value) of the parameters from models which are within R_{\min} and $R_{\min} + 0.2$, in order to really pick the best possible fits. The error on the parameter is then estimated using the models within R_{\min} and $R_{\min} + 0.5$, since these models all similarly fit, and is described in the next section.

Because we use exclusively the OH5 dust model, which we know overestimates the short-wavelength fluxes, we expect to overestimate the extinction required to match the observations. For this reason, we choose to ignore the 2MASS J and H band data points, which drive the extinction values up dramatically and sometimes leads the fit towards non realistic solutions. However, we choose to keep the 2.2 μm Ks Band data point to give some weight to the shorter wavelength data.

II.7.3 Overview of derived parameters

The distribution of the best fit solutions of the envelope mass and central luminosity is shown in Fig. II.11 for the clusters for which we have long-wavelength data (Ophiuchus and NGC1333). Our sample covers a broad range of masses, but is naturally biased towards high luminosities given SOFIA's instrumental sensitivity and our cluster selection.

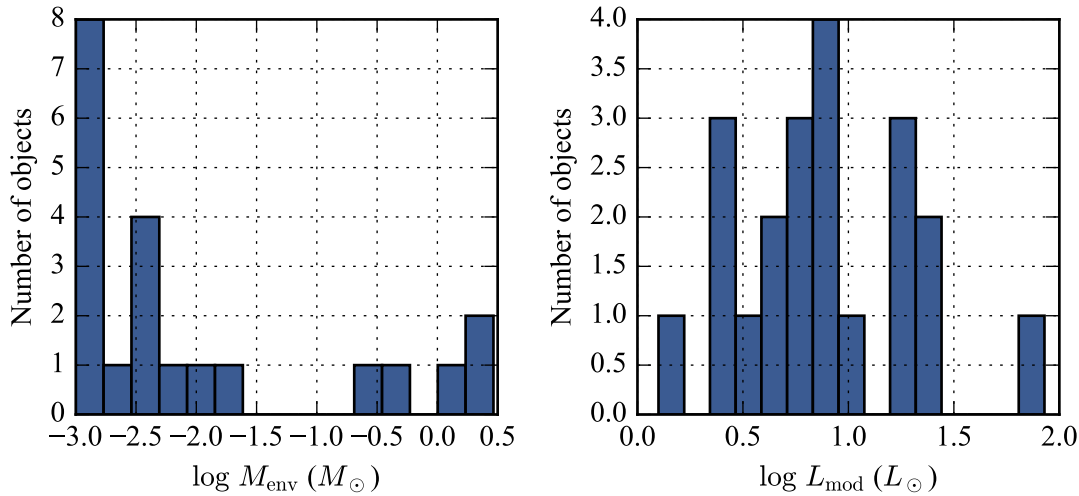


FIGURE II.11: Fitted envelope mass and luminosity distribution for all observed point sources in Ophiuchus and NGC 1333, where long-wavelength data is available.

From visual inspection, data with R less or close to 1 appear to fit the data well. Larger R show less good fits. The distribution of R for all the isolated point sources is shown in Fig. II.12. Note that targets where less data points are available, or where data points are more noisy, usually have lower R than targets with a lot of available data points, even if the fits are not necessarily as good. This has also been observed by (Furlan et al., 2016) and is one of the drawbacks of using the R metric.

One major limitation and inconsistency in all broad fitting works to date is the inclusion of a foreground material which provide extinction without emission. For example,

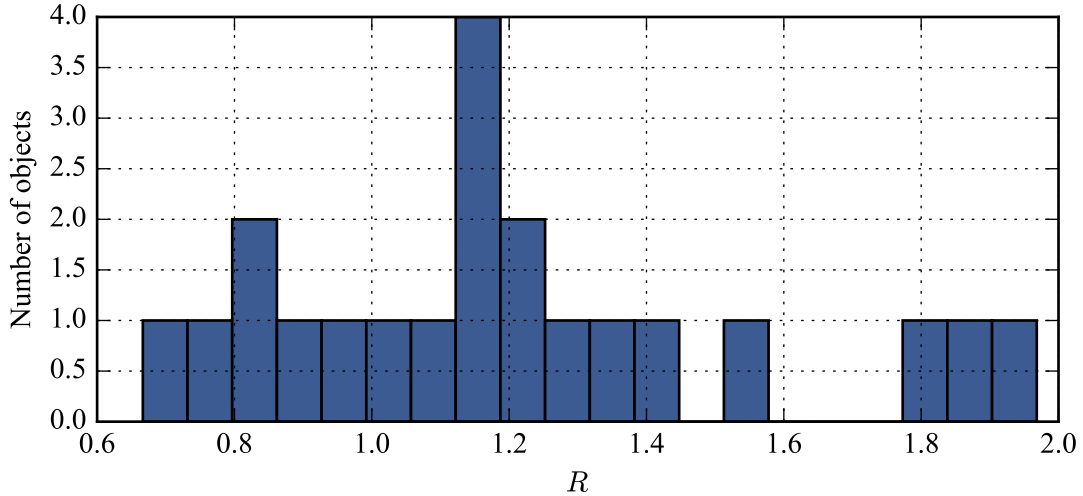


FIGURE II.12: R distribution across all observed point sources in Ophiuchus and NGC1333, where long-wavelength data is available.

Furlan et al. (2016) fit for external extinction up to $A_V = 40$ for some of their sources, and use all of the 2MASS bands in their fitting. It is not consistent to assume that so much material is present along the line of sight, while not also being observed at longer wavelengths. Since the dust is optically thin at longer wavelengths, the far-infrared and submillimeter observations should see emission from this material which is obscuring the shortest wavelengths.

Our exploration with the fitting routine shows that limiting the external extinction forces more inclined geometries, where the light from the central star passes through the disk before reaching us. However, we were not able to account for the entirety of the short wavelength extinction by doing this, as the mid-infrared wavelength (IRAC and FORCAST bands) are also affected by more inclined geometries, which can compromise the fits. This could indicate a fundamental limitation in our geometrical representation of YSOs or assumed dust properties, since there is no possible way to account for both the low amount of far-IR emission seen, e.g. by *Herschel* and high amount of extinction seen

from the 2MASS and IRAC bands. The highly cited publications, that we have referred to, adopt an external extinction factor, the rigor of which we now strongly question. However, we have not been able to find an appropriate solution to circumvent this issue. Hence, we choose to follow the examples of previous authors and adopt an external extinction factor. Unlike Furlan et al. (2016), which consider A_V as high as 40 mag, we choose to limit it to $A_V = 14$ mag, a moderate value of the diffuse extinction in our clusters of interest.

An external extinction of $A_V = 14$ mag means that fluxes at $2.2\mu\text{m}$ are reduced by a factor of ~ 17 , while $8\mu\text{m}$ fluxes are reduced only by a factor of ~ 2 . For most Class 0 and I sources, most of the emission has already been reprocessed by dust out to longer wavelengths, and the 2MASS $2.2\mu\text{m}$ data points are usually extremely low, so a difference of a factor of 17 in this small region of the spectrum will not lead to significantly different luminosity estimates when compared to the contribution from other parts of the spectrum. In fact, a small exploration of our fits reveals that for these sources usually the extinction from within the envelope itself is already much larger than this factor. However, at $A_V = 40$, the flux reduction at $2.2\mu\text{m}$ is > 3000 , at which point we argue this could become a problem. With such a large ratio, it is more difficult to claim that the fitted luminosity from the model is not overestimating the actual luminosity, since the external extinction reduces by many orders of magnitude the short-wavelength emission in order to fit the data.

For all sources we calculate the bolometric luminosity as the integral of all the available data points, even those which correspond to upper limits. This makes L_{bol} an upper limit as well on the observed luminosity. Since most of the upper limits are from long-wavelength data points, this impacts sources with a larger envelope more. We note that the fitted luminosity L_{mod} tends to be lower than the bolometric luminosity L_{bol} for

low inclination angles, but L_{mod} tends to be higher than L_{bol} for more inclined geometries. This is expected since for high inclinations a large fraction of the emission is not directed towards the observer (see, e.g. Furlan et al., 2016, for a discussion). On the contrary, when seen almost face-on, the observer sees both the emission from the source as well as the light scattered on the walls of the cavity and the disk.

Finally, for the clusters which have submillimeter data points, we calculate the traditional mass estimate described in Section I.3.2 using the 1.1 mm or 1.3 mm fluxes. For this calculation, we use an effective dust temperature of 20 K, assuming an opacity of $0.0114 \text{ cm}^2 \text{ g}^{-1}$ and $0.009 \text{ cm}^2 \text{ g}^{-1}$ for 1.1 mm and 1.3 mm, respectively, based on the expected emissivity for OH5 dust. These values for M_{env} are shown in Table II.17. Note that this measurement is very sensitive to these assumptions; for example, lowering the dust temperature estimate to 10 K increases the mass estimate by a factor of 3. In addition, these measurements can be overestimates by a large amount if the 1.1 and 1.3 mm fluxes are measured with single-dishes, and hence upper limits on the flux from the YSO environment.

A summary of our fit results for Ophiuchus and NGC1333 is shown in Table II.17. All fits results for all our sources are shown in Appendix D. Note that the luminosity that is used in this analysis is always the luminosity multiplied by the scaling factor s , under the assumption that the SED scales for small changes in luminosity. This scaling factor improved the fit but it must be remembered that the true luminosity is dependent on the distance. For example, a distance error of 10% would cause a luminosity estimate that would differ by 20%.

TABLE II.17: Fitted parameters for the point sources in Ophiuchus and NGC1333 where long-wavelength photometry is available.

SOFIA Name	Coordinates (J2000)	R37	α	R	M_{env} (M_{\odot})	Calc. M_{env} (M_{\odot})	L_{mod} (L_{\odot})	L_{bol} (L_{\odot})	i ($^{\circ}$)	A_V (mag)
NGC1333.1	03h29m08s +31d21m57s	0.75	0.28	3.40	0.004 ± 0.005	0.97	32.5 ± 7.8	8.4	51	14
NGC1333.3	03h29m02s +31d20m21s	0.90	0.71	3.39	0.004 ± 0.03	1.12	3.5 ± 2.1	8.1	0	14
NGC1333.4	03h29m11s +31d18m31s	1.10	1.86	0.83	2.919 ± 0.45	1.50	2.3 ± 0.4	3.1	19	11
NGC1333.5	03h29m11s +31d18m20s	1.62	1.70	0.77	1.297 ± 0.33	1.50	1.3 ± 0.3	2.8	19	14
NGC1333.6	03h29m13s +31d18m14s	0.95	1.00	1.21	0.001 ± 0.0007	0.47	7.5 ± 1.2	1.5	27	14
NGC1333.7	03h28m43s +31d17m35s	1.19	1.08	1.83	0.001 ± 0.001	–	9.6 ± 1.8	1.4	58	0
NGC1333.8	03h29m04s +31d16m04s	0.77	1.14	1.06	1.946 ± 0.75	2.02	17.0 ± 2.4	35.1	0	13
NGC1333.9	03h28m56s +31d14m37s	0.80	2.79	2.62	2.919 ± 0.35	1.72	17.0 ± 2.4	24.3	19	14
NGC1333.10	03h28m57s +31d14m15s	0.80	1.83	1.16	0.256 ± 0.18	0.45	5.6 ± 0.9	4.8	19	14
NGC1333.11	03h28m37s +31d13m30s	1.02	1.69	0.99	0.38 ± 0.18	0.27	7.7 ± 0.8	7.5	19	14
Oph.1	16h27m10s -24d19m13s	0.92	0.27	0.67	0.01 ± 0.002	0.04	7.9 ± 1.3	3.6	78	3
Oph.2	16h26m44s -24d34m48s	0.93	0.83	2.08	0.001 ± 0.002	0.05	32.3 ± 21.1	1.2	84	14
Oph.3	16h27m09s -24d37m18s	0.99	0.57	1.54	0.004 ± 0.002	0.04	85.0 ± 19.7	13.4	0	14
Oph.5	16h27m07s -24d38m15s	1.31	0.31	1.36	0.001 ± 0	0.03	4.3 ± 0.5	0.5	81	14
Oph.6	16h27m16s -24d38m46s	1.29	2.54	0.93	0.001 ± 0.001	0.02	26.6 ± 6.4	0.8	90	13
Oph.7	16h27m28s -24d39m34s	0.97	1.35	1.39	0.015 ± 0.002	0.03	26.6 ± 3.5	6.5	72	14
Oph.8	16h27m37s -24d30m35s	1.02	0.55	1.13	0.007 ± 0.002	0.03	17.7 ± 3.4	5.0	78	12
Oph.9	16h27m22s -24d29m54s	–	0.51	2.08	0.001 ± 0	0.01	11.8 ± 1.2	1.0	81	14
Oph.10	16h27m18s -24d28m55s	1.26	0.50	1.38	0.003 ± 0.0006	0.004	5.0 ± 1.6	0.6	81	14
Oph.13	16h27m30s -24d27m43s	0.00	-0.37	2.23	0.001 ± 0	0.01	17.7 ± 5.5	1.5	81	14
Oph.14	16h27m28s -24d27m21s	1.89	-0.13	1.00	0.001 ± 0.0009	0.02	4.3 ± 0.6	1.0	81	14
Oph.15	16h27m29s -24d39m17s	1.25	0.10	1.12	0.004 ± 0.0007	0.02	3.3 ± 0.4	0.6	27	14
Oph.16	16h26m24s -24d24m48s	1.80	-0.76	1.87	0.001 ± 0	–	17.7 ± 2.9	2.2	78	10
Oph.17	16h26m24s -24d24m39s	0.96	-0.09	1.21	0.001 ± 0	–	5.3 ± 0.6	1.3	81	14
Oph.18	16h26m17s -24d23m45s	1.18	0.63	1.34	0.003 ± 0.004	0.04	2.8 ± 0.9	0.3	81	14
Oph.19	16h26m30s -24d23m00s	2.51	0.57	0.89	0.001 ± 0.001	0.01	5.3 ± 1.0	1.2	75	14

II.7.4 Estimating parameter uncertainty

It is important to estimate the uncertainty in fitted parameters to quantify the confidence in a given fit. Without uncertainties, no meaningful conclusion can be drawn about the physical meaning of the fits. This estimation is also one of the most difficult aspect of the fitting process, since it really depends on the method used and the modeling strategy. It is also difficult to compare results with the findings of other authors who used a different approach to their fitting.

In this work, we propose a novel methodology to derive the uncertainty on the best fit. First, we determine the best fit for a given parameter as the mode of the parameter values from the models that fit within $[R_{\min}, R_{\min} + 0.2]$, where R_{\min} is the minimum value of R in the entire grid. This is statistically more robust than picking simply the model with the lower R , since, given our uncertainties and approximations, there is no statistically-significant difference between models that fit within that range.

Once this best fit value is determined for all parameters, the uncertainty is determined using all models that fit within $[R_{\min}, R_{\min} + 0.5]$. We determine three quantities from these models: the standard deviation from the best fit; the median absolute deviation from the best fit; and the skewness of the distribution.

The choice of the R intervals are empirical based on our fitting experience. Since the metric R is not model-dependent but instead is a distance of *distance* between models and observations, we think that similar values will still lead to reasonable parameter and uncertainty estimates in other future works. One limitation could occur from the density of the grid: if the models are so sparse that there are only a handful of model within each interval used in the uncertainty estimation, this could lead to poor estimate of uncertainties.

II.7.5 Discussion

Several factors have been omitted for simplicity our model fitting. First, the models we use have an axisymmetric geometry which is unlikely to account for realistic mass distributions in the envelope and the disk. Second, we ignore the surrounding medium and consider it devoid of emission. In reality, the transition to the surrounding medium is likely smooth and its emission relevant at the longest wavelengths. Third, we assume that the only heating source is located at the center of the YSO. The heating source consists of both the light from the star, and from the accretion luminosity, which can not be distinguished from our point of view. It is important to realize that external heating can also play a role in raising the dust temperature and changing the SED signature in the cluster environment. The impact of the interstellar heating is explored in Furlan et al. (2016), who show that it can have a substantial effect on the SED - but they nevertheless do not include this parameter in their grid, since it is too case-specific. The Hyperion radiative transfer code that is used to model our grid could accommodate external radiation fields as well, and this could become a future addition to our modeling. Finally, the observations that form our SEDs were not taken simultaneously, so it is possible for the YSO flux to change over the period of years. This YSO variability has been shown to be fairly common at the 10 to 20% level at near infrared wavelengths (Rebull et al., 2014) and larger optical outbursts in luminosity are known to occur in a small sub-class of T Tauri stars called FU Ori stars (Hartmann et al., 1996). However, we do not anticipate that YSO variability would drastically change the fit results, given typical variability amplitudes modest (e.g. Poppenhaeger et al., 2015).

Given the relative simplicity of our model grid, most of observations are fit reasonably

well and the fitted parameters have acceptable uncertainties for a large fraction of sources. Our range of R values is similar to that of Furlan et al. (2016) in their analysis, although they used more free parameters than just the luminosity and the envelope mass. This further confirms the degeneracies that exist when trying to fit for too much physics into very elaborate models. The difference in the resolutions, sensitivity, and photometric techniques for each wavelength in the SED limits the value of a more thorough analysis, especially when located in very clustered environment when extended emission and nearby sources can contaminate the measurements.

We argue that more complex models would not help in estimating the physical parameters of YSOs - but instead, this work highlights the need for higher angular resolution at wavelengths longward of $37\,\mu\text{m}$. Such data can be obtained in the future at arcsecond and sub-arcsecond resolution at millimeter and submillimeter wavelengths with ALMA at $> 350\,\mu\text{m}$. The new continuum cameras for large radio telescopes like the Green Bank 100-meter telescope and the 50-meter Large Millimeter Telescope can produce ~ 5 arcsecond images of the extended envelope and surrounding cloud material to provide strong constraints on the external extinction issue. It is also essential to improve the resolution of observations from 30 to $200\,\mu\text{m}$ to constrain the disk and envelope masses, and refine our knowledge of dust properties in the different regions of the circumstellar environment.

In our models, we have used OH5 dust as it was recommended by various authors (e.g. Dunham et al., 2010). However, the models for OH5 do not include scattering properties, which might jeopardize the accuracy of the models at short wavelengths, which are dominated by scattered light. However, it seems to have a opacity that fits best the clustered environments (Huard et al., 2016, in prep.). By ignoring the fact that grains are preferentially forward-scattering, we could cause the model to fit for larger extinction

values or higher inclination angles than desired. We are considering using other types of dust, such as the one used by Furlan et al. (2016), which has fully detailed scattering properties, but less long-wavelength opacity. Using this type of dust would require running a new model grid with considerably more photons for each model, which we estimate would take ~ 4 weeks on the UMD 8-core computer we have been using.

Finally, the issue of external extinction needs much more investigation. To date, we have not found in the literature a proper treatment of this problem. In order to re-establish self-consistency, we suggest exploring ways to add constraints on the long-wavelength flux when adding more extinction. Since the material that causes truly external extinction is presumably far away from the source, we can assume that it is at the temperature of the surrounding molecular cloud. The extinction A_V can be converted to a column density of material by assuming a dust composition and knowing its opacity at short wavelengths. By knowing the amount of material along the line of sight and assuming a temperature, we could infer how much emission is expected at long wavelengths and test if it is consistent with *Herschel* measurements along the line of sight. A second approach is to add the flux from the extinction material to the long wavelength emission from the model as part of the fitting process. This suggestion has not yet been tested or implemented.

II.8 A close look at IRAS 20050+2720

In this section, we focus our attention on IRAS 20050+2720 which shows very clustered sources that are resolved for the first time in the mid-IR with our SOFIA FORCAST observations. The fields that were observed are shown in Fig. II.13, superimposed with IRAC 3-color images to provide some context.

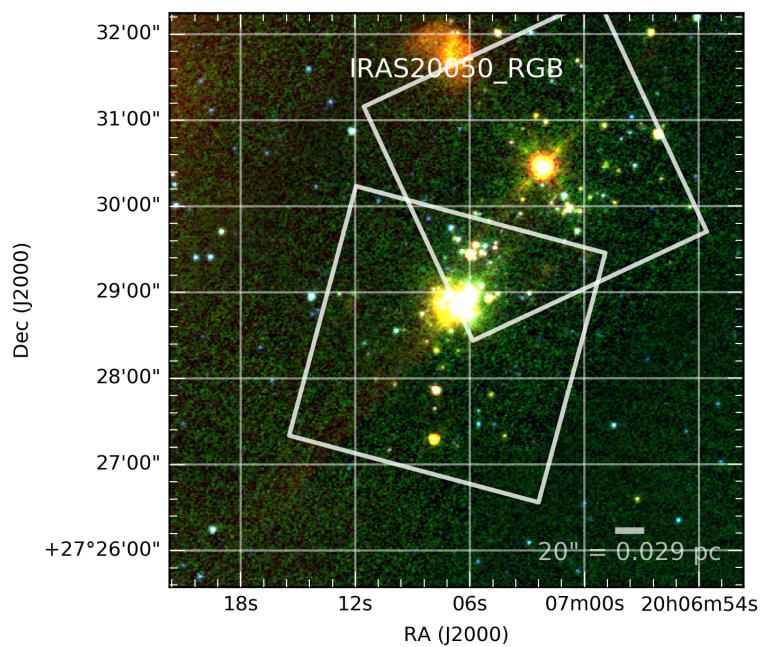


FIGURE II.13: IRAC 3-color images of IRAS 20050+2720. The two SOFIA fields corresponds approximately to the two white squares in the image.

II.8.1 Overview

IRAS 20050+2720 is part of an active site of intermediate-mass star formation in the Cygnus Rift located at 700 pc (Wilking et al., 1989), with the particularity that it doesn't seem to contain any massive stars (Günther et al., 2012). The main cluster core is associated with water and methanol masers (Palla et al., 1991; Fontani et al., 2010) and multipolar molecular outflows observed at millimeter wavelengths (Bachiller et al., 1995; Anglada et al., 1998; Beltrán et al., 2008), suggesting that the region might have experienced a episode of star formation in the past 0.1 Myr which contrasts with the average age of the cluster of 1 Myr (Chen et al., 1997; Gutermuth et al., 2005). Gutermuth et al., 2009 have identified > 170 YSOs surrounding the core and measured their continuum fluxes up to 8 μm with the *Spitzer* IRAC instrument. While measurements at longer wavelengths are able to provide estimates of the total luminosity of the cluster (e.g. using IRAS, Molinari et al., 1996, $388 L_\odot$), the measurements are confused in the densest region and it has not been possible to properly associate the far-IR emission with its short wavelength counterpart because of the small separation between IRAC-detected protostars. The IRAS point source was classified as a luminous class 0 protostar (Bachiller, 1996), and its emission associated with the bright millimeter source MMS1 to the northwest of the core (Chini et al., 2001), also called OVRO1 in Kempen et al. (2012). Beltrán et al. (2008) show strong evidence that this region has multiple generations of stars, and suggest that a group of low-mass stars first completed their main accretion phase, before the birth of new intermediate-mass stars at the core of this cluster. A recent study by Poppenhaeger et al. (2015) investigated the YSO variability in the IRAC 3.6 and 4.5 μm fluxes in the region, and found that a large fraction exhibit variability, some as large much as 0.55 mag over periods ranging from a

few days to ~ 30 days.

II.8.2 Observations and discussion

We observed two fields within the cluster (see Fig. II.13), including the brightest core at $20^h07^m06.70^s + 27^\circ28'54.5''$. Multiple sources in the core can be distinguished in the IRAC maps, but the core appears extended in *Spitzer* MIPS at 24 μm , and is identified as a single source with WISE. No high resolution far-infrared continuum data longward of 24 μm was available for this source. To our knowledge, our observations are the only mid-IR observations available that can properly resolve the YSOs in the dense region.

II.8.2.1 A clustered region with an outflow

We find 5 separate sources in the core which appear to share an envelope of extended emission at 37 μm . These sources are labeled in Fig. II.14, and their IRAC and FORCAST photometry is summarized in Table II.19. IRAS20050.4 is coincident with the source at the northwestern end of the cluster, which is named OVRO1 in Beltrán et al. (2008). Two more sources are identified with the blue millimeter wavelength continuum contours from Beltrán et al. (2008), to the south and east of OVRO1, but they do not appear to correlate with our SOFIA sources. The CO outflow axis (Outflow "A", Bachiller et al., 1995), which is associated with IRAS20050.4, appears to be aligned with extended emission that is visible to the east of the 5 sources. This extended emission is visible in both IRAC and FORCAST, and coincides with blue-shifted CO emission in the velocity maps from Beltrán et al. (2008). The emission, totalling ~ 6 Jy at 37 μm , appears diffuse and not connected to any particular YSO. A multi-wavelength view of the region is shown in Fig.II.15.

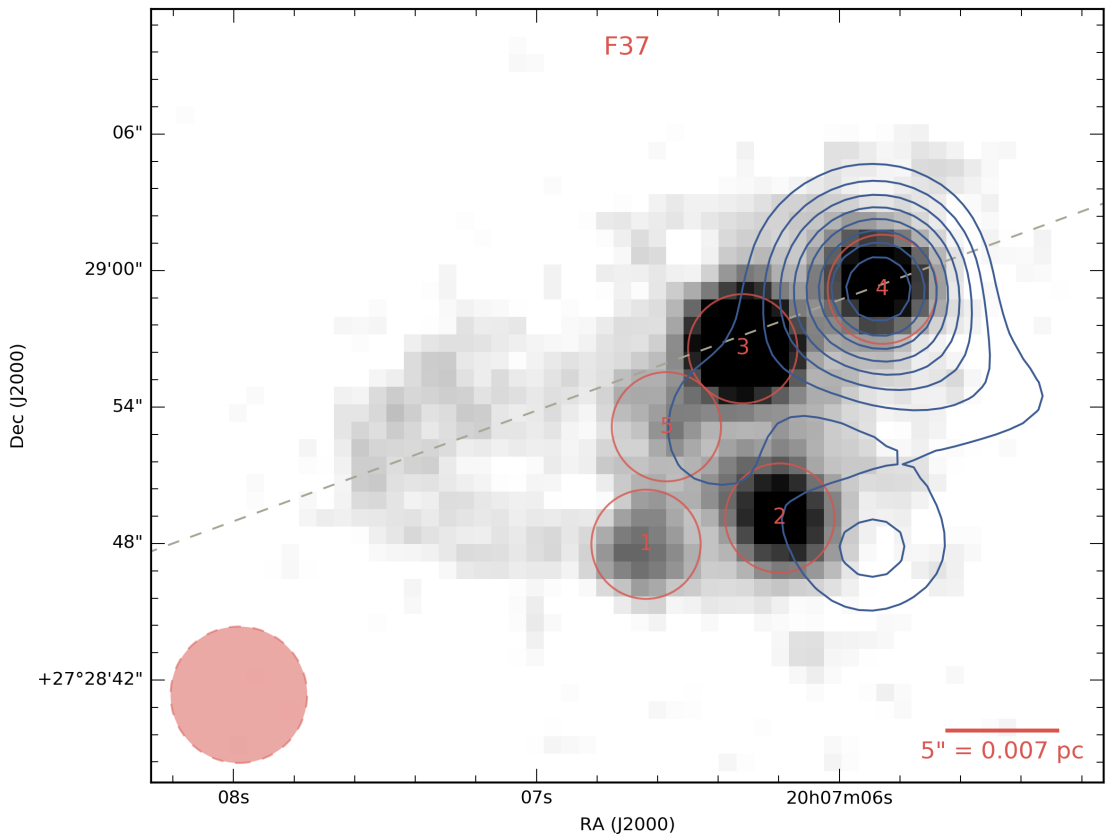


FIGURE II.14: 37 μm observations of the IRAS 20050+2720 core, with the 5 identified objects. The blue contours are from a 2.7 mm continuum emission observed by the OVRO array (Beltrán et al., 2008) at levels from 10 to 46 mJy beam^{-1} by increments of 4 mJy beam^{-1} . The resolution of the 2.7 mm beam is $\sim 4.8''$, while the r.m.s noise is $1.5 \text{ mJy beam}^{-1}$. The dashed line is the axis of a bipolar outflow identified by Bachiller et al. (1995). The beam shown at the bottom left represents the resolution of the FORCAST instrument.

TABLE II.19: Sources fluxes in IRAS 20050+2720.

SOFIA name	Coordinates J2000	ks	i1	i2	i3	i4	F11	F19	F31	F37
		Jy	Jy	Jy	Jy	Jy	Jy	Jy	Jy	Jy
IRAS20050.1	20h07m06.6s	0.214	0.489	0.57	0.731	0.858	0.64	1.93	4.50	6.32
	+27d28m48.0s	±	±	±	±	±	±	±	±	±
		0.021	0.049	0.057	0.073	0.086	0.07	0.20	0.35	0.59
IRAS20050.2	20h07m06.2s	0.002	0.041	0.142	0.264	0.308	0.06	1.45	9.31	11.96
	+27d28m49.1s	±	±	±	±	±	±	±	±	±
		0.002	0.004	0.014	0.026	0.031	0.06	0.19	0.72	1.19
IRAS20050.3	20h07m06.3s	0.028	0.09	0.218	0.339	0.429	0.18	2.58	12.53	19.34
	+27d28m56.6s	±	±	±	±	±	±	±	±	±
		0.003	0.009	0.022	0.034	0.043	0.06	0.27	0.94	1.41
IRAS20050.4	20h07m05.9s	0.002	0.023	0.039	0.053	0.055	0.06	0.25	8.54	12.85
	+27d28m59.2s	±	±	±	±	±	±	±	±	±
		0.002	0.003	0.004	0.008	0.008	0.05	0.20	0.80	1.25
IRAS20050.5	20h07m06.6s	0.042	0.118	0.176	0.235	0.32	0.19	1.03	2.97	5.65
	+27d28m53.1s	±	±	±	±	±	±	±	±	±
		0.004	0.012	0.018	0.024	0.032	0.05	0.21	0.33	0.65
IRAS20050.6	20h07m02.2s	0.155	0.537	0.771	1.113	1.805	1.81	2.29	1.64	1.22
	+27d30m26.0s	±	±	±	±	±	±	±	±	±
		0.016	0.054	0.077	0.111	0.181	0.13	0.17	0.14	0.38
IRAS20050.7	20h07m07.9s	0.002	0.004	0.024	0.06	0.072	0.06	0.11	1.15	2.09
	+27d27m15.8s	±	±	±	±	±	±	±	±	±
		0.002	0.004	0.002	0.006	0.007	0.05	0.06	0.14	0.31

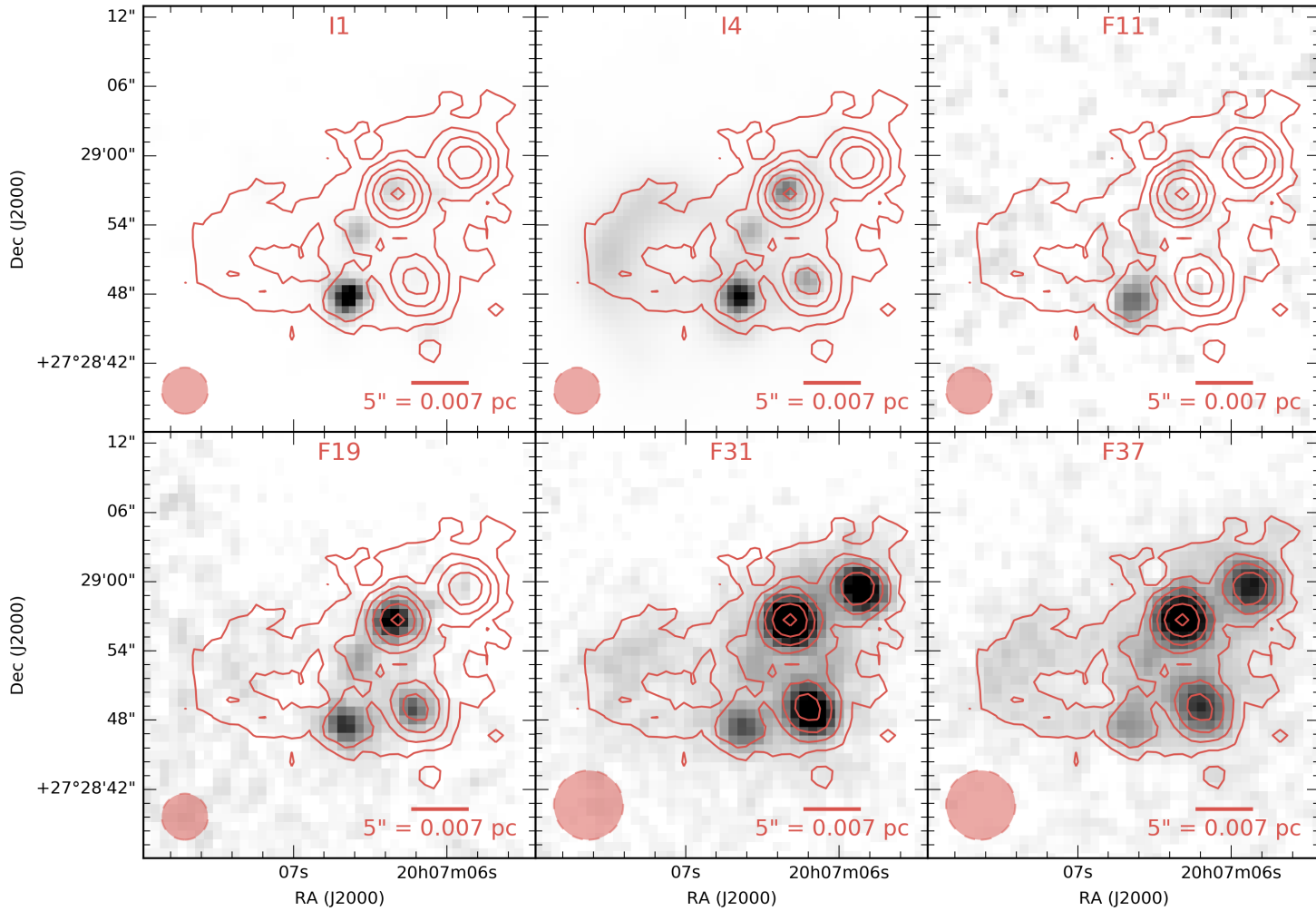


FIGURE II.15: The core of IRAS20050+2720 is seen in the four bands of the *Spitzer* IRAS instrument, as well as with the four FORCAST bands. The increased resolution of FORCAST compared to previous instruments allows to match the long-wavelength emission with its short wavelength counterpart. The stretch in each image is adjusted for optimal readability. The red contours correspond to the FORCAST 37 μm emission at 0.03, 0.07, 0.13, 0.2, 0.3 and 0.4 Jy.

A likely explanation for this emission is that the outflow from IRAS20050.4 (MMS1/OVRO1) is colliding with cold material in the surrounding cloud, creating a shock layer and heating the dust a few hundreds of K. This could explain the arc shape of the emission. The hypothesis is supported by the SED for the extended emission (Fig. II.16) which exhibits strong features at 5.8 and 8 μm (IRAC bands 3 and 4 respectively). These bands are known to have multiple PAH broad emission lines, and significant PAH emission has been found to be associated with other outflows (Noriega-Crespo et al., 2004; Hudgins et al., 2004) as the shock energy and the direct starlight hitting the dust through the outflow cavity excite these emission features. PAH emission is significantly weaker in IRAC band 1, while it is expected to be non-existent in band 2 (Noriega-Crespo et al., 2004). The presence of excess emission in bands 3 and 4 indicates that the emission is not purely thermal.

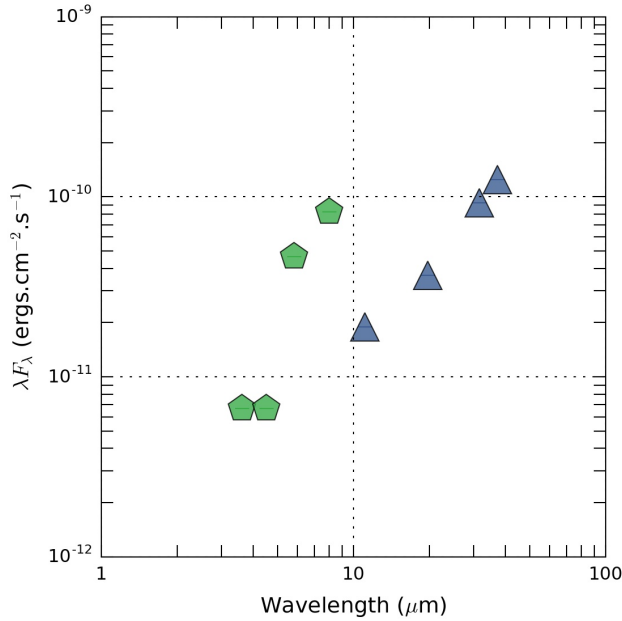


FIGURE II.16: SED from extended emission to the east of the cluster, using photometry from IRAC and FORCAST in a 2.4'' radius aperture. Excess emission at 5.8 and 8 μm (IRAC bands 3 and 4 respectively) can be attributed to PAHs excited by the shock and/or by the radiation from the outflow.

II.8.2.2 SEDs and fitted parameters

The 5 sources in the densest part of the cluster shown in Fig. II.15 are all highly extinguished based on the slopes of the emission in the 2MASS bands and the depth of the 10 μm silicate absorption feature (see Fig. II.17). IRAS20050.1 has a flat spectrum out to 37 μm , unlike the four other sources which are rising. IRAS20050.4 is the most steeply rising source, and is weak in the IRAC bands, suggesting that it is the most embedded source, which is corroborated by the fact that it is coincident with the strongest millimeter continuum source in the region.

The fitted parameters for the 7 identified sources in our two fields are shown in Table II.21. When the mass error is 0, it means that there is only one mass parameter for all the fits which are within 0.5 of R_{\min} . Since no long-wavelength data is available, the envelope masses are not very well constrained. Sources 6 and 7 are far away from the main core which was discussed previously, and do not appear to be associated with the first 5 sources. We interpret these results in several ways:

TABLE II.21: Fitted parameters of sources in IRAS 20050+2720.

SOFIA Name	Coordinates (J2000)	α	R	M_{env} (M_{\odot})	L_{mod} (L_{\odot})	i ($^{\circ}$)	A_V (mag)
IRAS20050.1	20h07m06.6s +27d28m48.0s	0.07	0.74	0.004 ± 0	128 ± 15.3	65	9
IRAS20050.2	20h07m06.2s +27d28m49.1s	1.65	0.77	0.58 ± 0.22	26.6 ± 6.0	19	14
IRAS20050.3	20h07m06.3s +27d28m56.6s	1.13	0.73	0.26 ± 0.11	48.5 ± 6.3	27	5
IRAS20050.4	20h07m05.9s +27d28m59.2s	1.71	0.27	0.38 ± 0.32	48.5 ± 8.8	43	5
IRAS20050.5	20h07m06.6s +27d28m53.1s	0.54	0.78	0.01 ± 0	49.4 ± 6.2	43	14
IRAS20050.6	20h07m02.2s +27d30m26.0s	-0.34	2.22	0.004 ± 0	201.6 ± 32.1	81	14
IRAS20050.7	20h07m07.9s +27d27m15.8s	1.29	1.50	0.015 ± 0.09	3.5 ± 3.6	0	14

Notes: The envelope masses are not well constrained due to the lack of long-wavelength emission. When the mass error is 0, it means that there is only one mass parameter for all the fits which are within 0.5 of R_{\min} .

- Generally, the best-fitting luminosity is better constrained than the masses (10–25% uncertainties in luminosity for $R < 1$);
- The sum of the protostellar luminosities is $\sim 300 L_{\odot}$, which is consistent with IRAS luminosity measurements of the entire region of $388 L_{\odot}$.
- Sources 1 and 5 appear to be at a later stage of their evolution, with a lower spectral index and much lower envelope mass. However, less models in our grid fit these models well, as all well-fitting models have the same mass at the very edge of our range of grid parameters;
- Sources 2, 3 and 4 are more embedded, with steeply rising SOFIA fluxes. They are consistent with having sub-solar mass envelopes, but the uncertainties on the envelope mass are large due to the lack of long-wavelength measurements;
- Source 6 fits less well and appears to have a very low envelope mass, as the SOFIA fluxes are decreasing with increasing wavelength.
- Source 7 has the most fractional scatter in terms of envelope mass, as well as in luminosity. The fits from this source do not allow to draw meaning conclusions. It would greatly benefit from having a high-resolution data point at long wavelength.

IRAS20050.6 is the poorest fit in this cluster, and it shows the limit of our grid of models. Judging by the shape of the SED and its negative spectral index, we can conclude that this object is not a Class 0 or Class I protostar with a large envelope. In fact, it is classified as a Class II YSO in Gutermuth et al. (2009), and our grid is not particularly well-suited to fit sources of this type. By doing some exploration of the parameter space around the best fit, it appears that the emission could potentially be fitted by a much smaller disk

outer radius with no envelope. The smaller disk size is required to reduce long-wavelength emission, as all the dust stays warmer and emits only at shorter wavelengths. In order to be thorough, we might decide to run a larger grid to fit this type of objects as well.

II.8.2.3 Diffuse emission

In testing the various scenarios of star formation, it is useful to obtain a measure of how much mass is available for the YSOs to grow after their original collapse. For this, clustered regions such as this one are an ideal laboratory since the YSOs appear to share an envelope. In this cluster, the typical separations between the sources are $6''\text{--}8''$, which correspond to projected distances of 4200–5600 au. This strongly indicates that the envelopes of individual YSOs are interacting with each other.

TABLE II.23: Clustered sources in the densest region of IRAS 20050+2720.

SOFIA name	F11 Jy	F19 Jy	F31 Jy	F37 Jy
IRAS20050.1	0.64	1.93	4.50	6.32
IRAS20050.2	0.06	1.45	9.31	11.96
IRAS20050.3	0.18	2.58	12.53	19.34
IRAS20050.4	0.06	0.25	8.54	12.85
IRAS20050.5	0.19	1.03	2.97	5.65
Sum of point sources in cluster	1.13	7.24	37.84	56.11
Total cluster emission	1.79	7.07	37.36	49.33
Ratio	1.58	0.98	0.99	0.88

Notes: The "total cluster" emission corresponds to the entirety of the region shown in Fig. II.15, which is then background-subtracted.

However, measuring the flux from each individual source in these clustered regions is challenging, since the sources are so close together. With an aperture of $2.4''$ (3-pixel radius on FORCAST), we managed to put non-overlapping apertures for all the 5 sources in IRAS 20050+2720. However, since the aperture correction was derived considering a

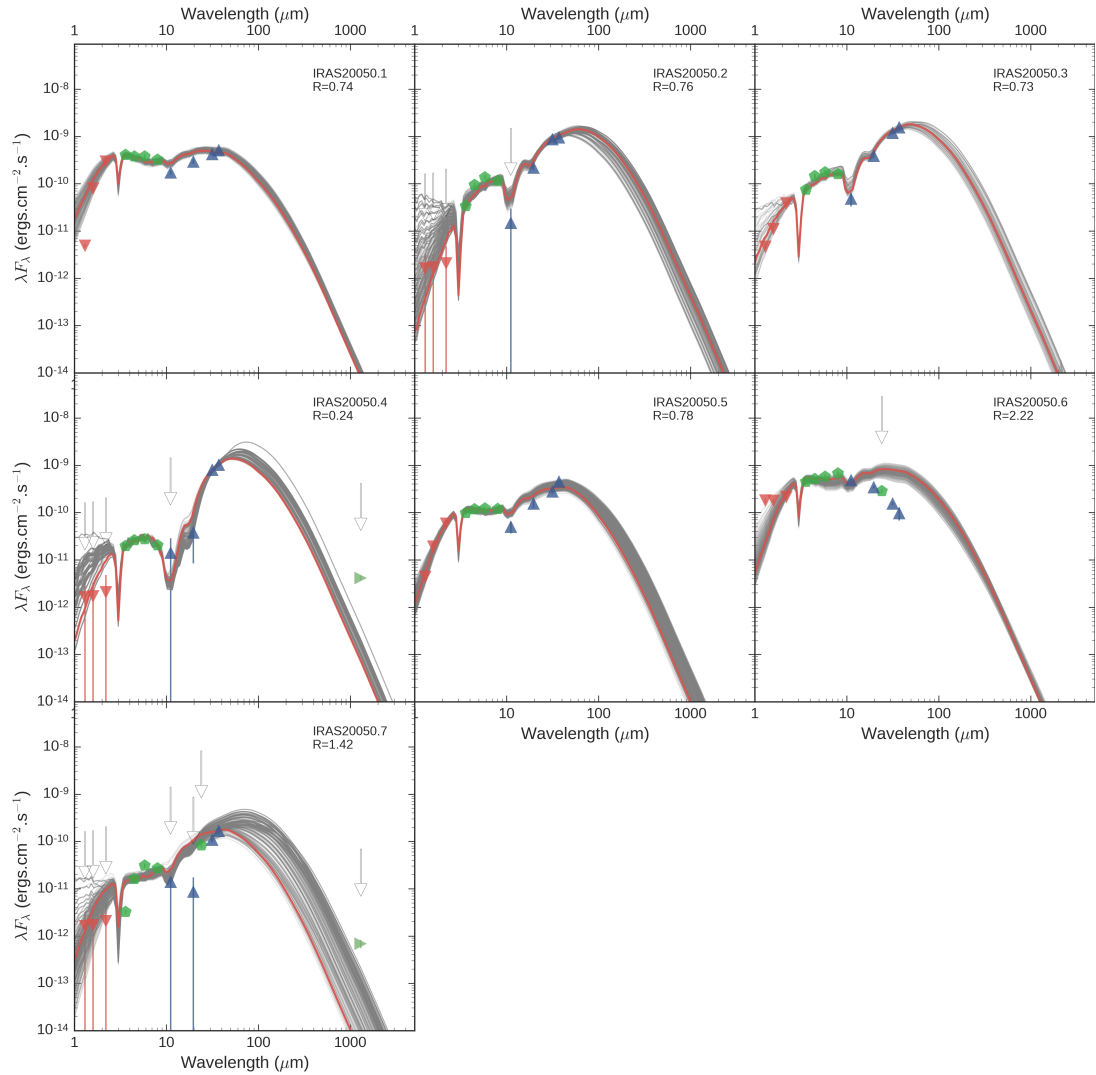


FIGURE II.17: SEDs of the 7 sources in the two fields.

"total flux" aperture to be \sim 12 pixel radius, we are accounting for the same flux multiple times, even if the apertures are not overlapping. We estimate the 37 μm flux from the eastern extended emission to total $\sim 6 \text{ Jy}$, we obtain about 22% of excess 37 μm flux when comparing the sum of the point sources and the total emission from the cluster (see Table II.23). At 31 μm , the flux excess is only about 10%. At 19 μm and below, the extended emission is within the noise uncertainty of the map.

This excess flux can only partially be explained by the tails of the PSF extending well below the aperture size (see Fig. II.2), with 10-15% of the total energy still existing in the annulus outward of 8 pixels (6'') from the aperture center. However, the contribution of a source to any given other source is only a fraction of this since it would only correspond to the amount of flux within a 3-pixel aperture. We conclude that the PSF shape is not responsible for the bulk of the observed excess flux at both wavelengths.

One possible explanation would be that diffuse thermal emission occurs across the entire region. This could be caused by heating internal to the cluster (powered by the outflow, for example, like the eastern extended emission) or by a population of stochastically heated very small grains, which are not in LTE. The high outflow activity in this region could carve out multiple cavities which facilitate short-wavelength photons from the individual stars to reach out to larger distances within the envelopes and the shared mass reservoir. At 37 μm , the level of diffuse emission required to account for the excess flux is about $0.05 \text{ Jy pixel}^{-1}$, which is the same as the average diffuse emission in the eastern region. Such an explanation would also help account for the high amount of external extinction that is needed to fit most of the SEDs in this region.

This tends to favor a scenario where protostars are fragmenting from a cloud and continue accreting material within that original envelope. The envelopes of neighboring

YSOs interact, and possibly can exchange material as some YSOs become more massive (competitive accretion).

II.8.2.4 Conclusions on IRAS 20050+2720

We have determined the photometry for 7 objects in IRAS 20050+2720. 5 of these objects are highly clustered and our FORCAST data is the first mid- to far-IR photometry for these sources. Our findings can be summarized as follows:

- Fitted luminosities for the 5 clustered sources are between 26 and $128 L_{\odot}$, with estimated scatter ranging from 10 to 25%.
- IRAS20050.1 and IRAS20050.5 have smaller envelope mass estimates compared to the other 3 sources, which is consistent with the different in their spectral index. Fitted masses are less robust and show more scatter for the most embedded sources 2, 3 and 4, which are limited by the lack of far-IR, high-resolution data points.
- We detect extended emission to the east of the main core, which is strongest in the 31 and 37 μm images. It appears to be associated with the blue lobe of the outflow coming from IRAS20050.1 (MMS1/OVRO1). We argue that the emission is arising from shock-heated material where the outflow is impacting the cloud, and we suggest that the enhanced IRAC band 3 and 4 fluxes are a signature of PAHs emission, which can be characteristic of such outflow regions.
- The grid might need to be expanded to lower masses and/or to smaller disk and envelope sizes to manage to fit Class II sources such as IRAS20050.6.
- Finally, the inconsistency between the sum of point source fluxes and the total cluster emission at 31 and 37 μm could be explained by the presence of an extended,

diffuse component the 5 clustered sources appear to share. This is consistent with competitive accretion theory of clustered star formation in which multiple cores will attempt to accrete mass from a same, shared envelope.

II.9 Conclusion and future work

We have used SOFIA FORCAST to image 42 fields in bright, nearby stellar clusters. We derive aperture photometry in 4 bands: 11.1 μm , 19.7 μm , 31.5 μm , 37.1 μm , for a total of 70 point sources and 14 extended sources. In many cases, our photometry is the only mid-to far-IR photometry available for these sources, since archival *Spitzer* observations were either saturated or confused.

In most cases, we complete our SOFIA photometry using *Spitzer* IRAC and 2MASS data to produce SEDs from 1.2 μm to 37 μm . In a limited number of cases, we also obtained *Herschel* data. When the photometry catalogs cannot be found, we use the same photometry pipeline that we developed for SOFIA on the *Spitzer* and *Herschel* calibrated images.

We proceed to SED fitting of a subset of our sources, based on a radiative transfer code called Hyperion. Starting from a standard model, we argue that there are 4 primary parameters that are needed to model the SEDs for Class 0 and I YSOs: the central luminosity, the envelope mass, the inclination angle, and an external extinction component. A scaling factor can be used as a proxy for finer luminosity sampling in the grid. We argue that as a system approaches the boundary between Class I and Class II, a fifth parameter might need to be varied in the model: the disk/envelope outer radius. Reducing this radius is necessary to appropriately reducing the emission around 100 μm while maintaining the fluxes at shorter wavelength, as exhibited for example in our source IRAS20050.6.

Fits for most our sources are reasonable. The luminosity of the family of best fits is usually constrained well, with scatter usually less than 25%. We attribute this good accuracy to the FORCAST 31 and 37 μm bands which really sample the envelope. This typical scatter does not change when long-wavelength data points are not available, for example in IRAS 20050+2720. Envelope masses, however, are constrained much better when long-wavelength data (such as *Herschel*) is available. Unfortunately, for most of our sources the long-wavelength data come from single-dish telescopes, which do not have sufficient angular resolution to guarantee that the measured flux is associated with the source; the measured emission could belong to an extended component, or to another nearby source.

We find that the fitted luminosity is substantially different from the observationally-defined bolometric luminosity of our sources (which corresponds to the integral of the observed data points), with a high dependence on the inclination angle of the fit. We argue that the fitted luminosity is a more accurate measurement of the central luminosity (which is composed of the source's luminosity and the accretion luminosity). Indeed, the bolometric luminosity is highly geometry-dependent, as a source seen edge-on will exhibit a dramatically lower bolometric luminosity as opposed to sources seen through the throat of the cavity, because of the line of sight passes through the disk which has a lot of opacity. SED fitting allows to lift this degeneracy and provide a more robust estimate of the actual luminosity.

Finally, we discuss several caveats with the fitting methods that are traditionally employed, such as the use of an external extinction factor which is modeled purely as extinction with emission counterpart. While this could matter substantially for estimating masses, we argue that its impact on the luminosity determination is small, provided that

the allowed range of extinction remains reasonable.

Chapter III

The Balloon Experimental Twin Telescope for Infrared Interferometry

III.1 Towards higher angular resolution in the far-IR

Observations at mid- to far-infrared wavelengths from the Earth’s surface are extremely limited by the large atmospheric opacity in this region of the spectrum. Space-based telescopes like IRAS (12-100 μm ; Neugebauer et al., 1984), ISO (2.5-240 μm ; Kessler et al., 1996), *Spitzer* (3.6-160 μm ; Werner et al., 2004), AKARI (1.7-180 μm ; Murakami et al., 2007), WISE (3.4-22 μm ; Wright et al., 2010) and *Herschel* (55-672 μm ; Pilbratt et al., 2010) have demonstrated the scientific value of observations at these wavelengths; but the spatial resolution of space-based observatories is limited by the cost and complexity of building and flying progressively larger aperture telescopes.

High-altitude platforms are a good compromise between ground and space observatories: while less sensitive because of the surrounding thermal emission from the atmosphere and the instrument components which are at ambient temperature, they can still feature larger optics and payloads, more experimental setups, and instrumentation that can be

changed on a more frequent and significantly less costly basis.

BETTII is an experiment that aims at breaking from the single-aperture paradigm by using interferometry between 30 and 110 μm from a balloon platform. Interferometry is commonly used on the ground at other wavelengths such as optical and radio, and is a viable path forward to obtain much higher resolution than what single apertures can reasonably provide.

BETTII is founded on a particular technique called *spatio-spectral interferometry* (Mariotti et al., 1988), which is a way to achieve high angular and moderate spectral resolutions at far-IR wavelengths, without the cost and limitations of large single apertures.

III.2 BETTII description

As a cryogenic payload flying at an altitude of 37 km (120 000 ft), BETTII is the first flying "direct detection" interferometer: it will attempt to coherently combine light from two different telescopes to provide increased angular resolution. Because it is operating from above most the atmosphere, it can see the far-infrared universe between 30 and 110 μm , and provide 0.5"-1" spatial resolution at these wavelengths - a key region of parameter space well-suited to study protostars evolving in dense clustered environments.

As a cryogenic payload flying at an altitude of 37 km (120 000 ft, BETTII is the first flying "direct detection" interferometer: it will attempt to coherently combine light from two different telescopes to provide increased angular resolution. Because it is operating from above most the atmosphere, it can see the far-infrared universe between 30 and 110 μm , and provide 0.5"-1" spatial resolution at these wavelengths - a key region of parameter space well-suited to study protostars evolving in dense clustered environments.

To provide this resolution (which matches that of JWST at 25 μm), BETTII needs to be have two collectors separated by $\sim 8 \text{ m}$; because of its operating wavelength, it needs to have a cryogenic instrument; because it is an interferometer, it needs optics with excellent surface quality (for far-infrared standards); and because it flies on a balloon platform, it needs to accommodate for large changes in temperature, large pointing errors, and severe shock resistance for the landing phase.

This chapter will first discuss the basics of double-Fourier interferometers, then present the general design of BETTII payload and most of its subsystems.

III.3 Basics of interferometry

Since the end of the 19th century, scientists have learned how to use the wave properties of light to learn about new astrophysical phenomena. It did not take long for what first started as a laboratory experiment by Michelson et al. (1887) to be applied to astronomy, with the Michelson Stellar Interferometer experiment.

The principle of interferometry is simple. Because light behaves like a wave, two beams of light coming from the same source can be combined *coherently*, provided that their amplitudes and phases are controlled. The intensity of the combined signal is a function of the brightness of the light beam, and the relative phase and wavefront of each beam. Changes in the relative phase create a modulation of that brightness.

Michelson et al. (1887) created what became the standard Michelson interferometer (Fig. III.1). It uses one single source of light and a 50/50 beam splitter that creates two coherent light beams from that one source. The two light beams go through two separate *arms* before being recombined. While adjusting the length of one arm with respect to the other, we modulate the phase difference between the two arms, leaving everything else the

same. This creates a modulation called an *interferogram*, which describes the measured intensity variation as a function of the phase difference between the two arms.

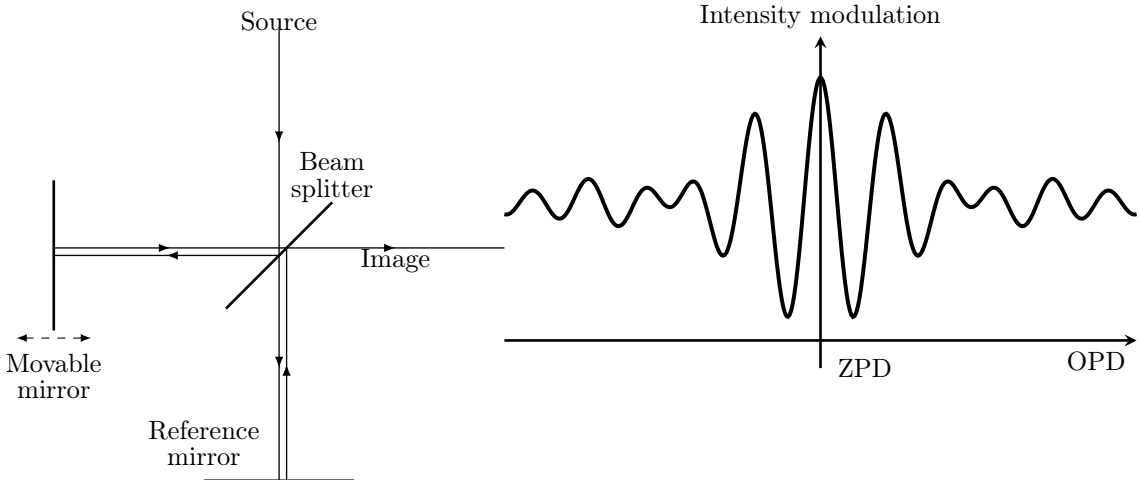


FIGURE III.1: *Left:* Schematics of a Michelson interferometer. *Right:* Intensity modulation resulting from the mirror linear motion. The center of the modulation, called "ZPD" for zero path difference, is the precise location of the mirror where the distance is equal in each arm.

The phase difference is expressed in radians and depends on the wavelength of the light that is used. In this work, we will usually refer to this difference in terms of an actual physical distance: the optical path difference (OPD). This has the advantage of being wavelength-independent and relate more easily to opto-mechanical considerations.

III.3.1 Fourier transform spectroscopy

One immediate consequence of the original Michelson experiment is to realize that the interferogram actually contains spectral information. For an ideal monochromatic source, the interferogram depends on the OPD only modulo a wavelength. This means that the modulation is identical whether we introduce an $\text{OPD} = \lambda$, or $\text{OPD} = n\lambda$, where n is an integer. This is because the monochromatic wave can essentially be represented by an amplitude times a cosine function of phase (a cosine function of $2\pi\text{OPD}/\lambda$).

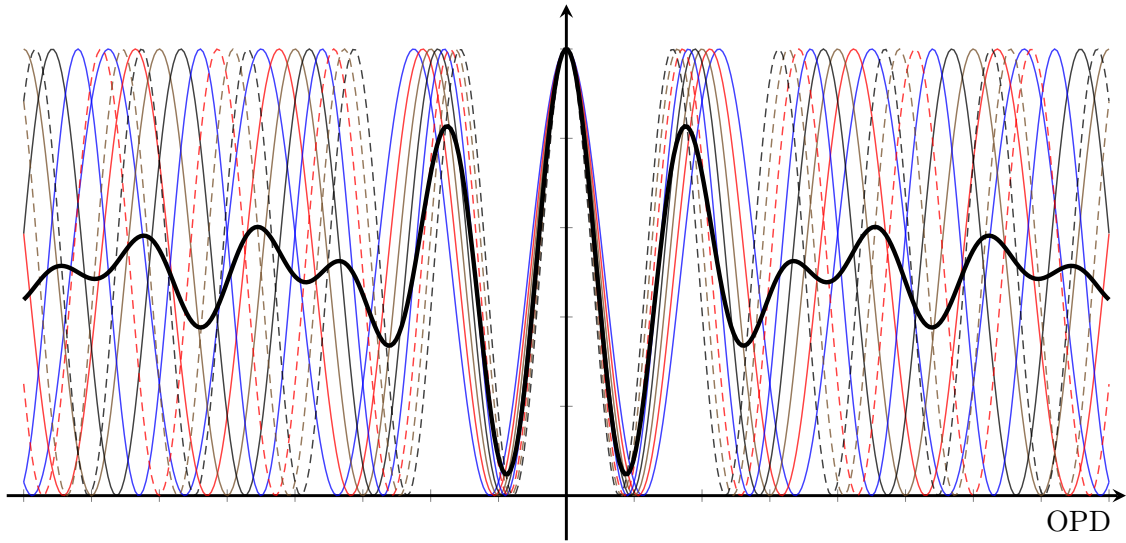


FIGURE III.2: An ideal interferogram here is shown as a sum of cosine waves of different frequencies.

The interferogram for a given wavelength is a cosine wave, with an amplitude related to the intensity of the signal, and a period equal to the wavelength of the incident light.

If we consider a polychromatic signal as a sum of monochromatic wavelengths, this phenomenon happens for each single wavelength, and the resulting intensity modulations add *coherently*: the total intensity is the coherent sum of the intensity modulations created by each individual wavelength (see Fig. III.2). This has the effect of smearing the resulting modulation in most places except around the precise location where the OPD is zero (which is called *ZPD*). Around this location, a modulation is always seen. This is commonly referred to as *white light fringes*, where a *fringe* represents one wavelength of the interferogram. The range of OPD in which fringes can be seen is called the *coherence length* L_c . When all wavelengths are weighted equally in a bandpass $\Delta\lambda$, the coherence length can be expressed as:

$$L_c = \frac{\lambda^2}{\Delta\lambda}, \quad (\text{III.1})$$

and the interferogram can be represented by a carrier frequency modulated by an envelope function.

Since the modulation is a coherent superposition of cosine waves, it contains spectral information. A cosine transform of the interferogram will decompose the contribution of each individual wavelength, hence reproducing the spectrum of the polychromatic source. This technique, called "Fourier Transform Spectroscopy", has led to many scientific discoveries in astronomy, chemistry and other fields over the last 100 years.

III.3.2 Aperture synthesis

An interferogram is produced by coherently combining photons from one single source of light. This can be applied for example for an infinitely distant astronomical source: as the light propagates from the source, by the time it reaches our instrument the radius of curvature of its wavefront is extremely large, and the latter can be approximated as being flat. The photons from this source nominally enter each arm of the interferometer with the same phase, when the alignment is perfect. When combined, these photons interfere and create an interferogram.

However, let's suppose that a second source is sufficiently far away from the first source that its wavefront enters the interferometer at an angle (see the red source in Fig. III.3). This means the photons from the second source enter one arm slightly later than the other - photons need to cross over more optical path in one arm than in the other. These photons would also create an interferogram, but the latter will be centered about a different position in OPD space than the interferogram created by the photons from the first source. Now let's suppose that the second source is exactly as bright as the first one, and that it is apart from the first by an angle θ such that $\mathbf{B} \cdot \hat{\mathbf{s}} = |\mathbf{B}| \sin \theta = \lambda/2$, where

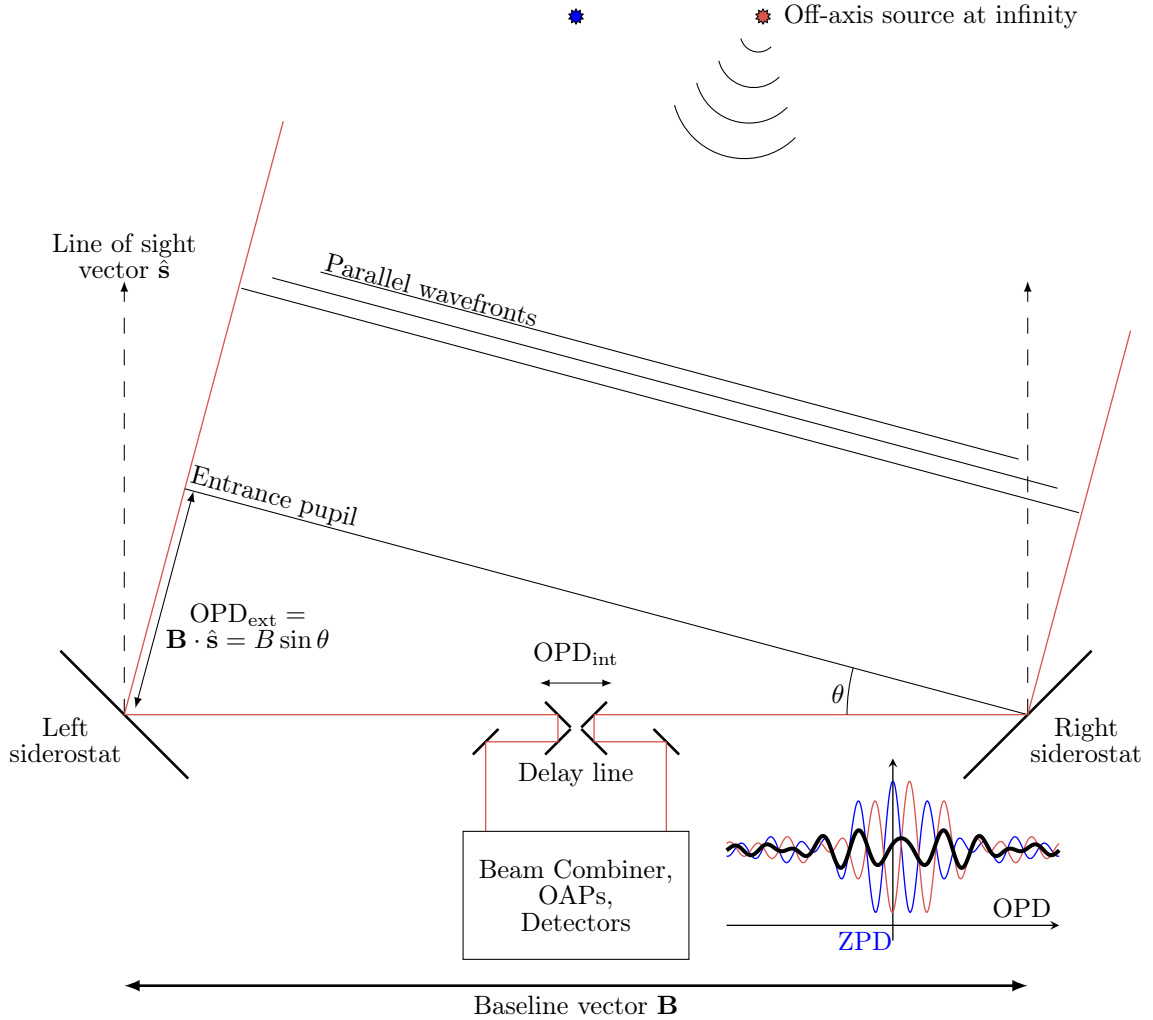


FIGURE III.3: Schematics of a Michelson Stellar interferometer. Two sources are shown at the top of the picture. The red source is off-axis by an angle θ . Since it is infinitely far away, its wavefront is essentially planar as it reaches us. The two siderostats sample the identical wavefront at different points, but because of the incidence angle, the light in the left arm travels slightly more path than the light in the right arm. As a result, the interferogram from that source will be shifted, since the position of ZPD is now offset by this extra distance the light has to cross. On the other hand, light from the blue source, which is perfectly on axis, produces an interferogram which has a ZPD at the nominal position. Those two intensity modulations co-add in the detector plane, and the sum is shown in black. By observing these summed interferograms over multiple baseline angles and distances, one can reconstruct entirely the spatio-spectral scene.

\hat{s} is a unity vector representing the line of sight of the telescope, and \mathbf{B} is the baseline vector projected on the plane of the sky. In this case, the interferogram created by the photons from the second source has the same amplitude as the first interferogram, but is

shifted by half a wavelength in OPD. As a result, the two (monochromatic) interferograms would exactly cancel each other, and we would say that the visibility (sometimes referred to as the *complex degree of coherence* (e.g. Mariotti et al., 1988)) between the two sources is zero. Although the sources are not coherent in the strict sense because they are completely independent sources, the interferograms caused by each source would, in this case, cancel out. If the angular separation was such that $|\mathbf{B}| \sin \theta = \lambda$, then the modulations would add up and the resulting modulation would have twice the amplitude of that with just one single source. We would say that the visibility between the two sources is unity. In the bottom right of Fig. III.3, we show the addition of two polychromatic interferograms (in blue and red), adding up to the measured curve in black. By measuring the curve in black, we know that there are two sources along our baseline vector. The spatial resolution of the interferometer is its ability to resolve nearby sources directly in the interferogram space - in other words, it is its ability to resolve fringe packets. Usually, this spatial resolution is equal to $\theta \sim \lambda/(2B)$. A summary of the relevant planes used in aperture synthesis is shown in Fig III.4.

One way to formalize the concept of spatial coherence is to consider an interferometer with a given baseline length and angle as a filter of the source's spatial distribution on the sky. For a given baseline length and angle with respect to the sky, the interferometer is only sensitive to a single angular frequency in a single direction on the sky (as well as the total power). Various sources observed simultaneously by the interferometer will all contribute to a single measured interferogram, which can be characterized in terms of the complex visibility between the sources for a given baseline angle and length.

The generalization of this property is called the Van Cittert-Zernike theorem (Zernike,

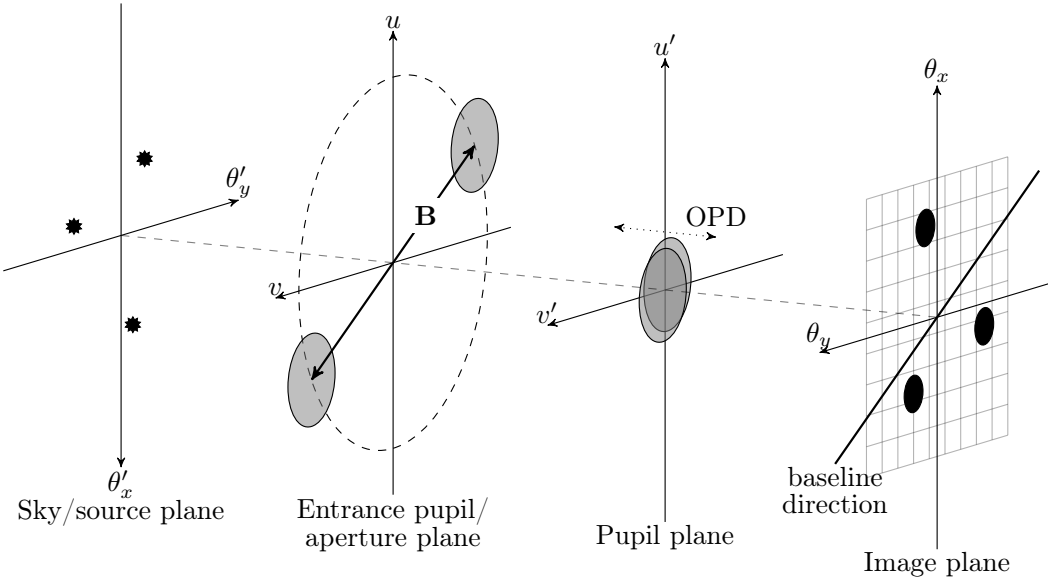


FIGURE III.4: Relevant planes in the optical train for aperture synthesis, inspired by Fig. 3.14 in Glindemann (2011). Three sources are shown on the sky on the left. The second relevant plane is the entrance aperture or pupil plane, which is the 2D Fourier transform of the source plane, which is also called the u,v -plane. The interferometer samples two apertures in this complex plane at each given baseline length and orientation with respect to the sky. In the third plane, we show that an optical delay is introduced between each sub-aperture in the pupil plane, and the pupils are overlapped. Finally, an image is formed out of the overlapped pupils, which is shown in the detector plane.

1938): the 2D Fourier transform of the intensity distribution on the sky is its complex visibility function. In other words, by mapping the complex visibility (through measuring interferograms) for all baseline angles and lengths, we can reconstruct the original image through an inverse Fourier transform. The plane of complex visibilities is commonly referred to as the (u,v) -plane (Thompson et al., 2008).

Interferometry and aperture synthesis is used commonly at radio wavelengths, where coherent detectors can retain the direct phase of the incoming light by mixing the signal with a local oscillator. Both the amplitude and the phase of the signal can be recorded for each antenna, and can be combined with all the other antennas at a later time.

Aperture synthesis has also been achieved at optical and near-infrared wavelengths from the ground, where a nearby guide star is used to determine a reference phase of

the incoming beam (e.g. Monnier et al., 2004; Gillessen et al., 2010). The interferograms measured for the science sources can then be non-ambiguously aligned with each other. This process requires very rapid imaging capabilities (on the order of 10 ms, a typical atmospheric coherence timescale, see discussion in Mariotti et al., 1988) to freeze the atmospheric variations across the synthetic aperture, which in turn requires bright guide stars. In addition, because of the large baselines, the field of view is very limited, so the targets accessible by optical interferometers are limited to scientific sources which are a few arcseconds of a bright guide star (Glindemann et al., 2000): this dramatically limits the capabilities of ground-based interferometry at these wavelengths.

III.3.3 Double-Fourier interferometry

In this work, we introduce the concept of Double-Fourier interferometry, which uses a standard Fourier Transform Spectrometer at the back-end of a Michelson stellar interferometer (see Fig. III.5 and Mariotti et al. (1988)).

We adopt a Michelson interferometer configuration with pupil-plane combination. Unlike image-plane combination, where fringes are seen across a single Airy disk in the image plane, no fringes are visible across the field of view at a given OPD. Instead, the intensity of the entire field of view is modulated as a function of OPD.

By scanning the OPD, we obtain a modulation of each pixel on the detector, which contains information on both the spectral (through the Fourier transform of the scan) and the spatial (through the amplitude and phase of the fringe packet) characteristic of the source, at that baseline orientation and length. By repeating the measurement over a full range of baseline angles and lengths, one can unambiguously retrieve both the spatial and spectral content of the astronomical scene by filling the synthetic aperture.

Pupil-plane combination allows for an interferometric response of the entire field of view. The price we pay is that the OPD scans need to be longer in order to cover enough range, going through ZPD for each pixel in the field of view. For a single-pixel detector, the OPD scan would only need to cover enough stroke to obtain the desired spectral resolution for the one single pixel.

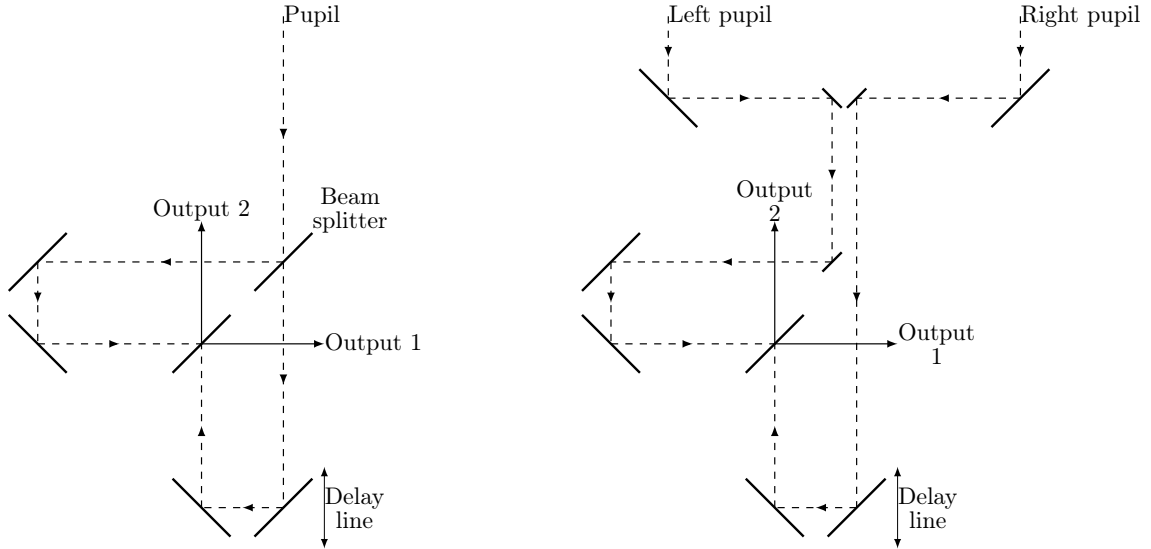


FIGURE III.5: Standard FTS telescope layout (left) versus double-Fourier telescope layout (right) (Mariotti et al., 1988).

A detailed derivation of the equations of Double-Fourier interferometry starting from first principles is presented, in Appendix A.1 and Chapter IV.

III.4 BETTII Instrument design

The BETTII payload is an 8 m fixed-baseline interferometer, equipped with two 50 cm siderostats. It operates in two wavelength bands, 30-55 μm and 55-110 μm . In these two bands, its theoretical angular resolution is $\sim 0.5''$ and $\sim 1''$, respectively. This is significantly better than all existing or previous facilities that operate in the far-infrared, which are limited by the mirror size. In addition, this matches the resolution of JWST at 25 μm ,

hence providing the ability to probe astrophysical phenomena at longer wavelength with the same angular resolution.

There are four major components to BETTII: the mechanical structure and design; the optics and their mounts; the cryostat and the detectors; and the control system. The latter will be discussed extensively in Chapter V. In this section, we first describe the balloon environment and its constraints, before discussing these four major BETTII components.

III.4.1 Stratospheric balloon environment

High-altitude balloons have for many years served as a test platforms for future space instruments, such as the FIRAS instrument on COBE (Fixsen et al., 2002a). These balloon platforms fly between 30 and 40 km, above more than 99% of the atmosphere, which make them particularly well suited for studying the universe at infrared, far-infrared and sub-millimeter wavelengths. Balloon launches occur year-round across multiple continents, including Antarctica. NASA and other agencies organize these campaigns for various areas of science.

For a typical launch, the scientific payload is attached on the bottom of a train of about 100 m that includes a parachute and a ladder. The top of the ladder attaches to the bottom of the large helium-filled balloon.

At float altitude, the air temperature is between 230 K and 250 K, while the air pressure is 0.5% of the sea level pressure (about 5 mbar). Upper altitude winds are large-scale laminar flows that move the balloon and the payload as one. This can excite pendulum motions about the pivots underneath the balloon and at the top of the payload, which are



FIGURE III.6: Picture of a balloon launch. The payload is captured by the launch vehicle (in yellow) until the balloon is inflated and released. The parachute assembly, which is a part of the long train from the top of the payload to the bottom of the balloon, can be seen in red. Credit: NASA.

typically of the order of a few arcminutes and have periods of a few to many tens of seconds (Fixsen et al., 1996a).

The payload's temperature distribution is influenced by the air temperature, infrared radiation of the Earth, and sunlight, which can result in complex temperature gradients across the instrument. A better temperature uniformity is expected for night flights, which is what BETTII is expecting.

Balloon experiments can also be affected by cosmic rays which can damage the electronics, lead to data corruption and or failures of the software/control system. However, this becomes more of an issue for long-duration balloon flights around Antarctica, during which the payloads are exposed for many weeks to the cosmic ray environment.

BETTII is expected to launch from Fort Sumner, NM, for its first engineering flight in September 2016. After a morning launch, we expect to wait until nightfall to achieve

proper thermal stabilization and achieve our science goals. We expect the flight to last about 16 h, although this is highly dependent on the weather and wind patterns.

III.4.2 Mechanical design

BETTII has two main structures. The first is a carbon fiber and steel truss that is used as our optical bench, and all our optical elements are attached to this structure. This was the first item that was designed in the project. The elements of this structure are built by bonding 7.5 cm diameter hollow carbon fiber tubes to custom-made steel conical ends, that we call *nose cones*. The steel nose cones are lightweight and strong, and have a threaded hole on the axis: they attach to multi-faceted steel nodes. There are three lengths of tubes on the truss. At the interface between the nose cones and the nodes, and depending on the location on the payload, we use either a combination of spherical washers and bellville washers or polypropylene washers. The difference of the washer material compensates for differential thermal contraction on the beams that form the long side of triangles.

The structure is about 9 m long. It is designed to be lightweight, strong, and have a first resonant mode above 20 Hz to ensure fast damping of residual mechanical oscillations. We measured the first resonance peaks to be within 1 Hz of their expected frequency, at 25 Hz (see Chapter VI).

The entire balloon payload needs to be robust to handle 10 g vertical force and 5 g force at 45 deg, which are the safety guidelines from the launch facility. With an expected total mass of 1000 kg, we need yield strength sufficient to hold 100 000 N of force.

An annotated rendering of BETTII is shown in Fig. III.7. The gondola is what holds the truss and attaches to the balloon train. It also holds the electronics, reaction wheels, batteries, and communications to the ground. The frame is made out of 80/20 T-slotted

aluminum bars that are attached together using T-inserts, and reinforced by screwed-on corner plates. The precision of this frame is of no importance to the optical alignment.

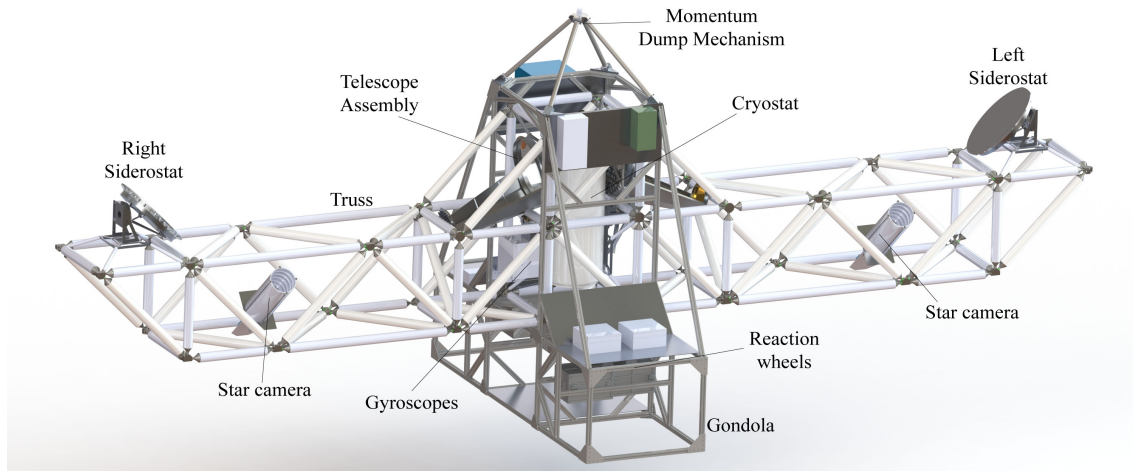


FIGURE III.7: CAD rendering of the BETTII payload in its final state.

The various electronic components of the system are attached to the gondola using aluminum or honeycomb aluminum plates, which are painted with white appliance paint for better thermal behavior. These plates act as radiator panels which allow us to dissipate the heat out to space.

The most critical portion of the gondola is the assembly that connects to the balloon train. This contains a single pin that needs to have the highest yield strength, since it is the only point of the payload that needs to support the entire weight. A more detailed description of the pin is presented in Section V.V.1.2.4.

The entire payload is designed, assembled and tested in the building 20 high bay at NASA GSFC (Fig. III.8).

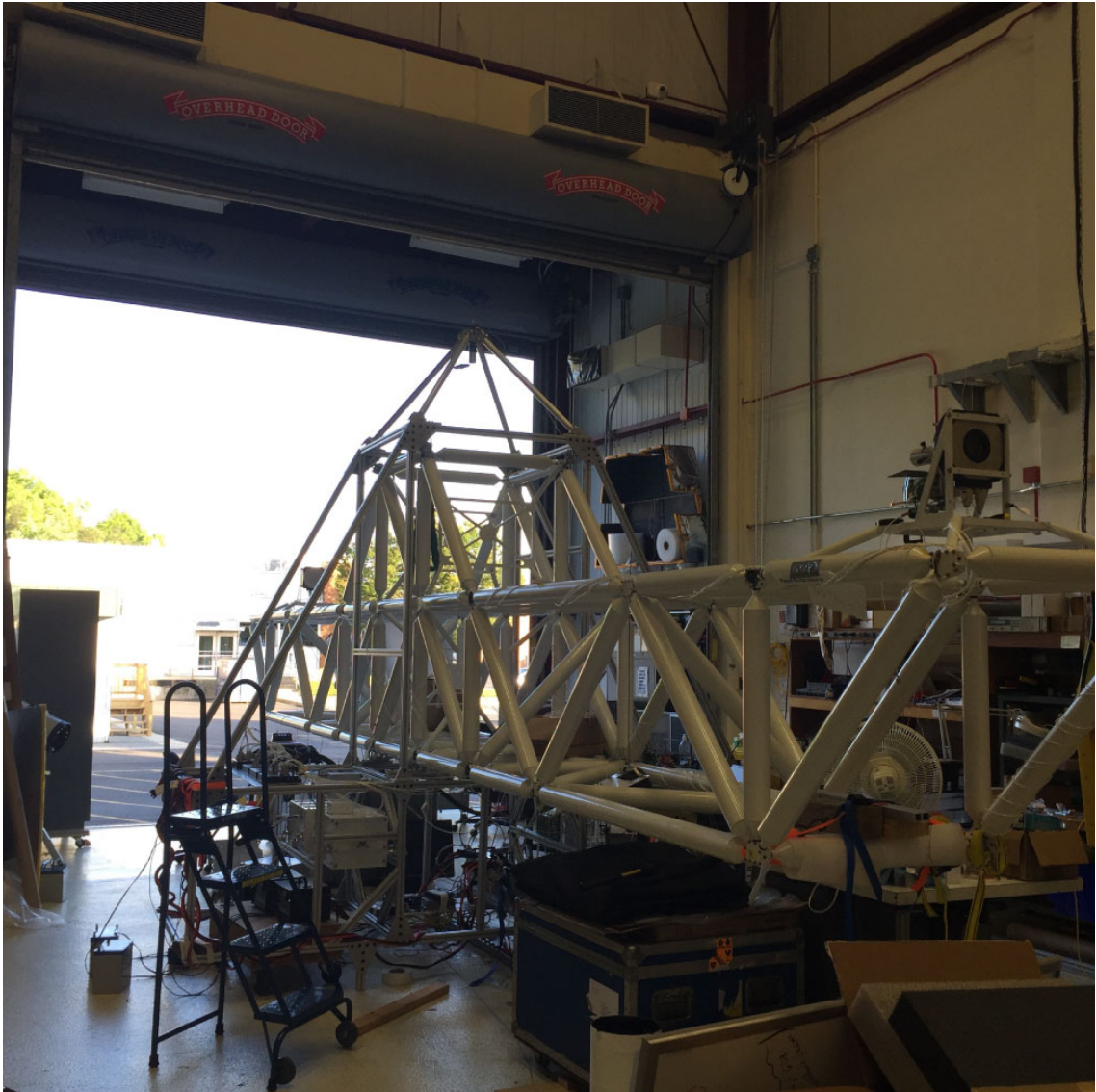


FIGURE III.8: Payload in the high bay before a controls test.

III.4.3 Warm optical system

The optical system was one of the most challenging design aspects of the project. It is beyond the scope of this work to go into details about all the considerations that went into the design, but we will review some of the main aspects: the overall optics layout, and the fabrication of the telescope assemblies.

III.4.3.1 Optics layout

Because the nature of balloon payloads, there can be extensive damage to the structure during parachute opening and landing. In order to minimize the repair costs from one flight to the next, it was decided to place the telescope assemblies - which are expensive, long lead-time items - away from the edges of the truss.

Instead, flat mirrors (that we call *siderostats*) are used to redirect the light towards the telescope assemblies, which are kept close to the center of the truss where damage is expected to be minimal.

The telescope assemblies (Fig. III.9) consist of 3 powered mirrors and a folding flat. They provide a 20:1 compression ratio of the beams with reasonable tolerance on the mirror positioning. As an all-aluminum assembly, they shrink homologously as the temperature varies during the different phases of the flight, hence maintaining optical prescriptions.

In order to perform double-Fourier interferometry, an extra reflection needs to be introduced in the system in order to properly combine the polarizations of the light at the beam combiner (see Fig. III.5). This asymmetry occurs after the telescope assemblies and before entering the cryostat. In one arm, a 3-mirror assembly (called the K-mirror assembly, or KMA) is used on a rotating stage to match the field of view rotations as the two siderostats change elevation. On the other side, a 4-mirror delay line assembly (called the Warm Delay Line, or WDL) is set at a fixed orientation. Its role is to compensate for the optical delays caused by the residual pointing errors.

On both the KMA and the WDL (Fig. III.10), one of the mirrors is actuated in tip and tilt, which provides the fine control required to properly overlap the two beams at the detectors. There is an extensive discussion of the control system in Chapter V.



FIGURE III.9: Telescope assembly model and layout.

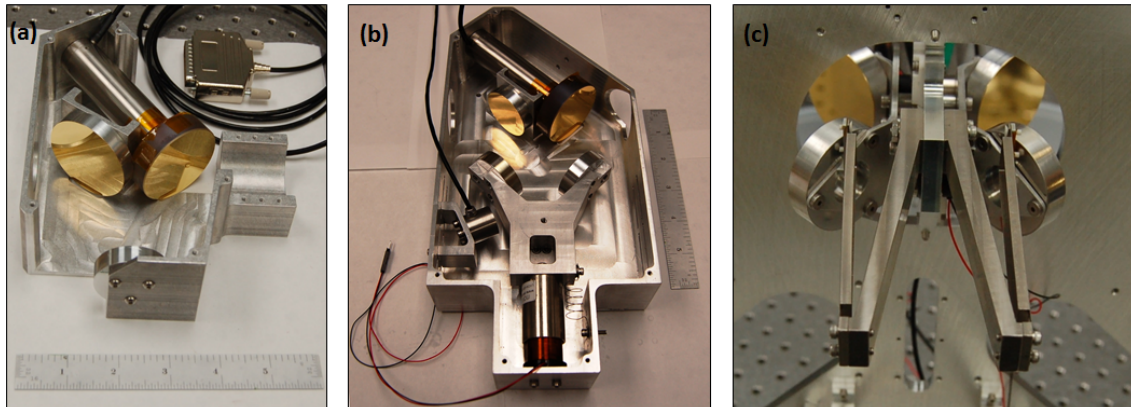


FIGURE III.10: K-Mirror Assembly, Warm Delay Line, and Cold Delay Line.

The beams from each side enter the cryostat through thin polypropylene windows. We tested different window thicknesses and selected the $15\text{ }\mu\text{m}$ thickness as our baseline design. Once the beams are inside the cryostat, they are split into a NIR tracking channel, and into the FIR optics train where they are delay-modulated by the Cold Delay Line

(Fig. III.10), combined, and image onto the detectors. A complete layout of the optics train is shown in Fig. III.11 (Dhabal *et al.*, 2016, in press).

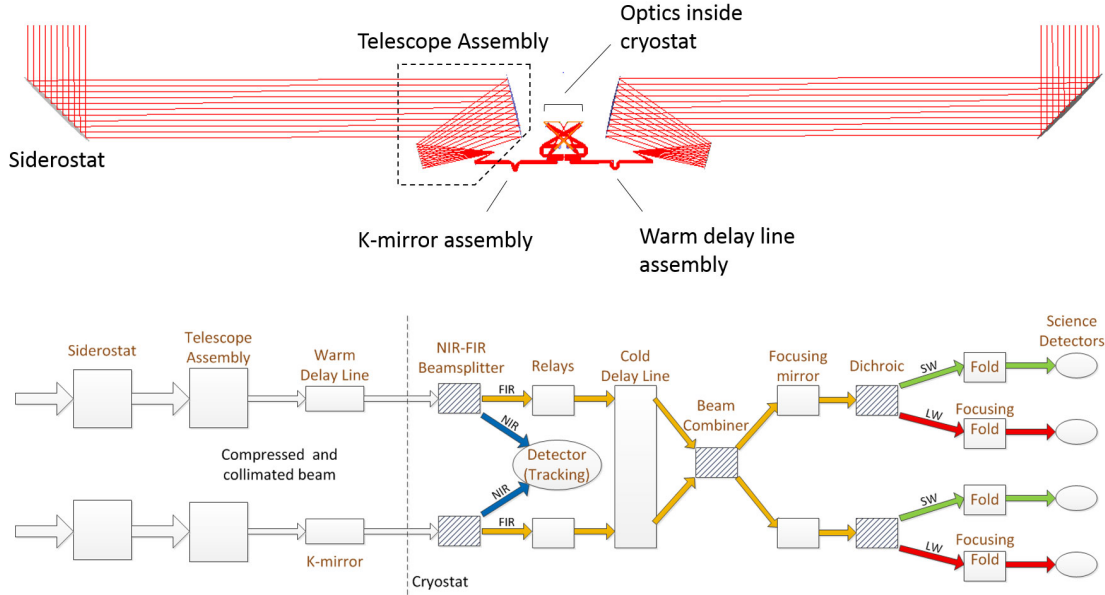


FIGURE III.11: Optics layout for BETTII (Dhabal *et al.*, 2016, in press).

III.4.3.2 Optics manufacturing

Despite working at relatively long wavelengths, the tolerance in the surface figure of all the mirrors is an important consideration. Differential wavefront errors between the two optics trains before combination will result in decreased contrast of the interferograms, which reduces our signal-to-noise ratio. As a result, the surface quality of the mirrors pre-combination needs to be much lower than a wavelength of light, since errors will stack after hitting many mirrors from both sides. We allocate $2\text{ }\mu\text{m}$ of total wavefront error at combination, which translates to $\sim 0.23\text{ }\mu\text{m}$ of surface error per mirror. Given that known processes exist to manufacture small mirrors below this requirement, we relax the requirement for the primary mirrors and the siderostats to a 300 nm r.m.s surface figure error over the entire aperture.

The company Nu-Tek, in Aberdeen, MD manufactured all of our small optics out of aluminum. The procedure includes an initial milling process, heat treatment using a method called *uphill quenching*, followed by diamond turning and gold coating to avoid oxidation.

However, very few manufacturers in the United States were able to diamond-turn the siderostats and the primary mirror assemblies, while ensuring the level of surface figure we needed. The diamond-turning process uses a slowly moving diamond blade that is controlled in 3 axes to carve out the required shape. This process requires extreme temperature stability, which is often not available in traditional machine shops. Companies which are familiar working with NASA on space missions were not affordable for a small project like us.

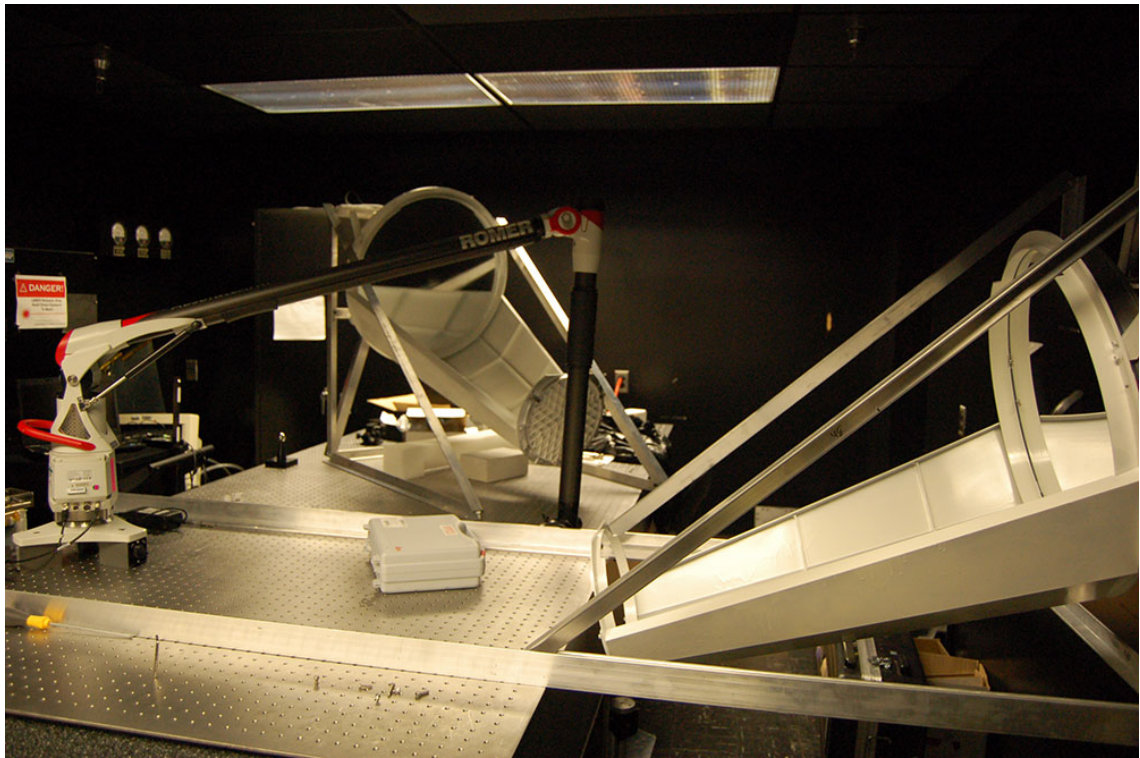


FIGURE III.12: Telescope assemblies in the optics lab.

proposed to manufacture our mirrors on a 'best effort' basis for a reasonable cost. The results are published in Furst *et al.* (2016, *in press*), although the surface quality has not yet been measured, due to difficulty with the equipment and setup in the optics lab at NASA Goddard. Each telescope assembly (see Fig. III.12) has a stacked r.m.s surface figure error of 300 nm, while the siderostats have a surface error of 100 nm r.m.s. The siderostats are more complicated because they did not exactly fit in their diamond-turning spindle. We decided to proceed with a two-step diamond turning, where they turned two sections of the ellipse consecutively. This does not guarantee that the two areas will be at the same height since they have to unmount the mirror off the spindle. However, our models show that even if different sections of the mirrors are at different heights, the beam combination can still be successful, as the parts of the pupil that are shifted in one arm are also shifted in the other.

III.4.4 Cryogenic instrument

The cryostat was designed by our team. Items were sent out for manufacturing to different companies and assembled in our lab. The cold volume is cooled by liquid nitrogen and helium and does not require any mechanical cryo-cooler. It is designed to operate for a duration of 40 h, which should give us enough margin considering the typical lengths of balloon flights from the U.S. of about 16 h.

The optics inside the cryostat are split into two sections: a near-infrared fine guidance system, and the far-infrared channels with the science detector (Fig. III.13). The incoming light beam is split right after entering the cryostat with a NIR/FIR dichroic beam splitter. This custom-made filter reflects the far-IR and transmits the near-IR. At the bottom of the cryostat, in the 77 K volume, the fine guidance sensor is composed of 12 optics and

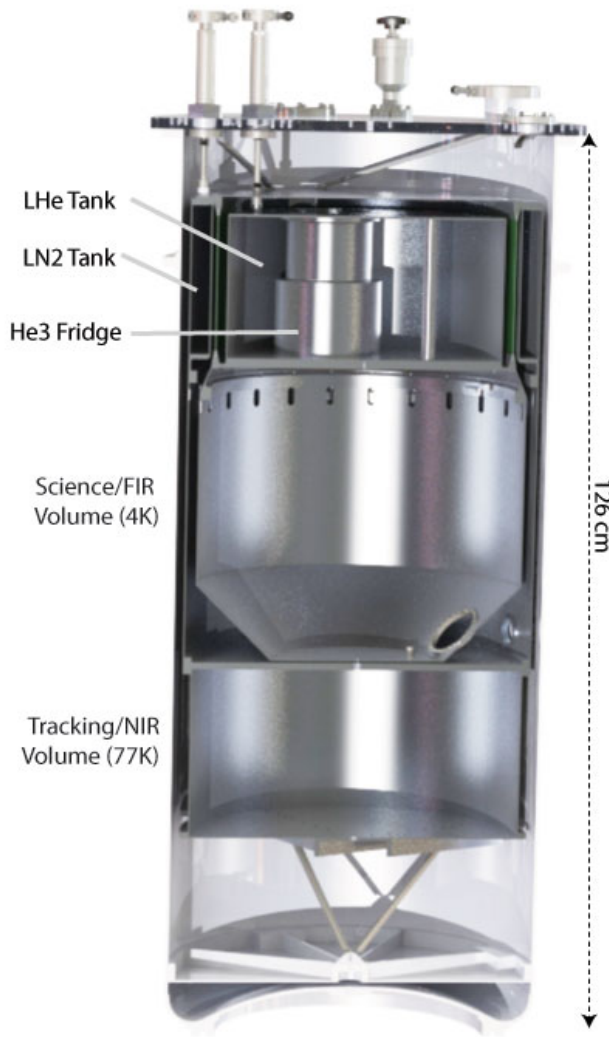


FIGURE III.13: Cryostat crosssection.

one HAWAII-1RG detector from Teledyne.

At the top of the cryostat and attached to the 4 K cold plate, there is a cold optics bench that holds all of the far-IR optics, filters, and the Cold Delay Line. All filters were manufactured by Cardiff University in the U.K. The layout of the optical system is shown in Fig. III.11, and more details can be found in (Dhabal *et al.*, 2016, in press). A picture of the cold optical bench with populated and aligned optics is shown in Fig. III.14.

The cold plate of the dewar is cooled down to 4 K with liquid Helium. A ($^3\text{He} + ^4\text{He}$)

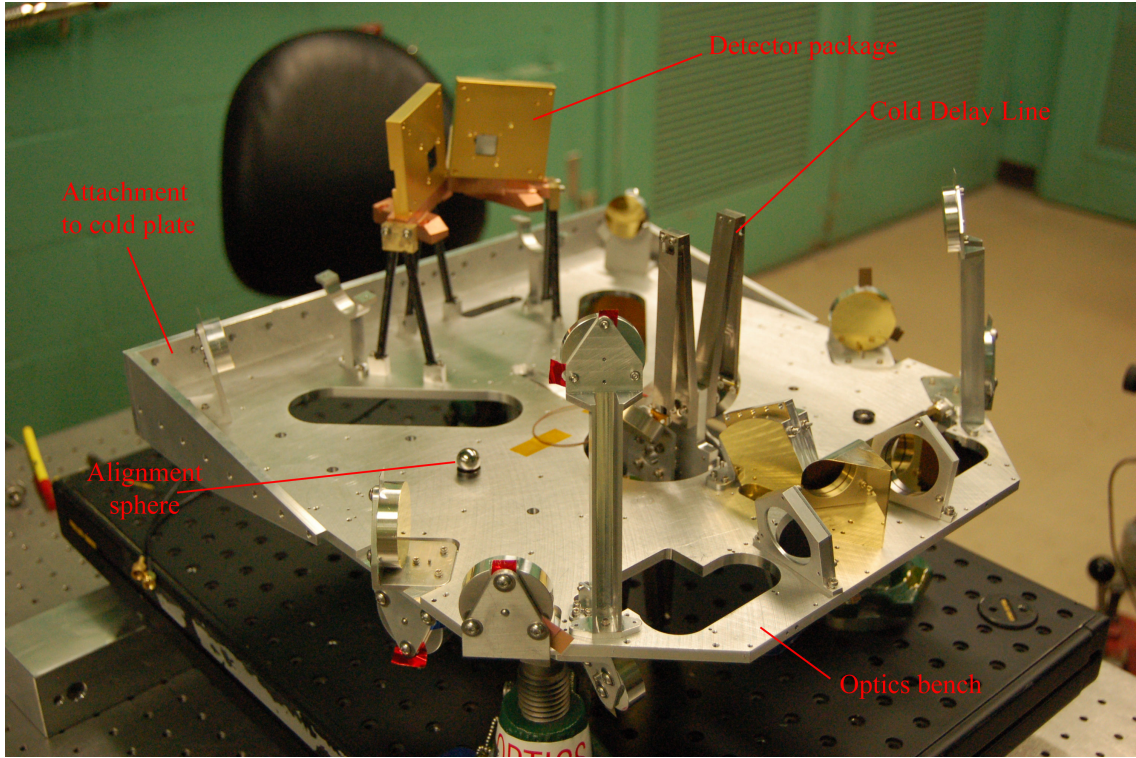


FIGURE III.14: Optics on the cold bench.

sorption refrigerator from Chase Research is used to obtain an intermediate cold finger at 1 K and a final stage that brings down the detector temperature to ~ 400 mK. Fig. III.15 shows a picture of the top plate of the cryostat while cold.

At the heart of the instrument are four 9×9 close-packed linear arrays of multiplexed superconducting transition edge sensor (TES) bolometers (Benford, 2008) incorporating the Backshort Under Grid (BUG) architecture (Allen et al., 2006). These arrays are scaled versions of similar arrays already built for ground-based instruments (e.g., GISMO, Staguhn et al., 2014a). Detectors are read out using advanced linear SQUID multiplexer and amplifiers. A 4×22 multiplexed readout is used for each array; the extra seven channels are used for calibration signals (unilluminated pixels, “dark SQUID” channels, and an “always on” channel), allowing monitoring of all potential noise contributors (Korte et al., 2003).

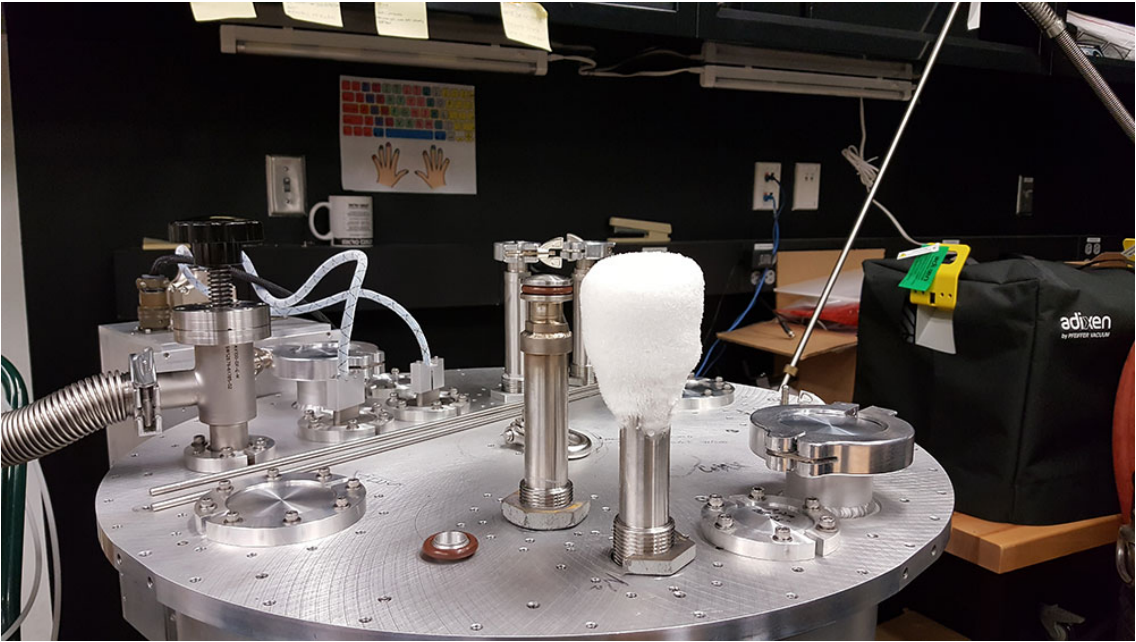


FIGURE III.15: Cryostat top plate during cool down.

III.4.5 Data products & analysis

Once in flight the payload operations consist of pointing at a target, stabilizing the attitude motions, and scanning the delay while recording detector data. A number of operational modes are required to ensure we reach this stable observing stage, and are described in more details in Chapter V.

Individual scans will last for a nominal duration of 2.5 s, and consist of 1024 individual detector frames, which are matched to a given OPD. To increase the signal-to-noise ratio (SNR), we expect to stack 10 min worth of data, which corresponds to 200 scans. For this duration, we expect that the change in the baseline angle due to the rotation of the Earth is negligible. It is critical to correctly stack the interferograms, as OPD errors from scan to scan can significantly reduce the fringe contrast (see Chap. IV).

To describe post-processing, let's consider a 10 min cube which is the OPD-corrected stack of images from the 200 individual scans. The cube has a cross-section of 9×9 (which

is the size of an individual detector frame), and a depth of 1024 frames. For each frame, the intensity of each source in the detector is determined for each OPD, and combined into interferograms. We repeat the process for the same field observed at different baseline angles.

Using starting points involving our existing SOFIA multi-wavelength observations, as well as the IRAC images, these interferograms will help determine the multiplicity of bright sources, their individual SED, and their position relative to the large-scale extended emission.

If BETTII had more baseline lengths and the reconstructed cubes filled the aperture more densely, it would be possible to feed them directly to an inversion software that was developed in Dr. Juanola-Parramon's Ph.D. thesis (Juanola-Parramon, 2016), which provides a final datacube corresponding to the images as a function of wavelength, with the spectral resolution that the user chooses.

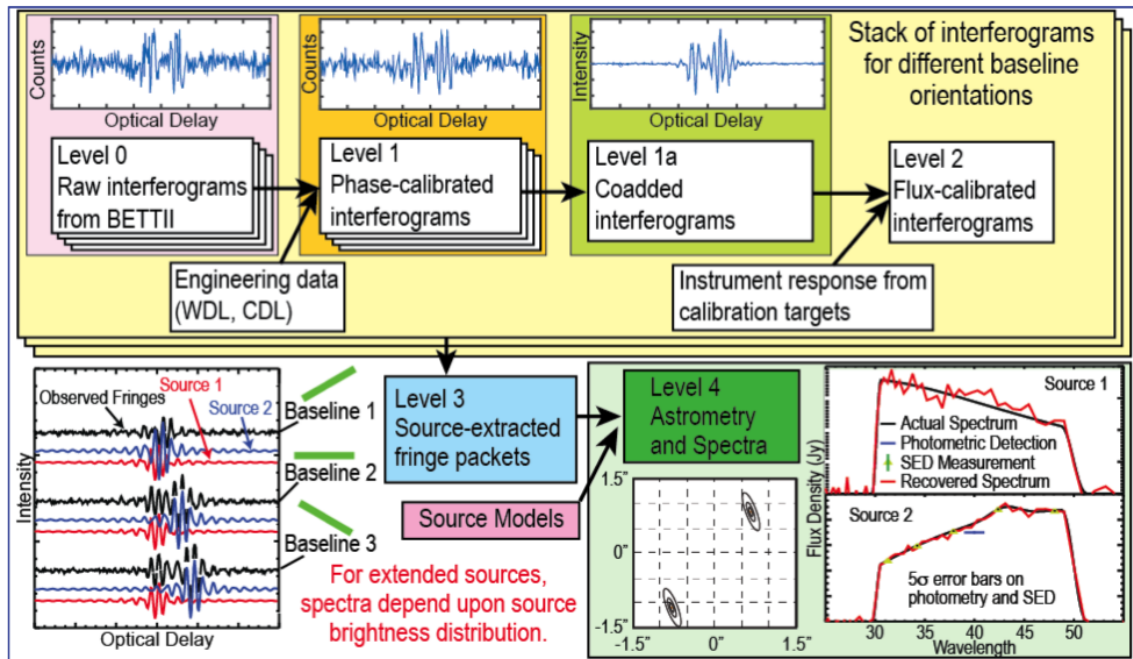


FIGURE III.16: BETTII data processing steps.

III.5 Sensitivity analysis

Early in my involvement with BETTII, I led the effort in trying to estimate the sensitivity of our instrument, in order to select relevant scientific targets, but also find astronomical calibrator objects which would help us understand the systematics of our payload.

This section summarizes the findings and gives details on the methods and equations we used. We were able to derive a new formalism to estimate the spectral sensitivity of double-Fourier interferometers for point sources. Our method uses propagation of gaussian errors through Fourier transforms, and is described in detail in Chapter IV. This can be useful to determine the sensitivity of other types of instruments, such as a space-based follow-up of BETTII, which we briefly discuss in the conclusion of this work.

III.5.1 Instrument and observing parameters

Table III.1 represents the key instrument parameters that are relevant for the sensitivity estimation of the two science channels of BETTII. The main impact of each parameter on some aspects of the science is shown. A detailed, custom calculator tool that we developed compiles most of the instrument parameters that flow down from these requirements, which in turn serve as design baseline for various subsystems. For example, the "OPD range required" is a derived output, depending on the baseline length, the field of view and the required spectral resolution.

III.5.2 Far-IR background noise estimation

We proceed to an estimation of the known far-IR background noise contributions from sources in thermal equilibrium. We assume that each source of noise emits like a Planck

TABLE III.1: Instrument design parameters for BETTII.

Parameter	Value	Units	Science driver/impact
Top-level parameters			
Input aperture	0.196	m ²	Sensitivity
Baseline length	8	m	Angular resolution
Detector pixels	9 × 9	pixels	Wide FOV
Detector quantum efficiency	70 %		Sensitivity
Integration time per full frame	2.5	ms	Sensitivity
Time per baseline orientation	10	min	Sensitivity
Number of data points per scan	1024	points	Wide FOV
OPD range required	8.2	mm	Wide FOV & spectral resolution
Optical system			
	Band 1	Band 2	
Central wavelength	40	82	µm
Fractional bandwidth	62.5 %	54.9 %	
Field of view	2	3	arcmin
Etendue per pixel	8.2×10^{-10}	1.8×10^{-9}	m ² sr
Estimated efficiency	20 %	24 %	
Pixel angular size	13.32	19.72	arcsec
Primary full width half max	17.31	35.49	arcsec

Notes: Instrument parameters that flow from the science requirement of 0.5'' and 1'' spatial resolution in bands 1 and 2 respectively, and spectral resolution $\mathcal{R} = 10$ in both bands.

function B_ν with a certain emissivity ϵ . In Table III.3, we list the number of photons generated per second for the amount of solid angle seen by a single pixel (with the exception of the atmospheric contribution, which is treated separately). The thermal emission is weighted by the normalized transmission function, which was measured in the laboratory (Fig III.17). By far the strongest contributors from our system are the warm optics and the cryostat's polypropylene window.

In addition to the noise of our own system and the astronomical background, we need to take into account the noise generated by the atmosphere, which results in a more complex calculation. For best accuracy, we use quantities from Harries, 1980, who measured the actual sky radiance in a large range of wavelengths from balloon altitudes. We obtain a radiance of $0.16 \text{ W m}^{-2} \text{ sr}^{-1}$ and $0.07 \text{ W m}^{-2} \text{ sr}^{-1}$ for band 1 and 2 respectively. This corresponds to $2.6 \times 10^{10} \text{ photons s}^{-1}$ and $5.2 \times 10^{10} \text{ photons s}^{-1}$, respectively.

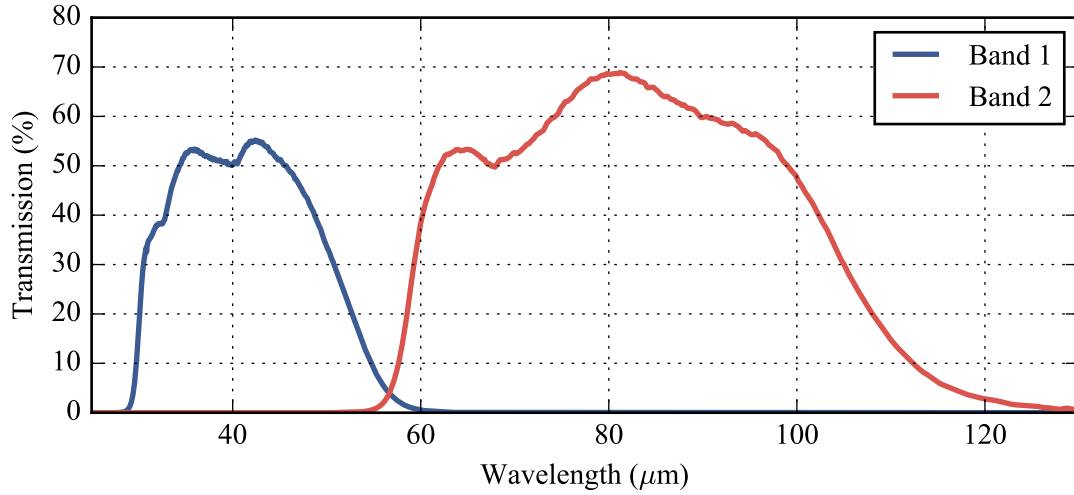


FIGURE III.17: BETTII total transmission curves $T_{\text{bp}}(\lambda)$ from all cold filters, excluding the beam combiner, cryostat window, and NIR/FIR dichroic. Bands are shown in different colors.

To know how much power is actually reaching the detectors, we need a measurement of our optical throughput. The throughput is the product of the efficiencies of the various

TABLE III.3: Thermal noise contributors

Noise source	T (K)	Emissivity	Photons s ⁻¹ Band 1	Photons s ⁻¹ Band 2	Reference
Warm optics	240	0.1	1.38×10^{11}	9.97×10^{10}	Assumes 99% per mirror
Window	240	0.02	2.76×10^{10}	1.99×10^{10}	Lab measurements
Zodi dust	245	3.00×10^{-7}	2.92×10^5	3.41×10^5	Fixsen et al., 2002b
Galactic Cirrus	20	1.23×10^{-4}	1.79×10^1	7.67×10^4	Bracco et al., 2011
Zodi scattering	5800	1.00×10^{-13}	1.47×10^1	1.31×10^1	Fixsen et al., 2002b
CIB	18.5	1.30×10^{-5}	2.19	9.68×10^3	Fixsen et al., 1998
Instrument	4	1	8.3×10^{-27}	3.60×10^{-7}	Conservative estimate
CMB	2.728	1	1.02×10^{-45}	9.35×10^{-17}	Fixsen et al., 1996b

Notes: The calculator was designed to be scalable to designing a space mission, which is why we kept track of terms which are negligible compared to the main contributors. In space, the warm optics and window contributions would be significantly reduced and more comparable to the other terms. These quantities do not yet include the losses from the instrument's throughput

elements along the optical train: the mirrors, the cryostat window, the NIR/FIR dichroic, and all the cold filters. The latter multiply to give the transmission profile shown in Fig. III.17, which we call \mathcal{T}_{bp} . We write $f_{\text{arm1-}>\text{detN}}$ (resp. $f_{\text{arm2-}>\text{detN}}$) the throughput of light from arm M (resp. arm 2) falling on the detector N, where N = 1, 2:

$$f_{\text{arm1,2-}>\text{det1,2}}(\lambda) = \tau_{\text{combiner}} \tau_{\text{window}} \tau_{\text{dichroic}} r^{N_{\text{mirrors}}} \mathcal{T}_{\text{bp}}(\lambda) \quad (\text{III.2})$$

$$\approx 0.38 \times \mathcal{T}_{\text{bp}}(\lambda), \quad (\text{III.3})$$

where we have used lab measurements to estimate $\tau_{\text{window}} \approx 0.98$, $\tau_{\text{dichroic}} \approx 0.95$, $\tau_{\text{combiner}} \approx 0.5$ and $r \approx 0.99$ is the far-IR reflection of each warm mirror, in both bands. There are $N_{\text{mirrors}} = 9$ within the warm optics train on the left side, and 8 on the right side. Until we obtain precise measurement of the throughput of each element as a function of wavelength,

TABLE III.5: Estimated power and NEP contributors for a single detector pixel.

Noise source	Power reaching the detector (pW)		NEP ($10^{-16} \text{ W Hz}^{-0.5}$)	
	Band 1	Band2	Band 1	Band2
Warm optics	92	45	9.6	6.7
Atmosphere	18	24	4.6	4.9
Window	21	9	4.3	3.0
Detectors	-		5	5
Total	131	77	17	10

Notes: These values are lower than the ones cited in Rinehart et al. (2014) and Rizzo et al. (2015) since we now have more precise measurements of the transmission as a function of wavelength.

we consider that this extra factor is wavelength-independent and represents an average over the band. This is valid since most of these materials do not have steep dependence at such a long wavelength. The transmission $\mathcal{T}_{\text{bp}}(\lambda)$ has an average of 27% (resp. 31%) for band 1 (resp. 2) respectively, so the throughput amounts to about $\sim 10\%$ (resp. $\sim 12\%$) efficiency for the light coming from one arm falling onto one detector.

After accounting for all losses, we approximate the total noise power per pixel as:

$$P_{\text{pix}} = (f_{\text{arm1-}>\text{detN}} + f_{\text{arm2-}>\text{detN}}) N_{\text{Photons s}^{-1}} E_{\text{ph}} \text{QE}, \quad (\text{III.4})$$

where $N_{\text{Photons s}^{-1}}$ is the total number of photons per second per pixel from the warm optics, the window, and the atmosphere, which are the three main contributors of noise (see Table III.3). We also use the photon energy E_{ph} and detector efficiency of the detector, $\text{QE} \approx 0.7$. Throughout most the design phase of BETTII, this equation was used for the band-averaged quantities, for lack of better knowledge of the exact wavelength dependence of the various optical components. However, this is also valid on a finer scale and can be

integrated over wavelength to provide more accurate estimates. In Table III.5, we used our knowledge of the bandpass transmission and integrate over the band. The Noise Equivalent Power (NEP), a common measure of noise in the far-IR, is calculated as $\text{NEP} = \sqrt{2P_{\text{pix}}E_{\text{ph}}}$. Note that the detectors are designed to contribute less than 30% of the total estimated photon NEP, so that their noise contribution is negligible.

III.5.3 Interferometric visibility budget

Estimating the noise from each arm separately can help us determine important quantities such as the photon loading and NEP, which can be used to design the detectors. However, the scientific signal from an interferometer also depends on how well the two arms combine. This is roughly a measure of how symmetric the optical system is. In table III.7, we identify two kinds of error contributions: the static contributors, which are caused by differential wavefront errors (WFE), amplitude mismatch, polarization errors and pupil area overlap. These are caused mostly by misalignments of the optics along each train, or by errors in the manufacturing of the mirror surfaces. Second, we have the dynamic contributors, which are caused by OPD errors and differential tip/tilt. These are errors which need to hold over the timescale corresponding to a single data point, so about 2.5 ms. The OPD errors correspond to fast uncorrected motion of the delay lines, while the differential tip/tilt corresponds to an error in co-aligning the two beams at the detector. Note that in Chap. IV, we discuss the various timescales involved with the OPD motions. In this table and for the calculation of the visibility, we only take into account the instantaneous, un-recoverable error in OPD. The error in OPD over longer timescales, resulting in a decrease in SNR as we co-add consecutive interferograms, is not taken into account here. For reference, the equations are explicitly stated here, as we have found it handy to gather

them all in one single place. The derivation for most equations can be found in Lawson (2000).

TABLE III.7: Interferometric visibility budget.

Term	Symbol	Alloc.	Effect on visibility	V_{loss}	
				Band 1	Band 2
Static contributors					
Total WFE in mirror surfaces	σ_{WFE}	2 μm	$\exp(-[2\pi\sigma_{\text{WFE}}/\lambda]^2)$	0.906	0.977
Amplitude mismatch	R	95 %	$2/(R^{1/2} + R^{-1/2})$	0.999	0.999
Polarization effects	θ	12°	$\cos(\pi\theta/180/2)$	0.995	0.995
Pupil area overlap	f_{overlap}	90 %	f_{overlap}	0.900	0.900
Dynamic contributors					
Error in OPD knowledge	σ_{OPD}	2 μm	$\exp(-[2\pi\sigma_{\text{OPD}}/\lambda]^2)$	0.906	0.977
Differential tip/tilt	σ_{tt}	1.5''	$2J_1(\pi D\sigma_{\text{tt}}/\lambda)/(\pi D\sigma_{\text{tt}}/\lambda)$	0.990	0.998
Total visibility			$\Pi(V_{\text{loss}})$	0.726	0.851

Notes: The dynamic contributors need to hold true for 2.5 ms, and consist of the residual amount that cannot be corrected in post-processing.

III.5.4 Science channel estimated sensitivity

Now that we know the noise per pixel and the efficiency of the interferometric beam combination, we can determine the SNR for a single source of known flux. For this, we use the formalism by Mighell (2005) who derive the proper equation for a matched filter representing a point-spread function (PSF) discretized on a noisy detector array. The efficiency η_{mf} of the matched filter is the inverse of the square root of the effective background area of the PSF, $\beta = 4\pi\mathcal{S}^2$, where \mathcal{S} is the standard deviation of the PSF in pixels, $\mathcal{S} = \frac{0.42\lambda/D}{\theta_{\text{pix}}}$. We obtain $\eta_{\text{mf}} \approx 0.55$ and 0.39 for band 1 and 2 respectively.

This matched filter efficiency is due to the uneven spread of the light from a PSF onto multiple pixels, and corresponds to the error in fitting the detector to the PSF assuming an even noise floor among all pixels. Pixels with more photons will have more SNR, hence should be weighted more when attempting to extract the flux from the PSF. In this sense, using a matched filter is a best-case scenario. Another approach would consist of simply dividing the PSF area by the area of one single pixel, which is a worst-case alternative that would lead to efficiencies of 0.13 and 0.07 in band 1 and band 2 respectively. In what follows, we are using the optimistic approach and assume we can recover the flux from the PSF using matched filtering.

We define the Minimum Detectable Line Flux (MDLF) as the flux per pixel which corresponds to a $\text{SNR} = 1$:

$$\text{MDLF} = \frac{\text{NEP}}{(f_{\text{arm1->detN}} + f_{\text{arm2->detN}})\mathcal{A}\sqrt{2T_{\text{int}}}}, \quad (\text{III.5})$$

where $T_{\text{int}} = 2.5 \text{ ms}$ corresponds to the integration time per pixel (or detector frame). The MDLF is expressed in W m^{-2} .

The Minimum Detectable Flux Density (MDFD) is the MDLF divided by the bandwidth. This is expressed in $\text{W m}^{-2} \text{ Hz}^{-1}$ and can be converted to Jy.

The faintest detectable interferometric point source with $\text{SNR} = 1$ is then given by $S_{\text{min}} = \text{MDFD}/\mathcal{V}_i/\eta_{\text{mf}}$, where the MDFD is increased due to the interferometric visibility losses and the spreading of the photons onto multiple pixels of the detector. S_{min} represents the smallest flux density that leads to an $\text{SNR} = 1$ within a single scan.

Co-adding consecutive scans will improve the SNR considerably, but it will also introduce errors and inefficiencies. We quickly realized the impact of systematic errors

in co-adding scans, so a significant amount of effort went into understanding the behavior of the various error contributions, and analyzing mitigation strategies. The result of this investigation was published in Rizzo et al. (2015), and is shown here in Chap. IV. In that chapter, we discuss the meaning and importance of the phase noise or OPD noise, and quantify the impact on the sensitivity. The OPD noise arises when residual uncertainties in the knowledge and control of the OPD result in errors while co-aligning and co-adding consecutive interferograms. For the rest of this discussion, we will assume that the OPD noise amounts to $5 \mu\text{m}$ r.m.s over 200 consecutive scans.

Using the formulas derived in Chap. IV, we can now correctly determine the SNR in the co-added interferograms. However, co-added interferograms are not the only goal of BETTII. Although interferograms allow for the distinction between multiple, nearby point sources, most of the scientific information is retrieved by analyzing the spectrum of each source in the field by taking the Fourier transform of the interferogram. Hence, we want to characterize the spectral sensitivity of the instrument, and establish this metric as the default observing metric for our science.

A summary of the results is presented in Table III.9.

TABLE III.9: BETTII sensitivity estimates

Quantity	Band 1	Band 2	SNR Target
Single scan (3 s)			
MDFD	77 Jy	113 Jy	$\text{SNR}_{\mathcal{I}} = 1$
Normal observing (200 scans, 10 min)			
MDFD	5 Jy	8 Jy	$\text{SNR}_{\mathcal{I}} = 1$

Notes: $\text{SNR}_{\mathcal{I}}$ represents the SNR in the interferogram.

III.5.5 Tracking channel estimated sensitivity

A similar sensitivity analysis is done for the tracking channel. This is simplified somewhat since the tracking channels consists only of two cameras, and does not involve beam combination. The levels of background noise are less obvious to estimate. We primarily use the findings of Matsumoto et al. (1994), which measured $2\text{ }\mu\text{m}$ emission line strengths from balloon altitude. This emission is thought to arise from a thin layer of OH radicals at $\sim 100\text{ km}$ altitude, and is sometimes referred to as *airglow*. Using the measurements by these authors, who span multiple balloon flights in the 60s and 70s, we obtain an average radiance in the NIR bands of $R_{\text{NIR}} \approx 1 \times 10^{-4} \text{ W m}^{-2} \text{ sr}^{-1}$. According to our estimates, this is two orders of magnitudes lower than the brightest astronomical noise source in the NIR, which is the zodi scattering.

Balloon altitudes provide significantly better atmosphere transmission in the NIR wavelength region, compared to ground observatories. Fig. III.18 illustrates this difference using a modelling software called MODTRAN. The transmission from an altitude of 4 km shows transmission windows (J, H, K bands) that would limit the design of a ground-based interferometer. At float, the bands are not limited by the atmospheric transmission and thus we can use larger bands than the traditional J, H and K in order to optimize our photon signal.

Due to the prioritization of the science channels, the NIR tracking channel is less advanced at the time of writing. Hence, we use estimates for the transmission and reflection efficiencies of the various components along the optical train. We estimate the efficiency of the major components: the mirrors (95% reflective), the cryostat window (90% transmissive), and the NIR/FIR dichroic (90% transmissive), which transmits the NIR light.

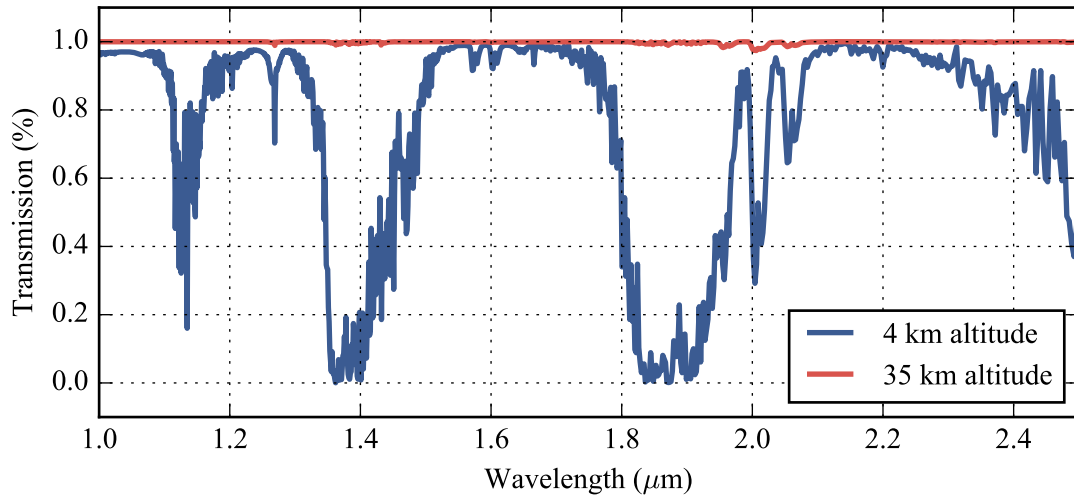


FIGURE III.18: Model atmospheric transmission, from Rizzo et al., 2012.

There is an additional filter just in front of the detector, which limits the bands from 1 to $2.5\text{ }\mu\text{m}$. The detectors are not responsive for longer wavelengths. The total amount of efficiency for this channel is expected to be on the order of $\epsilon = 20\%$. Using this, a 1 Jy source will correspond to a number of photons N_{ph} within a PSF at the detector:

$$N_{\text{ph}} = \frac{1 \times 10^{-26}}{h} \mathcal{A} \times \text{FBW} \times \epsilon T_{\text{int}} \approx 8100, \quad (\text{III.6})$$

where $\text{FBW} \approx 0.67$ corresponds to the fractional bandwidth, and h is the Planck constant.

The detector is expected to have a read noise of $\sigma_{\text{RON}} = 18$ electrons r.m.s in up-the-ramp sampling, according the manufacturer specifications. Its frame rate changes throughout the acquire mode (see Chapter V), but the fastest mode will have a frame rate of $\sim 50\text{ Hz}$. Since the detector does not read destructively, saturation is an issue and needs to be addressed carefully - having to reset the pedestals to avoid saturation can complicate the software and might require a lot of tuning. Our calculations take into account a 20 ms integration time, a quantum efficiency of 70%, and a $0.6\text{ arcsec pixel}^{-1}$ plate scale, which

provides an effective background area $\beta = 0.43$ for a diffraction-limited PSF of diameter $1.5''$ at $1.5\text{ }\mu\text{m}$. We consider that most of the photons will be spread on $1/\beta \approx 2.35$ pixels, so we expect about $N_{\text{e}^-} \approx 3440$ electrons per pixel from a 1 Jy source. A much more rigorous analysis is required once the efficiencies are measured.

For convenience, we express the SNR of a source using its flux S in electron per second:

$$\text{SNR} = \frac{S}{\sqrt{S + \beta(B + \sigma_{\text{RON}}^2)}}, \quad (\text{III.7})$$

where B is the number of electrons per pixel from the background. In our case, we calculate $B \approx 2.4$ electrons, which is negligible compared to the read noise, so we will ignore this term in the future.

The required flux density for a given SNR is then found by solving the previous equation for S :

$$S_{[\text{Jy}]} = \frac{\text{SNR}^2 + \sqrt{\text{SNR}^4 + 4\text{SNR}^2\beta\sigma_{\text{RON}}^2}}{2N_{\text{e}^-}}. \quad (\text{III.8})$$

For a $\text{SNR} = 10$, this corresponds to ~ 0.13 Jy, or ~ 9.66 H magnitude. For our first flight, all of our primary science targets have a star at least as bright within our field of view, which is usually embedded in the cluster itself.

III.6 Targets

The primary science targets for BETTII have fluxes that are above the spectral sensitivities from Table III.9, with a bright NIR guide star nearby. In addition, in order to correctly

know the OPD, we need sets of bright calibrator targets which provide high-SNR fringes in one single scan of the delay line.

The science targets need to be available during our launch window, and preferably cover a large range of projected angles (so we can study the source at multiple angles to retrieve more of the spatial distribution). For this reason, we favor circumpolar sources, since they are the ones which change orientation at the fastest pace.

III.6.1 Calibrators

Calibrators ideally need to be point sources $\gg 100 S_{\min}$ Jy in our FIR bands, and it is not straightforward to identify which astronomical sources exist that would provide this kind of flux density. The planets of the solar system and their moons are usually bright enough, but they are often resolved by our instrument, which dramatically reduce their interferometric contrast. For example, we estimate the Uranus is > 1000 Jy, but because it is so resolved, the actual fringe contrast is very small, hence drastically reducing the SNR. Nearby, bright A stars such as Alpha Boo are most likely point sources, but are usually not as bright as we would want, especially not in Band 2 since they are essentially thermal sources with temperatures of thousands of Kelvin. It is possible to use actual science sources as calibrators, but of course it is unknown whether or not they actually are extended (this is the purpose of a mission like BETTII!).

We find that bright asteroids such as Ceres, Pallas and Vesta are the best candidates for bright calibrators (respectively $> 320, 150 \text{ and } 120$ Jy). In addition, because of their albedo, they also reflect the sunlight so they would also be suitable for the tracking channels (e.g. Ceres has Hmag ~ 3 . Their only disadvantage is that they are not inertial targets - this complicates the pointing control system as their expected position moves across the

sky, which requires the payload to have accurate timing capabilities to know where the object is at a given time.

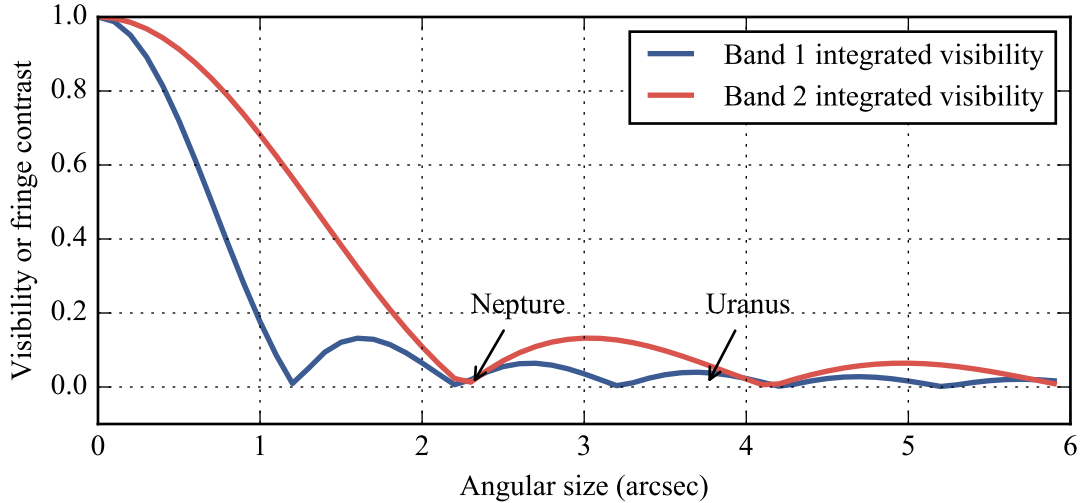


FIGURE III.19: Visibilities of calibrators.

III.6.2 Science targets

For our first flight, our science target list will be primarily composed of sources we have already observed with SOFIA FORCAST. In our source list, our best BETTII candidates are the sources which are bright at $37\text{ }\mu\text{m}$, have a large spectral index, appear point-like, are up in the sky at night during our flight, and are preferably circumpolar.

Table III.11 gives a list of such sources, and includes the fraction of time that the target spends above 10 degrees elevation and below 75° during the planned observing night of September 15, 2016. In addition, Fig. III.20 shows the tracks in the sky. The circumpolar targets S140, Cepheus A and NGC 7129 are available for the most time. All are located well in the East at the beginning of the night, which means we can point towards them as the Sun sets in the West. Note that when the source is at low elevations, we could

TABLE III.11: BETTII Targets

Cluster	Coordinates	Fraction of night time between 15-75° elevation
S140	22h19m23s +63d18m44s	100.0 %
Cepheus A	22h56m10s +62d03m26s	100.0 %
NGC 7129	06h41m07s +09d33m35s	100.0 %
IRAS 20050+2720	20h07m05s +27d28m51s	50.0 %

experience a substantial amount of additional atmospheric noise since the line of sight sees more airmass.

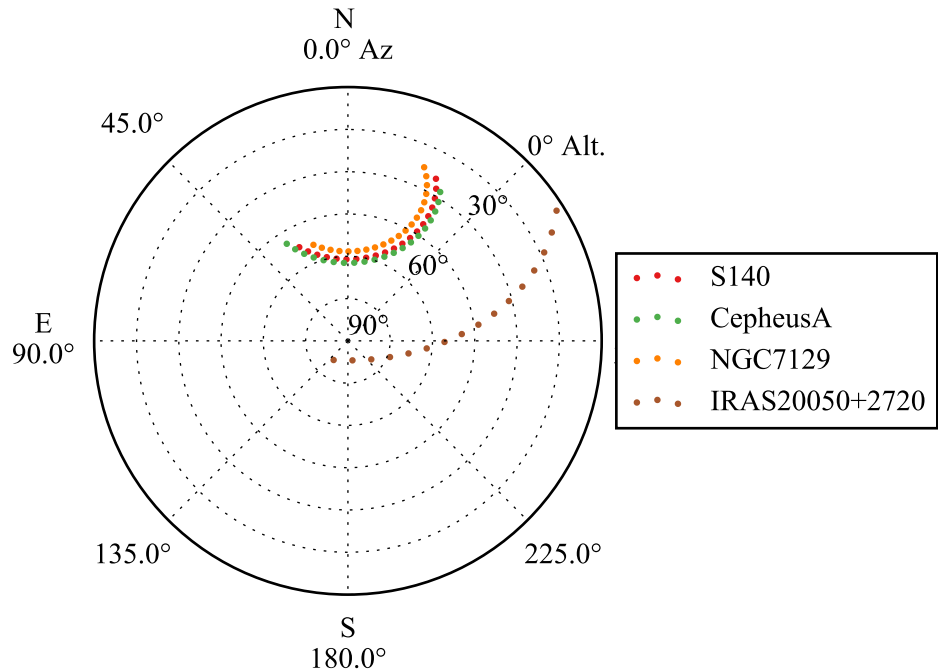


FIGURE III.20: Polar plot showing the tracks of our targets in the night sky, between 8pm on Sept 15th and 6am on Sept 16th. The coordinates represent the local azimuth (with respect to North) and elevation, which is 0° at the horizon. Note that NGC 2071 and NGC 2264 cannot be observed at night in this period of the year.

Chapter IV

Far-infrared double-Fourier interferometers and their spectral sensitivity

IV.1 Introduction

Several space-based interferometer concepts, the Far Infrared Interferometer (FIRI; Helmich et al., 2009), the Space Infrared Interferometer Telescope (SPIRIT; Leisawitz et al., 2007), and the Submillimeter Probe of the Evolution of Cosmic Structure (SPECS; Harwit et al., 2006), have been proposed and use spatio-spectral interferometry to achieve the much needed angular resolution to study astronomical processes such as the birth of stars and planetary systems, the activity in galactic nuclei and the formation of galaxies in the distant universe. The FIRI and SPIRIT concepts have two mirrors which are movable on one axis along a monolithic truss to provide a range of baseline lengths. SPECS consists of three spacecraft connected via tether to achieve baselines of order 1 km.

There are numerous engineering challenges to be addressed before such missions can

become reality. A number of them can be tackled with testbeds (e.g. Leisawitz et al., 2012; Grainger et al., 2012) and small-scale pathfinder missions. These missions will likely be two-element, single baseline interferometers in space or on balloon platforms, such as the Balloon Experimental Twin Telescopes for Infrared Interferometry BETTII; Rinehart et al., 2014 and to a certain extent the Far-Infrared Interferometric Telescope Experiment FITE; Kato et al., 2010. These pathfinders will have very limited baseline coverage and rather than producing full images, they will focus on reconstructing spectral information from closely-spaced sources. This paper explores aspects of the noise in spectral measurements specific to these instruments.

IV.1.1 Spatio-spectral interferometry

In their pioneering paper, Mariotti et al. (1988) lay out the principles of spatio-spectral (or double-Fourier) interferometry. A spatio-spectral interferometer consists of a Fourier transform spectrometer (FTS), where a delay line mechanism modulates the optical path difference (OPD) between two independent light beams before combining them in the pupil plane. The instrument produces interferograms, which are arrays of power measurements as a function of the OPD. Unlike traditional FTS, where a single incoming beam is split, delay-modulated, and recombined, a double-Fourier interferometer utilizes multiple light collectors pointing to the same astronomical source and combines the incoming light from the collectors pairwise in the pupil plane. The orientation and magnitude of the baselines - the vectors between each pair of light collectors - determines which spatial frequency of the astronomical image the instrument measures. Longer baselines correspond to higher angular resolutions. The “double-Fourier” aspect comes from the fact that the interferogram measured on a given baseline is related to the Fourier Transform (FT) of the spatial

and spectral distribution of the source emission. Two FTs are used to reconstruct the full spatio-spectral datacube representing the astronomical scene: the spectra which are more directly related to the power as a function of time delay difference between the two incoming beams (equivalent to the OPD) and the source 2D spatial structure on the sky which is more directly related to measurements accumulated from many different baseline vectors. The length of the baseline vectors can be changed by modifying the distance between the light collectors. The orientation of the vectors can be changed by rotating the baseline with respect to the source on the sky. The plane representing the source visibilities as a function of baseline vector is referred to as the (u, v) -plane and is a common notion in ground-based submillimeter and radio interferometry. This paper focuses on the reconstruction of the spectrum from closely-spaced point sources using single-baseline measurements, and does not address the techniques and sensitivities involved in using multiple baseline lengths to produce an image of the scene; a mathematical formalism that covers imaging is already proposed in Elias et al. (2007).

Proposed double-Fourier instruments at far-IR wavelengths distinguish themselves from operating interferometers at sub-millimeter and radio wavelengths in several ways. First, they do not directly measure the phase information. The fundamental measurement is a time series of real-valued power as a delay line modulates the OPD in a controlled sequence (for example a linear ramp). The OPD from the delay line, as well as other OPD contributors in each arm of the instrument, and the external OPD created when the line of sight to a source is not perpendicular to the baseline vector, add up to the total OPD. In double-Fourier instruments, the OPD can be determined by measuring or estimating the various contributors to the total OPD. For a given detector location along the projected baseline vector, there exists a value of the OPD in the delay line that exactly compensates

all other OPD contributors. This delay line position results in a zero net total OPD, and is called the Zero Path Difference (ZPD). At this value of OPD, an incoming plane wave traverses the two beam paths reaching the detector exactly with the same phase, for all wavelengths. ZPD corresponds to the center of an interferogram for that detector location. In the context of this paper, the phase for a given wavelength ϕ_λ is related to the OPD between the beams from each arm when they combine, at the time of a data point measurement: $\phi_\lambda = 2\pi\text{OPD}/\lambda$.

A second important difference for balloon and space interferometers is that collectors are not fixed to the Earth. In the case of BETTII and SPIRIT, the collectors are fixed to a truss structure which is part of the mechanical system for pointing the collectors. Consequently, baseline length and external OPD, as relevant to an astronomical source, are not independent of pointing errors. The impact of errors in baseline length is modest because the relevant measure is in terms of fractions of the collector diameter. Errors in pointing translate into external OPD as the sine of the error angle times the baseline length, while the relevant measure is the wavelength. This can easily become significant; for example, a 1" pointing error for an 8 m long baseline corresponds to a 38 μm shift in OPD.

Third, bolometer-type detectors, such as being built for BETTII and envisioned for SPIRIT, are easily, and indeed typically, configured as two-dimensional arrays. With pupil plane combination, the entire field of view has an interferometric response; hence wide-field interferometry over multi-pixel arrays is straightforward. Fig. IV.1 shows this concept and sketches the instrumental response. For the configuration shown with the detector array columns aligned perpendicular to the baseline vector, ZPD is the same along lines perpendicular to the baseline vector projected on the detector. As the OPD is

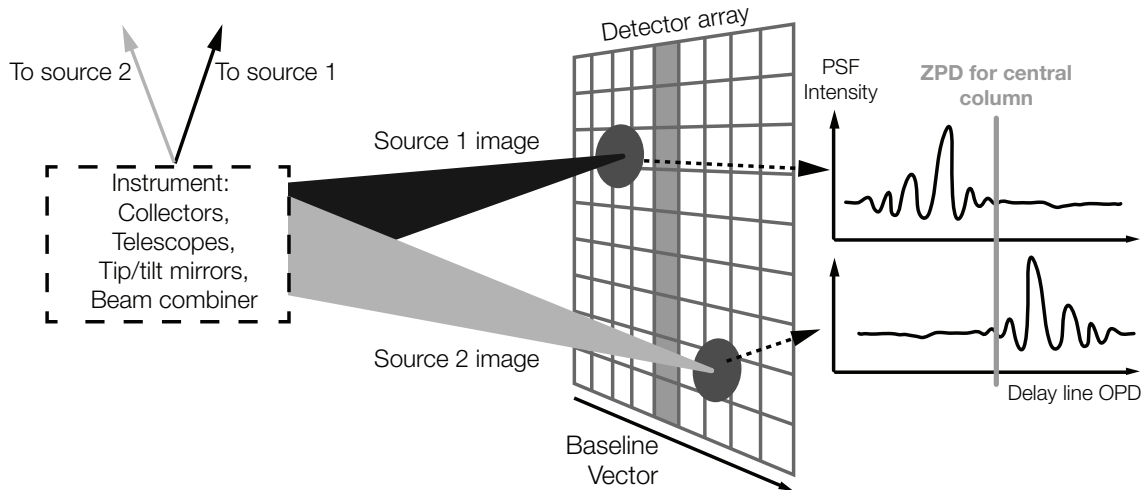


FIGURE IV.1: Concept of wide-field double-Fourier interferometry. Light from the instrument is focused after combination to an image of the sky on the detector array (represented as the grid). Each column of the detector has a distinct ZPD so the interferometric responses (right side) of two sources on different columns are centered around different delay positions. The gray stripe represents the central column on the detector array and its corresponding ZPD on the interferograms.

swept, it moves across ZPD for the different columns in the array, yielding interferograms with shifted centers corresponding to the changes in external OPD for each source location in the field.

By sweeping the OPD, the double-Fourier instrument measures interferograms which contain both spectral and spatial information over the detector array. The full spatial and spectral source information can be unambiguously recovered by repeating the delay line sweep over a range of baseline angles and lengths, which correspond to different spatial frequencies on the sky (Mariotti et al., 1988).

IV.1.2 The case study: BETTII

The BETTII project (Rinehart et al., 2014), is a motivation for this paper and a near-term application of spatio-spectral interferometry. BETTII consists of two 50 cm siderostats on a fixed 8 m baseline, with a far-IR beam-combining instrument at the center. It will

observe the far-IR universe in two wavelength bands, 30-50 μm and 60-110 μm . The instrument is currently under construction at NASA Goddard Space Flight Center and is scheduled to launch in the Fall of 2016 on a stratospheric balloon from Fort Sumner, New Mexico, to an altitude of 35 km in order to be above most of the atmosphere. For its first flight, BETTII will focus on the study of dense star formation in nearby clusters. While a complete image reconstruction is not possible due to the static baseline length, BETTII will help resolve point source objects that are 0.5-1" apart in the short and long band, respectively, more than ten times the spatial resolution of *Spitzer* at 24 μm and six times the resolution of SOFIA at 37 μm . Combined with a modest spectral resolution of $\mathcal{R} = 10 - 50$, BETTII will measure the spectral energy distributions (SEDs) of clustered young stars to determine their evolutionary stage, locate the origin of the far-IR emission, and improve our understanding of how stars accrete their mass in these very dense regions of stellar birth (e.g. see Tan et al., 2014, and references therein). For resolved sources, the fixed baseline will not completely lift degeneracies between the spectral and spatial information; however detailed source modeling can put constraints on the distribution of the far-IR emission (e.g Whitney et al., 2013).

In this chapter, we study how various types of noise propagate to the derived spectrum in an instrument like BETTII or SPIRIT. In section 2, we establish a mathematical formalism that can be used to represent interferograms. In section 3, we look at the dominant types of noise in the interferogram and define the relevant timescales associated with spatio-spectral interferometers. In section 4, we derive the spectral signal-to-noise ratio (SNR). In section 5, we apply these results to the special case of BETTII to derive its point source spectral sensitivity.

IV.2 Mathematical formalism

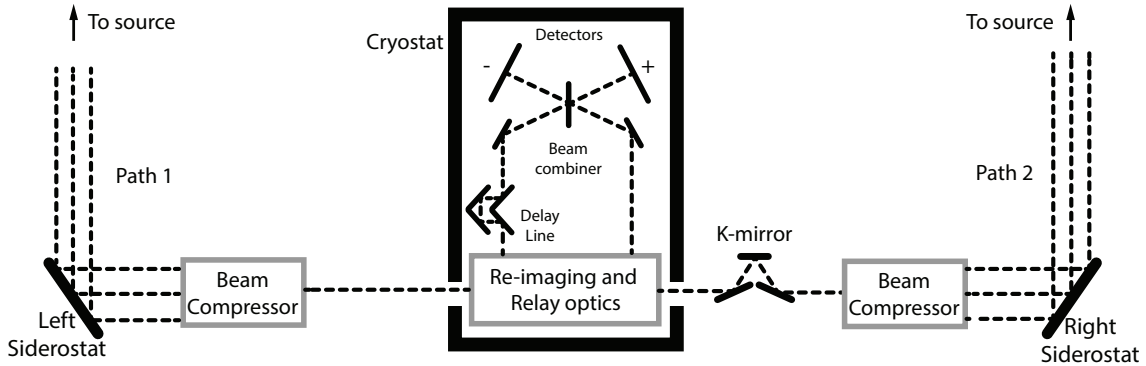


FIGURE IV.2: Optical train diagram of a typical far-IR, double-Fourier instrument. The K-mirror rotates the beam to align the fields of view of the two sides. Inside the cryostat, a set of optics re-image the pupil, implement a controlled instrumental delay between them with the Cold Delay Line, and relay them towards the central beam combiner. After the combiner, the beams are imaged onto the detectors. To see the BETTII-specific implementation of this design, see Rinehart et al. (2014).

The general optics layout for a double-Fourier system is shown in Fig. IV.2 for a single baseline. The combination of the siderostat and beam compressor acts as an afocal telescope which outputs a parallel beam with a diameter convenient for the rest of the optical train. The K-mirror in one beam path corrects for the pupil rotation so that the images of the sky from the two collectors are matched over the field of view. At the center of the instrument, there are optics for pupil re-imaging, filtering, and beam folding, as required by the specific implementation. The key components for our purpose are the delay line, beam combiner and detectors. The delay line introduces a controlled OPD between both arms. The two incoming beams are combined in the outputs from the beam combiner. We arbitrarily define one output as the "+" and the other as the "-". To conserve photon energy, the two outputs must be complimentary such that the summed power of the two is independent of the OPD. In an ideal double-Fourier system, the two

beam paths are symmetric about ZPD; hence, the power from the "+" and "-" outputs are equal at ZPD, and have odd symmetry about ZPD. In a traditional FTS at ZPD, one output has fully constructive interference while the other has fully destructive interference, with even symmetry about ZPD.

IV.2.1 Interferograms for a single baseline

The interferogram for a single frequency of light measured at the outputs of the ideal double-Fourier instrument can be described in terms of the normalized intensity:

$$\hat{I}_{\pm}(x, \sigma) = \text{Re}(1 \pm i \mathcal{V}_{\mathbf{B}}(\sigma) e^{-2i\pi\sigma x}), \quad (\text{IV.1})$$

where $\sigma \equiv \frac{1}{\lambda}$ is the wavenumber of the light in cm^{-1} as per the convention for the FTS literature, x is the instrumental OPD created by the delay line with $x = 0$ corresponding to ZPD, and $\mathcal{V}_{\mathbf{B}}(\sigma)$ is the complex spatial visibility of the astronomical source for the baseline vector \mathbf{B} . "Re(f)" indicates the real part of the complex-valued function f . The \pm indicates values for the two output beams: "+" and "-" in Fig. IV.2. The derivation of this expression is given in Appendix A.A.1.

The normalized complex spatial visibility $\mathcal{V}_{\mathbf{B}}$ has a magnitude of 1 for all baselines for which the source is completely unresolved. For extended sources, the spatial visibility depends on the source geometry, intensity distribution, and the instrument baseline vector as described in Chapter 2 of (Lawson, 2000) and Chapter 3 of Thompson et al., 2008. For a normalized source brightness distribution $\hat{\mathcal{F}}$, the spatial visibility with respect to a phase reference position on the sky can be written as:

$$\mathcal{V}_{\mathbf{B}}(\sigma) = \int_{\text{source}} d\Omega \hat{\mathcal{A}}(\xi) \hat{\mathcal{F}}(\xi) e^{-2i\pi\sigma\xi \cdot \mathbf{B}}, \quad (\text{IV.2})$$

where $\hat{\mathcal{A}}$ is the normalized reception pattern of the collecting area; \mathbf{B} is the baseline vector between the two collectors and ξ is the vector on the plane of the sky from the phase reference position to the infinitesimal solid angle $d\Omega$. The resulting visibility as a function of baseline vector is the 2-dimensional FT of the source's sky distribution. Since $\hat{\mathcal{F}}$ does not have to be symmetric with respect to the chosen phase center, $\mathcal{V}_{\mathbf{B}}$ is in general complex and can be expressed as an amplitude and a phase, $\Phi_{\mathbf{B}}(\sigma)$: $\mathcal{V}_{\mathbf{B}}(\sigma) = |\mathcal{V}_{\mathbf{B}}(\sigma)|e^{i\Phi_{\mathbf{B}}(\sigma)}$.

Real instruments have asymmetries, imperfections, and measurement errors which can create phase-shifts between the two optical paths and across the pupils. Fixed instrumental effects can be represented by a normalized instrumental visibility loss term, $\mathcal{V}_i(\sigma)$ where the complex quantity $\mathcal{V}_i(\sigma) = |\mathcal{V}_i(\sigma)|e^{i\Phi_i(\sigma)}$, as described in details in Chapter 3 of (Lawson, 2000), represents both amplitude losses and phase shifts (see Appendix A.A.1). Additional phase errors can arise from imperfect knowledge of the real-time optical path lengths which we will represent as $e^{i\Phi_r(\sigma,x)}$, where $\Phi_r(\sigma,x)$ is the "phase noise"; this term depends on the OPD x through time-dependent phenomena such as mechanical jitters, temperature variations in the optics support, or pointing errors. In the rest of this paper, we will mostly talk about this "OPD noise", which is the physical source of the noise, whereas phase noise represents its effects on the interferogram. The total complex visibility sampled at a single σ by the system is $\mathcal{V}_{\mathbf{B}}(\sigma)\mathcal{V}_i(\sigma)e^{i\Phi_r(\sigma,x)}$, and it is normalized such that, for an ideal instrument observing a point source, this quantity is equal to 1 at ZPD.

Using Eq. IV.1 for the monochromatic source, the polychromatic interferogram is the integral over σ of this dimensionless response at each wavenumber. The total amount of power coming into the 2-aperture interferometer within a small wavenumber range $d\sigma$ is $2\mathcal{A}B(\sigma)cd\sigma$ where $2\mathcal{A}$ is the total aperture area in m^2 , $B(\sigma)$ is the spectral flux density in $\text{W}\cdot\text{m}^{-2}\cdot\text{Hz}^{-1}$ and c is the speed of light in $\text{cm}\cdot\text{s}^{-1}$. Filters and optics in an instrument

cause a wavenumber-dependent transmission profile $\mathcal{T}_{\text{bp}}(\sigma)$. The quantum efficiency of the detector can depend on wavenumber, $\eta_D(\sigma)$. For multi-pixel detectors the interferogram is measured by matched filtering a point-spread function on a pixel array, which has some efficiency η_{mf} .

The actual power measured by the instrument can be represented as:

$$I_{\pm}(x) = \mathcal{A}c \int_0^{+\infty} \eta_{\text{mf}} \eta_D \mathcal{T}_{\text{bp}} B \times \text{Re} [(1 \pm i\mathcal{V}_i \mathcal{V}_B e^{i\Phi_r} e^{-2i\pi\sigma x})] d\sigma, \quad (\text{IV.3})$$

where the factor of 2 for the two apertures is dropped because it is implicit in Eq. IV.1. All quantities within the integral can be functions of wavenumber, and all the instrumental phase and interferometric loss terms are in \mathcal{V}_i and $e^{i\Phi_r}$.

Instead of considering each separate output, we use $I = I_+ - I_-$ as our interferogram expression, which cancels out the constant term. We also introduce an interferometric instrument transmission function, which can be complex, which represents the normalized amplitude and phase of the interferogram for a point source of uniform spectrum and no phase noise:

$$T_{\text{inst}}(\sigma) \equiv \mathcal{A}c \eta_{\text{mf}} \eta_D \mathcal{T}_{\text{bp}} \mathcal{V}_i = |T_{\text{inst}}(\sigma)| e^{i\Phi_{\text{inst}}(\sigma)}, \quad (\text{IV.4})$$

We can then write the modulated signal as:

$$I(x) = \text{Re} \left(2 \int_0^{+\infty} i|T_{\text{inst}}| B \mathcal{V}_B e^{i\Phi_r + i\Phi_{\text{inst}}} e^{-2i\pi\sigma x} d\sigma \right), \quad (\text{IV.5})$$

where B is real and \mathcal{V}_B can be complex.

Eq. IV.5 can be turned into a Fourier transform by mirroring all quantities to negative wavenumbers. This convention is explained in detail in Davis et al. (2001) for FTS

instruments; the odd symmetry of the interferogram for a system with one beam combiner and the complex instrumental transfer function means that the incident spectrum on the detectors must be mirrored to $-\sigma$ as the negative of the complex conjugate of $+\sigma$:

$$\mathcal{S}_e(\sigma) \equiv [T_{\text{inst}} B \mathcal{V}_{\mathbf{B}}]_e(\sigma) = \frac{1}{2} [T_{\text{inst}}(\sigma) B(\sigma) \mathcal{V}_{\mathbf{B}}(\sigma) - T_{\text{inst}}^*(-\sigma) B(-\sigma) \mathcal{V}_{\mathbf{B}}^*(-\sigma)].$$

We use the subscript e to denote the reflected function, and will apply this convention in the rest of this paper; this reflection ensures that the integrals keep the same value when expressed from $-\infty$ to $+\infty$, and does not affect the SNR estimates: although the signal appears to be divided by a factor of two, so is the noise, as it is spread between positive and negative frequencies. The interferogram expression is then:

$$I(x) = \text{Re} \left(\int_{-\infty}^{+\infty} i \mathcal{S}_e e^{-2i\pi\sigma x + i\Phi_r} d\sigma \right). \quad (\text{IV.6})$$

IV.2.2 Measured interferograms

In practice, the interferogram data are discrete measurements of a real-valued signal on the detectors. Like for most FTS instruments, each data point on the interferogram corresponds to an integration of the detector while the delay line is continually in motion. This decreases the amplitude of the interferogram due to the local smearing of the fringes, but it can be kept to low values by increasing the fringe sampling. At each delay x_n , the interferogram has a measured value $\mathcal{I}(x_n) = \frac{1}{dx} \int_{x_n-dx/2}^{x_n+dx/2} I(x) dx$. To first order, this has the effect of multiplying the power at each wavenumber by $\text{sinc}(\pi\sigma dx)$. For the purpose of this paper, we consider this term to be included as part of the instrumental transmission T_{inst} . Note that the value of the optical delay x_n is the path difference from ZPD, not the physical location of the delay line, since there could be a multiplying factor between the two due to beam folding (e.g., for BETTII, a motion of 1 mm of the delay line creates

4 mm of OPD).

A discrete Fourier transform (DFT) is used to transform a discrete interferogram of N measurements into a complex discrete spectrum with N points. The resolving power of the instrument, $\mathcal{R} = \lambda/d\lambda$, is dependent on the physical length scanned by the delay line L : $\mathcal{R} = L\sigma/2$ for a scan with symmetric length on both sides of ZPD. For these instruments where we scan through the whole interferogram, the data should be sampled at least at the Nyquist rate for the interferogram response frequency of $dx = \lambda/2$. For a sampling exactly equal to Nyquist, we have the relationship: $N = 4\mathcal{R}$.

For a double-Fourier instrument, as shown in Fig. IV.1, the ZPD for different columns on the array occurs at different delay positions x_{col} , related to the projected baseline length. The simplest way to express this is in terms of the angular offset on the sky of each column, ξ , along the direction of the baseline, \mathbf{B} :

$$x_{\text{col}} = |\mathbf{B}| \sin \xi \approx |\mathbf{B}| \xi = 48.7 \mu\text{m} \left(\frac{|\mathbf{B}|}{10 \text{ m}} \right) \left(\frac{\xi}{1 \text{ arcsec}} \right), \quad (\text{IV.7})$$

where we have filled in practical units for an infrared instrument. For a far-IR interferometer working at 50 μm , with 1-2 m diameter collectors, the delay shift across the collector point spread function (collector angular resolution) is several to ten wavelengths. Hence the scan length to cover a wide-field array detector is comparable to the scan length required to achieve \mathcal{R} 's of 100's to 1000's. This property is an important consideration for observation and data analysis strategies.

The ideal interferogram for a point source from a perfect instrument is an odd function of the OPD x , so its DFT is purely imaginary. The noise in the interferogram will be converted into spectral noise in both the real and imaginary axes so the real axis is a

proportional measure of the noise. Referring back to Eq. IV.6, phase shifts caused by the instrumental transfer function and source spatial visibility will break the anti-symmetry; in practice, the DFT of a measured interferogram is complex and the real and imaginary parts are of interest. The scientifically interesting quantities are the source spectrum and source spatial visibility: B and \mathcal{V}_B ; the fixed instrumental terms have to be calibrated or properly modeled by observing a bright point source of known spectrum. The techniques for calibrating FTS systems are well developed (e.g. Davis et al., 2001), and there are many methods proposed to correct some phase and amplitude errors (e.g. Forman et al., 1966; Sromovsky, 2003).

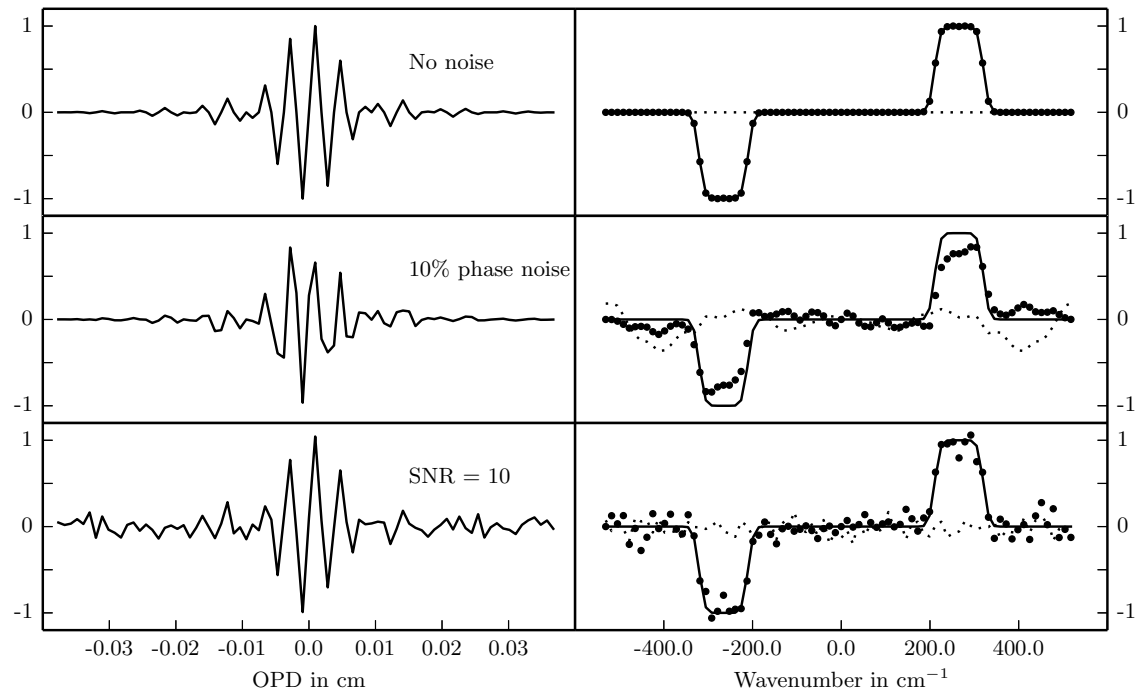


FIGURE IV.3: Effects of phase and intensity noise on the recovered spectrum (single realization of the noise). Left column: normalized interferograms, intensity as function of OPD. Right column: normalized DFT of interferograms. Solid: input spectrum multiplied by anti-symmetric transmission function; Solid circles: Imaginary part of DFT from interferogram; Dotted: Real part of DFT. First row: ideal measured signal, no noise; used for normalization of all other plots. Second row: results with a realization of phase noise of 10% at each point of the interferogram. Third row: results with a realization of intensity noise and $\text{SNR}_{\mathcal{I}} = 10$.

The phase noise term $\Phi_r(x, \sigma)$ in Eq. IV.6, and the SNR in the measured interferogram can have significant impact on the ability to recover the source spectrum with a real instrument. The upper panel in Fig. IV.3 shows an example of an interferogram (left), and the transformed $\mathcal{S}_e(\sigma_k)$ (right) for a source with flat power spectrum, multiplied by a flat bandpass function with smoothed edges. The middle panel of Fig. IV.3 shows the same source and instrument parameters as the upper panel, now with an assumed Gaussian OPD noise of standard deviation equal to 10% of the central wavelength of the band $\lambda_0 \equiv \frac{1}{\sigma_0}$ (*i.e.*, there is a $\lambda_0/10$ OPD uncertainty for each data point in the interferogram). The lower panel is the top panel observed with a incoherent background noise corresponding to $\text{SNR} = 10$ at the peak of the interferogram, and no phase noise. The next sections of this paper will analyze these noise contributions and quantify their impact on the derived spectrum.

IV.3 Noise sources

The two primary types of noise in a double-Fourier instrument are intensity and OPD noise. The intensity noise consists of the astronomical and thermal background noise, the photon noise from the source, and the detector noise. The OPD noise arises primarily from uncertainties and changes in OPD, which would prevent us from accurately knowing the x -values of measurements in the interferogram before the FT. For convenience, we usually refer to the OPD noise as a percentage of the carrier wavelength. In the rest of this paper, a "10% OPD noise" signifies that the OPD for each measurement in the interferogram is known to within an error of 10% of the carrier wavelength, or 10% of one full fringe cycle.

IV.3.1 Intensity noise

The measured signal has units of power and can be represented as the interferometric signal with additive noise:

$$I_{\text{measured}}(x_n) = \mathcal{I}(x_n) + n_{\mathcal{I}}(x_n), \quad (\text{IV.8})$$

with $n_{\mathcal{I}}$ being the difference of the noise in the two outputs of the interferometer, $n_{\mathcal{I}} = n_+ - n_-$. When the beam combiner, optical train, and detectors are symmetric, the residual $n_{\mathcal{I}}$ has zero mean. The total noise in $I_{\text{measured}}(x_n)$, expressed in Noise Equivalent Power, NEP_{tot} , is the sum of the three noise variances:

$$\text{NEP}_{\text{tot}}^2 = 2\text{NEP}_{\text{ph}}^2 + 2\text{NEP}_{\text{det}}^2 + 2\text{NEP}_{\text{sou}}^2, \quad (\text{IV.9})$$

where NEP_{ph} and NEP_{sou} are the thermal noise from the background (e.g. sky and warm optics in the case of a far-IR instrument) and source photon noise, respectively, in one output, and NEP_{det} is the noise-equivalent power characterizing each detector's noise (including phonon, readout and Johnson noise). The factor of 2 multiplies each term since we are considering the difference of both outputs. The relation between NEP_{tot} and the variance $\sigma_{\mathcal{I}}^2$ of the noise $n_{\mathcal{I}}$ during an interval dt is (Sromovsky, 2003):

$$\sigma_{\mathcal{I}}^2 = \frac{\text{NEP}_{\text{tot}}^2}{2dt}. \quad (\text{IV.10})$$

For space instruments, the noise will likely be dominated by the sky background (zodiacal light, galactic cirrus emission, or optics thermal emission) and detector for a very large fraction of astronomical targets, which tend to be faint; for balloon instruments, emission

from warm optics and the atmosphere sets the noise level in the far-IR.

IV.3.2 OPD noise

Observing from the ground at optical wavelengths with a double-Fourier interferometer is limited by the phase coherence between the apertures, which is related to the atmospheric coherence time, as discussed by Mariotti et al., 1988. The short coherence time forces fast scan rates, which degrades the sensitivity of the instrument due to short integration times and phase shifts between sequential scans. This is not a problem for flying platforms, since even at balloon altitudes the atmospheric coherence is not a significant issue (Rizzo et al., 2012). The major concerns for balloon and space missions are overall instrumental stability, knowledge of ZPD, and pointing errors, which can all contribute to OPD noise.

OPD noise arises in an interferogram when the OPD at the time of a measurement is uncertain, hence compromising the reconstruction of the true x -value. Since this uncertainty is a physical delay δ_x , the error in phase is wavenumber dependent: $2\pi\delta_x\sigma$. δ_x is the difference between the estimated x and the true x . For single-beam FTS instruments, internal laser metrology can provide optical path length measurements to high accuracy (e.g. Griffiths et al., 2007), and the separate paths the split beams need to travel can be kept small. For double-Fourier instruments, the entire optical paths upstream of the beam combiner affect the OPD, hence it is more challenging to accurately measure and estimate the OPD contributors. In addition, common-mode pointing errors of the collectors are directly converted to geometrical delay errors. Hence, it is critical to know the position and orientation of the baseline vector with respect to the astronomical target with high accuracy in order to properly reconstruct the interferogram.

For this analysis, we identify three timescales that can be used to examine the effects of OPD noise on the interferogram. These timescales are important to consider in the design of the OPD control system of any double-Fourier interferometer. Timescale 1 is the shortest and corresponds to the integration time for a single data point, typically a few milliseconds. In practice, this kind of OPD noise could be created by high-frequency mechanical jitters in the instrument (including the delay line bearing and motor, stiction behaviors and resonant modes, reaction wheels and other self-induced vibrations...). Timescale 2 is the time it takes to acquire one single interferogram over the full field of view and at the desired resolving power, typically on the order of seconds. The sources of noise that can affect this timescale include for example pointing errors and drifts, as well errors in the knowledge of the delay line position relative to a reference ZPD. Finally, the longest timescale to be considered, timescale 3, is the time it takes to complete one full "track" by co-adding several consecutive interferograms to achieve the desired SNR, typically a few minutes long. During this timescale, it is expected that the change in baseline orientation on the sky does not produce any significant change in the source spatial visibility function. The latter timescale is most importantly influenced by thermal variations and time-varying gradients that could change the optical alignment and mechanical configuration between the two arms.

IV.4 Spectral signal-to-noise ratio

IV.4.1 Effects of Gaussian intensity noise

In the presence of Gaussian intensity noise (thermal background and detector noise), the measured interferogram is of the form of Eq. IV.8. We suppose that the noise has a variance

$\sigma_{\mathcal{I}}^2$ and zero mean, and is independent of delay position. In particular, this assumes that the source photon noise is negligible. The noise in the spectral domain is the transform of the noise in the interferogram domain:

$$dx \mathbf{DFT}(n_{\mathcal{I}}) = dx \sum_{n=-N/2}^{N/2-1} n_{\mathcal{I}}(x_n) e^{2i\pi nk/N}, \quad (\text{IV.11})$$

where the dx factor is to normalize the noise to a sampling bin (Press et al., 1992), and k indexes the N discrete wavenumbers in the spectral domain. The interferogram interval is symmetric with about ZPD ($n=0$). The noise variance is equal in the imaginary and the real domain, and can be expressed as the variance of the noise transform:

$$\sigma_{\mathcal{S}}^2 = dx^2 \mathbf{VAR}(\text{Re}(\mathbf{DFT}(n_{\mathcal{I}}))), \quad (\text{IV.12})$$

where **VAR** is the variance operation. By writing out the variance we obtain:

$$\sigma_{\mathcal{S}}^2 = dx^2 \sigma_{\mathcal{I}}^2 \sum_{n=-N/2}^{N/2-1} \cos^2(2\pi nk/N) = \frac{N}{2} dx^2 \sigma_{\mathcal{I}}^2, \quad (\text{IV.13})$$

where we used $\sum_{n=-N/2}^{N/2-1} \cos^2(2\pi nk/N) = N/2$ for $k \neq 0$.

The signal at wavenumber σ_k in the discrete spectrum $\mathcal{S}_e(\sigma_k)$ is:

$$\mathcal{S}_e(\sigma_k) = \frac{1}{\delta\sigma} \int_{\sigma_k - \delta\sigma/2}^{\sigma_k + \delta\sigma/2} \mathcal{S}_e(\sigma) d\sigma, \quad (\text{IV.14})$$

where $\delta\sigma = (Ndx)^{-1}$. A line of power P_e at σ_{k_0} will thus have an apparent flux density $\mathcal{S}_e(\sigma_k) = Ndx P_e$ at $k = k_0$ and 0 for all other k . The signal-to-noise ratio in the spectrum

can be expressed in general as:

$$\text{SNR}_k = \frac{\mathcal{S}_e(\sigma_k)}{\sigma_{\mathcal{S}}} = \sqrt{\frac{2}{N}} \frac{\mathcal{S}_e(\sigma_k)}{dx\sigma_{\mathcal{I}}}. \quad (\text{IV.15})$$

Using Eq. IV.10 and the definition $x_{\max} = Ndx/2$, this becomes:

$$\text{SNR}_k = \frac{\mathcal{S}_e(\sigma_k)}{x_{\max}\text{NEP}_{\text{tot}}} \sqrt{Ndt}, \quad (\text{IV.16})$$

where dt corresponds to the integration time of one data point on the interferogram. As expected the SNR improves as the square-root of the total integration time, \sqrt{Ndt} , and is adversely affected by increasing NEP and scan length.

Defining the central wavenumber of the band as σ_0 , the spectral resolving power of the transformed interferogram is $\mathcal{R} = dxN\sigma_0/2$. We introduce the sampling parameter $s = (\sigma_0 dx)^{-1}$ which is the number of data samples per fringe for the central wavenumber in the band. The spectral resolving power at the band center can now be written $\mathcal{R} = \frac{N}{2s}$. In practice one wants to pick a value of s that ensures Nyquist sampling on the fringe for all wavenumbers in the band so $s \sim 3$ or greater is typically preferred. For a given integration time per data point (given $\text{SNR}_{\mathcal{I}}$), increasing the fringe sampling effectively increases the amount of time spent on the fringe, so the spectral SNR should increase with \sqrt{s} . Note that as long as we Nyquist-sample the fringe, there is no difference between multiplying the fringe sampling by some factor, and increasing the integration time per data point by the same factor, since in both cases the effective time on the fringe is equally increased.

It is useful to relate SNR_k to the SNR in the interferogram at the location of maximum intensity of the fringe, using physical quantities. The noise in each discrete measurement of the interferogram is $\sigma_{\mathcal{I}}$. The signal at maximum intensity is $\mathcal{I}_{\max} = d\sigma\bar{\mathcal{S}}$, where

$d\sigma$ is the width of the bandpass filter and $\bar{\mathcal{S}}$ is the average value of the signal in the band.

Defining $\text{SNR}_{\mathcal{I}} = \mathcal{I}_{\max}/\sigma_{\mathcal{I}}$, and noting that $\sqrt{Ndx^2/2} = \frac{1}{\sigma_0}\sqrt{R/s}$, we obtain:

$$\text{SNR}_k = \frac{\mathcal{S}_e\sqrt{2}}{\sqrt{Ndx\sigma_{\mathcal{I}}}} = \frac{\mathcal{S}_e(\sigma_k)}{\bar{\mathcal{S}}} \sqrt{\frac{s}{\mathcal{R}}} \frac{\sigma_0}{d\sigma} \text{SNR}_{\mathcal{I}}. \quad (\text{IV.17})$$

Thus, the SNR in a channel of the final spectrum depends inversely on the square root of the resolving power \mathcal{R} and the fractional bandwidth $\frac{d\sigma}{\sigma_0}$; and it depends directly on the square root of the number of samples per fringe \sqrt{s} .

For a given integration time, $\text{SNR}_{\mathcal{I}}$ is proportional to $\sqrt{\frac{d\sigma}{\sigma_0}}$, which means that SNR_k is inversely proportional to $\sqrt{\frac{d\sigma}{\sigma_0}}$. Hence, maximizing the SNR in the interferogram by increasing the bandwidth does not lead to a better spectral SNR. Although the central fringe has more SNR with a larger bandwidth, the fringe envelope is decreasing more rapidly, and we see less fringes with good SNR. With a smaller bandwidth, the envelope is broader and although each fringe has less SNR, we are seeing more of them within the scan, so we spend more time in an interesting region of the interferogram. The number of fringes within the main lobe of a standard sinc function is indeed inversely proportional to the fractional bandwidth. This is an important concept that can be used to tune the spectral resolving power appropriately: if the instrument has a large bandwidth, increasing the scan length (hence \mathcal{R}) well beyond the fringe pattern's main lobe will hurt the sensitivity, since many data points will be adding noise and almost no signal. The dependencies discussed above can be summarized as:

$$\text{SNR}_k^2 \propto \left(\frac{s}{\mathcal{R}}\right) \left(\frac{\sigma_0}{d\sigma}\right) dt. \quad (\text{IV.18})$$

IV.4.2 Effects of Gaussian OPD noise

This section derives analytic expressions for the effects of Gaussian-distributed OPD noise. We look at the general case in order to derive sensitivities for double-Fourier instruments. Here, we suppose that the OPD from the delay line, the OPD within each arm of the instrument, and the OPD caused by an off-axis source are all measured or estimated with some residual error. Hence, the data points measured in the interferogram are associated with a delay value relative to ZPD, and if necessary, resampled to produce an evenly-spaced delay axis. This is necessary to use the FT and retrieve the spectrum. The noise on the delay estimate can be characterized as a wavenumber-dependent phase error in the interference on the two beams. In the following, we quantify the impact of this noise on the spectral SNR, in order to understand how good our knowledge of the OPD needs to be to make sure the OPD noise effects are not dominant.

Let's consider a single frequency signal first, so that the phase is proportional to the OPD. If we suppose that these residual phase errors $\Phi_r(x)$ are represented by a Gaussian distribution with zero mean and variance σ_Φ^2 , then the primary effect of the noise is to change the instantaneous power in $I(x)$ by the factor $e^{i\Phi_r(x)}$. Now we consider a large ensemble of realizations of this noise distribution in order to predict its effect on the SNR. Using the expression from Richards, 2003, for sufficiently small phase errors ($< \pi$ radians), the intensity of the coherent signal is reduced, on average, by a factor $e^{-\sigma_\Phi^2/2}$. For Gaussian-distributed OPD uncertainties with standard deviation $\lambda/20$, where λ is the wavelength, the signal intensity is reduced by 5%; for $\lambda/10$ the amplitude is reduced by 18%. To give a practical example of the impact of this effect, we can consider the case of BETTII: if we assume that the uncertainty in the attitude of the payload is the only

source of OPD noise, then knowing the attitude to within 0.1" rms will reduce the signal, on average, by 18% at 40 μm .

For the polychromatic case, the delay position uncertainty, δ_x , creates larger phase errors the shorter the wavelength, $\Phi_r(k) = 2\pi\delta_x\sigma_k$. A given error distribution of variance σ_{OPD}^2 in position yields a degradation across the band, $e^{-\sigma_\Phi^2(k)/2}$, with $\sigma_\Phi^2(k) = (2\pi)^2\sigma_{\text{OPD}}^2\sigma_k^2$.

Of course, the power lost from the coherent fringe pattern is still present in the scan; it becomes part of the incoherent signal seen by each output. In the limit where there is no spectral noise from the background or detectors, defining $\mathcal{S}_k \equiv \mathcal{S}_e(\sigma_k)$ we have:

$$\text{SNR}_k = \frac{\mathcal{S}_k e^{-\sigma_\Phi^2(k)/2}}{\sqrt{\frac{1}{2s\mathcal{R}} \sum_{k'} [\mathcal{S}_{k'}^2 (1 - e^{-\sigma_\Phi^2(k')})]}}, \quad (\text{IV.19})$$

where k' designates an index on all positive wavenumber bins. Note that $N = 2s\mathcal{R}$. This relationship is identical to the one derived by Meynart (1992), and we suggest an alternate and more detailed justification for it (see Appendix A.A.2). Studying this relationship, all the wavenumbers contribute to the white noise at a given wavenumber σ_k . The strongest lines (strongest $\mathcal{S}_{k'}^2$) and the shortest wavelengths (strongest $1 - e^{-\sigma_\Phi^2(k')}$) contribute the most to the overall noise. To summarize, considering an ensemble average of interferograms, OPD noise degrades the spectral SNR in two ways: first, it reduces the overall signal in the interferogram; second, it converts this lost power into white noise.

More realistically, observations will have both intensity and OPD-generated spectral noise. In this case, the intensity noise and the scattered power add in quadrature to give:

$$\text{SNR}_k = \frac{\mathcal{S}_k e^{-\sigma_\Phi^2(k)/2}}{\sqrt{\frac{1}{2s\mathcal{R}} \sum_{k'} [\mathcal{S}_{k'}^2 (1 - e^{-\sigma_\Phi^2(k')})] + s\mathcal{R}dx^2\sigma_I^2}}. \quad (\text{IV.20})$$

The numerator of Eq. IV.20 shows that any amount of OPD noise will reduce the spectral SNR. However, the impact of OPD noise is even greater when the power lost from the fringe is comparable to the intensity noise, as the first term of the denominator starts to matter. In fact, for arbitrarily large source fluxes, this equation reaches an asymptotical value which depends only on the OPD noise, and sets the maximum SNR achievable on average in a single scan. This is relevant for astronomical calibrators which can be so bright that the intensity noise term is negligible. In that case, assuming constant OPD noise, more SNR is only achievable by co-adding consecutive scans, as we discuss in the next section and in Appendix A.A.3. For most astronomical applications, where targets are usually faint compared to the intensity noise, it is expected that the first term of the denominator will be negligible.

IV.4.3 Co-adding interferograms

Eq. IV.20 is the general case of a single interferogram with OPD and intensity noise. In practice, we would co-add M interferograms in one "track" to build up SNR, but this puts stringent requirements on the performance of the control system and OPD estimator, because consecutive interferograms need to stay aligned with each other to within a small fraction of the carrier wavelength, to avoid causing OPD noise. The design and performance of the OPD estimator is highly implementation-specific, but most balloon and space designs will likely include an estimator that either directly measures the OPD, or indirectly infers it from the measurement of another quantity.

A direct OPD measurement can be achieved for example with a fringe-tracking instrument, while an indirect OPD estimate can be an attitude measurement, which can be related to the OPD by simple geometry by using some assumptions. The latter scheme only

works if the OPD errors are only influenced by pointing uncertainties over the timescale of a track, and that all other OPD contributors are modeled and corrected with comparatively high fidelity. The spectral SNR over M scans can be determined from Eq. IV.20 by multiplying the whole equation by a factor of \sqrt{M} . The OPD noise term causing the phase noise variance σ_ϕ^2 then corresponds to the variance of the OPD uncertainties for each point of a scan, plus the variance of the OPD estimation error in determining the position of the center of each scan, which is necessary to properly co-align them (Appendix A.A.3).

IV.4.4 Implications for spectroscopy

A primary application for BETTII and proposed missions like SPIRIT will be the measurement of the spectral energy distribution from warm dust associated with star formation in different environments. These types of measurements require broad wavelength coverage but not especially high spectral resolution since the emission can be characterized as a sum of Planck functions over a range of temperatures. For an instrument like BETTII, covering from 30-50 μm and 60-110 μm simultaneously, $\mathcal{R} \sim 10$ in each band is sufficient to accomplish much of the science.

Spectral measurement with $\mathcal{R} \sim 10$ requires covering a delay range of $\pm 10 \lambda_0$ for a single source. On the other hand, a delay range of 35-70 λ (see Eq. IV.7) is needed to move ZPD across 1 arc-minute of sky. Hence, typically, the delay requirements for spatial coverage creates interferograms with higher resolution than needed to measure the continuum, and the full scan needs to be cut into smaller arrays around each target in the field. The size of these smaller arrays depends on the desired spectral resolving power \mathcal{R} , and the required sensitivity, as shown in Eq. IV.17. However, the additional data can be used for higher-resolution spectroscopy, for example to measure specific atomic lines in

the far-IR. The SNR for lines is actually increasing with the square root of the number of data points in the interferogram, as the broadband noise gets more diluted in increasingly narrower spectral bins (see Eq. IV.14, IV.15).

As discussed for FTS instruments (e.g. Davis et al., 2001), apodization, the weighting of the points of the measured interferogram before applying the DFT, is one method for optimizing the SNR in the spectrum. The weight scheme is optimized to measure a specific type of spectrum: narrow line, broad features, continuum. The method relies on the fact that the data points close to the center or edges of a fringe packet contain information about low or high spectral frequencies, respectively. For example, if the purpose of an observation is to study continuum, it is appropriate to apply smaller weights to data points far away from the central fringe, since they add noise and very little SNR.

A common low-resolution spectroscopy case can be derived analytically if a source has a spectrum following a power law distribution over the covered band. We can write $\mathcal{S}(\sigma) \propto \sigma^\alpha$ where the exponent α is the quantity of interest. Several methods have been developed to properly fit these power laws using maximum entropy and other techniques (e.g. Clauset et al., 2007). Here we use a simple estimator and provide a ready-to-use formula to help quantify the sensitivity of double-Fourier instruments.

By taking the logarithm of the spectrum, the problem is turned into a weighted linear fit in log-log space, where we want to determine the slope of a line. The noise in the new domain is $\sigma_L = \left| \frac{d(\ln(\mathcal{S}))}{d\mathcal{S}} \right| \sigma_{\mathcal{S}} = \sigma_{\mathcal{S}}/\mathcal{S} = 1/\text{SNR}_{\mathcal{S}}$. The weights $w_k = 1/\sigma_k^2$ of the linear fit are then simply the values of the spectral SNR squared at each data point, SNR_k^2 . The error on the weighted least square estimate of the slope is (Bevington et al., 2003):

$$\sigma_\alpha^2 = \frac{\sum w_k}{\sum w_k \sum w_k X_k^2 - (\sum w_k X_k)^2}, \quad (\text{IV.21})$$

where $X_k \equiv \ln(\sigma_k)$ is the natural logarithm of the wavenumber for data point k . In the case of uniform spectral signal-to-noise ratio $\text{SNR}_{\mathcal{S}}$ over m points of the spectrum, this expression simplifies to:

$$\sigma_{\alpha}^2 = \frac{1}{m \times \text{SNR}_{\mathcal{S}}^2 \times \mathbf{VAR}(X_k)}. \quad (\text{IV.22})$$

This equation indicates that the variance of the spectral index estimate decreases with the number of points used to calculate the estimate, the spectral SNR squared, and the variance of the points distribution on the logarithmic wavenumber axis. For example, for 10 data points spread evenly from 30 to 55 μm , each with a spectral SNR of 5, we obtain an error on the slope determination $\sigma_{\alpha} \sim 0.3$.

IV.5 Spectral sensitivity analysis for BETTII

This section applies elements of the above discussion to BETTII. A general discussion on the details of BETTII can be found in (Rinehart et al., 2014). On BETTII, two mirrors collect light with an altitude-azimuth pointing system. The truss that holds the two mirrors moves in azimuth and determines the baseline vector, while the mirrors themselves move only in elevation. While BETTII does not physically rotate about the line of sight to cover different baseline angles, the payload always stays horizontal and the projection of its baseline vector changes as a source moves across the sky, hence covering different angles in the (u, v) -plane. The absolute OPD and ZPD of the instrument cannot be measured, maintained, or known with perfect accuracy, especially during the flight itself, due to attitude estimation errors leading to our inability to perfectly estimate the orientation of the baseline vector in real time. In fact, a significant component of the mission's design and implementation involves the selection and coordination of the suite of instruments

which provide attitude measurements to construct the OPD estimator.

A second relevant aspect of BETTII is that the detectors are cryogenic bolometers see Staguhn et al., 2014b, for similar architectures with $1/f$ noise which sets an optimal read-out time for the detectors of around 2.5 milliseconds (timescale 1). With BETTII’s designed field coverage of 2 arcminutes, full field scans consist of 1024 points and take 3 seconds to complete (timescale 2). Due to thermal emission from the atmosphere, warm mirrors, and cryostat windows, BETTII will be in the background noise limited case for all science targets. It is anticipated that 200 scans will typically be co-added to create one single visibility measurement over 10 minutes (timescale 3). For most source locations, the variation of the baseline orientation due to change in parallactic angle is not significant over this period.

IV.5.1 Noise sources and control system

Table III.5 showed our estimates of the background power levels associated with the atmosphere, warm optics, and windows in the two BETTII bands. The detectors themselves have been designed to have a noise level comparable to the background to optimize the use of the dynamic range of the devices. The total NEPs of the short and long bands are expected to be $\sim 1.7 \times 10^{-15} \text{ W.Hz}^{-0.5}$ and $\sim 1 \times 10^{-15} \text{ W.Hz}^{-0.5}$, respectively. The source photon noise is negligible compared to the total NEP.

Balloon instruments are subject to low frequency ($< 0.5 \text{ Hz}$) pendulum modes and other oscillations introduced by the system’s geometry and mass distribution, which make pointing a challenge. However, it is expected that the balloon environment is free of perturbations at any higher frequency (other than the instrument specific perturbations). Hence, sensors with high electrical bandwidth can robustly estimate the pendulum modes to gain

accurate knowledge of the attitude, which can be used as our indirect OPD estimator since it is geometrically related to the phase on sufficiently short timescales.

The BETTII control system is organized with three different levels of control loops (Rizzo et al., 2014): the coarse pointing loop, the fine pointing loop, and the OPD loop. The coarse pointing loop uses gyroscopes and star cameras to keep the baseline oriented within 10-15'' of an appropriate near-IR guide star. A dichroic splits the near-IR (1-2 μm) from the far-IR (30-110 μm) inside the cryostat before the scanning delay line. The guide star is imaged through each of the two arms on two separate readout windows of a near-IR detector array that shares most of the optical path with the science channels. The fine control loop uses fast-steering tip-tilt mirrors, located at the pupils of each arm, to control the guide star image on each window and maintain good overlap of the beams at the science detectors. This loop reads the near-IR detector and generates a tip/tilt correction at 100 Hz. We expect to achieve beam overlap to within better than 1.5'' at all times when a guide star is available. The spatial resolution of an individual BETTII beam is 17'' in the short wavelength band so this is a little better than 1/10th of a resolution element. The interferometric visibility loss for this overlap error is anticipated to be less than 0.5%.

We do not expect to be able to maintain the three dimensional orientation of the truss, and hence the baseline vector, to much better than 15'' rms, due to the various pendulum modes mentioned above and large inertia of the payload. However, the errors in OPD introduced by pointing errors can be corrected directly using a delay line. BETTII uses a delay line external to the cryostat to correct the OPD at the entrance of the cryogenic volume. This delay line is completely separate from the science delay line which scans the OPD to produce the interferogram. Two delay lines are not a requirement for a double-Fourier instrument in general as the job can be done in theory by a single mechanism, with

sufficient range and mechanical bandwidth. The external delay line on BETTII allows for the possible future upgrade of correcting and monitoring the OPD outside of the cryostat using the near-IR channel by implementing a fringe tracker (Rizzo et al., 2012).

For the OPD loop on BETTII, the angles of the tip/tilt mirrors which are used to maintain overlap of the beams act as an estimator of the baseline orientation, and hence as an indirect estimator of the OPD. The attitude estimates computed from these angles are fed to the external delay line so that the OPD at the entrance of the cryostat stays as constant as possible. Because the pendulation modes have periods of a few to tens of seconds and should be well-behaved, we expect to be able to trust the control signals and estimate the attitude of the baseline vector to $\sim 0.12''$ rms, which corresponds to a fifth of a detector pixel in the near-IR tracking array. A $0.12''$ attitude error indirectly corresponds to a delay uncertainty of $5 \mu\text{m}$, or 12% of a wavelength at 40 microns. This is a critical consideration when co-adding consecutive interferograms. With this amount of OPD noise, we expect, on average, a $\sim 25\%$ degradation in SNR for all sources in the short band, simply from the effects of phase noise in reducing the coherent signal (see Eq. IV.20).

Even with a stable OPD estimator, the absolute ZPD of the instrument must be measured during flight and tracked over long timescales as the instrument and the truss cool down to ambient temperatures (~ 240 K). This can be accomplished by observing a bright point source with known position periodically during a flight and identifying the center of the interferogram response (see Appendix A.A.3).

IV.5.2 Derived sensitivity and faintest detectable targets

Incorporating these sources of noise with the formulas derived in the previous sections leads to the sensitivity values shown in Table IV.1. In this table we show the sensitivity in the two bands. The minimum detectable flux density (MDFD), which is the flux that provides $\text{SNR}_{\mathcal{I}} = 1$ in a single interferogram, is 77 Jy and 113 Jy in band 1 and 2 respectively. For 200 scans averaged with a OPD noise between scans of 5 μm , the MDFD is 5 Jy and 8 Jy, using a matched filter efficiency of 0.5 and 0.4, respectively (Mighell, 2005). The faintest detectable spectroscopic point source that leads to a spectral $\text{SNR} = 5$ is 34 Jy and 17 Jy, respectively. These are determined for "normal observing", which consists of co-adding 200 scans in 10 minutes that span the whole 2'x2' field of view, using a spectral resolution of $\mathcal{R} = 10$ and a nominal OPD noise of 5 μm rms.

TABLE IV.1: BETTII sensitivity estimates

Quantity	Band 1	Band 2	SNR Target
Single scan (3 s)			
MDFD	77 Jy	113 Jy	$\text{SNR}_{\mathcal{I}} = 1$
Normal observing (200 scans, 10 min)			
MDFD	5 Jy	8 Jy	$\text{SNR}_{\mathcal{I}} = 1$
Faintest pt. source	34 Jy	17 Jy	$\text{SNR}_k = 5$
Enhanced sensitivity (200 scans, 10 min)			
Faintest pt. source	19 Jy	10 Jy	$\text{SNR}_k = 5$

At the bottom of the table, we also show the results in case we were using the instrument in an "enhanced sensitivity" mode. This mode is mentioned here to illustrate the flexibility of the interferometer and its observing modes. It consists of increasing the

individual integration time for each point in the interferogram by a factor of 3, while reducing the interferometric field of view by the same factor of 3: while the intrinsic field of view is unchanged at the detector, for the same scan time we only cover enough OPD range to cross ZPD for a subset of the pixels of the detector (and obtain a scan of the same length). This mode could be used for example for isolated targets which are located in less crowded star fields, by optimizing the time spent close to ZPD, where there is more signal (as we are interested in low-resolution spectroscopy). BETTII’s observing parameters can be changed during flight so that the instrument stays flexible to optimize the chance of seeing fringes.

Finally, we show the overall sensitivity as a function of point source flux density (Eq. IV.20) for both observing modes and both bands in Figure IV.4. In normal background-limited regime, the sensitivity curves should be straight lines. Here, OPD noise creates a decrease in overall sensitivity as a reduction in coherent power, but also, for brighter targets, from the power lost from the fringe that is converted to white noise (which causes a deviation from straight lines). For very bright targets of 50 Jy or more, it is possible to measure the OPD accurately within each interferogram by tracking the fringes in the science channels themselves (see Appendix A.A.3). For sufficiently large SNR, this process has less error than the assumed 5 μm OPD noise coming from the indirect OPD estimation, so the OPD noise decreases for these very large fluxes to become negligible. This is particularly attractive for in-flight testing and calibration.

It is important to note that for sufficiently faint targets, it is impossible to accurately measure the OPD using single scans or co-adds of scans: we rely on the OPD estimator to have sufficient stability to properly co-add scans until the next calibration measurement. This needs to be considered carefully when planning the observation strategy, as long

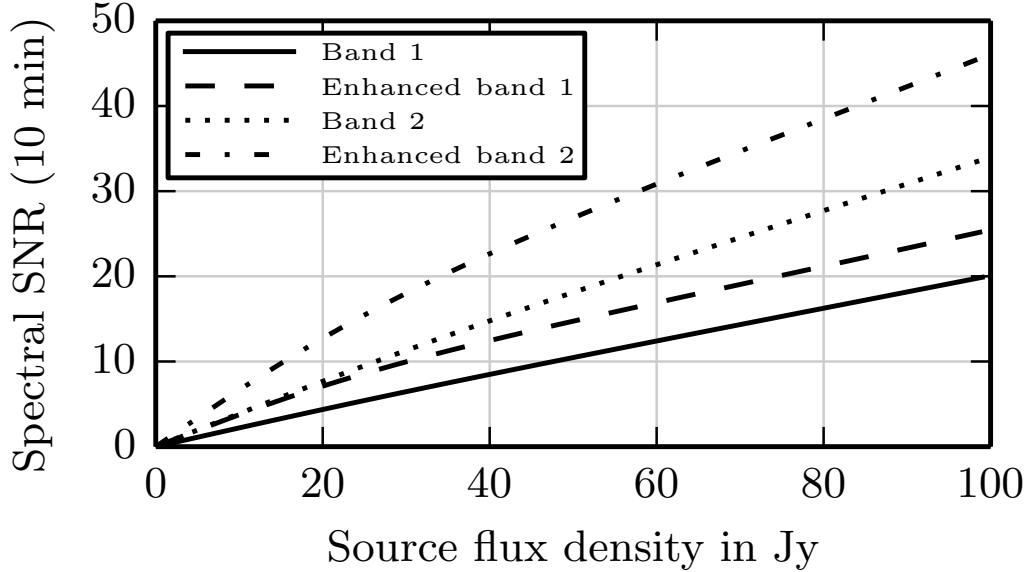


FIGURE IV.4: BETTII’s spectral sensitivity. Solid: Normal observing mode, band 1; Dashed: Enhanced sensitivity mode, band 1; Dotted: normal observing mode, band 2; Dot-dashed: Enhanced sensitivity mode, band 2. This plot includes the technique of fringe tracking in the science channel for sufficiently bright sources (see Appendix A.A.3). As the source flux rises, the effects of the phase noise become larger and the SNR should reach an asymptotical value. However, with fringe tracking, the phase noise itself becomes smaller since one can see fringes in one single or a few consecutive scans, so the co-adding becomes easier. Thanks to the fringe-tracking, there is no regime where the phase noise is expected to be dominant on BETTII, provided that the control system performs according to expectations.

stretches without calibration could lead to a total loss of the OPD information (hence a total loss in scientific data), due to other OPD noise contributors such as thermal drifts that impact the payload on long timescales.

IV.6 Conclusion

Spatio-spectral interferometry can enable high resolution spectral imaging of wide fields at far-IR wavelengths. Implementation of the technique provides some new instrumental

challenges compared to traditional Fourier Transform Spectroscopy, such as the fact that the measured spectrum is a mix of the source's spectral and spatial information.

In a double-Fourier system, the zero path difference for each detector pixel occurs at a different delay setting of the delay line. The delay stroke needed to cover a scientifically interesting field of view is equivalent to a spectral resolving power of 100's to 1000's for the central pixels.

We present an analysis of the impact of Gaussian intensity and OPD noise on the spectral sensitivity. Intensity noise, essentially thermal noise from the optics, sky, astrophysical background, and detector, is similar to noise in FTS systems with the exception that the longer scan lengths required to cover the spatial field add noise; this can be mitigated by cutting the interferogram for each pixel into smaller arrays centered on each source's ZPD to match the desired spectral resolving power, and by apodizing the interferogram to increase sensitivity to the spectral properties of interest. OPD noise is not usually relevant for FTS systems, but is intrinsic to double-Fourier instruments, since the two incoming beams go through long separate paths before combination. For instruments on balloons or in space, the OPD noise is expected to be dominated by disturbances from the instrument and from pointing errors. On average, OPD noise reduces the coherent power in the interferogram, and converts the power lost from the fringe into additional white noise in the spectrum. We argue that there are three relevant noise timescales: the time to take a single data point, the time to collect a complete interferogram, and the time to co-add M interferograms together in a track. The latter corresponds to the timescale that the source spatial visibility function changes significantly, due to the rotation of the baseline angle on the sky.

We derive the spectral sensitivity of double-Fourier instruments to intensity and

OPD noise. The expressions in this paper are derived in the general case and can be used to design any instrument that implements this method.

Applied to the case of BETTII, these equations lead to spectral sensitivity estimates of 34 and 17 Jy in its 30-50 μm and 60-110 μm bands, respectively, to achieve a spectral SNR = 5 in 10 minutes with $\mathcal{R} = 10$ and an assumed OPD noise of 5 μm rms.

Chapter V

Attitude estimation and control for BETTII

Don't bother just to be better than your contemporaries or predecessors. Try to be better than yourself.

W. Faulkner

Chapter IV sets the general background to double-Fourier interferometry when used mostly in spectroscopy mode. It sets the mathematical formalism to estimate the spectral sensitivity, given various sources of gaussian noises.

In this chapter, we see more directly how this applies to BETTII, and how the system is designed to satisfy these requirements in order to guarantee good observations. First, we describe the overall architecture and system-level strategy that we use, before going into some details of BETTII's subsystems. Second, we describe the main algorithm used in the flight software, which estimates the position of the payload at all time. Because of the importance of this algorithm, and its potential usability by others, we decided to elaborate on some of the mathematical derivations that define the attitude estimator.

V.1 Control system architecture

V.1.1 Overall strategy

V.1.1.1 Requirements

The strategy that we developed aims at satisfying the requirements established in the previous chapter, under the cost, time and personnel constraints of the BETTII project. It fundamentally relies on the fact that *knowledge* is more important than *control*. While several research groups (such as the WASP team at Wallops Flight Facility) are attempting to provide sub-arcsecond balloon gondola control, we are not. Our strategy uses the fundamental advantage that the interferometer has over traditional pointed observatories: the decoupling of the phase with the telescope pointing. This feature of interferometers refers to obtaining electromagnetic interference even when the telescopes are slightly mispointed from the target.

There are three levels of requirements for our instrument to produce interferograms. First, both arms need to be pointed at the target, in order for an image of the target seen through each arm to be formed on the detector. When a target is not exactly on-axis with the telescope, it can still fall on the detector if tip/tilt correction happens downstream. The tip/tilt correction will create aberrations, but these are relatively well behaved at our wavelengths. Hence, this requirement can be expressed as an overall pointing requirement of the instrument to some amount that can be corrected in tip/tilt in each individual arms. We set this to $\pm 15''$. This also roughly corresponds to one single pixel on the short band detector, and half a primary beam's FWHM.

Once the instrument is pointed to the desired target to within $\pm 15''$, there needs

to be a fine guiding system in each arm that allows for the remaining tip/tilt correction. This level of control needs to overlap the beams to a small fraction of a pixel to get maximum overlap and minimum visibility losses. We set this requirement to $1.5''$ r.m.s., which corresponds to a tenth of a pixel size and keeps a high visibility in the science channels. The fine guidance system needs to operate over a range of at least $\pm 15''$ to pick up where the previous level of requirements stops. It also needs to happen with high bandwidth to ensure that only minimal motion is occurring at timescales comparable to a data acquisition timescale. This system is described in Section V.1.2.8.

Finally, an angular mispointing of the baseline vector with respect to the target can still exist, even if both beams are overlapped properly. This introduces an unwanted optical delay that can push the fringe packets outside our nominal OPD scanning range. Control of this optical delay is critical for interferometry, as it is required to properly reconstruct the OPD axis of the interferograms that are the elementary data blocks of the instrument. The OPD tracking can be achieved using a delay line. This is commonly done for all interferometers on the ground (e.g. Blind et al., 2011), and we implement such a device on BETTII, which is described in Section V.1.2.6. For this to work, we need to be able to monitor the changes in OPD accurately, which is equivalent, on short timescales, to accurately estimating the attitude of the payload.

A good estimate of the attitude of our payload can lead to an accurate angular difference between our baseline vector and our target. This angular difference can be converted to an OPD using simple geometric arguments, and can then be fed to the delay line for correction. With an 8 m baseline length, a mispointing of $1''$ along the baseline direction corresponds to an OPD of about $40\text{ }\mu\text{m}$, or one full wavelength of BETTII's short-wavelength band. In order to produce quality interferograms, we will need to know

the OPD to a fraction of this (see Chapter IV).

V.1.1.2 BETTII Coordinate systems

Before going into the details of the controls architecture, it is important to set key nomenclature and properly define our reference frames. On BETTII, multiple coordinate systems are involved in the control system. The main systems are described in Fig. V.1. These coordinate systems need to be aligned before flight for the control system to operate well.

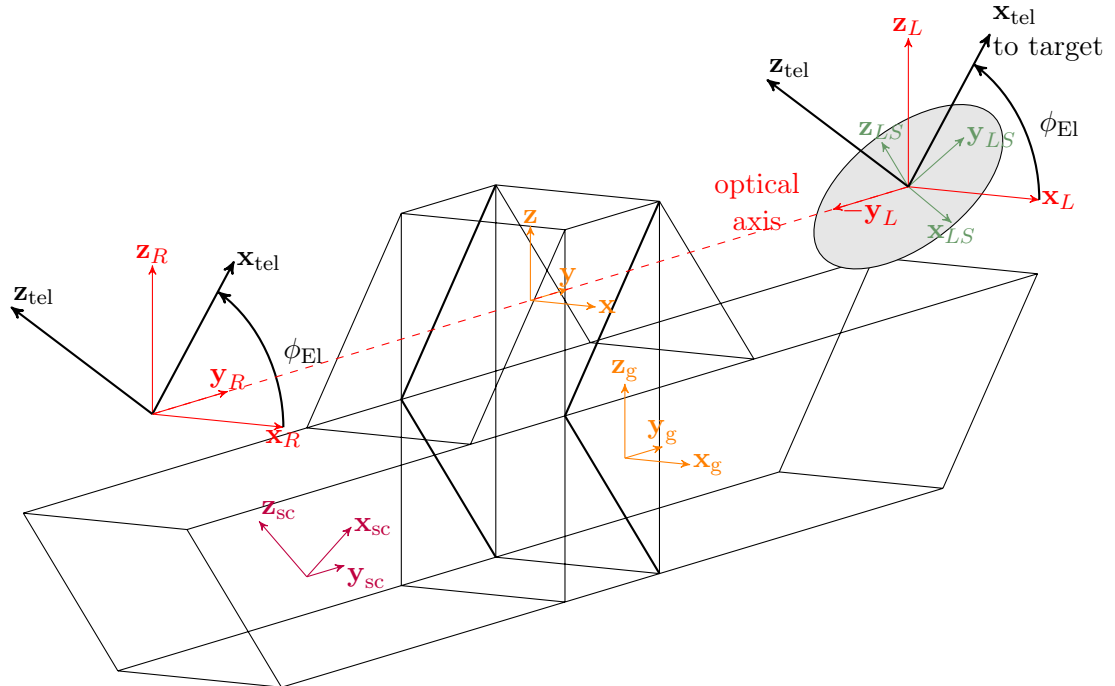


FIGURE V.1: Coordinate systems relevant to the pointing control system (see text for details).

The truss reference frame (in orange and with no subscript for the rest of this document) is tied to the gyroscope reference frame (also in orange, with subscript ‘g’), and we will consider that these two reference frames are aligned with each other. The **z** axis of the payload points up, while the **x** axis points ‘forward’. The arrow formed by the truss members of the center section hence points towards the right, or in the **-y** direction.

The star cameras (in purple and with subscript ‘sc’) are nominally aligned with the gyroscope reference frame, except for a rotation about \mathbf{y}_g of -45° .

The main optical axis of the payload joins the centers of the two siderostats, and is coaligned with the centers of the two telescope assemblies (not shown on Fig. V.1). Each siderostat has its own reference frame (in green and subscript ’LS’ or ’RS’, for left siderostat or right siderostat, respectively) which is tied to its shape, and which is used during alignment procedures. Most importantly for the control system, the reference frame that matters is that of the optical beam reflecting off the siderostat. This is called the telescope reference frame (in black and with subscript ‘tel’). With this notation, \mathbf{x}_{tel} is our instrument’s line of sight vector. Note that there are actually two ‘telescope’ reference frames (one for each side), although for most of the discussion presented here, we will only consider one global telescope reference frame.

Not shown in Fig. V.1 are the reference frames of the tip/tilt actuators which we will discuss in Section V.1.2.8, as well as many other coordinate systems used for optical alignment.

In addition to the payload’s own coordinate systems, it is important to properly understand the various astronomical coordinate systems that play a role in the pointing system. This is represented on Fig. V.2. In this complicated cartoon, the celestial sphere is shown as the outermost circle. For our purposes, a location in the sky is represented by a pair of spherical coordinates on this unit sphere, the right ascension (RA) and declination (DEC). The vernal equinox is shown as our zero for RA and DEC, and corresponds to one of the two nodes at the intersection of the celestial equator and the ecliptic plane. In yellow, a sample guide star is shown, with its RA and DEC coordinates.

Our payload is arbitrarily placed on the inside sphere which represents the Earth.

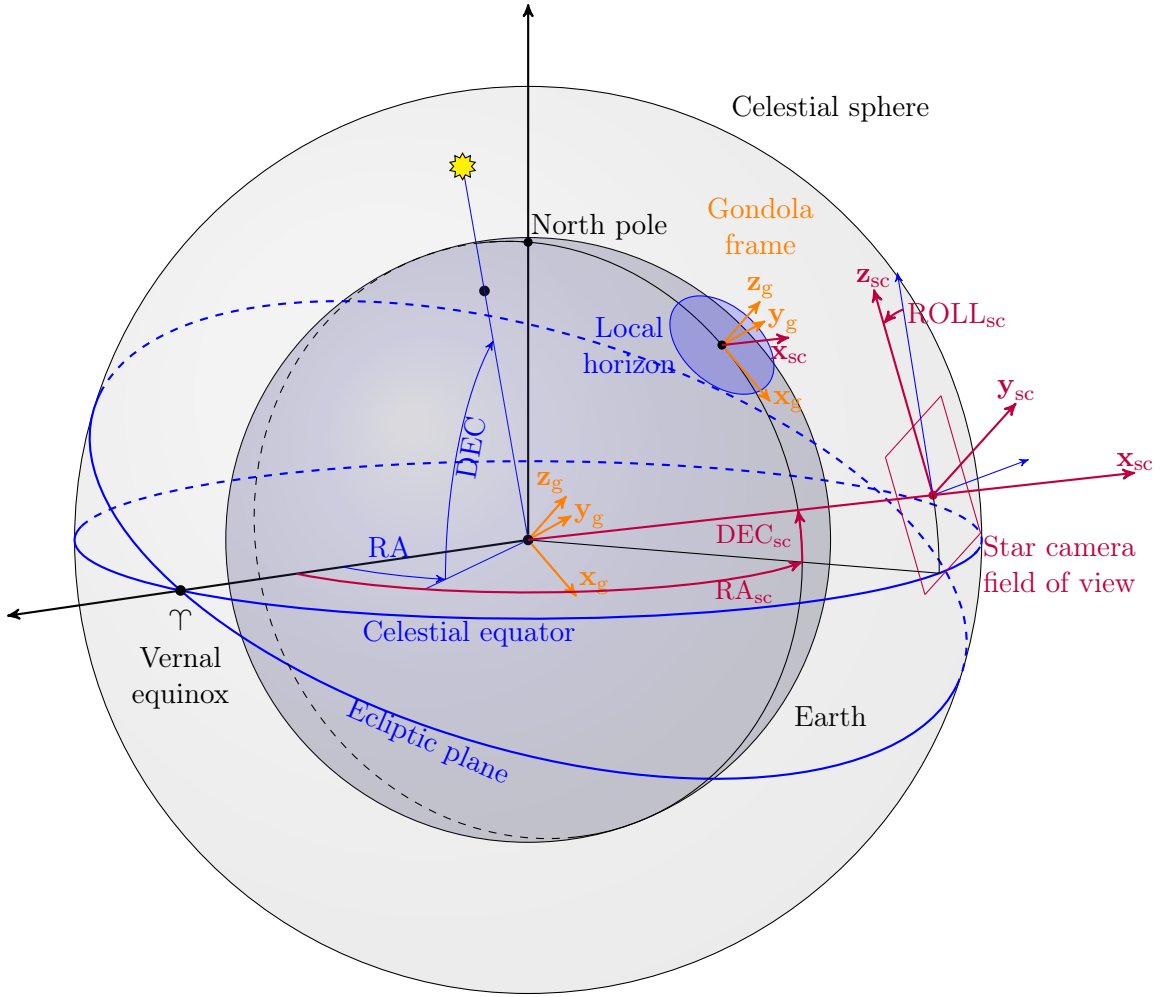


FIGURE V.2: Gondola and star camera frames on the celestial sphere (see text for details).

The gondola/gyroscope coordinate system is shown, as well as the local horizon, which corresponds to the tangent plane at our location. The boresight vector of the star camera, \mathbf{x}_{sc} is also shown. To properly define the relevant pointing angles, however, we need to consider that the observer is always located at the center of this sphere, so we translated the gyroscope reference frame to the center of the celestial sphere. Here, for clarity, we increased the size of the star camera boresight vector, to show its intersection with the celestial sphere. The star camera field of view is represented as a rectangle, and the rest of the star camera axes are drawn as well. The star camera measured the celestial coordinates

of its boresight vector, RA_{sc} and DEC_{sc} , as well as the Roll angle of its field of view with respect to the local meridian.

The telescope reference frame is omitted from Fig. V.2 for clarity. Once the star camera determines its orientation, the orientation of the gyroscope reference frame, gondola and telescope can be calculated. The error signal which is relevant to the control system is the measure of the distance (in terms of local spherical coordinates: elevation $\Delta\phi_{\text{El}}$ and cross-Elevation $\Delta\phi_{\times\text{El}}$) between our current telescope reference frame boresight coordinates and the chosen target position on the sky (see Fig. V.3). The goal of the control system is to minimize this vector. Nominally, the error in elevation is corrected by moving the siderostats about the optical axis. The cross-elevation error is corrected by moving the entire payload in azimuth.

A more detailed illustration of the high-level pointing strategy is offered in Fig. V.4. In this picture, we now show the point of view of the payload with its local horizon plane. The same yellow star is shown for reference to the previous figure. In this particular configuration, the payload determines its orientation with the star camera, and calculates a correction in local azimuth and desired local elevation, ϕ_{Az} and ϕ_{El} . Note that the azimuth does not refer to any particular cardinal direction. For us, the azimuth angle is simply the angle between our \mathbf{x}_g vector and its desired position when the telescope points at the target.

V.1.1.3 Control architecture and operating modes

To summarize the previous discussion, the three levels of control that we need are:

1. Coarse control of the entire gondola to within $\pm 15''$ of the target,
2. Fine pointing control of each beam to $1.5''$ r.m.s. at the science detector,

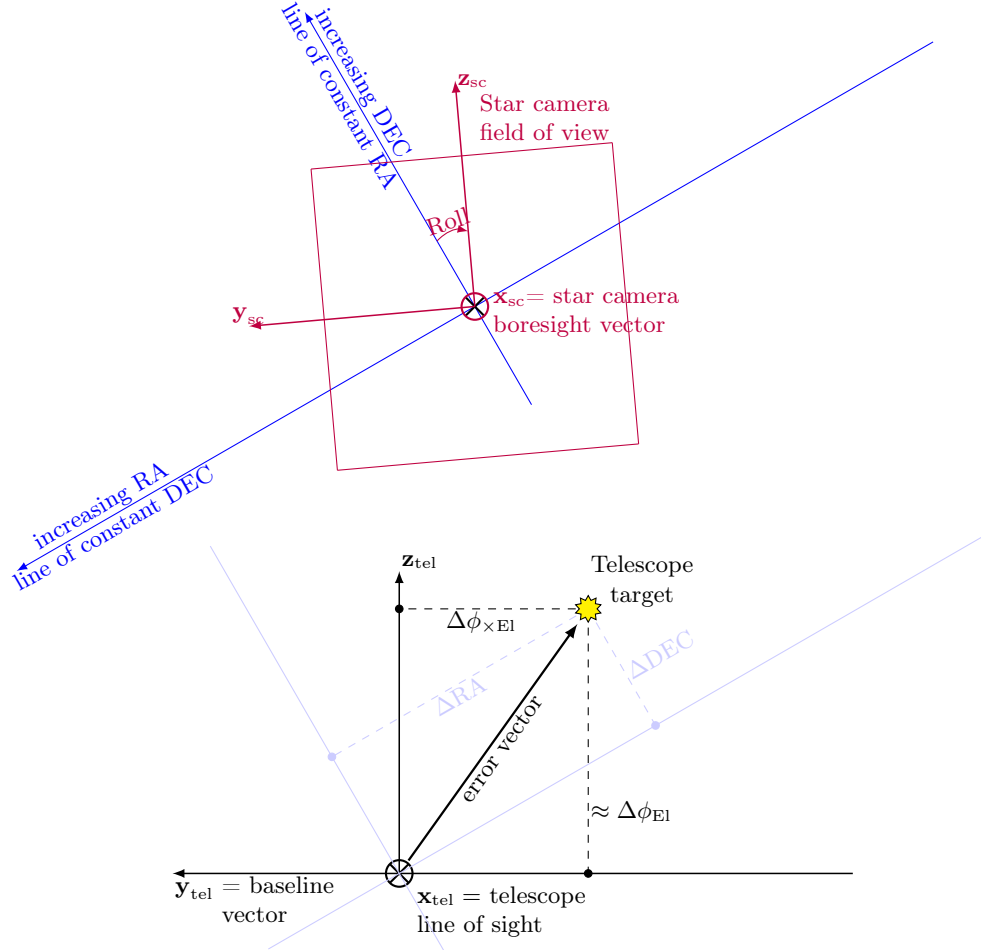


FIGURE V.3: The star camera reference frame (see text for details).

3. Fine knowledge of the inertial attitude to $\approx 0.15''$ r.m.s., followed by appropriate OPD control

Goals 1 and 2 need to be achieved during the flight, while goal 3 needs to be achieved at post-processing, as the OPD information can be corrected provided sufficient amount of information is available.

At its fundamental level, the problem is to implement a system that satisfies these requirements, starting with only the target's location in right ascension (RA) and declination (DEC). Ideally, the system needs to be able to achieve these goals autonomously. All of the operating modes follow from this.

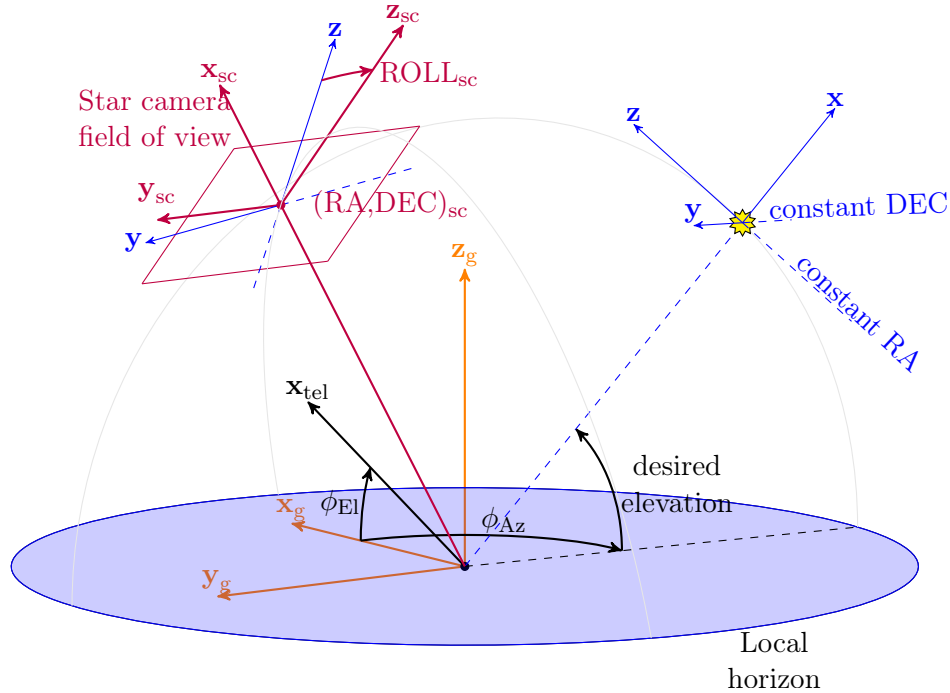


FIGURE V.4: Azimuth and elevation of a target. See text for details

All of the pointing will be done in the reference frame of the gondola, which is tied solidly to the reference frame of the gyroscopes (nominally they are the same) and the star cameras (nominally off by -45° about the y axis). In the following sections, we describe how the inertial attitude of the gondola is determined. Once it is known, a target's RA and DEC can be converted to a desired local azimuth ϕ_{Az} and elevation ϕ_{El} in the spherical coordinates attached to the gondola reference frame (see Fig. V.4). Note that the elevation angle is defined as being zero in the (x_g, y_g) -plane.

Once the turbulence from the ascent has died out, the control system determines where the gondola is currently pointing using the star cameras. For the software to process the star camera image, the payload has to be still to avoid blurring of the stars on the sensor. Hence, the first order of business is to slow down the payload's inertial velocity, which is measured by the gyroscopes. This is also called BRAKE mode.

The first time the system receives a star camera frame and identifies its inertial position, this triggers the estimator algorithm that constantly combines gyroscope and star camera information. From this point on, we have a reasonable estimate of where the gyroscope reference frame is pointed with respect to the inertial frame.

When a new target in RA and DEC is set by the flight computer, the system will enter the SLEW mode. This creates a profile of desired azimuth position and velocity as a function of time. The software commands the reaction wheels to turn the payload about its **z** axis. At the same time, it commands the rotation stages that control the telescopes' elevation, to go to the desired elevation. The control in elevation and control in azimuth are entirely decoupled.

When we complete the deceleration phase as we get close to our target, we switch to TRACK mode. This mode tries to maintain control of the telescope within $\pm 15''$ of our target.

Finally, for each of the two arms, we need to acquire a guide star onto our guide camera (Section V.1.2.8). This requires a fast imaging capability and a fast-steering tip/tilt correction mechanism to freeze the motion of the sky on the guide camera. This is ACQUIRE mode. Two images of the sky are made on the detector, one from each arm; the guide star is located in each image, and the tip/tilt mechanisms are actuated to center this star onto a location of the detector that corresponds to maximum overlap at the science detectors. Once the star is centered onto that location, the window size of the camera decreases, and the acquisition speed increases. Ultimately, we will get two patches of 35×35 pixels at ≈ 50 Hz. When this acquisition speed is reached we consider ourselves in LOCKED mode.

In both ACQUIRE and LOCKED mode, the position of the two tip/tilt platforms contains information on the overall mispointing of the optical train: when the actuators

are both off in the same direction with respect to their nominal position, it means that the entire truss is off the guide star by this amount. When available, this information is used by the estimator along with the gyroscope and star camera information to compute the best possible attitude estimate. Since the tip/tilt is tied to the actual optics train, its information is heavily weighted compared to the other sensors.

When the two guide star images are centered, this means proper overlap of the far-infrared beams at the science detectors. Hence, we are in a position to spot interferometric signal, which will translate to a modulation of the intensity of the coherently combined image as a function of OPD. The OPD is constantly modulated with the Cold Delay Line (Section V.1.2.6), independently of the mode in which we are. However, residual mispointings can create large unwanted OPD perturbations. Hence, during TRACK and ACQUIRE mode, the Warm Delay Line mechanism is activated. Its goal is to use the estimated change in baseline position to predict the resulting OPD variations - and correct them directly in OPD space.

During the LOCKED mode, we need to consider what happens if we lose the guide star. Since the field of view is relatively small compared to the expected motions of the gondola, the guide star could technically walk outside the range of the guide camera - at which point the attitude estimation relies temporarily on the gyroscopes as we switch back to ACQUIRE mode and the guide camera increases its field of view (and decreases its speed) until it finds the guide star.

Note that the Cold Delay Line (CDL) is running in closed loop during all the modes. Since the environment inside the cryostat is not changing from test to flight, there is no reason to ever turn the loop off or keep different sets of gains for different operating modes. The CDL is its own closed system.

The various operating modes will assign different gains for different subsystems, and all modes are summarized in Table V.2. Each actuator has its own PID control loop (see Appendix C for more details about a description of PID control loops).

Mode	Description	Actuators	Sensors
SAFE	All PID gains set to 0; siderostats point towards zenith; azimuth is not commanded; used during ascent, emergencies	– CDL	– Gyros – Star cameras
BRAKE	Used to slow down the payload after undesired motion; derivative gains only, no position loop	– CCMG – Rotators – CDL – Mom. Dump	– Gyros – Star cameras – Elevation encoder – Gimbal encoder
SLEW	Used to move to target with a set velocity profile	– CCMG – Rotators – CDL – Mom. Dump	– Gyros – Star cameras – Elevation encoder – Gimbal encoder
TRACK	Used to stabilize payload after slew, track target coarsely	– CCMG – Rotators – CDL – Mom. Dump – WDL	– Gyros – Star cameras – Elevation encoder – Gimbal encoder
ACQUIRE	The guide camera grabs images for each arm and identifies the location of a guide star in increasingly smaller quadrant sizes	– CCMG – Rotators – CDL – Mom. Dump – WDL – Tip/Tilts	– Gyros – Star cameras – Elevation encoder – Gimbal encoder – Tip/Tilt encoders – Guide camera
LOCKED	The intensity of the target in the science detector is measured, and the central phase is estimated	– CCMG – Rotators – CDL – Mom. Dump – WDL – Tip/Tilts	– Gyros – Star cameras – Elevation encoder – Gimbal encoder – Tip/Tilt encoders – Guide camera – Science detector

TABLE V.2: BETTII operating modes.

V.1.2 Subsystems

Multiple actuator and sensing subsystems are mentioned in the previous section. They are summarized in Table V.2, and each discussed in more detail in this section.

V.1.2.1 Gyroscopes

We purchased three SRS-2000 fiber-optic gyroscopes from Optolink. This gyroscope technology uses the Sagnac effect and is the cutting edge in inertial rotational velocity measurements (for a review of the state-of-the-art see, *e.g.* El Badaoui et al., 2014). We chose these devices for their incredibly low angular random walk, which is a measure of their inherent noise. If we were to trust the gyroscope measurement and integrate its velocity to obtain a position estimate, the estimation error we would make after 1 hour of integration has a standard deviation of about 2 arcseconds.

The devices have a bandwidth of 50 Hz, but can be triggered at up to 2000 Hz. Their extreme stability is contingent upon proper temperature stabilization, which is done with a closed-loop set at their calibration temperature of $23.5\text{ }^{\circ}\text{C} \pm 0.5\text{ }^{\circ}\text{C}$ using an active built-in Peltier element. This Peltier element transforms electric power into either heating or cooling (Peltier, 1834).

The three single-axis gyroscopes are assembled in an orthogonal mount configuration shown in Fig. V.5. In the following, we describe how we measure the various properties of the gyroscopes, and discuss how they compare to the specifications. The gyroscopes' sensitivity has complicated some of their testing. As soon as we attach a gyroscope to any structure, it measures its vibrational modes, which makes it hard to make a stable measurement of the gyroscope's drift stability. This includes the vibrations that are inherent to the building in which they are placed.

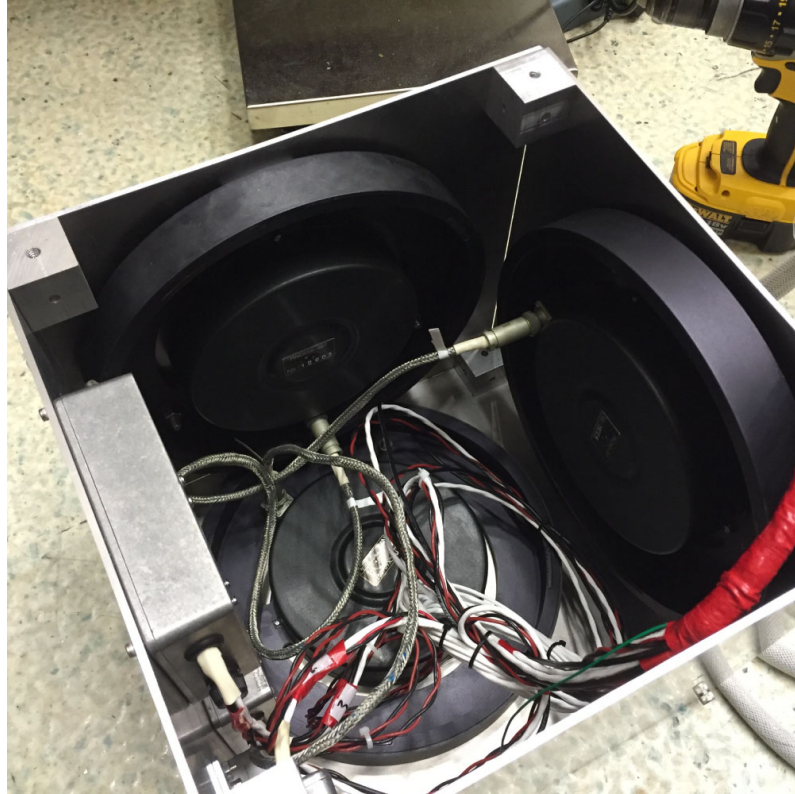


FIGURE V.5: Three single-axis Fiber Optic Gyroscopes are mounted in an orthogonal assembly and attached to the truss.

We were successful at measuring the gyroscope properties over long periods of time by attaching them flush to a heavy slab of metal, and putting the slab of metal flush on the vibration-isolating floor of one of NASA Goddard's optics labs in building 34.

We proceeded to an identical series of tests for each gyroscope:

1. We acquired data at 2000 Hz for 10 min to measure a proper power spectral density and characterize the noise;
2. We acquired data at 100 Hz for ~ 8 h to study the drift properties.

The properties that we are looking for are typical instantaneous angular random walk, and the overall drift instability of the gyroscope's mean. When the gyroscopes are set on the floor, they measure a component of the Earth's rotation vector in inertial space.

The mean of the measurement depends on the exact angle at which the device is placed with respect to the zenith vector, and is of no importance for this noise study. We seek to understand how much the mean varies over long periods of time. To avoid disturbances from the building vibrations (opening/closing of doors, etc), we operated entirely after regular working hours.

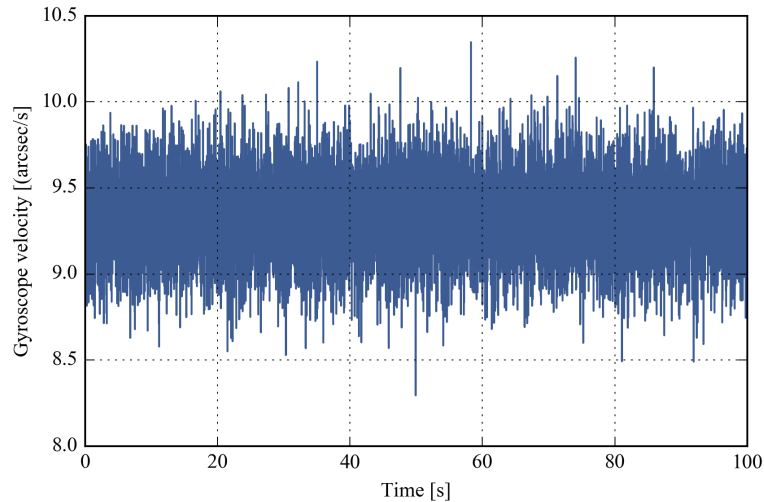


FIGURE V.6: Snapshot of 100 s of gyroscope data, taken from our 8 h data sample.

The angular random walk (ARW) is a measure of the effects of integrating a noisy velocity measurement. The specification from the manufacturer is $\text{ARW} = 5 \times 10^{-4} \text{ deg h}^{-0.5}$. This means that if we integrate the gyroscope's rate for 1 hour, the $1 - \sigma$ uncertainty on our position would be $5 \times 10^{-4} \text{ deg} \sim 1.8''$. For an integration time of 1 second, it would be $0.03''$. For a single integration time step $\Delta t = 10 \text{ ms}$, it would be $0.003''$.

The manufacturer specification gives a maximum bias instability over a wide range of temperatures less than 0.005 deg h^{-1} . This represents how much the mean angular velocity is expected to vary. These tests are an attempt to verify these numbers.

V.1.2.1.a Power spectral density

The usual frequency-domain analysis tool is the power spectral density (PSD). This allows us to spot any frequency peaks in the data, and let us look at the $1/f$ noise behavior, which is the typical low-frequency behavior that indicates drifts in the signal. The 100 Hz data is all we need, as the gyroscope's bandwidth is 50 Hz. Hence, the 2000 Hz data does not contain any more information than the 100 Hz. In fact, while plotting the PSD of the 2000 Hz data, we can see clearly the break at 50 Hz characteristic of a 50 Hz low-pass filter.

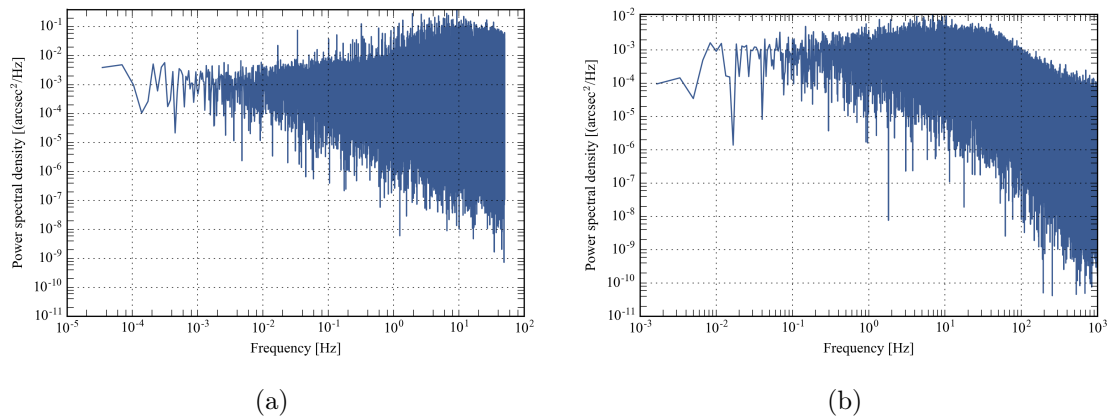


FIGURE V.7: (a): Single-sided power spectral density for gyro 11005, an 8 h sample with a sampling rate of 100 Hz, showing no particular feature (large peaks or resonances). (b): Single-sided power spectral density for gyro 11005, a 10 min sample with a sampling rate of 2000 Hz, showing no electronic resonance peak or other feature. We can notice the -3 dB break at around 50 Hz.

It is important to note that in their factory settings, the gyroscopes' noise distribution was not normal at all. It exhibited electronic peaks with many harmonics, at frequencies that were varying as a function of the gyroscope inclination (as it was measuring different components of the Earth's rotation). After talking to the manufacturer, we determined that it was caused by the closed-loop algorithms inside the gyroscope electronics. The problem was known by them, and the remedy was to inject a random phase

perturbation in the closed loop. This had the effects to get rid of those frequency peaks, at the cost of increasing the overall noise variance by a factor of 4. The noise levels that are specified by the company are very close to the noise seen when using that random phase modulation. Hence, if one does not care as much at the frequency content of the gyroscope, it is possible that this device could work even much better than it does for us.

V.1.2.1.b Normality tests

We ran a few standard normality tests on chunks of the 8-hour data for each gyroscope. While the tests on individual small chunks of data never reject the null hypothesis (that the distribution is normal), the distribution of the total 8 hours does with a very high probability, using both the Anderson-Darling and the Kolmogorov-Smirnov test. It means that it is extremely unlikely that the measured noise over 8 h is coming from a normal distribution.

Since the data is always consistent with being normally distributed over timescales of tens of minutes, after close inspection of the long-term quartile plots and histograms, we determined that it would be safe to consider the distribution as normal for the purpose of our attitude estimator (see Fig. V.8).

V.1.2.1.c Allan variance

Another common tool to study of the gyroscope's performance is to plot the Allan variance. The Allan variance gives a time-domain analysis of the gyroscope's noise that is complementary to the power spectral density, by plotting the variance (or standard deviation) between the means of clusters of data over various lengths. On the Allan deviation plots shown for our gyroscopes in Fig. V.9, the angular random walk (ARW) can be measured

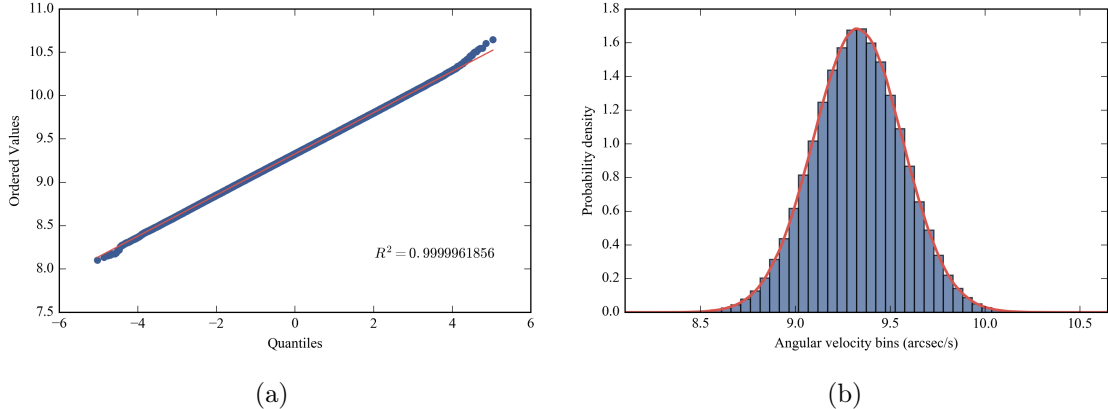


FIGURE V.8: Normality analysis of the gyroscope signal over 8 h of data taken at 100 Hz. (a): Normal quantile-quantile plot for an 8 h sample with a sampling rate at 100 Hz. Here the measured quantiles (fraction of the measured values under a certain value) are plotted against the theoretical quantiles from a normal distribution. The red line is the theoretical distribution if the data were taken from a normal distribution. (b): Probability density distribution for an 8 h sample with a sampling rate at 100 Hz. In red, the theoretical normal distribution we obtain with the measured mean and standard deviation from the sample. While the data is not strictly normally distributed, we consider that it is sufficiently close to a gaussian distribution.

as the deviation at 1 s cluster interval, and the bias drift measured as the deviation for 10 000 s cluster interval.

TABLE V.3: Gyroscope properties

Measured property	Gyro #11005	Gyro #12003	Gyro #12004
Standard deviation (deg h^{-1})	0.237	0.199	0.217
Angular random walk ($\text{deg h}^{-0.5}$)	4.31×10^{-4}	3.79×10^{-4}	4.02×10^{-4}
Bias instability (deg h^{-1})	3.11×10^{-4}	1.8×10^{-3}	3.05×10^{-4}

Notes: Properties of the gyroscopes determined from the Allan variance analysis on an 8 h sample with a sampling rate at 100 Hz. Note that $1 \text{ deg h}^{-1} = 1 \text{ arcsec s}^{-1}$, and the Earth rotates at about 15 arcsec s^{-1} about the line joining the two poles.

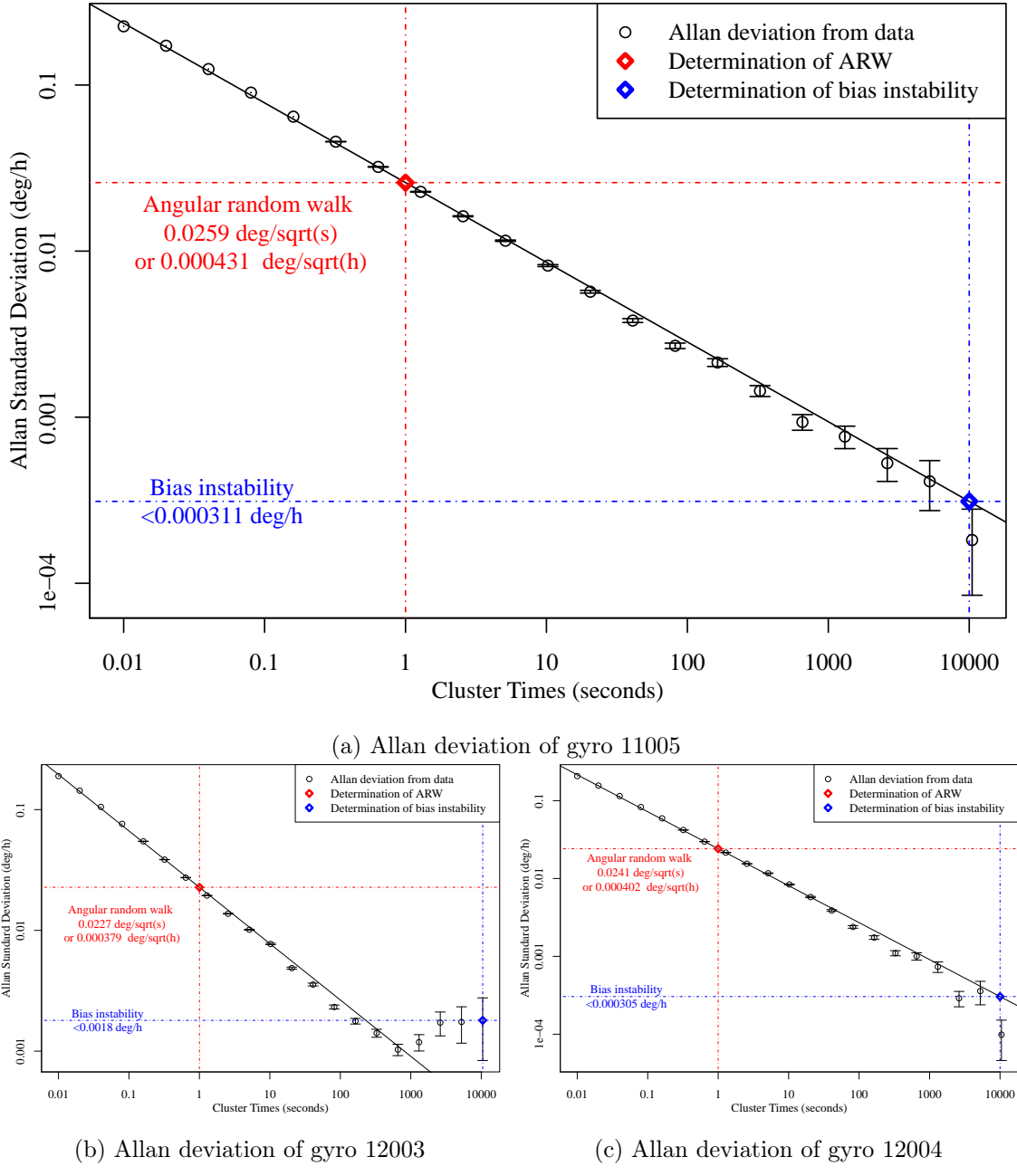


FIGURE V.9: Allan deviation plots

V.1.2.2 Star cameras

V.1.2.2.a Design

We have designed, built and tested a custom star camera setup that provides higher accuracy measurements than commercially available devices. An image of our assembly is

shown in Fig. V.10. Our collaborators from Cardiff University provided the star camera software, which solves for the inertial orientation from a given picture. This software is a C++ set of routines that was originally developed for the EBEX balloon experiment (Oxley et al., 2004).

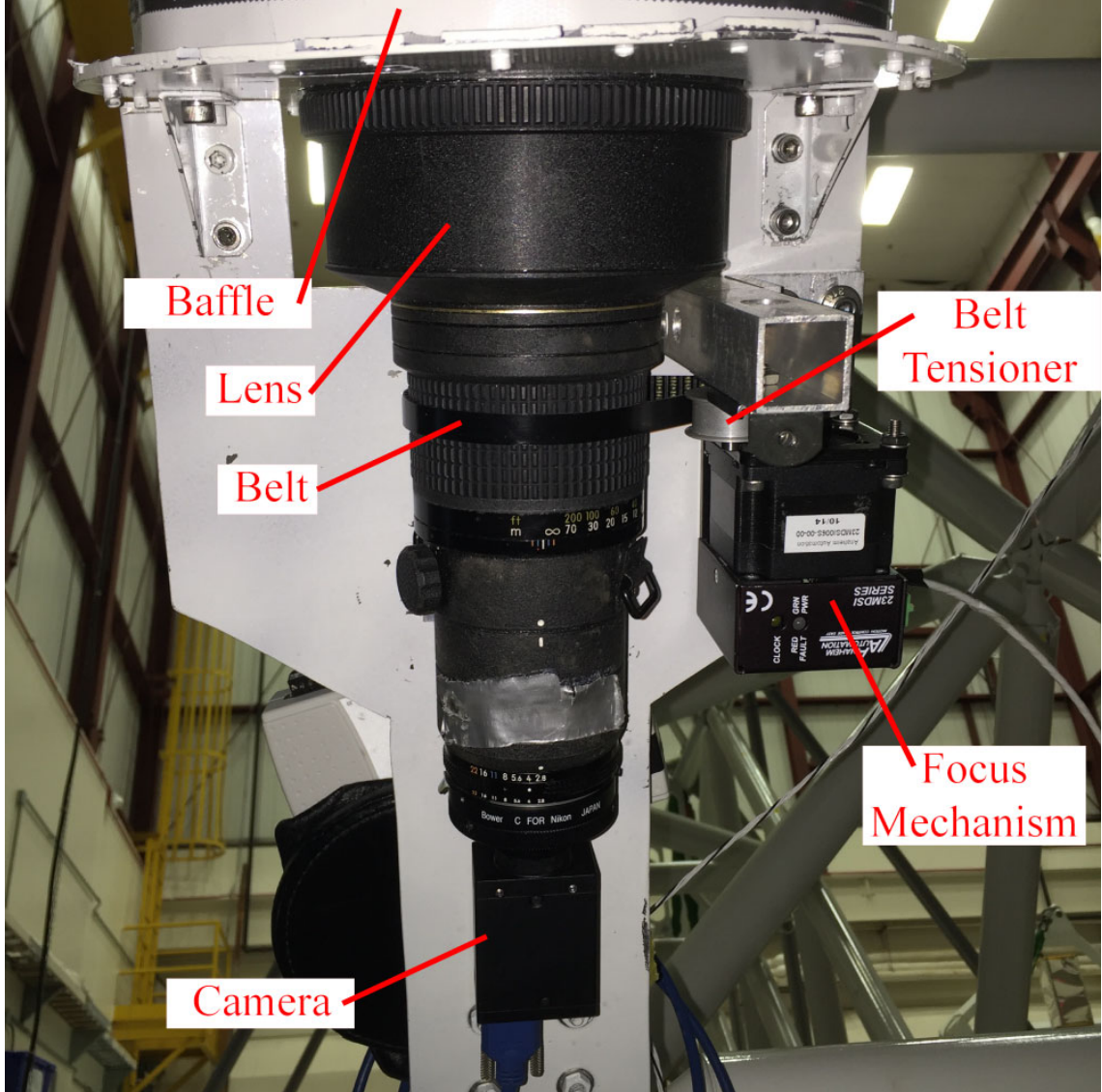


FIGURE V.10: Star camera assembly.

Our star camera design features an old Nikon Nikkor 300 mm f/2.8 telefocal lens with manual focus and extended hood. These lenses were manufactured between 1977 and 1982 and can be found today online through websites like e-Bay. The lens provides

low chromatic aberration, a magnification of $688'' \text{ mm}^{-1}$, a wide field of view ($\approx 10^\circ$) and a collecting area of 90 mm^2 which is larger than most star tracking assemblies. This old lens does not feature a built-in autofocus or any of the image stabilization actuators commonly found in modern lens assemblies: these could have become a liability in the severe balloon environment.

Our camera is a USB3.0 Point Grey Grasshopper3. The sensor is a Sony Pregius IMX174 CMOS sensor with 1920×1200 pixels at $5.86 \mu\text{m}$ pitch. This provides a field of view of $2.14^\circ \times 1.34^\circ$ and a pixel scale of $4.02''/\text{pixel}$. It features a very convenient Linux-compatible software suite which works with all the Point Grey camera products, and leaves room for future potential upgrades of the camera. The detector characteristics are summarized in Table V.4.

TABLE V.4: Star camera properties

Property	Value	Description
Quantum efficiency at 525 nm (%)	76	Fraction of incoming photons that create signal
Read noise (electrons)	6.83	Error made when reading the pixel's value
Absolute sensitivity threshold (photons)	9.77	Minimum number of photons required to get a SNR = 1 on a pixel
Well depth (electrons)	32 513	Maximum number of electrons a pixel can store

We have successfully cycled the camera in the environmental chamber all the way until the camera's internal thermometer indicated a temperature of -80°C , and it continued operating nominally.

V.1.2.2.b Focusing strategy

Focusing the camera could be required at float due to the change in temperatures that could create a shift of the focal plane. We implemented our own autofocus mechanism, a

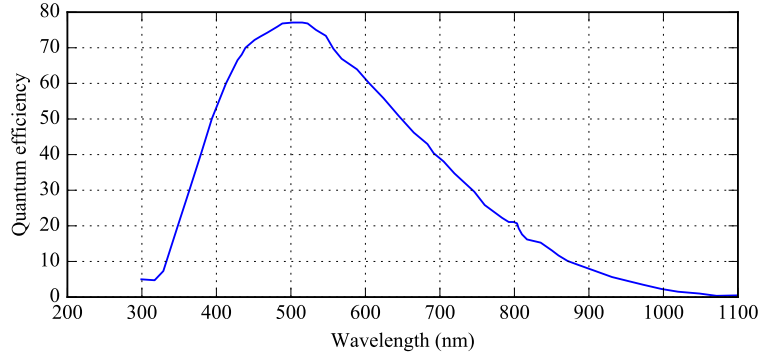


FIGURE V.11: Quantum efficiency of star camera sensor.

belt is attached between the lens' focus ring and a stepper motor. When the stepper motor turns, it turns the focus ring. We tested this very simple configuration in our environmental chamber only to realize that the belt was loosing grip when the temperature was too cold. To fix this problem, we added a spring-based belt tensioner which adds $\approx 10\text{ N}$ of force to the belt.

At cold temperature and low pressure, we noted that the glass in the lens began to exhibit radial cracks, presumably caused by the CTE difference between the steel housing and the glass material. These cracks don't noticeably affect image quality, but of course they could cause the glass to shatter if they become too large. Hence, it was decided to maintain the outside temperature of the lens above 0°C at all times during flight.

V.1.2.3 Azimuth control

The Compensated Controlled Moment Gyros (CCMG) is a system with two counter-rotating reaction wheels on a gimbal that we use to control our azimuth, designed and built by E. Gorman's group at NASA GSFC. It features multiple encoders and motors. First, there is a brushless DC motor that spins each wheel, with a relative 13-bit encoder

that monitors where the wheel is in its rotation. Second, there is a Beckhoff AS1050 stepper motor that controls the wheels' shaft angle. On the gimbal, there is a 13-bit absolute magnetic encoder that measures the angle of the wheels from some reference. We use the latter to know where the gimbal is positioned at all times. Hard stops prevent the wheels from moving far past $\pm 90^\circ$ from their nominal position.

The motion controller that we use to monitor the wheel's speed is a brushless-DC Galil Motion controller DMC-4020. It reads out the wheel encoders and controls the current to the wheels accordingly. It directly and independently implements the closed-loop system of the wheels, including all of the gains, acceleration/deceleration, and jogging speeds associated with the desired motion.

The motion controller was modified to accept an external clock pulse in order to synchronize the wheels' motion with our master clock signal. It requires a clock pulse at 1.024 kHz, and deviations from this value will require changing some of the gains - it is our understanding that the controller internally uses a nominal 1.024 kHz crystal oscillator to generate its time basis, as some of the gains and parameters to the controller can directly be entered as, for example, "steps per second".

At power-up, the wheels immediately start accelerating to their cruising speed of 3000 rpm. They take about 10 minutes to reach their target. The wheels' frequency is set for the entire duration of the flight.

The gimbal is controlled with another Galil Motion controller, a 2-axis stepper driver DMC-4020, which is synchronized with an external clock. Only one axis is used for the CCMG, while the second axis is used by the momentum dump motor (see section V.1.2.4). The controller operates in micro-stepping mode and has a very smooth response, in contrast to previous controllers we tested which create a lot of vibrations. The controller is set

always to use 64 micro-steps per step, and the motor is a Phytron VSS200 with 200 steps per revolution. The motor is outfitted with a Beckhoff AG1000 planetary gearhead with a 3.7:1 reduction ratio. The gearbox itself has a ratio of 25, which creates a total gear ratio of 92.5. Hence, a 360° revolution of the stepper corresponds to $360/92.5 = 3.9^\circ$ motion of the shaft.

In practice, all of the control is done using the regular stepper motor encoder. The magnetic encoder is used for limit-checking and to feed back to the momentum dump mechanism. With this in mind, we can now relate the control signal (stepper motor micro-steps per second) to the physical torque that the wheels provide.

$$\Delta\theta_{[\text{rad}]} = \frac{2\pi}{92.5 \times 200 \times 64} \Delta(\text{micro-steps}) \quad (\text{V.1})$$

$$\sim 5.3 \times 10^{-6} \Delta(\text{micro-steps}) \quad (\text{V.2})$$

$$\Delta\theta_{[{}'']} \sim 1.09 \Delta(\text{micro-steps}) \quad (\text{V.3})$$

At 3000 rpm, the CCMG has a total stored momentum $M_{\text{CCMG}} = 20.8 \text{ N m s}$. Of course, depending on the orientation of the wheels, the momentum along the **z** axis is only the projection of this momentum vector,

$$M_{\text{CCMG},z[\text{N m s}]} = 20.8 \sin \theta, \quad (\text{V.4})$$

where $\theta_{[\text{rad}]}$ is the angle between the horizontal axis and the rotation axis of the wheels. This makes sense: when the wheels are horizontal, there is no momentum projected on the **z** axis because the rotation vectors of the wheels are orthogonal to **z**. When the rotation axes are aligned with **z**, we have the maximum momentum.

The torque \mathcal{T}_{CCMG} is the variation of the momentum with time. So we can write:

$$\mathcal{T}_{CCMG}[\text{N m}] = \frac{d}{dt} M_{CCMG,z} \quad (\text{V.5})$$

$$\mathcal{T}_{CCMG}[\text{N m}] = 20.8 \times \dot{\theta}_{[\text{rad s}^{-1}]} \cos \theta \quad (\text{V.6})$$

$$= 1.1 \times 10^{-4} \times n_{[\text{micro-step s}^{-1}]} \cos \theta \quad (\text{V.7})$$

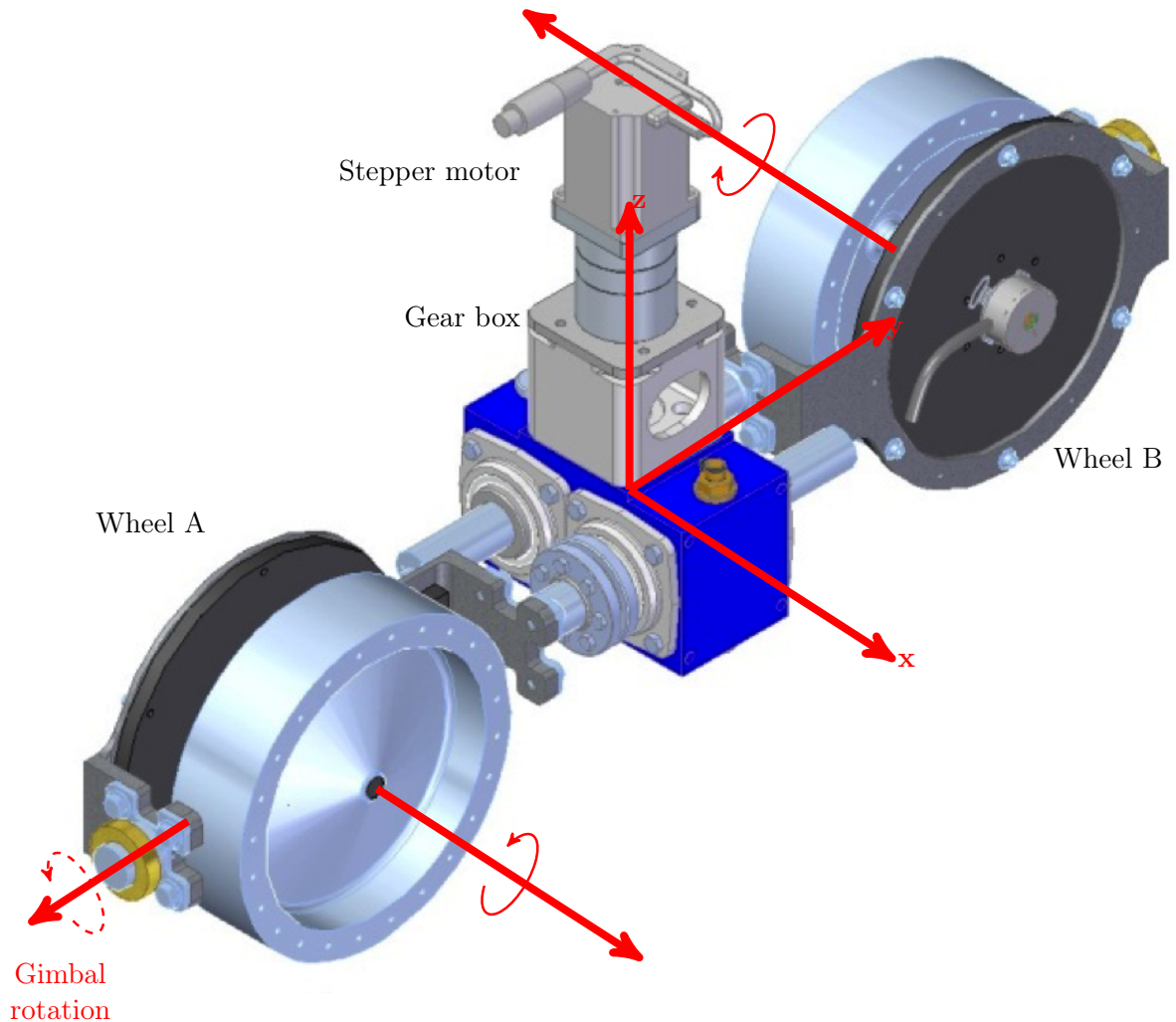


FIGURE V.12: CAD rendering of the CCMG design.

The entire CCMG assembly was tested in a vacuum chamber at cold temperatures.

Several heaters are strategically located in the assembly to allow some thermal control for

all the electronics in case issues arise.

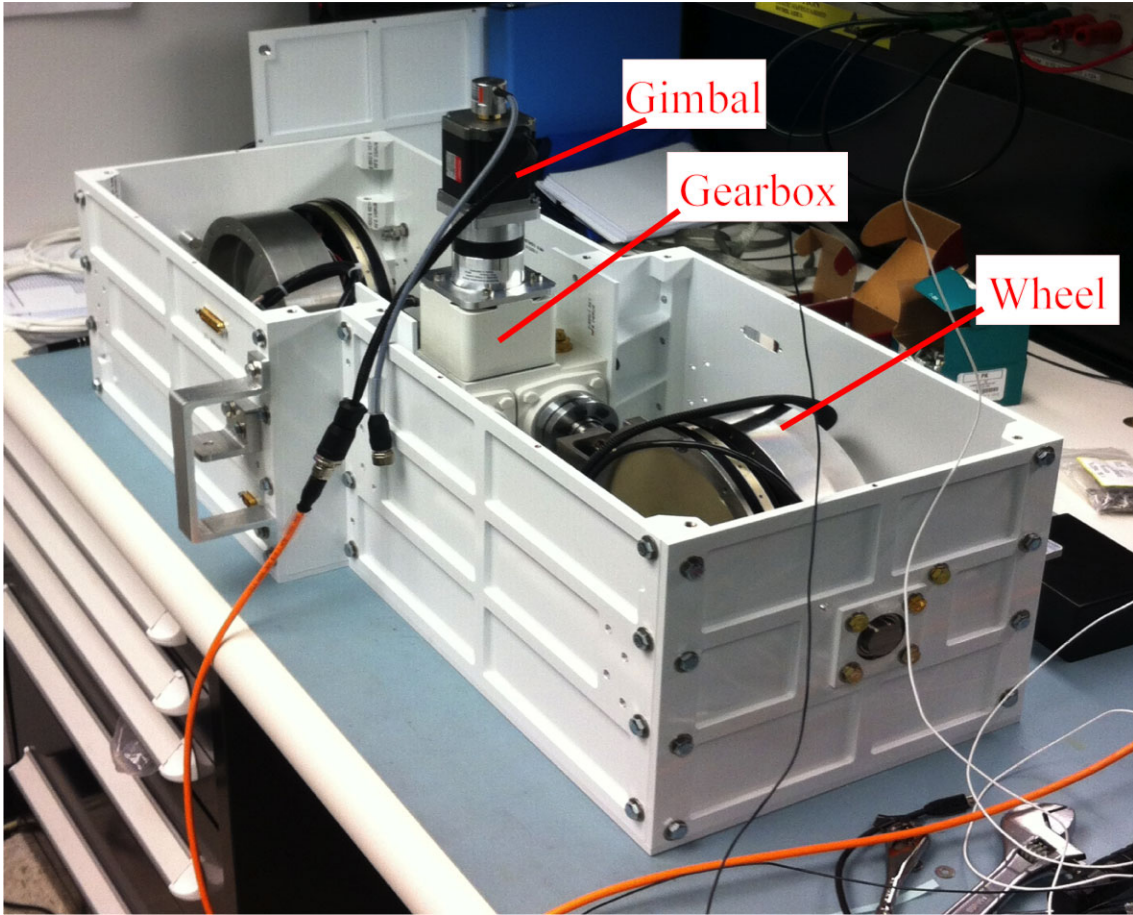


FIGURE V.13: Compensated controlled moment gyros during testing.

V.1.2.4 Momentum dump mechanism

The momentum management strategy consists of using the balloon as a large momentum reservoir. The control system then needs to be equipped with a system that allows a transfer of momentum between the gondola and the balloon, which are connected through the parachute and ladder.

For this purpose, BETTII uses a design which has successfully flown on previous balloon payload (Fig. V.14), with several improvements over its predecessors. It consists of a steel and titanium setup which will make the junction between the bottom of the

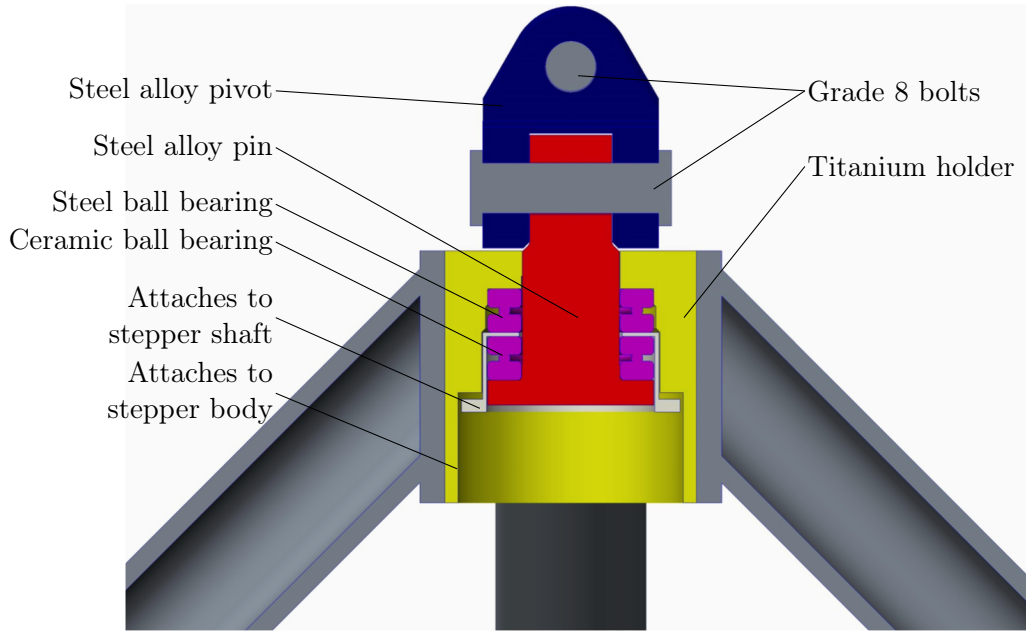


FIGURE V.14: Cross-section of the momentum dump mechanism in an earlier version of the design.

balloon train (at the very bottom of the ladder) and the very top of the gondola. The critical material is an alloy of steel that has been heat treated and is particularly strong. The setup consists essentially of a pivot and a pin made with this alloy, connected together with grade 8 bolts. The top of the pin is attached to the pivot, and has a lip at the bottom on which two circular bearings are stacked: the bottom one uses ceramic balls (for their excellent friction properties and long lifetime), and the top one uses steel balls (for their excellent strength). Between the two bearings, there is a metal holder that extends all the way down below the pin. On top of the steel bearing, a titanium case sits, which attaches to the entire gondola.

The momentum dump mechanism is a simple rotary stepper motor. Its housing attaches to the steel case of the assembly - while its shaft attaches to the metal holder between the two bearings. With an assembly like this, when a vertical upward force is exerted, the gondola's weight pushes on the bearings, which then push onto the pin's lip.

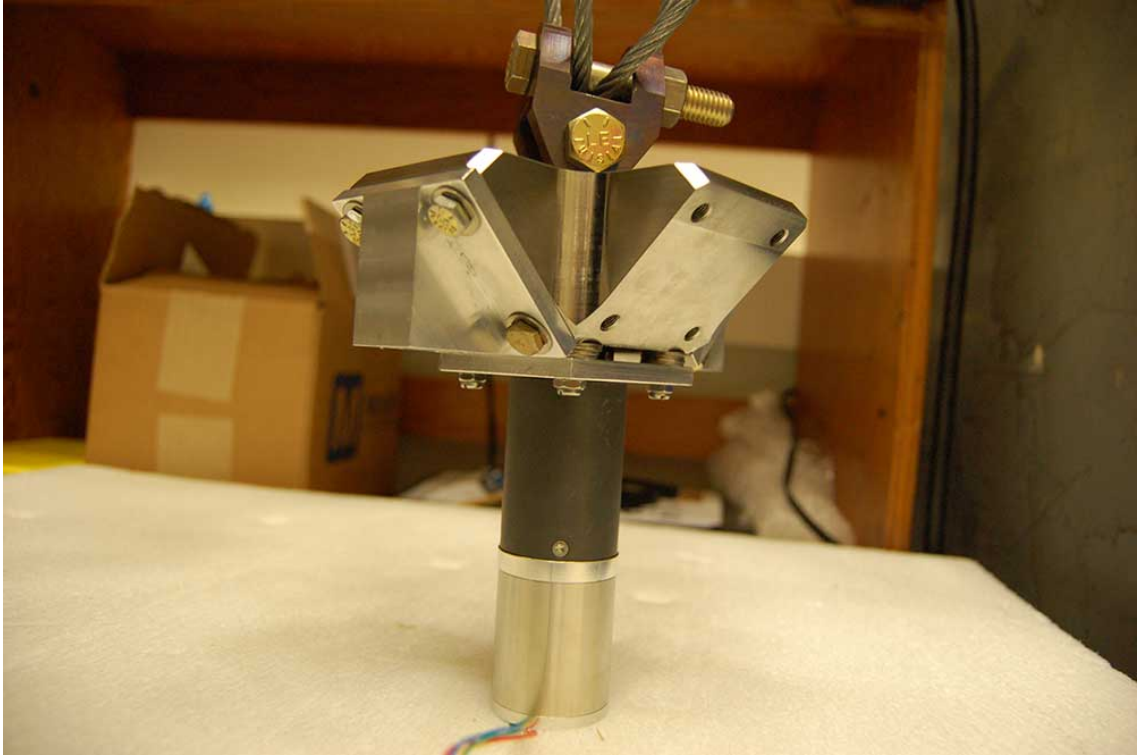


FIGURE V.15: Momentum dump mechanism that was actually built, with a cross-section which is very close to Fig. V.14.

When the stepper motor starts spinning, it spins only the top part of the bottom bearing, and the bottom part of the top bearing: the friction force that this exerts allows to slowly dump momentum into the pin, hence into the balloon train.

Given that the entire weight of the payload rests on the two bearings and the pin's bottom lip, this can be hazardous during descent when the parachutes open and the payload can experience up to a 10 g vertical load. Hence, this piece of the assembly needs to be thoroughly tested and certified before launch.

In practice, the momentum unloading happens quite slowly due to the very low friction of the bearing. As the stepper turns the bearing, it slowly turns the entire train along with the pivot for a few tens of seconds. When the train has experienced sufficient twist, it then unfurls and gives a slight kick in the opposite direction.

The momentum dump mechanism has not been tested in the environmental chamber

- however, the stepper motor was rated for vacuum and extreme environments. One of the big unknowns is the value of the bearings' friction coefficients in the balloon environment. When powered, the stepper motor dissipates quite a large amount of heat, which will help maintain the whole assembly to a reasonable temperature.

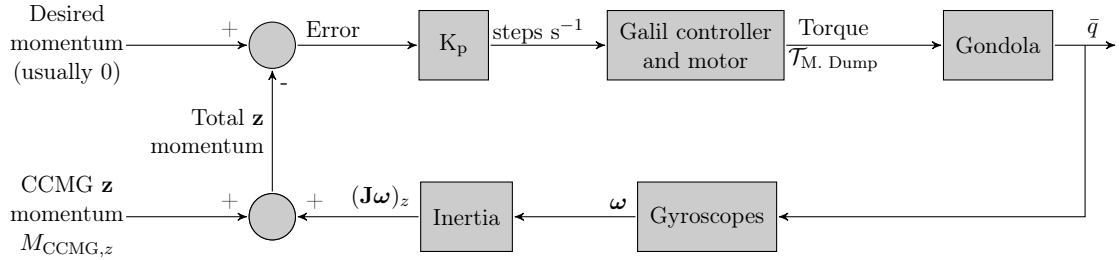


FIGURE V.16: Momentum dump control loop.

V.1.2.5 Elevation control

When put in terms of ground-based telescopes, BETTII is fundamentally an Alt-Az telescope: to reach a target, it has to move in azimuth, and in elevation (also called *altitude*). Instead of moving the entire payload in elevation, which would have conserved the optical setup constant for all targets, we chose to move only the siderostats for increased reliability. We paid one cost: as the siderostat cover different elevations, the fields rotate on the detector in opposite directions in the two arms. So as the elevation changes, an active compensation needs to happen, which is done with a third rotation mechanism located downstream.

These rotation mechanisms have multiple requirements: they need to operate at 90° from the gravity axis; they need to operate well at -40 °C; they need to have an inner clearance to let our 2.5 cm beam through; they need to be able to support many kilograms of cantilevered mass; and they need to have a precise encoder that allows not only smooth

motion, but also accurate knowledge of the elevation angle. Griffin Motion LLC makes an industrial rotator that satisfies all of these conditions (Fig. V.17).

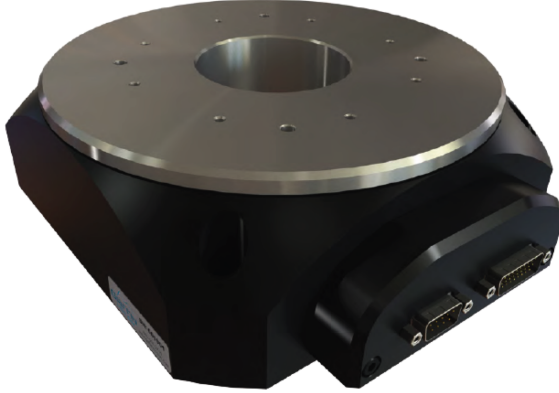


FIGURE V.17: Rotation stages from Griffin Motion LLC.

These are industrial-grade brushless DC rotators. They are controlled by a three-axis Galil Motion controller DMC-4030 with sinusoidal drives. The requirement for sinusoidal drives as opposed to pulsewidth-modulated (PWM) drives stemmed from the fact that these motors were going to be 5 m away from their controller at the end of each arm, and we wanted to avoid creating electromagnetic noise by having high-frequency pulses going through such a large distance. The rotary encoder is a RENISHAW RESOLUTE absolute encoder with 26 bit resolution, which corresponds to a $0.019''$ angular resolution. However, the controller ignores the two bits of lowest significance, effectively giving a 24 bit resolution, corresponding to a $0.08''$ angular resolution.

An old version of these rotation stages was tested in our environmental chamber, but not under load. These devices are rated to operate nominally down to -40°C , but because of their self-heating, we do not expect that they will reach that temperature. During our cold tests of the device, we noted that the friction seemed to change, which required a re-adjustment of the PID coefficients inside the Galil controller. Given that only

the encoder has been changed between the old and new generation of rotation stages, we expect a similar behavior. We have the capability to change the PID gains of all systems during flight.

V.1.2.6 Delay lines

We have designed, built and tested two linear mechanisms that change the OPD on BET-TII: the Cold Delay Line (CDL) and the Warm Delay Line (WDL). Both of these mechanisms have optics attached to them and have been briefly discussed in Chapter III. The rationale behind using two delay lines requires some explanation. First, we realized that we had two very different problems to solve in terms of OPD. One was to produce a periodic, very repetitive modulation to produce our interferograms. This requires very small range, high bandwidth. This was originally set out to be a cryogenic mechanism for symmetry reasons, and the team used a heritage design from the FIRAS delay line mechanism, using titanium flexures, voicecoil actuators, and capacitive sensors to close the PID loop. The design, fabrication, and procurement of this delay line was already underway when we realized that we needed significantly more range to tackle the second problem: the variation of OPD due to geometrical pointing errors. With the pendulum modes of balloon payloads extending to multiple arcminutes, and the large lever arm given by our baseline length, excursions in OPD can be considerable. In addition, we learned from our optical design that we had to introduce an asymmetry in the system to properly overlap the polarizations within the pupils, which most easily was achieved by having a 4-mirror set in one arm and a 3-mirror set in the other. We then decided that given the required difference in dynamic range of the two requirements and the maturity of the CDL, to implement a second delay line, the WDL, also based on voicecoil actuators and capacitive sensors. This device does

not have any requirement to be operated at cryogenic temperatures, so we chose to have it operate at ambient temperature.

V.1.2.7 Tip/tilt

Our tip/tilt mechanisms are Physik Instrumente S330 piezo-electric actuators that move a flat platform in tip and tilt. We attach a mirror to that platform, and put that mirror close to a pupil of the optical system, to correct for angular errors without creating beam walk (e.g. in the K-mirror assembly, see Fig.V.18). After long discussions with the company's engineers, we ordered a custom strain gauge sensor especially tune and tested to resist low temperatures: this sensor tells the angle of the platform, which is important for our control system. Similar devices have been successfully used on sounding rocket before to provide milli-arcsecond angular control (Mendillo et al., 2012).

The piezo-electric driver electronics provide the required 100 V to operate the platform, and amplify 10 times an analog 0-10 V command signal. Despite its broad range of motion (≈ 10 mrad), they can still operate at multiple hundred Hz bandwidth, even with a mirror load on top of the platform. The resonant frequency of the structure under load, which needs to be avoided at all costs to avoid severe damage, is at more than 2 kHz, way beyond the frequency at which we need to command the device.

The platform can be controlled in open-loop mode, where there is a simple gain between the command and the voltage applied to the piezo crystals. However, we baseline the closed-loop mode during flight. In this configuration, the electronics close the loop using the strain gauge sensor and the command corresponds to an angle rather than simply a voltage. The drawbacks of the closed-loop mode are a slightly decreased bandwidth and overall range of motion. In case more range is needed during flight, it is possible to switch

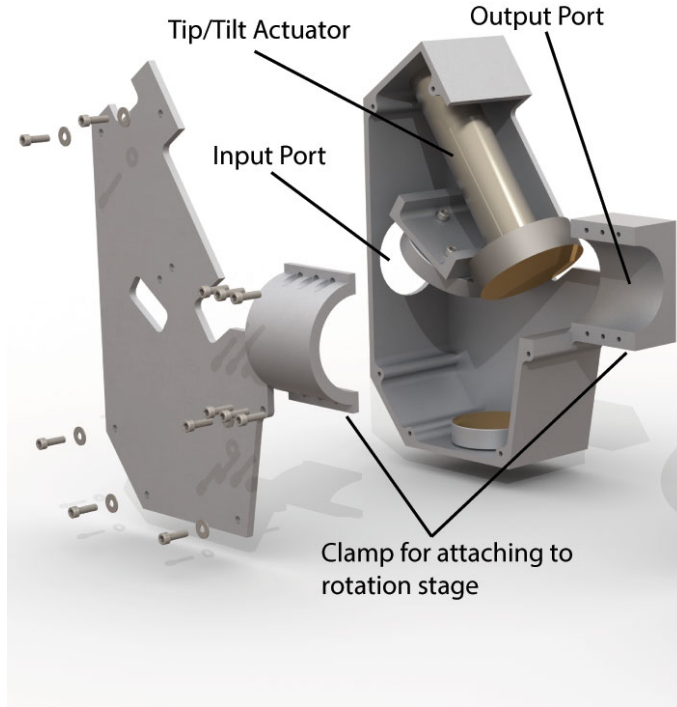


FIGURE V.18: K-mirror assembly model with a piezoelectric tip/tilt actuator.

back to open-loop mode.

V.1.2.8 Fine guidance sensor

The fine guidance sensor is a HAWAII-1RG detector from Teledyne with 1024×1024 pixels that is sensitive to infrared wavelengths between $1\text{ }\mu\text{m}$ and $2.5\text{ }\mu\text{m}$. The plate scale is $0.6''\text{s}^{-1}$. The device will be operated at a cryogenic temperature of 77 K , at which the expected read noise is 18 electrons r.m.s. The readout is accomplished using a San Diego State University GENIII (Leach et al., 1994) controller. The readout scheme accommodates simultaneous read of two windows on the array, one for each arm of the interferometer. The software can switch window size quickly, hence accommodating our ACQUIRE mode needs.

The centroid of a guide star in each window is determined, and the error between this

centroid and a pre-registered location on the sensor is fed back to the tip/tilt actuators after proper rotation, to ensure overlap of the two beams in the science channels. The amount of correction required by the tip/tilt actuators to overlap the two beams is then used by the attitude estimator and converted to an overall baseline error.

V.1.2.9 Clocks and timing

Synchronization of the sensors and actuators are of prime importance for our payload. As an interferometer, we are extremely sensitive to vibrations which could be injected in our system by the motors. While everything was designed to maintain a very good symmetry, slight differences in the inertias or mass distribution of the reaction wheels, for example, could create a beat frequency that would be noticeable in our science data. The existence of multiple clocks, each with their own slight temperature-dependent drift, can dramatically complicate the proper retrieval of the data.

To avoid future complications, all BETTII actuators and sensors are slaved to one single 50 MHz master clock, or an integer divider of that master clock. The cascade of the various clock dividers meets at the common value of 124 800, which corresponds precisely to 2.496 ms. This is BETTII's heartbeat. Hence, 124 800 master clock ticks correspond to the elementary cycle of all critical processes:

- The CDL moves of one single step
- The fine guidance sensor reads one single frame
- The science detector reads one single frame
- The CCMG wheel position about its axis is checked and a correction is applied.

A diagram of all the clocks in the system is shown in Fig. V.19.

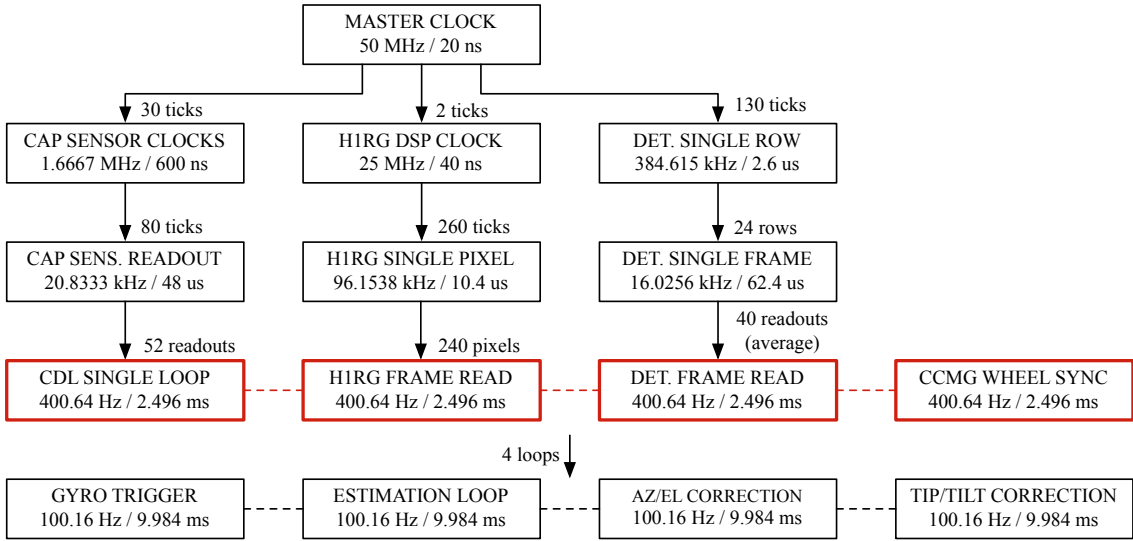


FIGURE V.19: BETTII's clocks are all derived from one single master clock.
The heartbeat at 2.496 ms is highlighted in red.

The advantage of this strategy can be illustrated as follows. The time it takes for a wheel to complete a revolution is set to be an integer multiple of this heartbeat, $998\,400 = 124\,800 \times 8$ master clock ticks (about 50 revolutions per second). Hence, every 8 heartbeats, each wheel is supposed to be in the same position, and it will be controlled 8 times during one revolution to make sure it is. This completely locks in their relative velocities, on average. Let's suppose now that in their 8th position, a mechanical defect in the wheel or the bearing triggers a small vibration. This vibration will occur at a frequency which is locked with respect to our science data, such that we will see its effects every 8 data samples. In the case where these clocks are not synchronized and would unpredictably drift with respect to each other, a perturbation that occurs every 8th of a revolution has repercussions not exactly at every 8 data samples. If we think about this in the frequency domain, it means that the power peak caused by the vibration is now broadened, whereas it is very sharp in the synchronized case.

The attitude control and sensing occurs every 4 heartbeats, which corresponds to ≈ 100.16 Hz. In the rest of this discussion, we will always refer to this frequency as being at

100 Hz for simplicity of notation - but it is important to remember that it is in fact derived from the master clock.

V.1.2.10 Computers

TABLE V.5: BETTII on-board computers.

Name	Description & tasks
<i>boopFPGA</i>	<ul style="list-style-type: none"> • Generate 50 MHz master clock • Generate all other system clocks derived from master clock • Trigger all sensors • Read sensors: gyroscopes, galil controllers, <i>ford</i> at 100 Hz • Send actuator commands at 100 Hz • Implement hardware protection (limit, overdrive, etc)
<i>boopRT</i>	<ul style="list-style-type: none"> • Collects all sensors from <i>boopFPGA</i> and estimate the inertial attitude and velocity • Create proper commands to all actuators and sends them to <i>boopFPGA</i> • Manages operating modes (see Section V.1.1.3) • Manages FIFOs and communication channels with <i>ford</i>
<i>ford</i>	<ul style="list-style-type: none"> • Processes star camera frames to determine attitude • Processes science detector frames • Processes fine guidance sensor frames • Handles communication with the ground (through the CIP) and from/to <i>boop</i> • Automatically applies observing plan if no commands from the ground: send targets to <i>boopRT</i>

BETTII will have two on-board computers (see also Fig. V.20):

1. a computer which operates a real-time Linux kernel will be used to store all the date, process the up/down telemetry, acquire star camera images, solve for inertial attitude, and process the science detector and H1RG frames. This computer is named *ford*.
2. an FPGA and real-time computer from National Instruments to process the sensor input/outputs, implement the attitude estimation, and synchronize all the control loops. This computer is named *boop*. This is the brain of the control system.

ford is an Adlink Extreme Rugged Express-IBR 3517UE with a dual-core i7 CPU and 4 GB of ECC (Error Checking and Correction) memory. The ECC memory is helpful in mitigating some of the side effects of cosmic ray hits on the memory chips. The computer has a low power consumption, which allows it to function with a simple radiator instead of a fan. *ford* has been successfully tested at in the environmental chamber, and the temperatures of its cores under maximum CPU stress have been monitored over long periods of time.

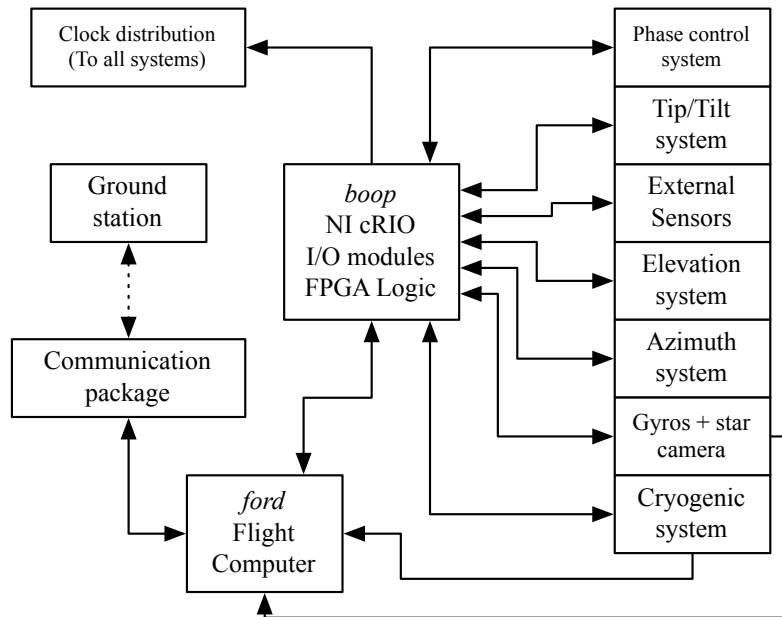


FIGURE V.20: Relationships and communications channels between the various subsystems, from Rizzo et al. (2014).

boop is a National Instrument cRIO- system. It features a reprogrammable FPGA chip in addition to a dual-core real-time operating system. NI LabView is the software interface to the system. *boop* will generate and distribute BETTII's master clock signal at 50 MHz.

The various relationships and communications channels between the subsystems is shown in the diagram on Fig. V.20.

V.1.3 Software architecture

A diagram showing the flow of the main loop of the control software is shown in Fig. V.21.

This loop is operated at a nominal frequency of 100 Hz, which is the speed at which we read out the gyroscopes and issue new commands to the control system. The star camera, as well as other absolute sensors are being processed by the Real time software, and appropriately propagated since they often correspond to a measurement that was taken some number of loops ago. Using a robust synchronization scheme slaved to our system's master clock, we can align the various pieces of information with very high accuracy.

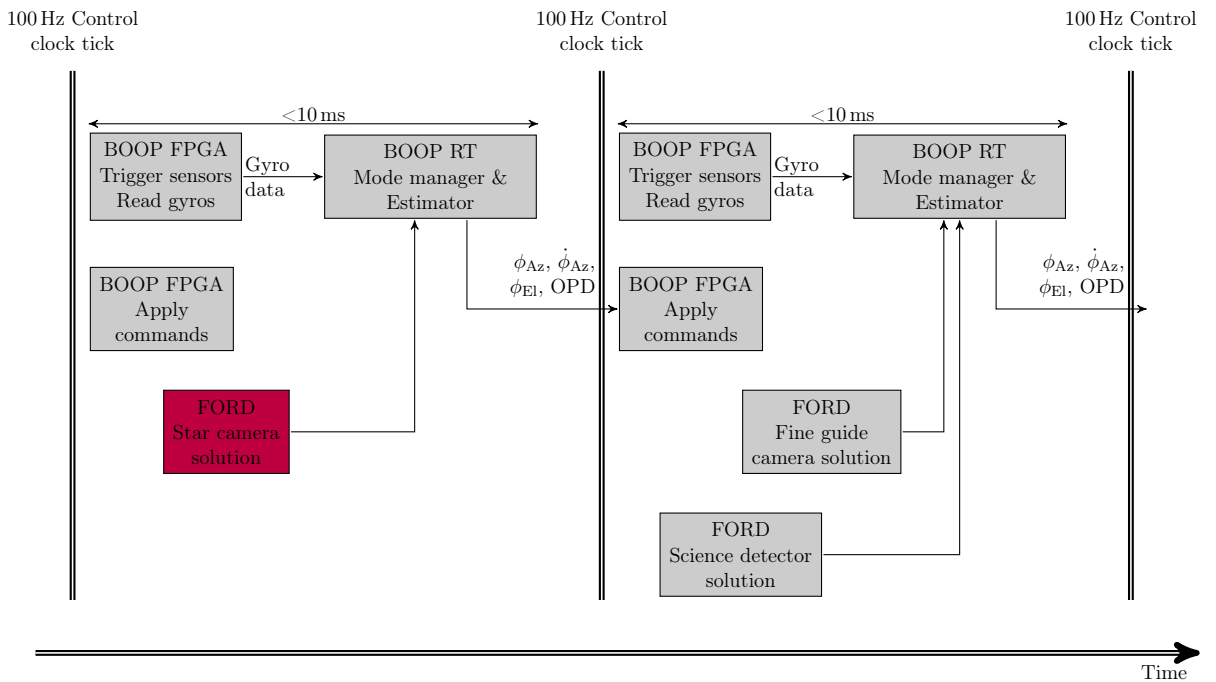


FIGURE V.21: Two loops of the main control software. Right at each clock tick, the gyros are triggered in *boop* FPGA and read out. Once the sensors are triggered and read out, it triggers the loop in *boop* RT, which has then less than 10 ms to complete and send new commands back to the *boop* FPGA. These commands are not applied by the actuators until the next clock tick. This has the advantage to completely lock all moving parts of our payload to our heartbeat. The commands sent are using information from exactly 1 loop ago. This constant lag is preferred, as opposed to a scenario where the commands are applied as soon as possible, which would lead a variable lag which would depend on the processing time within *boop* RT.

V.1.4 Controls architecture summary

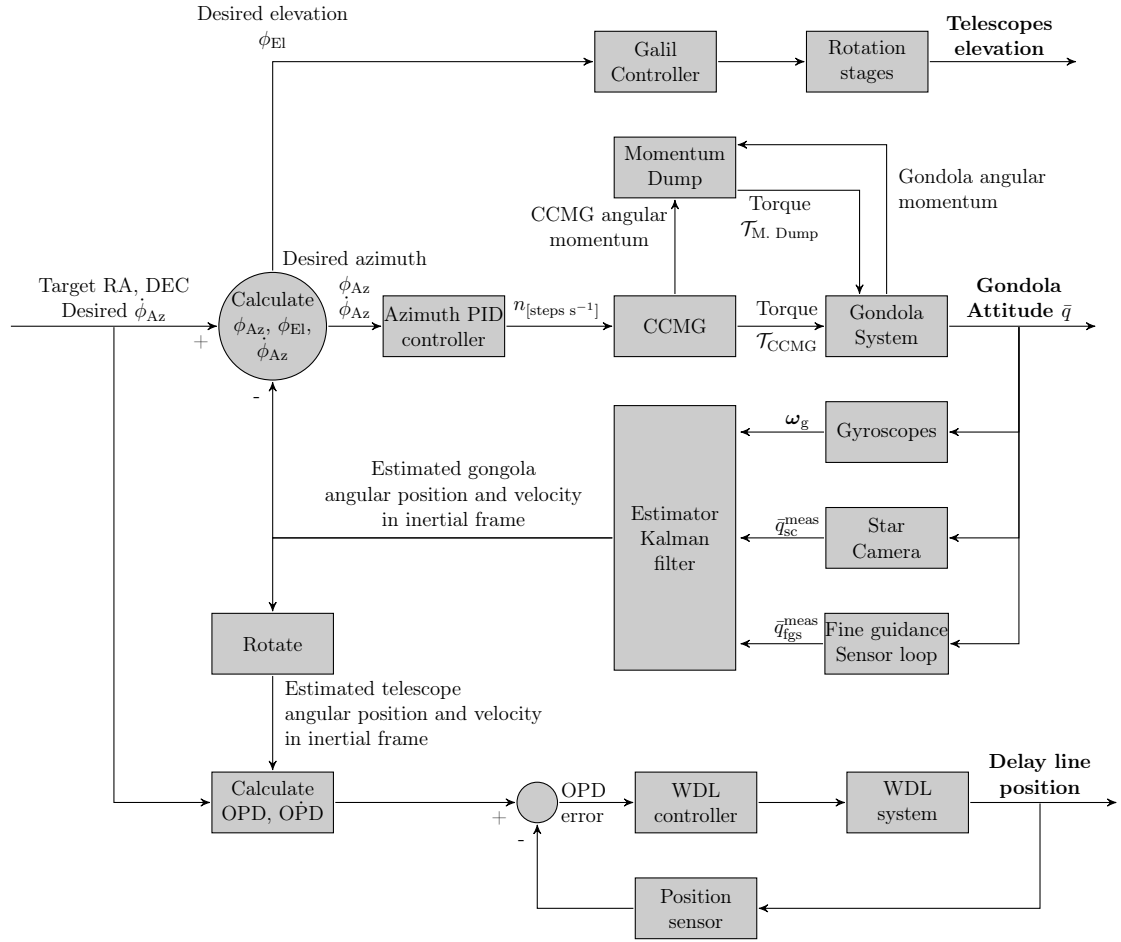


FIGURE V.22: Control system architecture

To summarize our entire strategy, we show the control diagram in Fig. V.22. This diagram shows both the estimation loop as well as the actuation loop, although it omits several aspects for clarity: first, the fine guidance sensor loop has its own PID loop using the H1RG sensor and two tip/tilt mirrors, and only sends back the common-mode errors in azimuth and elevation, from which we can compute \bar{q}_{fgs}^{meas} ; and second, the cold delay line constantly works in its own closed-loop system, with a pre-determined position and velocity profile.

V.2 3D attitude estimation and sensor fusion

The attitude estimation consists of combining high-frequency angular velocity measurements of the payload with low-frequency attitude measurements. The high-frequency measurements, usually from gyroscopes, are relative measurements, and exhibit biases. The attitude measurements are absolute. The Kalman filter (Kalman, 1960) combines these two types of measurements in a mathematical formalism that uses a model of the physical relationship between them. For the simplest version of this filter, the goal is to estimate the bias of the high-frequency measurements, hence providing bias-corrected, drift-less, trustworthy dynamical information that can be used to estimate the attitude at all times, even when there is no absolute measurement. In the general sense, the filter finds the state parameters that minimize the covariance of the error between a predicted quantity (in our case, the predicted attitude from integrated gyroscope velocities), and a measured quantity (in our case, an absolute attitude measurement from the star cameras).

This filter is very common for spacecraft attitude and control, although a large number of variations exist. It continues to be an active field of research today (e.g., Crassidis et al., 2011; Markley et al., 2014). Under certain circumstances and assumptions, the Kalman filter is the optimal filter, which means that it is the filter that has the fastest possible convergence towards the minimum steady-state error covariance.

One of the complexities of the Kalman filter is that it involves inverting matrices to find the optimal solution when new absolute measurements are received. This has implications in terms of numerical complexity which often will limit the bandwidth of the filter, especially in the context of resource-limited FPGA computers on spacecraft. In practice the trade-off is the following: either limit the bandwidth of the filter, or limit the

number of state parameters (*i.e.* limit the rank of the matrix to invert). On the ground, this limitation is usually not an issue. But even our powerful embedded computer will be limited in the speed at which it can find solutions.

In order to set up the Kalman filter, we choose quaternions to describe our attitude, which are discussed extensively and compared to other attitude representations in Appendix B. In addition to the various advantages explained in this appendix, quaternions have a nice behavior when it comes to small angles, so we can use them in their linear, small angle approximation to create a *multiplicative, extended* Kalman filter (MEKF) (Lefferts et al., 1982). It is *extended* because it operates in the small angle approximation, hence it is a local approximation of a non-linear relationship. And it is *multiplicative*, instead of being additive, because we use the quaternion multiplication operation to describe the "difference" or error between measured and predicted attitudes. One popular instance where this filter was successfully implemented on board the WMAP spacecraft (Harman, 2005).

First, we need to choose a representation for our sensor suite: the gyroscopes and the star cameras. Second, we describe the equations that govern the physics of our system and connect the sensors together: this is critical for the Kalman filter to produce robust estimates, and the more accurate our representation is, the more accurate our predictions can be. Third, we discuss the Kalman setup, and two phases of the algorithm: prediction and update. And finally, we discuss potential improvements of the filter that can be used for ground-based analysis of the data.

V.2.1 Sensor models

This section describes the chosen mathematical model that will be used to represent our sensors. These are necessarily approximations, as they do not encompass all of the possible physical effects that will be observed. The residual, non-modeled physical effects need to be small with respect to this representation in order for this filter to work optimally. In the ideal case, when all physical contributors are accounted for, and when the residual noises have a normal distribution, the Kalman filter is the optimal filter.

V.2.1.1 Gyroscope model

For our baseline design, the gyroscope model that we use is: $\boldsymbol{\omega}^{\text{meas}} = \boldsymbol{\omega} + \mathbf{b} + \mathbf{n}_g$, where $\boldsymbol{\omega}^{\text{meas}}$ is the measured angular velocity vector, $\boldsymbol{\omega}$ is the true angular velocity vector, \mathbf{b} is the bias vector, and \mathbf{n}_g is the angular velocity noise vector (also called the "rate noise"). This implies that we have ideal alignment between each gyroscope and what we define to be the gyroscope reference frame. We consider that \mathbf{n}_g is a white noise process with a diagonal covariance matrix $\mathbf{N}_g = \sigma_{c,g}^2 \mathbf{I}_{3 \times 3}$.

We consider that the derivative of the bias \mathbf{b} is also a white noise process: $\dot{\mathbf{b}} = \mathbf{n}_b$, where \mathbf{n}_b has a diagonal covariance matrix $\mathbf{N}_b = \sigma_{c,b}^2 \mathbf{I}_{3 \times 3}$.

Assuming that the covariance matrices are diagonal help to set up the filter, but is not a necessary assumption in the general case. The following implementation is not relying on this assumption.

The angular random walk (ARW) that we measure is $\text{ARW} \approx 5 \times 10^{-4} \text{ deg h}^{-1}$. This means that if we integrate the gyroscope's rate for 1 hour, the 1σ uncertainty on our position would be $5 \times 10^{-4} \text{ deg} \sim 1.8''$. For an integration time of 1 second, it would be $0.03''$. For a single integration time step $\Delta t = 0.01 \text{ s}$, it would be $0.003''$.

The units required for σ_g are [rad s $^{-0.5}$], so we convert:

$$\sigma_{g[\text{rad s}^{-0.5}]} = \frac{\pi}{60 \times 180} \times \text{ARW}_{[\text{deg h}^{-0.5}]} \sim 1.5 \times 10^{-7} \text{ rad s}^{-0.5}. \quad (\text{V.8})$$

Note that we can relate the ARW to the measured discrete rate noise uncertainty

$\sigma(\mathbf{n}_g^{\text{meas}})$ with:

$$\sigma(\mathbf{n}_g^{\text{meas}})_{[\text{deg s}^{-1}]} = \text{ARW}_{[\text{deg h}^{-0.5}]} \times 60 \sqrt{\text{BW}_{[\text{Hz}]}} , \quad (\text{V.9})$$

where $\text{BW}_{[\text{Hz}]}$ is the gyroscope's bandwidth, equal to 50 Hz for our system. We obtain a quantity close to the measured quantity, $\sigma(\mathbf{n}_g^{\text{meas}}) \sim 0.2 \text{ arcsec s}^{-1}$.

The bias instability units are [rad s $^{-3/2}$]. We adopt the manufacturer's specification for a worst-case scenario bias instability over a wide range of temperatures equal to 0.005 deg h $^{-1}$. This is for a bandwidth of 50 Hz, so we obtain the bias instability term, which also corresponds to the process noise of our Kalman filter:

$$\sigma_b_{[\text{rad s}^{-3/2}]} = 0.005 \text{ deg h}^{-1} \times \sqrt{\text{BW}_{[\text{Hz}]}} \sim 1.8 \times 10^{-7} \text{ rad s}^{-3/2}. \quad (\text{V.10})$$

This represents how much what we are trying to estimate is expected to vary. While this drift appears to be very slow, it increases linearly with time (as opposed to the ARW which increases as the square root of the time). Hence, the bias drift quickly increases the position uncertainty when integrating the gyroscopes, which justifies the efforts in trying to properly estimate its properties and correct for it as often as possible.

V.2.1.2 Star camera model

The star camera takes a picture of the sky to make noisy measurements of the right ascension (RA) and declination (DEC) of the boresight, as well as the roll angle (ROLL) in which the frame is taken. The RA and DEC typically are much more accurate than the roll angle. Each angle can be used as an Euler angle to define the attitude of the payload in the inertial frame (or equivalently, the rotation from the inertial frame to the current attitude). Each angle corresponds to a quaternion rotation about a single axis:

$$\bar{q}_{\text{RA}} = [0, 0, \sin(\text{RA}/2), \cos(\text{RA}/2)]^T, \quad (\text{V.11})$$

$$\bar{q}_{\text{DEC}} = [0, \sin(\text{DEC}/2), 0, \cos(\text{DEC}/2)]^T, \quad (\text{V.12})$$

$$\bar{q}_{\text{ROLL}} = [\sin(\text{ROLL}/2), 0, 0, \cos(\text{ROLL}/2)]^T, \quad (\text{V.13})$$

$$\bar{q}_{\text{sc}}^{\text{meas}} = \bar{q}_{\text{ROLL}} \bar{q}_{\text{DEC}} \bar{q}_{\text{RA}}. \quad (\text{V.14})$$

The errors associated with the three Euler angles are assumed to be a random vector \mathbf{n}^{SC} , also with a diagonal covariance matrix \mathbf{R} . Typical star camera noises are $1\text{-}2''$ in RA and DEC and $100''$ r.m.s. in ROLL (see Chapter VI).

The star camera is oriented at a fixed position on the payload, which is not necessarily aligned with the gyroscope reference frame. In that case, the attitude quaternion needs to be rotated by the quaternion representing the transformation between both reference frames. In addition, the covariance matrix needs to be rotated by the direction cosine matrix corresponding to the same transformation. This would not have an effect if the covariance matrix was a multiple of the identity matrix, but it usually is not the case since the Roll measurement is often much less sensitive. This can have implications while

designing the balloon payload and deciding on the placement and orientation of the star camera: the attitude estimation will be less precise about the Roll axis of the star camera.

V.2.2 Continuous state equation and error

We want to use the Kalman filter to obtain an estimate of the attitude quaternion $\bar{q}_k \equiv {}_I^G\bar{q}(t)$, but also use it to estimate the gyroscope biases $\mathbf{b}(t)$ to improve our attitude predictions and lower the errors between predicted and measured. The "state" of our system is described by the vector:

$$\mathbf{x}(t) = \begin{bmatrix} {}_I^G\bar{q}(t) \\ \mathbf{b}(t) \end{bmatrix}. \quad (\text{V.15})$$

The evolution of the state is governed by the two differential equations that follow:

$${}_I^G\dot{\bar{q}}(t) = \frac{1}{2}\boldsymbol{\Omega}(\boldsymbol{\omega}(t)) {}_I^G\bar{q}(t), \quad (\text{V.16})$$

$$\dot{\mathbf{b}}(t) = \mathbf{n}_b(t), \quad (\text{V.17})$$

with $\boldsymbol{\omega} = \boldsymbol{\omega}^{\text{meas}} - \mathbf{b} - \mathbf{n}_g$. These equations represent the exact relationship between our quantities of interest, assuming that the noise values are known. In practice, we will create an *estimator* that is used to evaluate the expected value of these quantities. This estimator, $\hat{\mathbf{x}} = [\hat{\bar{q}}(t), \hat{\mathbf{b}}(t)]^T$, is governed by the following equations:

$${}_I^G\dot{\hat{\bar{q}}}(t) = \frac{1}{2}\boldsymbol{\Omega}(\hat{\boldsymbol{\omega}}(t)) {}_I^G\hat{\bar{q}}(t), \quad (\text{V.18})$$

$$\dot{\hat{\mathbf{b}}}(t) = \mathbf{0}, \quad (\text{V.19})$$

The Kalman filter's goal is to minimize the variance of the estimator's error - that is, the covariance of the error vector $\mathbf{x} - \hat{\mathbf{x}}$. However, in our case, we have constraints in the system since we force the quaternion to be of unit length: this introduces a singularity in the covariance matrix of the error vector, and is prone to numerical complications. It is possible to circumvent this problem by using the multiplicative properties of the quaternion used in the small angle approximation. This is called a "multiplicative" Kalman filter, as opposed to a more traditional "additive" filter.

To do this, instead of following the evolution of the state $\hat{\mathbf{x}}$ itself, we will follow the evolution of the error vector $\tilde{\mathbf{x}} = [\delta\boldsymbol{\theta}, \Delta\mathbf{b}]^T$, where $\delta\boldsymbol{\theta}$ corresponds to the 3-dimensional angular error between true and estimated attitude quaternion taken from the difference quaternion $\overset{G}{\dot{q}} = \overset{G}{q} \otimes \overset{G}{\dot{q}}^{-1} \approx [1, \frac{1}{2}\delta\boldsymbol{\theta}]^T$, and $\Delta\mathbf{b} = \mathbf{b} - \hat{\mathbf{b}}$.

The evolution of $\tilde{\mathbf{x}}$ as a function of time can be obtained by taking the quaternion derivative of the true attitude quaternion $\dot{\bar{q}} = \dot{\delta\bar{q}} \otimes \hat{\bar{q}} + \delta\bar{q} \otimes \dot{\hat{\bar{q}}}$. With our gyroscope model, we can write:

$$\boldsymbol{\omega}^{\text{meas}} = \boldsymbol{\omega} + \mathbf{b} + \mathbf{n}_g, \quad (\text{V.20})$$

$$\hat{\boldsymbol{\omega}} = \boldsymbol{\omega}^{\text{meas}} - \hat{\mathbf{b}}, \quad (\text{V.21})$$

$$\text{so } \boldsymbol{\omega}^{\text{true}} = \hat{\boldsymbol{\omega}} - \mathbf{n}_g - \Delta\mathbf{b}. \quad (\text{V.22})$$

After a lengthy derivation to express $\dot{\delta\boldsymbol{\theta}}$ from $\dot{\delta\bar{q}} = [0, \frac{1}{2}\dot{\delta\boldsymbol{\theta}}]^T$ (Trawny et al., 2005), we obtain:

$$\dot{\delta\boldsymbol{\theta}} = -\hat{\boldsymbol{\omega}} \times \delta\boldsymbol{\theta} - \Delta\mathbf{b} - \mathbf{n}_g. \quad (\text{V.23})$$

Note that the cross-product $\hat{\boldsymbol{\omega}} \times \delta\boldsymbol{\theta}$ is equal to the matrix multiplication $[\hat{\boldsymbol{\omega}}_\times]\delta\boldsymbol{\theta}$, where $[\hat{\boldsymbol{\omega}}_\times]$ is the skew-symmetric matrix made out of the elements of $\hat{\boldsymbol{\omega}}$.

The bias equation is:

$$\dot{\Delta\mathbf{b}} = \dot{\mathbf{b}} - \dot{\hat{\mathbf{b}}} = \mathbf{n}_b. \quad (\text{V.24})$$

We can now write the linearized equations representing the evolution of the error state $\tilde{\mathbf{x}}$:

$$\dot{\tilde{\mathbf{x}}} = \begin{bmatrix} \dot{\delta\boldsymbol{\theta}} \\ \dot{\Delta\mathbf{b}} \end{bmatrix} = \mathbf{F} \begin{bmatrix} \delta\boldsymbol{\theta} \\ \Delta\mathbf{b} \end{bmatrix} + \mathbf{G} \begin{bmatrix} \mathbf{n}_g \\ \mathbf{n}_b \end{bmatrix}, \quad (\text{V.25})$$

with

$$\mathbf{F} = \begin{bmatrix} [\hat{\boldsymbol{\omega}}_\times] & -\mathbf{I}_{3 \times 3} \\ \mathbf{0}_{3 \times 3} & \mathbf{0}_{3 \times 3} \end{bmatrix}, \quad (\text{V.26})$$

and:

$$\mathbf{G} = \begin{bmatrix} -\mathbf{I}_{3 \times 3} & \mathbf{0}_{3 \times 3} \\ \mathbf{0}_{3 \times 3} & \mathbf{I}_{3 \times 3} \end{bmatrix}. \quad (\text{V.27})$$

It is important here to introduce the expression of the propagation error covariance matrix of this continuous representation. Writing the noise vector $\mathbf{n} = \begin{bmatrix} \mathbf{n}_g \\ \mathbf{n}_b \end{bmatrix}$, the covariance matrix is the expected value of the product of two noise vectors taken at different times (Trawny et al., 2005), but since we suppose that the noise samples are independent, the covariance is not a function of this time difference τ :

$$\mathbf{Q}_c = E[\mathbf{n}(t + \tau)\mathbf{n}^T(t)] = \begin{bmatrix} \sigma_{c,g}^2 \mathbf{I}_{3 \times 3} & \mathbf{0}_{3 \times 3} \\ \mathbf{0}_{3 \times 3} & \sigma_{c,b}^2 \mathbf{I}_{3 \times 3} \end{bmatrix}. \quad (\text{V.28})$$

V.2.3 Integration of continuous equations

Since our system has a fast sampling rate compared to the characteristic times of the system, we can consider that \mathbf{F} is constant over a time step in order to express the state evolution in a discrete sense, which is appropriate for a computer implementation. We can integrate the state equation between t_{k-1} and $t_k = t_{k-1} + \Delta t$, which leads to a discrete state transition matrix Φ_k :

$$\Phi_k = \Phi(t_k, t_{k-1}) = \exp(\mathbf{F}\Delta t) \equiv \begin{bmatrix} \Theta_k & \Psi_k \\ \mathbf{0}_{3 \times 3} & \mathbf{I}_{3 \times 3} \end{bmatrix}, \quad (\text{V.29})$$

with $\Theta_k \sim \mathbf{I}_{3 \times 3} - \Delta t [\hat{\omega}_\times] + \frac{\Delta t^2}{2} [\hat{\omega}_\times]^2$ and $\Psi_k \sim \mathbf{I}_{3 \times 3} \Delta t + \frac{\Delta t^2}{2} [\hat{\omega}_\times] - \frac{\Delta t^3}{6} [\hat{\omega}_\times]^2$. The exponential function in this equation refers to the matrix exponential.

These expressions are now what we need to establish a discrete version of the state equations, which are based on this transition matrix Φ_k .

V.2.4 Discrete covariance matrices

Since we have a discrete system, it is also necessary to also represent the propagation error covariance matrix discretely. The discrete propagation covariance matrix \mathbf{Q} sampled between time t_k and $t_{k+1} = t_k + \Delta t$ is related to the continuous matrix \mathbf{Q}_c through the relationship (Maybeck, 1982):

$$\mathbf{Q} = \int_{t_k}^{t_{k+1}} \Phi(t_{k+1}, \tau) \mathbf{G}(\tau) \mathbf{Q}_c \mathbf{G}^T(\tau) \Phi^T(t_{k+1}, \tau) d\tau.$$

The full result of this integration is given in (Trawny et al., 2005). To the second order in Δt , the equations simplify when $\boldsymbol{\omega} \rightarrow \mathbf{0}$ into:

$$\mathbf{Q}_{11} = \sigma_g^2 \Delta t \cdot \mathbf{I}_{3 \times 3}, \quad (\text{V.30})$$

$$\mathbf{Q}_{12} = -\sigma_b^2 \frac{\Delta t^2}{2} \cdot \mathbf{I}_{3 \times 3}, \quad (\text{V.31})$$

$$\mathbf{Q}_{22} = \sigma_b^2 \Delta t \cdot \mathbf{I}_{3 \times 3}, \quad (\text{V.32})$$

with

$$\mathbf{Q} = \begin{bmatrix} \mathbf{Q}_{11} & \mathbf{Q}_{12} \\ \mathbf{Q}_{12}^T & \mathbf{Q}_{22} \end{bmatrix}. \quad (\text{V.33})$$

V.2.5 Discrete Kalman filter setup

Now that we obtained all discrete representation of our system, we can write the algorithm's steps. The Kalman filter will estimate the current attitude quaternion and gyroscope bias value, while minimizing the covariance of the error $\tilde{\mathbf{x}}$. Below, we summarize the relevant physical equations that are used to set up this filter. This is useful if one wants to build a physical model of the dynamic system.

1. **Velocity estimate:** $\hat{\boldsymbol{\omega}}_k = \boldsymbol{\omega}_k^{\text{meas}} - \hat{\mathbf{b}}_k$,
2. **Attitude propagation:** $\hat{\tilde{q}}_k = \exp\left(\frac{1}{2}\boldsymbol{\Omega}(\hat{\boldsymbol{\omega}}_k)\Delta t\right) \hat{\tilde{q}}_{k-1}$,
3. **Error state evolution:** $\tilde{\mathbf{x}}_k = \Phi_k \tilde{\mathbf{x}}_{k-1} + \mathbf{G}_k \mathbf{n}_k$,
4. **Error covariance to be minimized:** $\mathbf{P}_k = \text{cov}[\tilde{\mathbf{x}}_k]$,
5. **Error covariance evolution:** $\mathbf{P}_k = \Phi_k \mathbf{P}_{k-1} \Phi_k^T + \mathbf{Q}_k$,

6. **New attitude measurement:** \bar{q}_k^{meas} ,

7. **State error measurement:** $\tilde{\mathbf{z}}_k = \mathbf{H}_k \tilde{\mathbf{x}}_k + \mathbf{n}_k^{\text{meas}}$.

Note that in that last step, the error measurement $\tilde{\mathbf{z}}_k$ is determined by extracting $\delta\theta_k^{\text{meas}}$ from the difference quaternion $\delta\bar{q}_k = \bar{q}_k^{\text{meas}} \otimes \hat{q}_k^{-1}$ using the small angle approximation. Furthermore, we have $\mathbf{n}_k = [\mathbf{n}_g \quad \mathbf{n}_b]^T$, $\mathbf{n}_k^{\text{meas}}$ is the measurement noise, and in our case $\mathbf{H}_k = [I_{3 \times 3} \quad \mathbf{0}_{3 \times 3}]$.

At each step, we will attempt to produce our best estimate of the state $\hat{\mathbf{x}}$, and keep track of the evolution of the state error $\tilde{\mathbf{x}}$ and its covariance matrix \mathbf{P} . There are two distinct phases in the Kalman filter: the prediction, and the update.

In the prediction phase, we use our best estimates from the previous step, along with the velocity measurements and the expected propagation relationships to predict what the estimates should be at the current step. If we don't get a new attitude measurement at that step, then these new estimates are the best we can do.

When we do get a new attitude measurement, then in addition to the prediction phase, we also do an update phase. We compare the best estimate from the prediction phase to our new measurement, and use the difference to compute a correction to our state. This uses the weights of the various noise contributors in the system, as well as additional weights that can be defined by the user. This phase most importantly estimates the bias of the gyroscopes, to allow robust propagation of the state from one step to the next.

In this section, however, we assume that the attitude measured by the star camera \bar{q}_k^{meas} corresponds to the attitude at the current step. In reality, when we receive the star camera, it represents an attitude that was taken some number of steps ago. This is due to the slow processing of the star camera images and the catalog search. Our software

cannot solve the star camera position in one single loop iteration. We tackle this issue in Section V.2.8.

V.2.6 Kalman filter: prediction

The notation $\tilde{\mathbf{x}}_{k|k-N}$ corresponds to the estimate made at step k knowing the value at step $k - N$, where $k - N$ corresponds to the step at which we received the last absolute attitude measurement.

The algorithmic steps for this phase are:

1. **Predict the bias:** $\hat{\mathbf{b}}_{k|k-N} = \hat{\mathbf{b}}_{k-1|k-N}$ since there is no new information to allow us to update the bias.
2. **Estimate the angular velocity:** $\hat{\boldsymbol{\omega}}_{k|k-N} = \boldsymbol{\omega}_k^{\text{meas}} - \hat{\mathbf{b}}_{k|k-N}$.
3. **Predict the attitude:** $\hat{\boldsymbol{q}}_{k|k-N} = \exp\left(\frac{1}{2}\boldsymbol{\Omega}(\hat{\boldsymbol{\omega}}_{k|k-N})\Delta t\right) \hat{\boldsymbol{q}}_{k-1|k-N}$.
4. **Compute the state transition matrix:** $\Phi_k = \begin{bmatrix} \boldsymbol{\Theta}_k & \boldsymbol{\Psi}_k \\ \mathbf{0}_{3 \times 3} & \mathbf{I}_{3 \times 3} \end{bmatrix}$ using $\hat{\boldsymbol{\omega}}_{k|k-N}$ in the expressions of $\boldsymbol{\Theta}_k$ and $\boldsymbol{\Psi}_k$.
5. **Compute the added noise covariance matrix:** \mathbf{Q}_k . This corresponds to the noise that is added by the new gyro measurement.
6. **Update the state covariance matrix:** $\mathbf{P}_{k|k-N} = \Phi_k \mathbf{P}_{k-1|k-N} \Phi_k^T + \mathbf{Q}_k$

We have now propagated our system from step $k - 1$ to step k , and we have three new quantities: the bias $\hat{\mathbf{b}}_{k|k-N}$, the attitude estimate $\hat{\boldsymbol{q}}_{k|k-N}$, and the state covariance matrix $\mathbf{P}_{k|k-N}$. If we do not get any star camera measurement, then at the next step we will just continue propagating with this procedure.

V.2.7 Kalman filter: update

The star camera information provides us with a measurement of the attitude \bar{q}_k^{meas} , which is compared to our predicted attitude. We use the difference between our prediction and the measurement to update the bias and the state covariance matrix. Under certain circumstances, the Kalman filter is the optimal estimator: it converges towards the correct solution with the minimum amount of iterations.

For the Kalman filter update procedure, we form a measurement vector $\tilde{\mathbf{z}}_k$ that corresponds to the difference of an attitude measurement at step k and the predicted attitude at step k .

7. **Compute the innovation:** $\tilde{\mathbf{z}}_k = \delta\boldsymbol{\theta}_k^{\text{meas}}$ with $\delta\boldsymbol{\theta}_k^{\text{meas}}$ extracted from the difference

$$\text{quaternion } \delta\bar{q}_k = \bar{q}_k^{\text{meas}} \otimes \hat{q}_{k|k-N}^{-1}.$$

8. **Compute the innovation covariance:** $\mathbf{S}_k = \mathbf{H}_k \mathbf{P}_{k|k-N} \mathbf{H}_k^T + \mathbf{R}_k$.

9. **Compute the Kalman gain:** $\mathbf{K}_k = \mathbf{P}_{k|k-N} \mathbf{H}_k^T \mathbf{S}_k^{-1}$.

10. **Update error state:** $\tilde{\mathbf{x}}_{k|k} = \mathbf{K}_k \tilde{\mathbf{z}}_k = \begin{bmatrix} \delta\boldsymbol{\theta} \\ \Delta\mathbf{b} \end{bmatrix} = \begin{bmatrix} 2\delta\mathbf{q} \\ \Delta\mathbf{b} \end{bmatrix}$

11. **Update attitude estimate:** $\hat{q}_{k|k} = \delta\bar{q} \otimes \hat{q}_{k|k-N}$ with $\delta\bar{q} = \begin{bmatrix} \sqrt{1 - \delta\mathbf{q}^T \delta\mathbf{q}} \\ \delta\mathbf{q} \end{bmatrix}$ if

$$\delta\mathbf{q}^T \delta\mathbf{q} \leq 1, \text{ or } \delta\bar{q} = \frac{1}{\sqrt{1 + \delta\mathbf{q}^T \delta\mathbf{q}}} \begin{bmatrix} 1 \\ \delta\mathbf{q} \end{bmatrix} \text{ otherwise.}$$

12. **Update the bias:** $\hat{\mathbf{b}}_{k|k} = \hat{\mathbf{b}}_{k|k-N} + \Delta\mathbf{b}$.

13. **Update the angular velocity estimate:** $\hat{\boldsymbol{\omega}}_{k|k} = \boldsymbol{\omega}_k^{\text{meas}} - \hat{\mathbf{b}}_{k|k}$

14. **Update state covariance matrix with Joseph's form:** $\mathbf{P}_{k|k} = (\mathbf{I}_{6 \times 6} - \mathbf{K}_k \mathbf{H}_k) \mathbf{P}_{k|k-N} (\mathbf{I}_{6 \times 6} - \mathbf{K}_k \mathbf{H}_k)^T + \mathbf{K}_k \mathbf{R}_k \mathbf{K}_k^T$.

V.2.8 Delayed star camera solution

In general, the star camera takes much longer than one single loop cycle to produce an attitude estimate. Between the time we trigger the star camera frame and the time we receive the attitude measurement, we need to keep track of the propagation matrices that will allow to express both the attitude and its covariance matrix in the current reference frame, where the measurement can be combined with the a priori estimate from the Kalman filter.

While no new star camera measurement is available, the attitude transition is expressed by $\hat{q}_k = \exp\left(\frac{1}{2}\Omega(\hat{\omega}_k)\Delta t\right) \hat{q}_{k-1}$, and the new covariance is $\mathbf{P}'_k = \Phi_k \mathbf{P}_{k-1} \Phi_k^T + \mathbf{Q}_k$, where we assume that \mathbf{Q}_k is a constant. We can consider that the gyroscope bias does not change significantly during the time between two star camera measurement (typically on the order of a few seconds). With this we can create a recursive relationship and $\bar{q}_k = [\Pi_{i=k-N}^k \exp\left(\frac{1}{2}\Omega(\hat{\omega}_i)\Delta t\right)] \bar{q}_{k-N}^{\text{meas}}$ where $k - N$ again represents the index at which the star camera image was taken. Similarly, we have: $\mathbf{P}_k = \mathbf{A}_k \mathbf{P}_{k-N} \mathbf{A}_k^T + \mathbf{B}_k$ where \mathbf{A}_k and \mathbf{B}_k are defined recursively as $\mathbf{A}_k = \Phi_k \mathbf{A}_{k-1}$ with $\mathbf{A}_0 = \mathbf{I}_{6 \times 6}$, and $\mathbf{B}_k = \mathbf{Q}_k + \Phi_k \mathbf{B}_{k-1} \Phi_k^T$ with $\mathbf{B}_0 = \mathbf{0}_{6 \times 6}$. \mathbf{A}_k can also be written $\mathbf{A}_k = \Phi_k \Phi_{k-1} \cdots \Phi_{k-N} = [\Pi_{i=k-N}^k \Phi_i]$.

Hence, once we trigger the star camera, we need to start keeping track of the matrices \mathbf{A}_k , \mathbf{B}_k , and $\mathbf{C}_k = \Pi_{i=k-N}^k \exp\left(\frac{1}{2}\Omega(\hat{\omega}_i)\Delta t\right)$, appropriately reset them when a new star camera trigger has occurred, and propagate them until the estimator receives the star camera value.

V.2.9 Enhancing the Kalman filter models

The simple gyroscope model that we adopt is incomplete, and can cause some issues that need explanation. In our simplified representation, gyroscope models using only a bias to

account for the measurement errors. The bias, which combines linearly with the measured velocity, is adjusted by the Kalman filter to correct the errors and minimize the covariance of the error.

However, this supposes that the gyroscopes are perfectly orthogonal, with unity scale factor, and the transformation between the absolute measurement sensor (the star camera) reference frame and the gyro reference frame is known perfectly. An alignment error in either of these two components will translate to multiplicative errors on the velocities, which will have a large effect when the velocity dramatically changes (for example, after a slew) and will not be accounted for by a simple bias model. Eventually, the bias would adjust to be in agreement with the star camera measurements - but it can take a while, and during this time, the velocity that we think we are moving at is incorrect. To put this in perspective, a 1% error on the gyroscope velocity in one axis for a 10° slew at $400''\text{s}^{-1}$ corresponds to a position error of 6 arcminutes, a considerable amount given our pointing requirements.

For spacecraft projects, alignment issues and calibrations are allocated a large amount of resources to minimize these issues and come close to the ideal configuration. Our project has not dedicated enough resources to ensure exquisite alignment and calibration between the gyroscopes and the star camera, due to lack of time and resources. We nevertheless propose elements of solution in the next section.

If this error persists during flight, the poor man's solution is as follows. Instead of tracking the Kalman filter during the entire duration of the slew, we discard the star camera measurements during the slew and reset the estimator after the slew is complete. This resets our starting position with the first solution from the star camera. Since we will be off our target, we will slew again to the desired target, which will be much closer. Each

time this needs to be repeated, we minimize the effects of the alignment errors.

For our scientific purpose, even a 1% error in the gyroscope scale factor or angular velocity alignment is not a deal breaker, since their main purpose is to maintain sufficient stability to lock onto a guide star with the fine guiding sensor. The fine guiding sensor is by definition in the correct reference frame, since it observes through the optical train.

V.2.9.1 Estimating angular error between reference frames

Here, we propose an appropriate approach to estimate the gyroscope misalignment using a different Kalman filter. In this filter, the global misalignment error of the entire reference frame is set as part of the state, and is being estimated at each step. A global misalignment error can be represented by a rotation matrix which, in the small angle approximation, can be written $\mathbf{C}' \approx \mathbf{I}_{3 \times 3} + \mathbf{C}$, with:

$$\mathbf{C} = \begin{bmatrix} 0 & c_{xy} & c_{xz} \\ -c_{xy} & 0 & c_{yz} \\ -c_{xz} & -c_{yz} & 0 \end{bmatrix}. \quad (\text{V.34})$$

We now have $\boldsymbol{\omega}^{\text{true}} = (\mathbf{I}_{3 \times 3} - \mathbf{C})\boldsymbol{\omega}^{\text{meas}}$, so the gyro error introduced by the misalignment is $\Delta\boldsymbol{\omega} = -\mathbf{C}^T\boldsymbol{\omega}^{\text{meas}}$. The new state components are $\mathbf{c} = [c_{xy} \ c_{xz} \ c_{yz}]^T$, and we can rearrange the matrix terms to express $\boldsymbol{\Omega}_c$ as a function of the components of $\boldsymbol{\omega}^{\text{meas}}$ and write: $\Delta\boldsymbol{\omega} = \boldsymbol{\Omega}_c\mathbf{c}$. Similarly to the error-representation equations in the Kalman filter model expressed in the previous sections, we then obtain the new upper right block of the transition matrix:

$$\boldsymbol{\Psi}_k = -\boldsymbol{\Omega}_c\Delta t. \quad (\text{V.35})$$

This is useful because the three additional state elements can replace the gyroscope

bias for initial calibration and determination. When on the ground, it is then possible, with minimum software changes, to estimate the three components of a rotation matrix instead of the three components of a bias vector.

V.2.9.2 Estimating the orthogonalization error and scale factor error

The full orthogonalization matrix for the three gyroscopes is a non-orthogonal matrix \mathbf{M} :

$$\mathbf{M} = \begin{bmatrix} k_x & m_{xy} & m_{xz} \\ m_{yx} & k_y & m_{yz} \\ m_{zx} & m_{zy} & k_z \end{bmatrix}, \quad (\text{V.36})$$

where $\mathbf{k} = [k_x \ k_y \ k_z]^T$ is the scale factor of the gyroscopes, and the cross terms correspond to the misalignments between the different axes. This can also be rearranged and rewritten in terms of the three scale factor unknowns and the 6 cross terms unknowns $\mathbf{m} = [m_{xy} \ m_{xz} \ m_{yx} \ m_{yz} \ m_{zx} \ m_{zy}]^T$:

$$\Delta\boldsymbol{\omega}_k = \boldsymbol{\Omega}_k \mathbf{k}, \Delta\boldsymbol{\omega}_m = \boldsymbol{\Omega}_m \mathbf{m}, \quad (\text{V.37})$$

for a total error in velocity $\Delta\boldsymbol{\omega} = \Delta\boldsymbol{\omega}_k + \Delta\boldsymbol{\omega}_m + \Delta\boldsymbol{\omega}_b$ if we also include the bias that we discussed in our standard estimator. We have here:

$$\boldsymbol{\Omega}_k = \begin{bmatrix} \omega_x & 0 & 0 \\ 0 & \omega_y & 0 \\ 0 & 0 & \omega_z \end{bmatrix} \quad (\text{V.38})$$

and

$$\boldsymbol{\Omega}_m = \begin{bmatrix} \omega_y & \omega_z & 0 & 0 & 0 & 0 \\ 0 & 0 & \omega_x & \omega_z & 0 & 0 \\ 0 & 0 & 0 & 0 & \omega_x & \omega_y \end{bmatrix}. \quad (\text{V.39})$$

This is now a 15-state Kalman filter, with the error state: $\tilde{\mathbf{x}} = \begin{bmatrix} \delta\theta & \Delta\mathbf{k} & \Delta\mathbf{m} & \Delta\mathbf{b} \end{bmatrix}^T$.

The top right block of the transition matrix can be written:

$$\Psi_k = -\Delta t \begin{bmatrix} \Omega_k & \Omega_m & I_{3 \times 3} \end{bmatrix}. \quad (\text{V.40})$$

This is handy for data analysis on the ground, but not appropriate for flight since increasing the state vector size quickly increases the computational cost of the filter. While running this Kalman filter implementation in the Real Time OS on *boop*, we measured average run times of ~ 0.4 s, largely caused by the 15×15 matrix inversion process that happens during the update phase of the filter.

V.2.10 Conclusions on sensor fusion

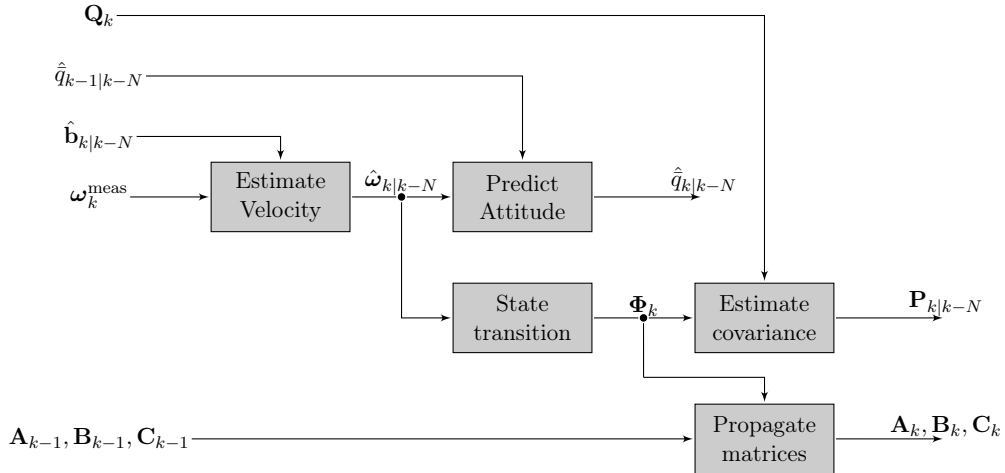
We have defined, designed, implemented and tested a complete sensor fusion algorithm based on an multiplicative, extended Kalman filter, which has several steps summarized in Fig. V.23.

This software, implemented entirely in Labview Real Time OS, has been the workhorse of our testing of the control system. Similarly, we have implemented several variations of the software for use on the ground, in order to estimate the residual misalignments between the individual gyroscopes, as well as between the gyroscope frame and the star cameras.

The software merges the information gathered from the gyroscopes and the star cameras, while appropriately correcting for the lag in the star camera measurements, and accounting for user-defined weights.

While this software is deeply integrated with our hardware and flight software architecture, its critical components are quite independent. We plan on sharing this software

Kalman Filter: Prediction



Kalman Filter: Update

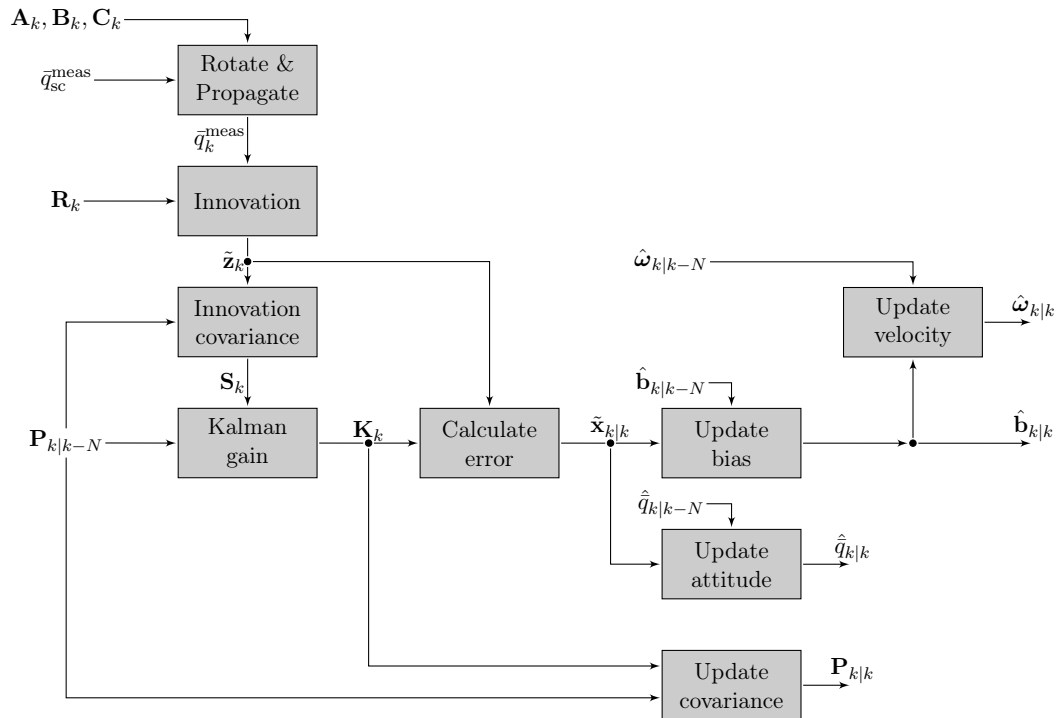


FIGURE V.23: Kalman filter steps

with an open-source license after the pointing test results are published. It is quite versatile

and allows for many user improvement and modifications.

Chapter VI

Implementation and on-sky testing

*Ever tried. Ever failed. No matter.
Try again. Fail again. Fail better.*

S. Beckett

It is only in the past year that we were able to obtain system-level results that would validate some of our design choices. In order for us to collect test data from this observatory while looking at the sky, many different subsystems need to be operational, and we have mostly focused on the electronics and software architecture. In the Spring of 2016, enough of the systems became operational to allow on-sky testing of the coarse pointing loop, which is what is discussed in this section. As this document is being written, progress is very rapid as the team is getting ready to ship our for the flight campaign out of Fort Sumner, New Mexico in the middle of August. As a result, the payload every day becomes more "flight-like".

This section is organized as follows. First, we describe key procedures that we developed that are necessary before flight. Elaborating these procedures and interpreting their results has been an important part of our testing phase. Second, we present our test setup in the high bay at NASA Goddard and discuss results of the sensor fusion implementation described in the previous chapter while the payload is sitting on the ground, but looking

out to the sky. Third, we show results of the sensor fusion implementation while the payload is hanging and looking out on the sky. This is the most flight-like tests that were achieved by mid-June, 2016.

VI.1 Key pre-flight procedures

VI.1.1 Inertia measurement

While CAD models allowed to us to estimate the moment of inertia of the payload, this is only an approximation. For testing and for launch, the payload will be different than the model we have: we will either miss some components because they are not yet installed, or have additional components such as the ballasts, the crush pads, or the weights that are used to balance the payload.

We use a simple procedure to estimate the moment of inertia about \mathbf{z}_g of the payload while hanging from a crane. For this purpose, we command the CCMG to input a torque to the payload by moving the gimbal at a constant velocity. According to Eq. V.7, $\mathcal{T}_{CCMG} = 20.8 \times \dot{\theta} \cos \theta$. According to conservation of angular momentum, the rate of change of the total angular momentum about \mathbf{z}_g is $(\mathbf{J}\dot{\omega})_{\mathbf{z}} = \mathcal{T}_{CCMG} = 20.8 \times \dot{\theta} \cos \theta$.

We measure the inertia $\mathbf{J}_{\mathbf{z}}$ by averaging measurements of the angular acceleration $\dot{\omega}_{\mathbf{z}}$, divided by the instantaneous input torque, which is numerically more stable than averaging its inverse since the accelerations, expressed in rad s^{-1} are typically very small. A measure of the inertia is then the inverse of this average. We consistently measure an inertia of roughly 1700 kg m^2 , which is about 15% higher than the expected CAD model estimates. This reflects some errors in assigning the proper masses in the CAD model.

VI.1.2 Sensor alignment and calibration

While the intrinsic noise of our sensors has been characterized in Section V.V.1.2.1, it is important to test them while mounted to the payload, align their axes to the other reference frames, and study their spectral energy distribution. Mounting the gyroscopes in a 3-dimensional mount on the truss will inevitably lead to alignment errors and the contribution of new vibration frequencies present in the structure and excited by the moving parts on the payload.

VI.1.2.1 Gyroscope spectral analysis in flight configuration

The gyroscopes were characterized in quiet laboratory environment that was designed for precision optical interferometry, with special foundations to prevent vibrations being transmitted through the ground. This allowed us to measure the gyroscopes down to their noise levels. However, as soon as we attach the gyroscopes to any structure, the gyroscopes measure their mount's vibration modes.

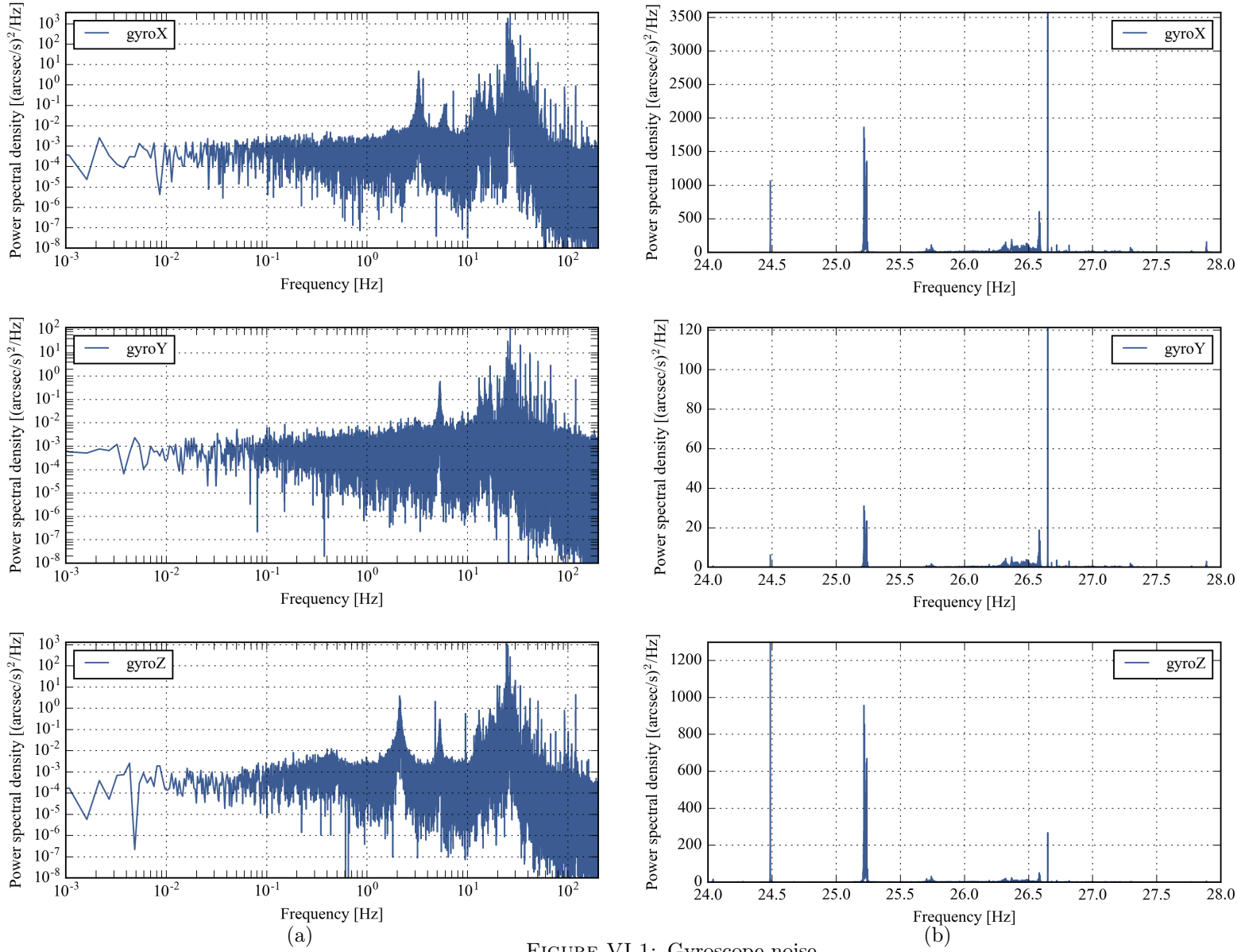


FIGURE VI.1: Gyroscope noise

We estimate that, once in the box and attached onto the truss, the gyroscope has ~ 20 times its natural noise levels. Looking at the power spectral density of the velocity time series (Fig. VI.1a), almost all of the noise power is contained in three strong and sharp peaks, which coincide with the expected first resonant modes of carbon fiber truss structure, obtained through finite element analysis. These modes are precisely located at 24.49, 25.23 and 26.7 Hz with the mass configuration of the time the data was taken, which omits the large siderostat mirrors on each end (Fig. VI.1b).

The positive conclusion is that the truss has its first resonant frequencies precisely where they were designed to be from CAD modeling, and they are above 20 Hz, which is out of the bandwidth of the attitude control. This noise can then be drastically attenuated either by notch filters (if the frequencies do not shift) or by low-pass filters with a break frequency at a few Hertz. For example at 2.5 Hz, a single-pole low-pass Butterworth filter would attenuate these peaks by 20 dB, or an attenuation factor of 100.

One less encouraging result is that these modes do not seem to damp, which means that they are continually being excited. One of the ideas behind bringing the first resonant frequencies above 20 Hz was to have low amplitudes and relatively fast damping. We hypothesize that the truss vibrational modes are excited by the ambient vibration spectrum coming from the air, in particular from the A/C unit.

Examining the PSD in Fig VI.1a, we also notice some broad peaks at 3, 5.5, and 2 Hz for the x, y, and z axes respectively. These are attributed to motions of the truss within the gondola about the vibration isolators that were installed to decouple the two mechanical structures.

VI.1.2.2 Orthogonalization of gyroscope mount

An orthogonalization procedure was established to determine the correction matrix to apply to the gyroscope velocity vector to make sure measurement were independent from one another. The procedure involves spinning the 3-axis gyroscope mount on one of the rotation stages that we use for flight (which are used for elevation control).

The system to solve is:

$$\boldsymbol{\omega}^{\text{meas}} = \begin{bmatrix} M_x & m_{xy} & m_{xz} \\ m_{yx} & M_y & m_{yz} \\ m_{zx} & m_{zy} & M_z \end{bmatrix} \boldsymbol{\omega}^{\text{true}} = M \boldsymbol{\omega}^{\text{true}} \quad (\text{VI.1})$$

The 9 matrix elements can be found by commanding the 3-axis mount to rotate at a known velocity about each axes. Hence, by knowing the vector $\boldsymbol{\omega}^{\text{true}}$ (one component is the commanded velocity and the two others are zero) and measuring the velocities on the three axes, we can determine the matrix element for the column corresponding to the current spin axis.

The gyroscopes are so sensitive that they measure the rotation of the Earth accurately. This corresponds to a bias in the commanded velocity. To mitigate this issue, we spin the 3-axis mount in two opposite directions. The perceived difference in the velocities corresponds to the Earth velocity about that axis.

Because of cabling constraints, we are only able to spin the 3-axis mount for small angles. This method works very well when the gyroscope can spin freely and do 360° rotations, since a lot of the systematics of the setup will cancel out after multiple revolutions. Unfortunately, we do not have access to a state-of-the-art rotation table with a slip-ring.

The matrix we obtain suggests typical alignment errors on the order of 0.1-0.3%,

which correspond to angular errors of a few degrees. While the measurements appear to be repeatable, we noticed that the sum of the squares of the velocities was typically 2% off from its expected value, which we know since it corresponds to the square of the Earth's rotation velocity. Further, this error varies with different orientations of the gyroscope mount. The typical errors that are seen are consistent with a residual misalignment of a few tenths of degrees between the gyroscopes - a considerable amount.

This could lead to multiple interpretations. First, it is possible (even likely) that the mount deforms under its own gravity in different ways depending on its orientation. Unfortunately, it is not simple to proceed to this orthogonalization method with the mount in its flight orientation, and would require some ground support equipment (GSE) not available at the moment.

A second possible interpretation is that the gyroscope internal scale factor is changing. We noted that the temperature of the gyroscopes was increased by about 5 °C when they are inside the mount on the thermal isolators. This can potentially change their scale factor (which effectively multiplies the measured velocity) as a result of the fiber optics' length changing slightly.

The path forward towards orthogonalization of the mount is to use a laser tracker to measure the orientation of each plate on which the gyroscope is mounted. This would allow us to find the components of the matrix M for the mount on the payload in its final flight configuration. It will also allow us to precisely align the mount to the other important reference frames, such as the star camera reference frame and the telescope reference frame.

The scale factor on the \mathbf{z} gyroscope can also be precisely determined if the payload is aligned horizontally with precision. Because of the size of the payload, a good lever

arm provides an accurate measure of its horizontal position. The gyroscope on the **z** axis can thus be aligned with the gravity vector precisely, at which point the expected angular velocity is known, and the scale factor correction can be determined.

VI.1.2.3 Alignment of gyroscope mount to star camera mounts

Once the gyroscope is orthogonalized, it remains to be properly referenced to the star camera mount. While a good alignment on the ground can be achieved with a laser tracker, our star camera lens design does not permit a perfect alignment because of uncertainties in the angle of the glass pieces in the lens, and uncertainties in the location of the sensor.

To correct for small deviations from the original alignment, we developed a variant to the traditional Kalman filter described in Chapter V which, instead of estimating the bias, estimates the rotation matrix between the gyroscope mount and the star camera, as explained in V.2.9. Running this filter can be done seamlessly, even in flight, since the number of unknowns is the same as the flight model which estimates bias drifts.

VI.1.3 Star camera

VI.1.3.1 Tuning tests

We proceeded to multiple stages of tuning for the star camera, spanning many nights over the past year. In this section, we propose an small excerpt of the data acquired during one night when we varied the exposure time of the camera, to determine the most suitable value for flight. We list here (Table VI.1) five experiments starting with an exposure time of 250 ms and decreasing the exposure time down to 31 ms. During these tests, we compute some statistics on the observations, and are most interested in the success rate, which is the ratio of solutions found over the total number of images taken. By computing

these statistics from the outputs of the star camera software, we also noted that the fitted exposure time, which corresponds to the best fit between the known star brightness and the measured camera digital counts, was remarkably accurate when solutions were found. In addition, on the occasion when a false positive was found (that is a solution that is not correct), the exposure time was, predictably, very inaccurate. We decided to add this fitted exposure time information as an additional metric to determine the accuracy and reliability of the star camera software. From the results, we determine that an exposure time of 125 ms provides good results, while minimizing the amount of smearing that occurs when slewing. With exposures of 125 ms, a smearing of 1 pixel occurs when the payload moves at $30''\text{s}^{-1}$, which is well above the detectable and correctable velocity.

TABLE VI.1: Star camera exposure time tests.

	Exposure time (ms)	Number of images in run	Fitted exposure time (ms)	Number of matching stars	Fit ra & dec error (arcsec)	Fit roll error (arcsec)	Processing time (s)	Solution success rate (%)
Exp1	250	118	260 ± 92	9.12 ± 1.67	1.46 ± 0.43	114 ± 40	1.48 ± 0.77	98
Exp2	125	36	113 ± 13	9.75 ± 1.95	1.46 ± 0.39	118 ± 32	1.05 ± 0.26	100
Exp3	62	49	70 ± 53	8.43 ± 1.55	1.72 ± 0.64	155 ± 66	1.01 ± 0.21	96
Exp4	62	132	66 ± 23	7.32 ± 1.34	1.75 ± 0.65	151 ± 55	1.22 ± 0.59	76
Exp5	31	35	44 ± 53	6.54 ± 0.84	2.33 ± 0.79	180 ± 65	1.19 ± 0.48	37

Notes: The fitted exposure time is estimated from the best fit between the expected number of photons from the catalog stars and the number of counts measured on the sensor. A good agreement between actual exposure time and fitted exposure time further ensures that we are looking at the correct region of the sky (the matching algorithm does not use the fluxes of each star to determine the attitude solution, so the fitted flux is simply an extra protection against false positives. Although we only show small number statistics here, we have experimented very robust results in the lab over many clear nights using a 125 ms exposure. The exposure time is a parameter that can be set remotely and changed during flight if necessary.

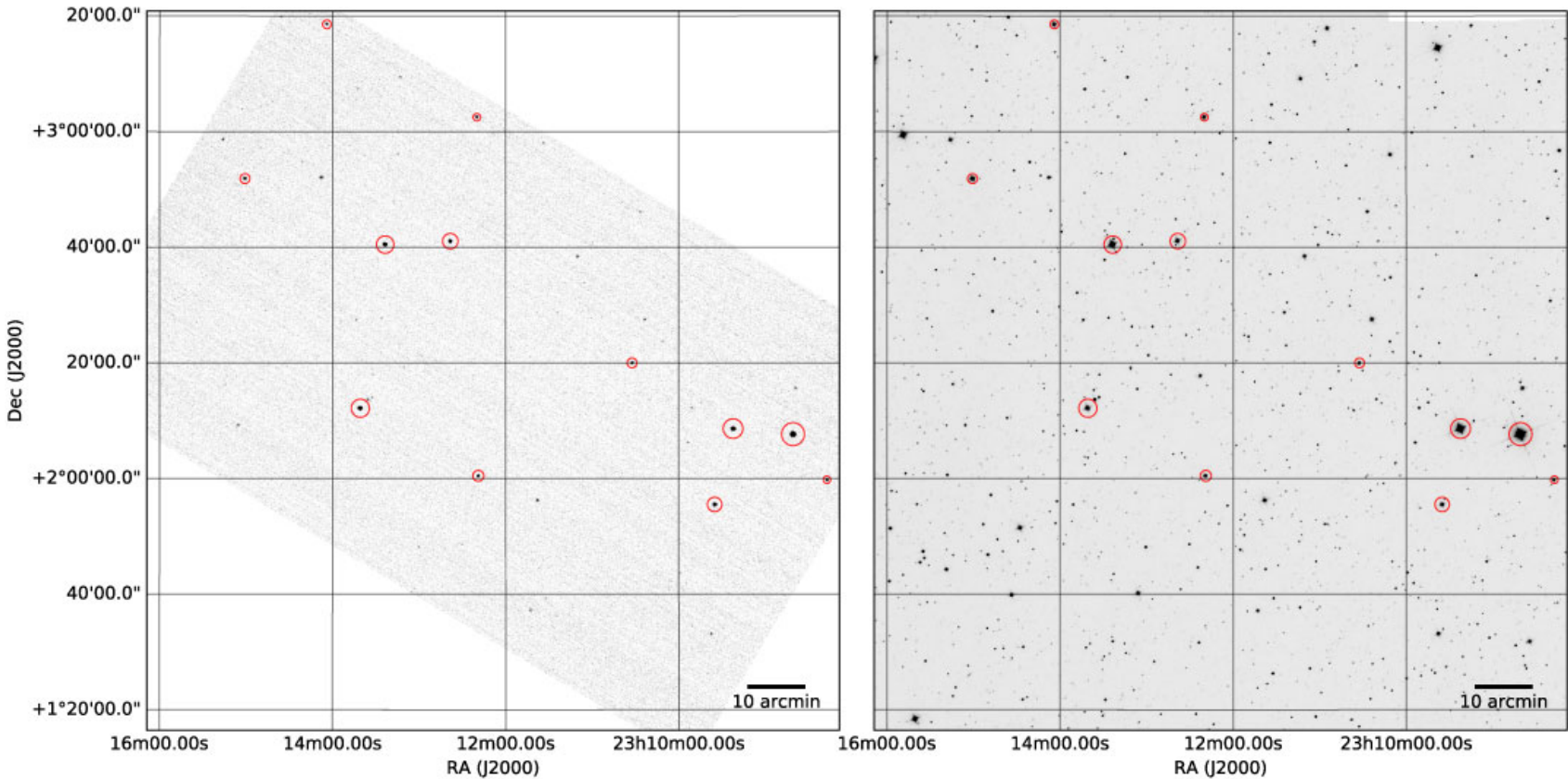


FIGURE VI.2: *Left:* Example of a background-subtracted star camera image with identified $> 5\sigma$ sources circled in red. The orientation of the image on the celestial sphere is the one provided by BETTII's embedded star camera solver. This image corresponds to a field in the Scorpius constellation. *Right:* WISE 3.4 μm mosaic from the online archive, centered on the same location. This image is composed of 9 individual WISE images that we patched into a mosaic using the *Montage*[CITE] software package.

VI.1.3.2 Live star camera diagnostic software

During our test operations, a lot of information is available and it can sometimes be challenging to understand the full system status and diagnose the issues. To help mitigate this, we created a suite of small Python routines which help quickly diagnose the star camera behavior. For example, one piece of software displays the latest image from the star camera, and overlays the "blobs" (contiguous regions of bright pixels) that the star finder software finds. At a glance, this can tell us if blobs are not found in the image, or if the star camera appears out of focus, or if there is a cloud cover. During flight, however, we will not have access to all this information because of the low bandwidth. Hence, the software also cuts the star camera image (a 1920×1200 array of 16-bit integers) into a smaller mosaic composed only of the regions around the blobs the software identified. Further, the type of all blobs is reduced to 8 bits. This constructs a much more modestly-sized piece of information that can be sent down for diagnostics.

Other metrics are useful to understand the star camera's behavior. For example, the star finder and catalog matching software solves for the best fit of exposure time, by comparing the known brightness of the stars and the measured number of digital counts on the detector. We find that this is accurate to $\sim 10 - 20\%$ in a vast majority of the cases, and values that are wildly off this estimate usually indicate either a false positive or some other sort of issue associated with the solving. This is used in two ways: first, it offers a quick sanity check that the solving happens correctly and robustly; and second, it can offer one additional protect against false position information, which we can use in the Kalman estimator when we decide to incorporate a star camera solution or not.

VI.2 Estimator implementation

VI.2.1 Test setup and limitations

The testing is done indoors in the Building 20 Highbay at NASA GSFC. The payload is sufficiently close to the rolling doors that one arm can see a small patch of sky while hanging from the indoor crane.

The payload is entirely run with 7 Marine Deep Cycle batteries, which provide all the required power for ≥ 8 h of continuous operations. BETTII is entirely wireless and uses a Wi-Fi router on board to provide high-bandwidth communication through a TCP/IP connection, which is useful for testing and displaying large quantities of information.

The mechanical, electrical, and communication setup is different than it will be in flight in several ways. First, the crane is about five times shorter than the balloon train, which results in higher pendulum frequencies. Second, the payload can only see one arm at a time through the high bay doors, making it difficult to test the entire control system with the fine guidance sensor loop. Third, when the rolling doors are open, gusts of winds can move the payload as it is hanging, resulting in considerably larger pendulum motions than expected in flight. And finally, in flight, the communication bandwidth is expected to be 1 MB/s down and ~ 1 B/s up. The astonishingly low uplink rate forces a minimalistic approach where most commands are only one or two bytes long.

The star camera is also not put in its final, flight mounting position. The reason for this is that if the payload is lifted enough to clear most non-movable obstacles in the high bay, the angle at which the star camera can look and still see a patch of sky has to be less than $\sim 30^\circ$. In previous months, star camera testing was done with the star camera positioned at the very end of one of BETTII's arms to increase the amount of sky

coverage available. While discussions are underway to modify the high bay structure and open up portions of the wall, it is not reasonable to expect any actual changes for any of our relevant timescales for BETTII.

VI.2.2 Autofocus implementation

Since the payload is close to the high bay door, changes in temperature occur and slightly change the focus of the star camera. These changes are expected to be more dramatic at float. For this reason, we implemented a very simple, yet very robust autofocus mechanism that we tested both on the ground and while hanging.

The algorithm relies on the fact that the focus ring of the lens has a hard stop. The stepper motor that controls the focus ring through a belt cannot pass this stop, and when it tries, the belt always slips. In addition, we also know that the focus position for the ring will always be very close to this hard stop, which is a little past infinity focus for the lens.

Hence, we design an algorithm as follows:

1. Drive the stepper a large number of steps to guarantee hitting the hard stop.
2. Take a picture and move one step backward (away from the stop).
3. Calculate the variance of all the pixels in the image (which is a measure of sharpness).
4. Repeat a sufficient amount of times to guarantee passing through focus.
5. When done, go back to the position which maximized the variance.

This very simple algorithm proved to be very robust in all situations. The variance metric was the simplest to implement, as opposed to more complicated sharpness metrics used in modern photography. We inspected the results by eye and they were always

satisfactory. The small backlash usually present when the stepper motor changes direction to go to the best position is not noticeable in the results.

VI.2.3 Gyro attitude estimator

We present here the results of the on-board Kalman filter estimator which was described in Chapter V. The data gathered through the many test runs is archived on the ground computer. We developed a framework in Python to process this data and align all quantities properly to BETTII's heartbeat.

The results shown in this section correspond to data gathered when the payload was sitting on the ground. This served as the simplest possible test to ensure the Kalman filter could appropriately correct for the errors given by the star camera.

In Fig. VI.3, we show the standard attitude plot. The red line indicates the inertial RA and DEC of the gondola or gyro reference frame estimated by the Kalman filter, while the blue dots indicates the measured inertial attitude of the same reference frame. In this plot, time goes from left to right (increasing RA). For each star camera data point, a line is drawn to show which estimator data point it corresponds to. This is necessary since the star camera solution is delayed with respect to the estimation. While the estimation starts as soon as the flight computer boots up, the first star camera solution resets it and sets a new starting point for the estimate.

In order to understand this plot in more details, we show two zoomed-in plots in Fig. VI.4. The plot in (a) shows the beginning of the estimation process. At first, the star camera solutions appear systematically off from the estimates obtained from simply propagating the gyroscopes. Each time this happens, the Kalman filter adapts the bias to attempt minimizing this difference. After about ~ 20 solutions, it appears that the filter

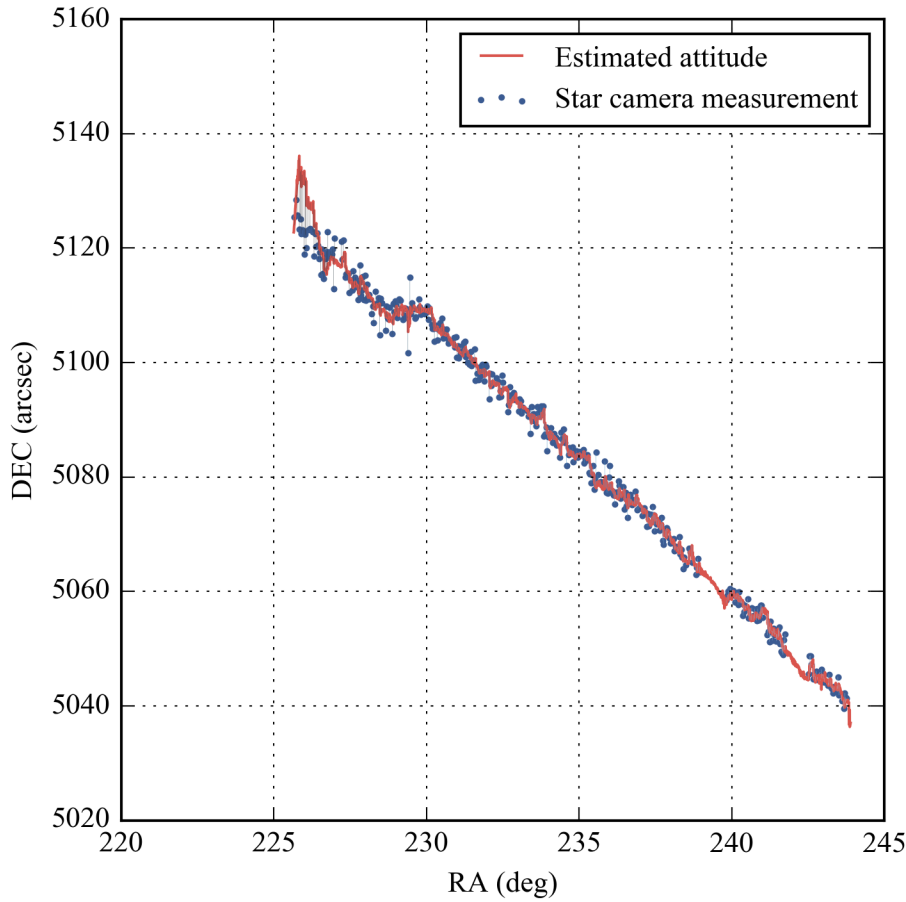


FIGURE VI.3: Attitude estimation while on the ground (see text for description).

has converged to a mean deviation around zero. In (b), we show a zoomed-in snapshot towards the end of the run, where for some amount of time, no star camera solution was found - but given the slow drift of the gyroscopes, it is not too much of a problem and the solution found after some time is still very close to the estimate.

For each star camera solution, the software estimates a correction to apply to the bias that modifies the perceived gyro velocity. The results of this bias estimation for this particular run are shown in Fig. VI.5. Note that since the star camera is inherently less sensitive in roll (about X), the X bias estimate is more noisy and takes longer to converge.

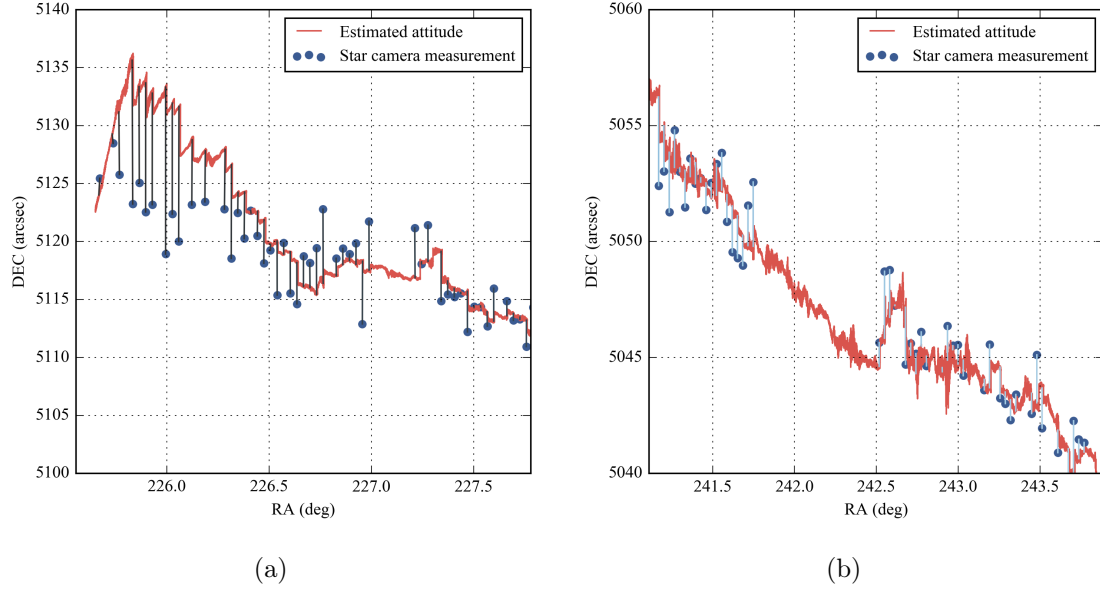


FIGURE VI.4: Zoom on attitude estimate plot (see text for description).

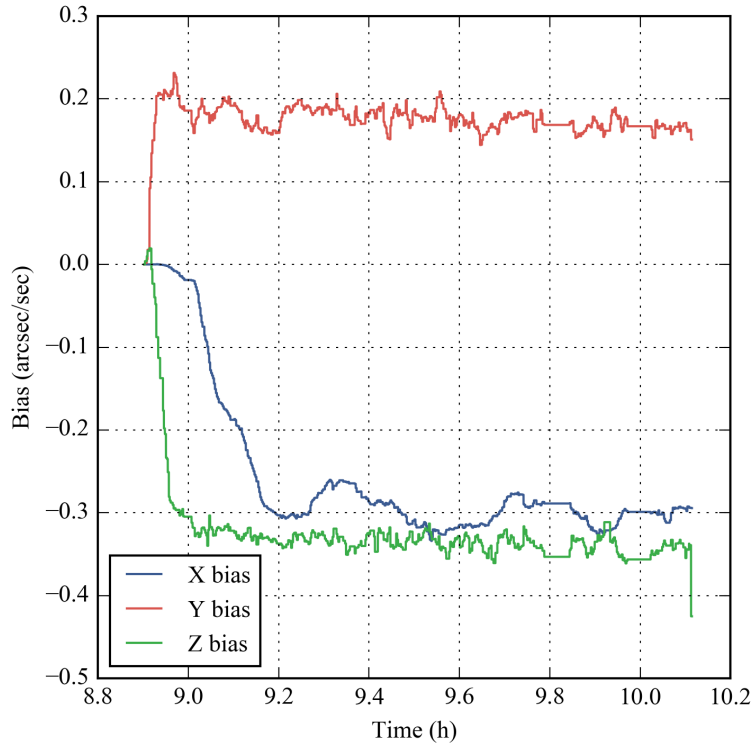


FIGURE VI.5: Bias estimation while on the ground.

Finally, we can display the error between the estimated and measured attitude in a single scatter plot (Fig. VI.6). The contours show a 2D Kernel density estimation on the dataset, indicative of how peaked the probability distribution is. For this particular run and including the Kalman filter learning process at the beginning, we obtain an overall standard deviation of $2.3''$. Note that the peak of the distribution is not exactly located at $(0, 0)$, which indicates an error in the alignment of the star camera solution with the corresponding estimator loop number. This is a known mistake from the processing software that was corrected since then.

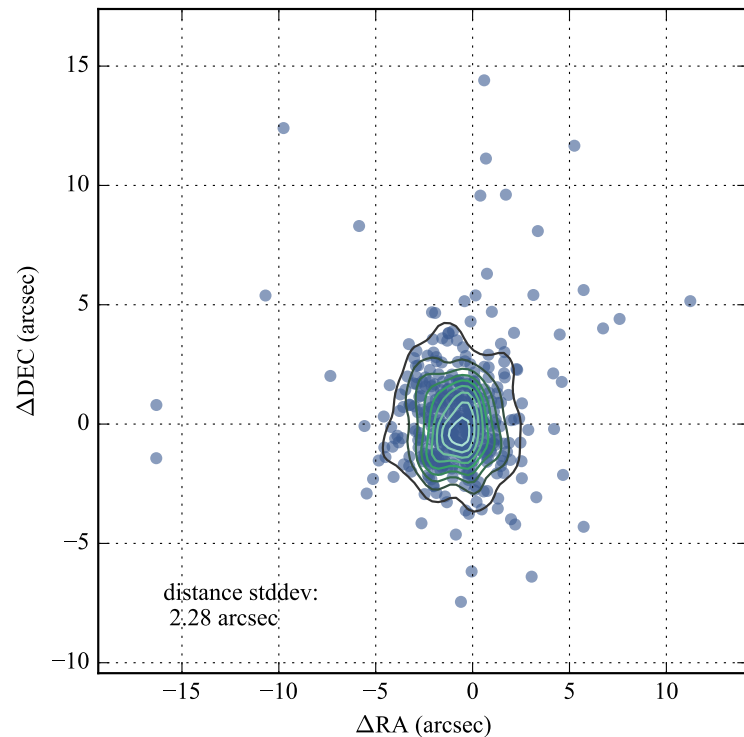


FIGURE VI.6: Error between measured position and estimated position.

VI.2.4 Telescope attitude estimator

While knowing how the gyroscope gondola is oriented is critical to properly command the actuators (which are in that reference frame), the real error perceived by the instrument and the optics is the error in the telescope reference frame. The figure we used in the previous chapter is put here again for convenience and to set the context of the relevant reference frames (Fig. VI.7). What is not shown on this picture is the fact that the telescope reference frame itself is rotated about \mathbf{y}_{tel} by some elevation angle with respect to the gyro reference frame.

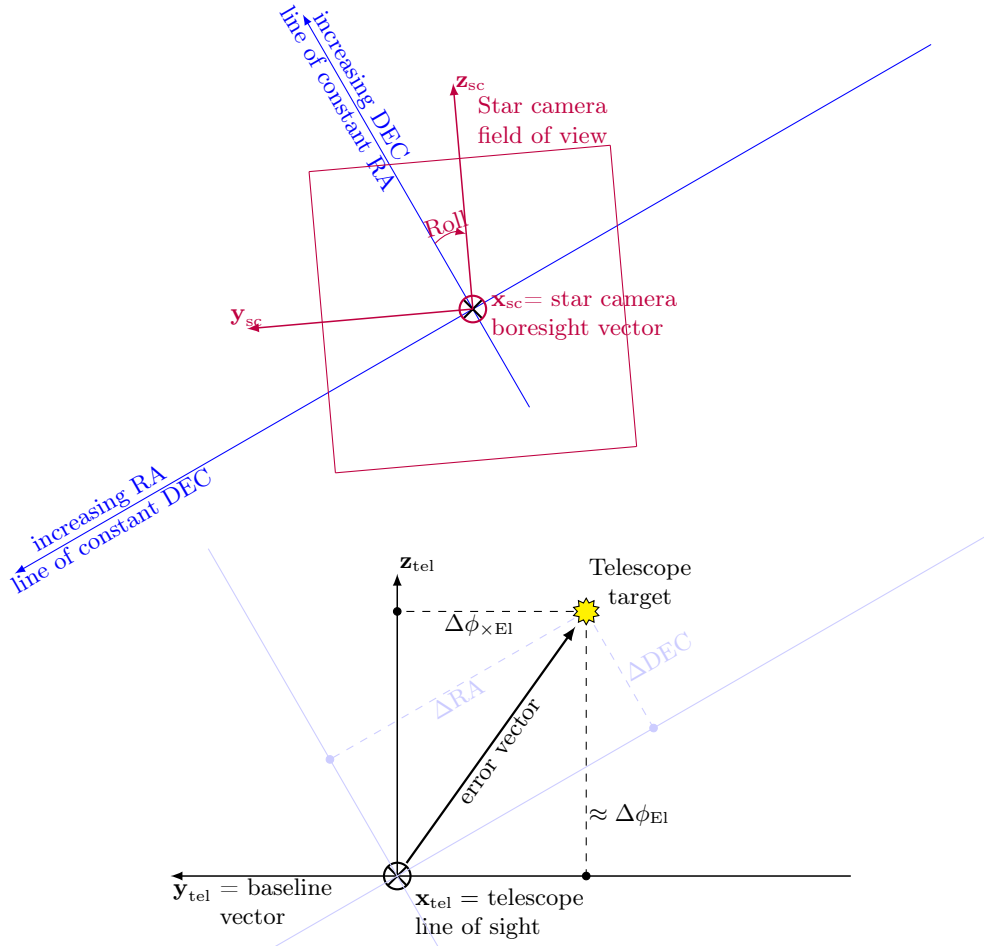


FIGURE VI.7: The star camera and telescope reference frames (see text for details). This figure is identical to Fig. V.3, and is repeated here for the reader's convenience.

The error vector is estimated in the local telescope reference frame by knowing the inertial attitude of the telescope, which is related to the inertial attitude of the star camera and the gyro reference frame. The target's coordinates can then be determined in the telescope reference frame, since we know the target's inertial coordinates. The two spherical angles that we obtain are $\Delta\phi_{x\text{El}}$ and $\Delta\phi_{\text{El}}$, which are the cross-elevation and the elevation angles, respectively.

VI.2.5 Phase estimator

The phase estimator is perhaps the most constraining aspect of this mission. Indeed, in order to properly reconstruct interferograms, the phase uncertainty needs to be extremely small, which leads to a desired attitude knowledge uncertainty the order of $\sim 0.1''$ for periods of minutes. This quantity is exclusively in cross-elevation, as elevation errors do not contribute any pathlength error.

The various components that create delay are summarized here. By far the largest delay errors will be introduced by attitude pointing errors, which correspond to the errors in cross-elevation. These errors are corrected by the Warm Delay Line to some uncertainty. In addition to those errors, the Cold Delay Line is also adding some errors. Finally, there can remain errors introduced by thermal variations of the structure.

The zero-point adjustment of the delay can be done using fringe tracking in the science channels using a bright calibrator star (see Appendix A.3). This will allow corrections for errors that are large on longer timescales. Assuming that this scheme works (it can only be tested in flight), then the only errors that are present on short timescales are the errors from the two delay lines and the attitude motion.

Without an absolute zero-point correction on shorter timescales, the phase estimator

relies exclusively on our attitude estimator, which will consist of the bulk of the error. The phase or OPD estimate is then $\text{OPD} = \phi_{\times \text{El}[\text{rad}]} \times 8 \text{ m}$, which is then fed to the WDL for correction. For scaling, a $1''$ attitude error corresponds to $40 \mu\text{m}$ error of OPD.

The tuning of the WDL and CDL was successfully achieved and is discussed elsewhere (Dhabal *et al* 2016, in press).

VI.3 Pointing tests and performance results

VI.3.1 Control system in practice

In a system that has to be remotely controlled, it is of interest to limit the number of parameters required for operations. In practice, there are only a few key parameters that are required to pilot BETTII to its inertial attitude. The most sensitive are the PID gains for the azimuth loop and the momentum dump loop, as they drastically change the response of the payload.

The Kalman filter imposes more parameters, which have a more abstract role in the attitude estimation phase of the code. For our 6-state Kalman filter estimator, 9 parameters are nominally available. They as three sets of ($\mathbf{x}, \mathbf{y}, \mathbf{z}$) weights to increase or decrease the relative importance of the measurements and process noise. The three sets control: 1) the weight of the gyroscope measurements; 2) the weight of the bias rate of change; and 3) the weight of the star camera solution. The weights multiply the expected variance of the various contributors, and will influence the way the estimator treats each incoming piece of information. The software uses by default the theoretical values for the relative weights, computed in Section V.2.1 of the previous chapter, but allows the user to tweak those parameters.

For example, increasing the weight of the bias variance indicates to the estimator that the bias is expected to vary more, allowing for faster convergence to its final solution, but with larger statistical variation in steady-state. On the contrary, a very small weight to the bias indicates that the bias is almost not expected to change, so the steady-state will have very little variation, but the impact of a new star camera measurement will be much decreased: hence, it will take a long time to reach the steady-state solution.

The star camera uses default weights that are directly measured by the solving software. When a catalog pattern match is found, a least-square estimate of the best position naturally leads to errors in RA, DEC, and ROLL. As shown in Table VI.1, the error in ROLL is considerably larger than the error in RA and DEC, so the ROLL component of the star camera solution should not be trusted as much as the other two components: it has a heavier weight on its variance.

One indirect impact of these weights is how much change is going to be induced each time a new measurement comes in. Fig. VI.4 shows distinct jumps in the gyroscope estimated position, which are caused by the fact that the camera is trusted perhaps too much. These jumps are getting smaller as the solution converges, but could still cause controls problems, as they are injected directly in the determination of the errors in the PID controllers. Hence, the star camera gains should be small when the star camera first attempts to determine the bias steady-state values (indicating that we trust the camera a lot), but should be increased when tracking to avoid trusting new measurements too much and causing jumps in the control system.

For flight, we plan to reduce these 9 Kalman filter parameters to only three (one per system, as opposed to one per axis for each system), hence simplifying the commanding from the ground. We have determined the validity of this approach in the lab.

VI.3.2 Gondola pointing stability with high bay doors closed

The most common test that we do routinely is to test the pointing stability indoors, without using the star camera. This corresponds to a pure controls test, since the star camera is not functional and we do not have knowledge of the real RA and DEC of the payload.

When the payload is lifted and hangs uncontrolled, the motion about \mathbf{z} is shown in Fig. VI.8, and the power spectrum of the velocities is shown in Fig. VI.9a. The motion can be mostly characterized by an oscillation with a ~ 100 s period, which likely is caused by the restoring torque from the crane's geometry. The excitation is likely caused by the A/C of the high bay room, as well as small motions of the high bay structure itself.

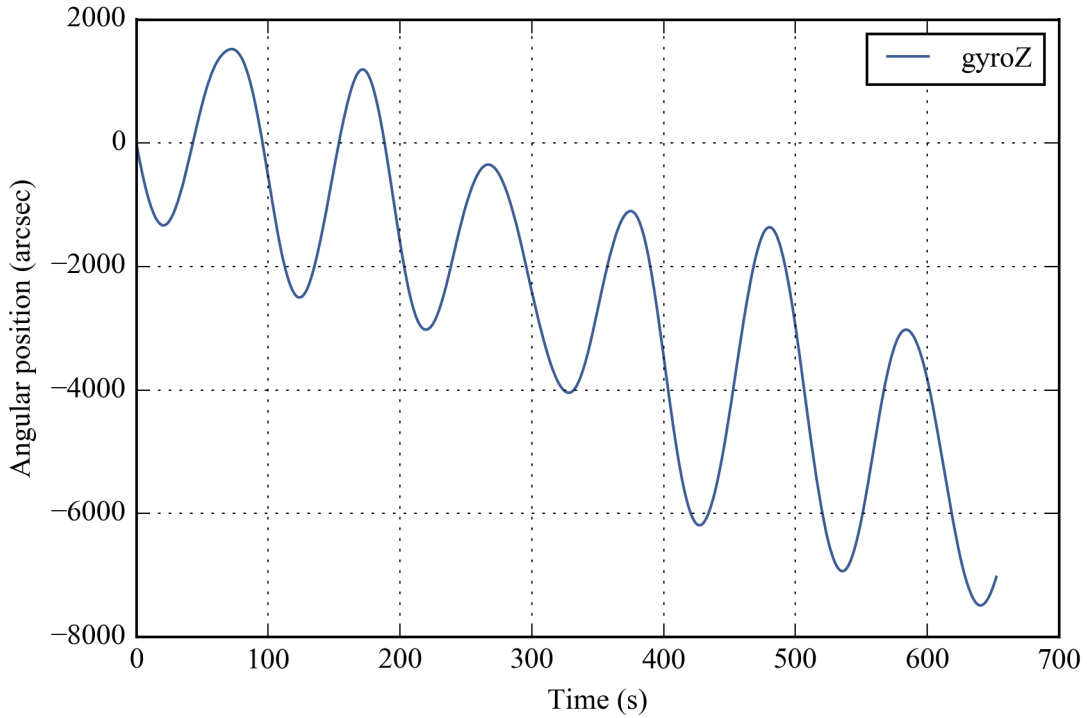


FIGURE VI.8: Integrated gyro time series while hanging and no motor on.

The PSD plots in Fig. VI.9a show that most of the motion occurs in \mathbf{z} at about 0.01 Hz. This motion is 3 orders of magnitude higher than any other contributor about

z. We can also notice a peak at 0.7 Hz that is visible in all axes, which we believe is an uncontrolled pitch motion of the payload about its long axis. This can be caused for example by a pivot mode about the gondola attachment pin. Since we see the signature of this peak in all axes, this is further indication of the non-orthogonality of the gyroscope mount. The peak at 0.5 Hz is thought to be caused by a pivot mode about the same point but about the **x** axis. The ratio of the two peak frequency roughly corresponds to the expected ratio of the moment of inertia about **y** and **x**. The peak at 0.15 Hz seen in both **x** and **y** is attributed to the pendulum mode about the crane attachment on the rook. This is consistent with a pendulum frequency $\frac{1}{2\pi}\sqrt{\frac{g}{L}}$ for $L \sim 20\text{ m}$. In flight, we expect that last mode to be at even lower frequency, by at least a factor of $\sqrt{5}$, as the balloon train is expected to be at least 5 times longer.

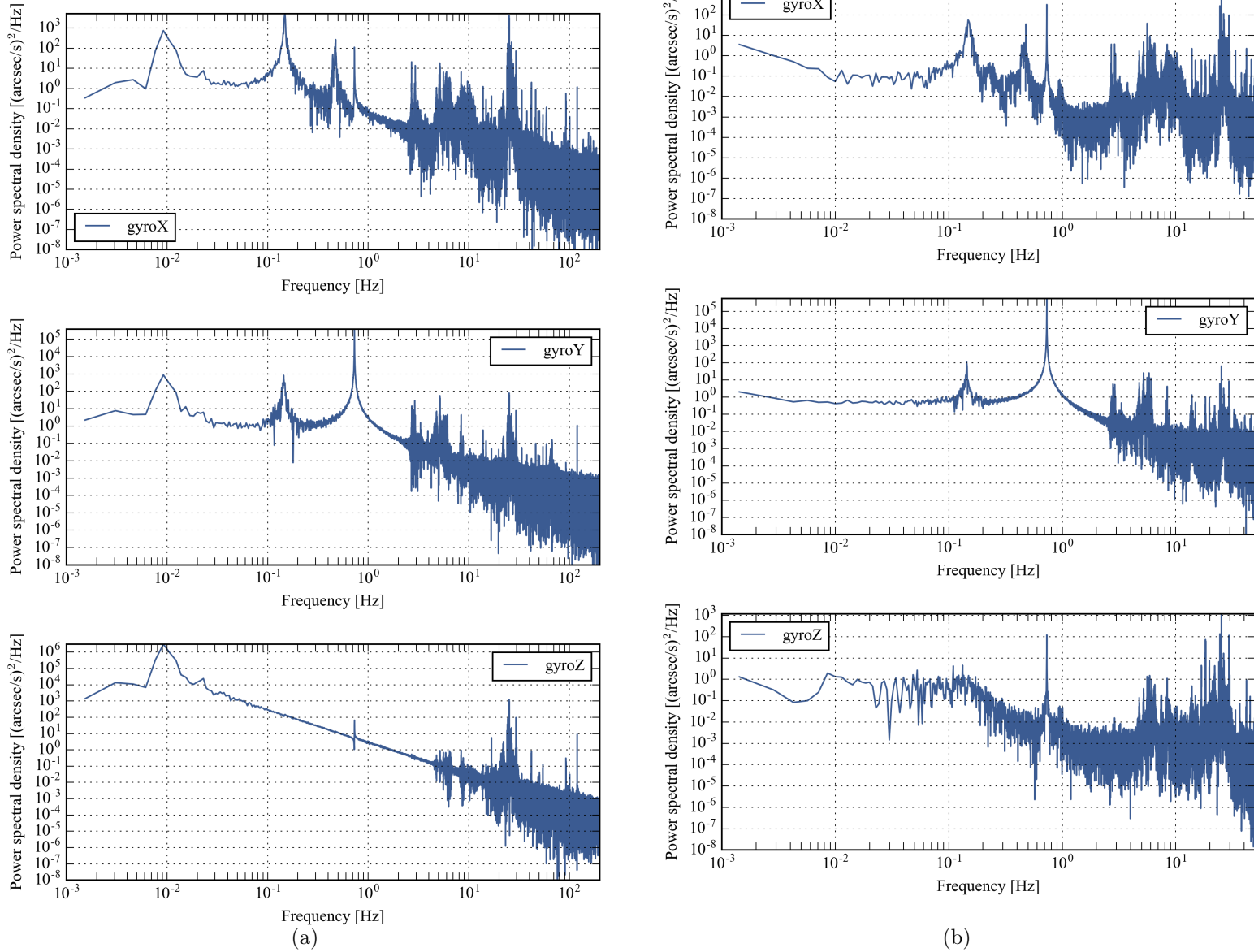


FIGURE VI.9: Noise while hanging indoors

Once lifted, the gyro PSD about **z** is quite different (see Fig. VI.9b). We are indeed able to cancel out most of the drift by about 6 orders of magnitude in power at 0.01 Hz. The resulting time series showing the cross-elevation angle is shown in Fig. VI.10. The 1σ r.m.s noise of this 700 s run is $\leq 1''$. This reflects a 1000:1 rejection ratio when the control loop is on.

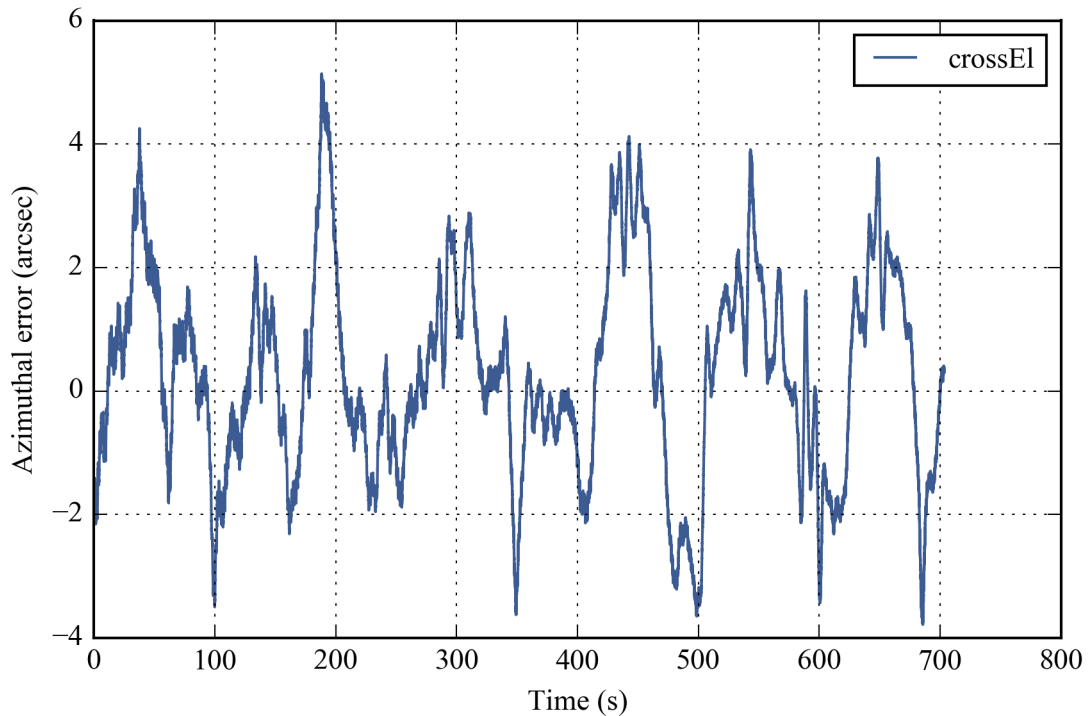


FIGURE VI.10: Cross-elevation error indoors.

Note that this behavior also implies the momentum dump loop working well. While we do not have the data to show due a mistake in the archiving software, the CCMG gimbal angle was staying for all this time within a few degrees of zero, and has been working consistently well for multiple months before this writing. This has allowed us to always maintain the gimbal in the middle of the range, and ensured long-term stability.

VI.3.3 On-sky pointing control

On-sky, lifted pointing test is the ultimate test that we can run from the ground without having the optics in place. We show two sets of data; the first one (configuration 1) was taken with the star camera positioned at $\sim 43^\circ$ elevation at the very end of the BETTII boom (pointing in the (\mathbf{y}, \mathbf{z}) plane). This gave access to a large patch of sky, as the boom could be almost sticking out through the high bay door. The second set (configuration 2) features the star camera installed at a temporary $\sim 23^\circ$ angle from horizontal in the (\mathbf{x}, \mathbf{z}) plane. This configuration is more similar to the final flight configuration where it will be at a nominal 45° from horizontal in that same plane. Putting it at an elevation of $\sim 23^\circ$ angle allows coverage of a reasonable patch of sky, although it remains very constraining.

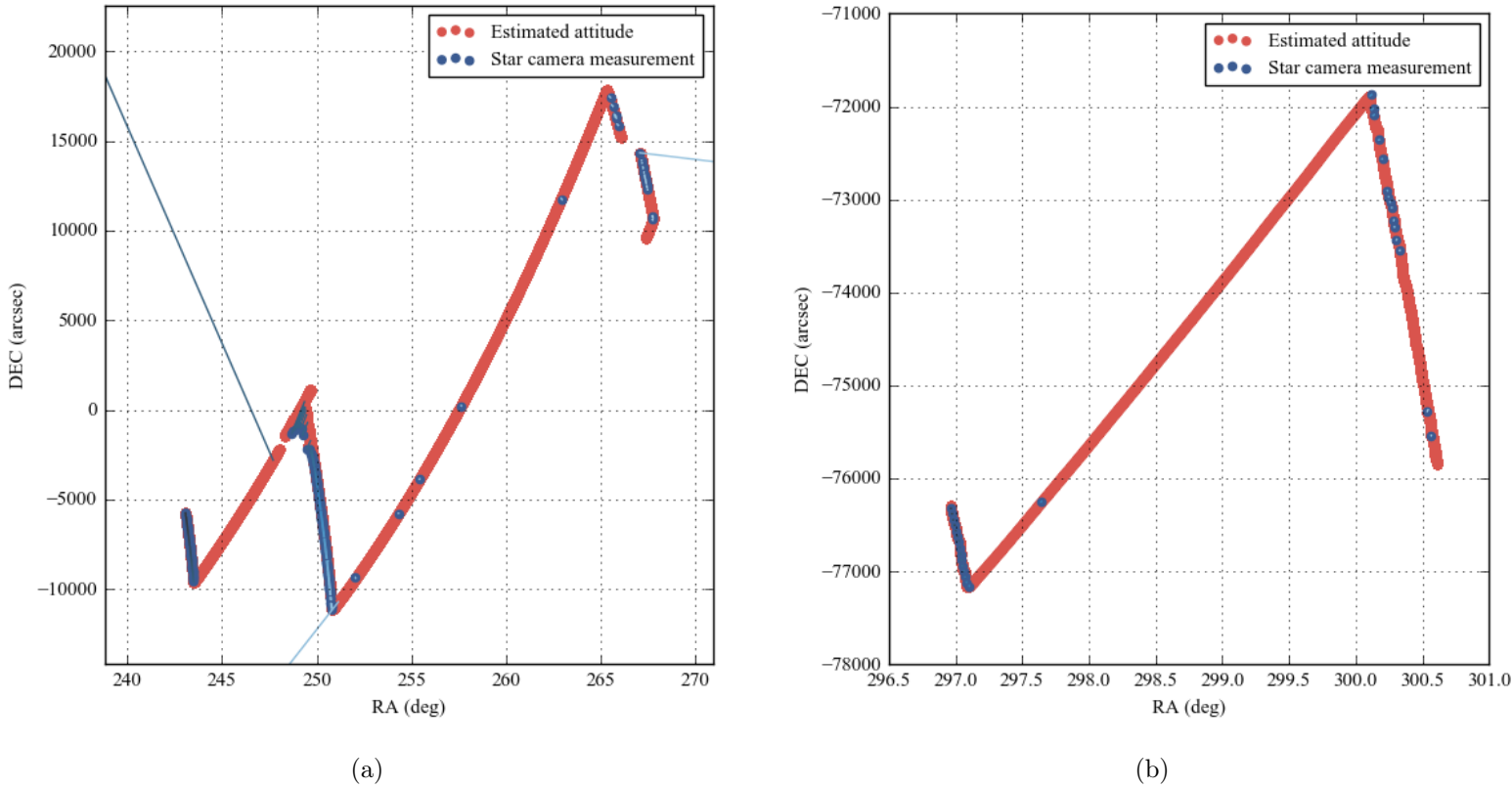


FIGURE VI.11: Slew and point on the sky. (a): Two consecutive slews with the camera in configuration 1 totalling $\sim 25^\circ$ in azimuth. The time flows from left to right on this graph. (b): Point, slew and point with the camera in configuration 2. The low rate of star camera solutions towards the end of the run is due to increased cloud coverage and increased surrounding light in the very early morning.

In Fig. VI.11 we show two typical pointing runs during a night in June 2016. That night marked the transition to configuration 2 and a reorganization of the high bay to accommodate rotating the payload so that it faces the door, and so that the telescopes can see out of the door.

For the first run that night, shown on Fig. VI.11a, we tested the new gyroscope mount, new algorithms, and new flight procedures. The run shows two consecutive slews (the swathes with little to no star camera solutions) spanning a total of about 25° in RA. Note that the scales are different in RA and DEC for display convenience. There are two noticeable features to this figure. The first is that some star camera solutions appear to be false positive, a result from non-optimal star camera parameters which involved too few stars required to confirm a match. This can be easily fixed by increasing this parameter.

The second, and more concerning problem is the apparent drift of the star camera solution after the first slew. This is what made us realize that correcting for biases only was not capturing the entire behavior of the gyroscope-star camera system pair. We interpret the resulting large error at the end of the first slew as a misalignment between the star camera orientation and the 3D gyroscope mount, and have developed flight software to properly estimate this out (see Chapter V, Section V.2.9).

If this is a problem during flight, we anticipate resetting the estimator's position each time we finish slewing, to restart the Kalman filter using the original biases.

The second run of the night, which was also our first run in configuration 2, does not exhibit this behavior, partly due to a better alignment between the gyros and the star camera, and also because the slew is half as long as the first slew in the other picture.

For this second run, we show the pointing stability in cross-elevation in Fig. VI.12. This picture is to be compared with the test done indoors, showed in Fig. VI.10. Here

the peak-to-peak errors are increased by a factor of ~ 5 , but the r.m.s deviation is still $\leq 5''$. This satisfies the $\pm 15''$ requirement for more than 95% of the points, which is very encouraging.

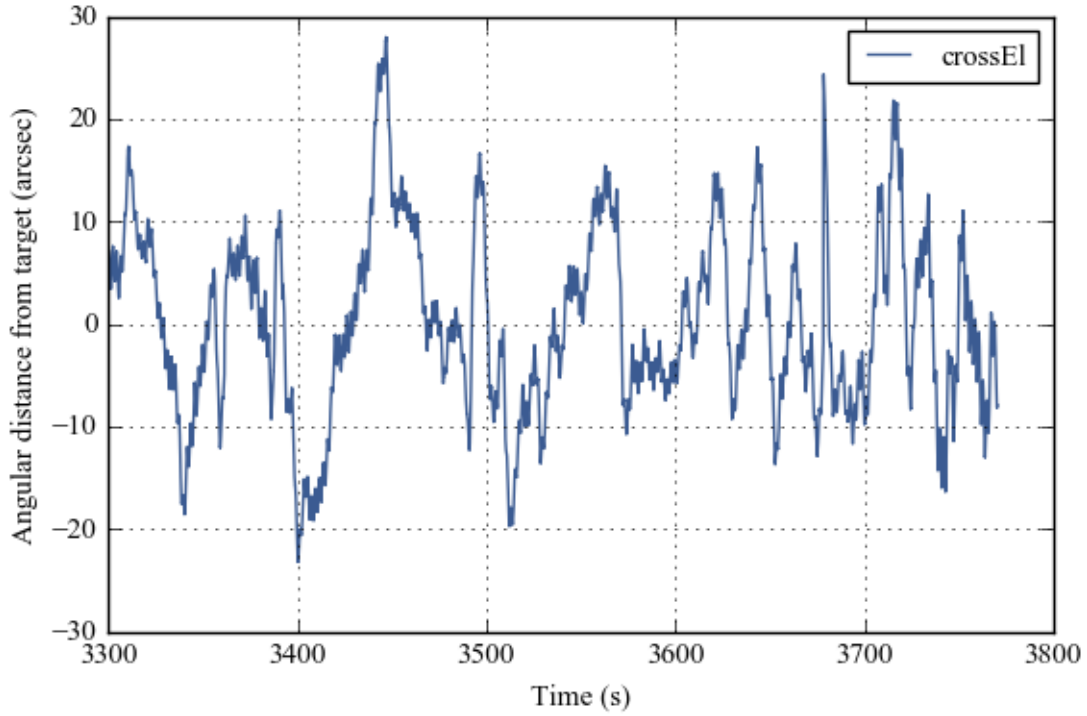


FIGURE VI.12: Cross-elevation error for a test on the sky (see text for description).

Another view at the pointing stability is proposed in Fig. VI.13, which presents the data as a 2D plot of the error in both elevation and cross-elevation, augmented by a 2D Kernel density contour plot to better show where the density peak lies. Note that contours are separated linearly, so that data is 10 times more likely to be inside the brightest contour than outside the black outer contour. The values of the contours are not meaningful, since they refer to lines of same probability density, which doesn't easily relate to a percentile value.

The striking asymmetry of this plot reveals that the elevation control is, for now,

much more accurate than the cross-elevation loop, which is to be expected due to the much lower inertia of the rotators (at the time of this run, the mirrors were not installed on the rotators). We expect degradation of the elevation accuracy once the siderostats are mounted on the rotators, even after tuning the PID gains.

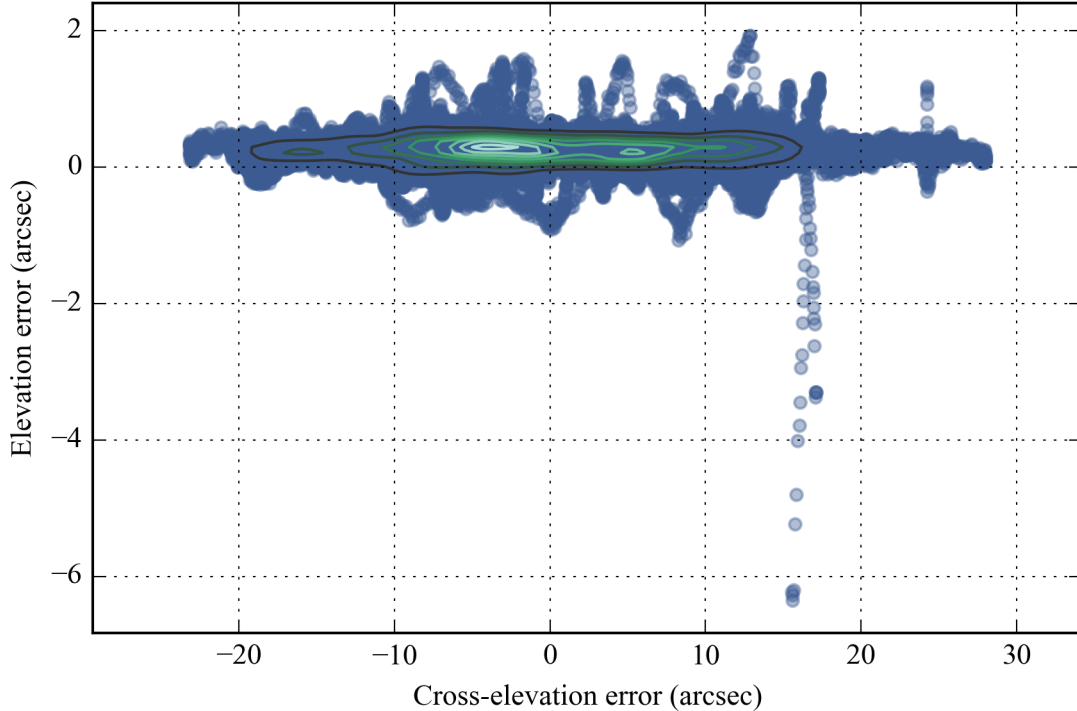


FIGURE VI.13: Elevation and cross-elevation error for a test on the sky.

VI.3.4 What's left: Fine guiding sensor loop implementation

The last on-sky pointing tests have consistently shown:

1. our ability to always know where we are pointed using a robust star camera solution
2. our ability to slew large amounts while maintaining the wheels close to their zero position (which indicates a successful momentum dumping loop)

- 3. our ability to keep the telescope vector pointed to an inertial target to within the specified $\pm 15''$ more than a large fraction of the time

- 4. our ability to have small attitude errors which can be fed to the delay line for further correction

However, despite this relative success, one key item has yet to be implemented before flight: the fine guiding loop, which brings both beams to overlap better than $1.5''$. In order to be implemented, the optics, cryostat, and tip/tilt mechanisms all have to be integrated into the payload in order to make it function.

We have started planning for this upcoming integration by designing a C++ software to handle the task at hand. In this section we present the notional architecture for this last piece of software, but warn the reader that many unknowns will remain until the optics are installed in the truss. In particular, our main concern lies in the transition mode that we called "ACQUIRE", which might require a lot of tuning.

The role of the fine guiding loop is to use the fine guiding sensor (FGS, an H1RG detector with two window readouts, one for each arm) to determine the centroid of a known source within the field of view. The location of this source on each of the readout windows of the detector (each window shows what is seen by each arm) will then be compared to known pixel locations that ensure overlap between the two science beams. The error signals are then Δx_L , Δy_L , Δx_R , Δy_R , where the subscripts designate the left and right arm, respectively. These error signals are rotated to the proper reference frame and fed to the tip/tilt mechanisms, which zeroes them out very quickly thanks to their very large actuation bandwidth and very small inertia.

Since the errors are zeroed out almost instantaneously, these error signals cannot be used to determine the attitude of the entire payload. However, the angular deviation of

each tip/tilt stage from their nominal position has information about the overall pointing error of the truss. To illustrate this feature, let's suppose that both windows are perfectly aligned and the detector axes (X,Y) match the elevation and cross-elevation, respectively. In this case, if both tip/tilt stage need to correct for a positive elevation error, it means that the entire truss is mispointed in elevation. Similarly, if the cross-elevation correction happens in the same direction, it means that a movement of the truss in cross-elevation will correct it and bring the tip/tilt stages to their nominal position.

We can generalize this statement by saying that the common-mode deviations from the nominal position of the tip/tilt stages represent an estimator for the attitude difference between the payload and the guide star. This information is processed, rotated in the correct reference frame, and injected into the Kalman filter estimator in replacement of a star camera measurement. The weight (or variance) of this new measurement is considerably smaller than the star camera, since it is the most trusted attitude measurement that we can have.

At full speed and sampling only $15'' \times 15''$ windows, the fine guiding loop can provide these absolute position estimates at 50 Hz.

There are many challenges with this system. The first is to robustly, autonomously identify the chosen guide star within the field of view. For this, we design a blob-finding software which examines the images received from the fine guiding sensor and identifies the brightest N blobs in the image. The targets are carefully chosen so that the guide stars are the brightest sources in the image, which enhances the chances of finding the correct star.

ACQUIRE mode involves progressively reducing the size of the FOV in the fine guiding sensor, starting with a $5' \times 5'$ FOV at 2 s per frame, down to $15'' \times 15''$ at 50 Hz.

Chapter VII

Concluding remarks

There is nothing like a dream to create the future.

V. Hugo

High angular resolution observations in the far-infrared are essential to determine the physical properties of young stars, which are preferentially forming in embedded stellar clusters. Using SOFIA FORCAST, we showed results of a survey of 10 nearby clusters, which observed 70 YSOs and 14 extended sources, between 11 and 37 μm . The higher angular resolution of FORCAST allowed us to map these regions at an effective resolution which compares with *Spitzer* IRAC at 8 μm . We use a radiative transfer modelling tool to fit physical parameters of the point sources in our clusters with sufficient amount of data, and propose a detailed study of IRAS 20050+2720. The poor angular resolution at long wavelengths cause uncertainties in the SEDs, since it is not clear that the measured fluxes are associated with their short-wavelength counterparts. This is an inherent limitation which can cause over-interpretation of SED fitting results, and can be lifted through obtaining higher angular resolution between \sim 30 μm and \sim 300 μm , which no existing instrument can provide.

BETTII is a far-infrared balloon-borne interferometer, and a pathfinder towards this type of instruments. It is schedule for its commissioning flight in the Fall of 2016. We discuss the design of the balloon payload and the instrument, and derive its expected

sensitivity. As part of this sensitivity analysis effort, we developed a new technique to more accurately determine the spectral sensitivity of spatio-spectral interferometers such as BETTII. These sensitivity predictions are used as requirements to design every aspect of the mission.

In this work we detail our contribution to one aspect of the mission, which is the control system. As a remote-controlled, flying interferometer, achieving phase stability is challenging and requires detailed attention. We propose a control strategy that ensures appropriate phase control and allows us to gain appropriate phase knowledge to reconstruct the interferograms, which contain the scientific data. Finally, we discuss the practical implementation of this strategy, and some preliminary test results which occurred in the Spring of 2016.

Over the course of 5 years, the BETTII project went from paper drawings to its first flight campaign. I have had the opportunity to be involved in all aspects of the project, which provided me with a unique view of how to build instruments to address a specific scientific question. In addition to the day-to-day engineering challenges, a global vision of the process was acquired, which made this experience irreplaceable.

The mechanical, cryogenic, optical, electrical, and software infrastructure developed from scratch for BETTII form a powerful pointed observatory platform that can host various instruments in the future. If BETTII succeeds and is able to obtain more funding over the years, the versatility of its subsystems make them relatively straightforward to repair, enhance, or adapt to future goals.

The work and thoughts spent on BETTII during the past years, combined with

the approaching Decadal Survey discussions, have converged towards a new concept for a potential Probe-class space telescope: the Space High Angular Resolution Probe for the InfraRed (SHARP-IR, pronounced "sharper"). This new concept, which is currently going through the Architecture Design Lab and soon through the Instrument Design Lab at NASA GSFC, could see the full potential of double-Fourier interferometry come to fruition, and provide transformational science in the far-infrared. The concept was unveiled for the first time at the SPIE conference in Edinburgh (Rinehart *et al.* 2016), and synthesizes all of our lessons learned from designing and building BETTII.

Appendix A

Far-IR double-Fourier

interferometers and their spectral sensitivity

A.1 Deriving the Interferogram Equation in a Double Fourier System

The interferogram from a double-Fourier system is different from the interferogram for an FTS in several ways that derive from the fact that the double-Fourier system starts with two independent input beams viewing the same astronomical target. For this derivation, we will follow the convention in the FTS literature and consider the propagation of a single plane wave (radiation from a point source at infinity) at wavenumber $\sigma \equiv 1/\lambda$ through the system.

Figure 2 in the main text shows the setup for a typical double-Fourier system with the K-mirror on one arm to keep the sky images at the same rotation on the two paths, and the delay line in the other arm to allow adjustment of the relative path lengths between

path 1 and 2. The plane wave travels a distance x_1 on path 1 from an entrance aperture an arbitrary distance above the siderostat to the beam combiner: $a_1(\sigma)e^{-2\pi i \sigma x_1 + \phi}$, where a_1 is the amplitude of the electric field and ϕ corresponds to an arbitrary phase offset. For convenience of notation, in the following derivation we drop the amplitudes' dependence on wavenumber by writing a_1 instead of $a_1(\sigma)$.

The wave also undergoes phase shifts caused by reflections and partial reflections along the path. A full reflection for light traveling in air or a vacuum causes a 180 deg phase shift; a 50% reflection at the beam splitter/combiner causes a 90 deg phase shift between reflected and transmitted beam (Lawson, 2000). Since the instrument measures the combined light at the detectors, what matters is the difference in the numbers of reflections along path 1 and 2. In the case of the particular BETTII implementation, path 1 contains one more reflection than path 2.

The electrical fields arriving at the "+" and "-" detectors are then:

$$A_- = a_1 e^{-2\pi i \sigma x_1 + i\pi + i\pi/2 + \phi} + a_2 e^{-2\pi i \sigma x_2 + \phi}, \quad (\text{A.1})$$

$$A_+ = a_1 e^{-2\pi i \sigma x_1 + i\pi + \phi} + a_2 e^{-2\pi i \sigma x_2 + i\pi/2 + \phi}, \quad (\text{A.2})$$

where the π phase shift on path 1 occurs because there is one extra reflection compared to path 2 (see Fig. IV.2), and ϕ corresponds to an arbitrary phase offset. The detectors are power detectors so defining the intensity $I = A^* A$:

$$I_- = a_1^2 + a_2^2 + a_1 a_2 \left(e^{-2\pi i \sigma (x_1 - x_2) + 3i\pi/2} + e^{2\pi i \sigma (x_1 - x_2) - 3i\pi/2} \right), \quad (\text{A.3})$$

$$I_+ = a_1^2 + a_2^2 + a_1 a_2 \left(e^{-2\pi i \sigma (x_1 - x_2) + i\pi/2} + e^{2\pi i \sigma (x_1 - x_2) - i\pi/2} \right). \quad (\text{A.4})$$

Defining $x \equiv x_1 - x_2$ and expanding the complex exponentials, the equations can be simplified to:

$$I_- = (a_1^2 + a_2^2) \left(1 - \frac{2a_1 a_2}{a_1^2 + a_2^2} \sin(2\pi\sigma x) \right), \quad (\text{A.5})$$

$$I_+ = (a_1^2 + a_2^2) \left(1 + \frac{2a_1 a_2}{a_1^2 + a_2^2} \sin(2\pi\sigma x) \right), \quad (\text{A.6})$$

where x is now the difference in the physical length between the two light paths. For the case of equal wave amplitudes on path 1 and 2 ($a_1 = a_2 = a$):

$$I_{\pm} = 2a^2(1 \pm \sin(2\pi\sigma x)). \quad (\text{A.7})$$

The generalization of this equation to a source distribution on the sky requires the recognition that a_1 and a_2 are complex values such that $|a_1|^2(\sigma)$ and $|a_2|^2(\sigma)$ are power from the source at wavenumber σ , while $a_1 a_2^*$ is the correlated power seen through the two apertures which is the source spatial visibility, $\gamma(\mathbf{B}, \sigma)$, and is in general a complex valued function. $\gamma(\mathbf{B}, \sigma)$, which is a function of the baseline vector \mathbf{B} connecting the two light collectors, and σ , is the Fourier transform of the source emission distribution on the sky. For the general case, the previous equations become:

$$I_- = |a_1|^2 + |a_2|^2 + \gamma(\mathbf{B}, \sigma)e^{-2\pi i\sigma(x_1-x_2)+3i\pi/2} + \gamma^*(\mathbf{B}, \sigma)e^{2\pi i\sigma(x_1-x_2)-i3\pi/2}, \quad (\text{A.8})$$

$$I_+ = |a_1|^2 + |a_2|^2 + \gamma(\mathbf{B}, \sigma)e^{-2\pi i\sigma(x_1-x_2)+i\pi/2} + \gamma^*(\mathbf{B}, \sigma)e^{2\pi i\sigma(x_1-x_2)-i\pi/2}. \quad (\text{A.9})$$

The same simplification as before can be done except that $\gamma(\mathbf{B}, \sigma)$ is a complex-valued function. If we define the normalized spatial visibility as

$$\mathcal{V}_{\mathbf{B}}(\sigma) = \frac{2\gamma(\mathbf{B}, \sigma)}{a_1^2 + a_2^2}, \quad (\text{A.10})$$

then the equation for I_{\pm} becomes:

$$I_{\pm} = (|a_1|^2 + |a_2|^2) [1 \pm (\text{Re}(\mathcal{V}_{\mathbf{B}}(\sigma)) \sin(2\pi\sigma x) - \text{Im}(\mathcal{V}_{\mathbf{B}}(\sigma)) \cos(2\pi\sigma x))], \quad (\text{A.11})$$

$$I_{\pm} = (|a_1|^2 + |a_2|^2) [1 \pm \text{Re}(i\mathcal{V}_{\mathbf{B}}(\sigma)e^{-2\pi i\sigma x})], \quad (\text{A.12})$$

where $\text{Re}(f)$ is the real component of f and $\text{Im}(f)$ is the imaginary component.

The same style of derivation can be done with for a realistic instrument with a complex transfer function. If we characterize the spectral transmission function as $t_1(\sigma) = |t_1(\sigma)|e^{i\Phi_1(\sigma)}$ along path 1, and $t_2(\sigma) = |t_2(\sigma)|e^{i\Phi_2(\sigma)}$ on path 2, then the amplitude mismatch of the spectral transmission function in each path reduces the power in the interferogram and the phase differences introduce a phase factor $\Phi_i = \Phi_1 - \Phi_2$ into the exponential term. As a result, the source visibility in the previous equations is multiplied by a normalized, instrumental visibility loss term, $\mathcal{V}_i = |\mathcal{V}_i(\sigma)|e^{i\Phi_i(\sigma)}$:

$$I_{\pm} = (|t_1|^2|a_1|^2 + |t_2|^2|a_2|^2) [1 \pm \text{Re}(i\mathcal{V}_{\mathbf{B}}(\sigma)\mathcal{V}_i(\sigma)e^{-2\pi i\sigma x})]. \quad (\text{A.13})$$

A.2 Spectral noise in presence of gaussian phase noise

Suppose that the signal is a line of power density $2\mathcal{S}$ centered on bin number k corresponding to wavenumber σ_k . In the complex interferogram, the line has a power density

\mathcal{S} in bin k and $-\mathcal{S}$ at $-k$, and zero everywhere else. To simplify the analysis, let's focus on the positive frequencies, which only contain half the noise. The interferogram at delay $x_n = ndx$ is $\mathcal{I}_k(x_n) = \mathcal{S}\delta\sigma e^{-2i\pi\sigma_k x_n}$. Through a simple DFT, the value of the line in the spectrum in ideal conditions is:

$$dx \mathbf{DFT}(\mathcal{I}_k(x_n))[k'] = dx \sum_{n=-N/2}^{N/2-1} \mathcal{S}\delta\sigma e^{-2i\pi\sigma_k x_n} e^{2i\pi n k'/N} = dx \sum_{n=-N/2}^{N/2-1} \mathcal{S}\delta\sigma e^{-2i\pi(k-k')n/N}, \quad (\text{A.14})$$

which is equal to $dx N \mathcal{S} \delta\sigma = \mathcal{S}$ for $k = k'$ and zero everywhere else. Note that we have $\sigma_k x_n = k\delta\sigma ndx = kn/N$. and $\delta\sigma = (Ndx)^{-1}$. The phase noise degrades the effective power of the line, so it is now $\mathcal{S}e^{-\sigma_\Phi^2/2}$ (Richards, 2003). The noisy interferogram is $\mathcal{I}_k(x_n) = \mathcal{S}\delta\sigma e^{-2i\pi kn/N} e^{i\Phi_r(x_n)}$.

Designating the operator $\langle \rangle$ as the ensemble average, the noise $\sigma_{\mathcal{S}}^2$ in the interferogram is the variance of the DFT:

$$\begin{aligned} \sigma_{\mathcal{S}}^2[k'] &= \mathbf{VAR}(dx \mathbf{DFT}(\mathcal{I}_k(x_n))[k']) \\ &= dx^2 \left(\left\langle \left| \sum_n \mathcal{I}_k(x_n) e^{2i\pi n k'/N} \right|^2 \right\rangle - \left| \left\langle \sum_n \mathcal{I}_k(x_n) e^{2i\pi n k'/N} \right\rangle \right|^2 \right), \\ &= dx^2 \left(\sum_n \sum_{n'} \langle \mathcal{I}_k(x_n) \mathcal{I}_k^*(x_{n'}) \rangle e^{2i\pi(n-n')k'/N} - \sum_n \sum_{n'} \langle \mathcal{I}_k(x_n) \rangle \langle \mathcal{I}_k^*(x_{n'}) \rangle e^{2i\pi(n-n')k'/N} \right), \\ &= dx^2 \sum_n \sum_{n'} [\langle \mathcal{I}_k(x_n) \mathcal{I}_k^*(x_{n'}) \rangle - \langle \mathcal{I}_k(x_n) \rangle \langle \mathcal{I}_k^*(x_{n'}) \rangle] e^{2i\pi(n-n')k'/N}. \end{aligned}$$

We can write $\langle \mathcal{I}_k(x_n) \mathcal{I}_k^*(x_{n'}) \rangle = \langle \mathcal{S}^2 \delta\sigma^2 e^{-2i\pi(n-n')k/N} e^{i(\Phi_r(x_n) - \Phi_r(x_{n'}))} \rangle$. This quantity is equal to $\mathcal{S}^2 \delta\sigma^2 e^{-2i\pi(n-n')k/N} e^{-\sigma_\Phi^2}$ when $n \neq n'$ and equal to $\mathcal{S}^2 \delta\sigma^2$ when $n = n'$. The quantity $\langle \mathcal{I}_k(x_n) \rangle \langle \mathcal{I}_k^*(x_{n'}) \rangle$ is equal to $\mathcal{S}^2 \delta\sigma^2 e^{-2i\pi(n-n')k/N} e^{-\sigma_\Phi^2}$ for all n and n' . Hence, the term in the sum is nonzero only for $n = n'$, for which it is $\mathcal{S}^2 \delta\sigma^2 (1 - e^{-\sigma_\Phi^2})$. The value

of the sum is then:

$$\sigma_S^2[k'] = dx^2 \sum_n S^2 \delta\sigma^2 (1 - e^{-\sigma_\Phi^2}), \quad (\text{A.15})$$

$$= dx^2 N S^2 \delta\sigma^2 (1 - e^{-\sigma_\Phi^2}), \quad (\text{A.16})$$

$$= \frac{1}{N} S^2 (1 - e^{-\sigma_\Phi^2}). \quad (\text{A.17})$$

This quantity is independent of k' , so the noise is white. The negative frequencies contribute the same amount, doubling the noise variance. However, we are only considering the imaginary part of the spectrum, so only half the noise variance is important in our calculation of our SNR. The last expression thus represents the variance of the noise that is useful for our SNR calculations.

A.3 Fringe tracking in the science channels

For sufficiently bright sources, it is possible to self-calibrate the OPD between subsets of the M interferograms in a track, to prevent the drift of an indirect OPD estimator. The idea is to bin consecutive interferograms in subsets in order to build up enough SNR to clearly see a fringe and be able to estimate its position with sufficient accuracy. Then, the different subsets within a track can be offset and co-added with better accuracy (smaller OPD noise) than if we were co-adding the M interferogram individually with only the instrument OPD estimator noise. The best scenario would be when the fringe has a high SNR in each single interferogram - which will be the case of calibrators for BETTII.

There are many ways to fit the location of the fringe center, and the error associated with each method is highly implementation-specific. Here, we consider the simple example of a fringe tracking algorithm in two steps (Rizzo et al., 2012): a Hilbert

transform of the interferogram to obtain its envelope; and a centroid of the points of the envelope above a certain $\text{SNR}_{\mathcal{I}}$ threshold. The Hilbert transform doubles the error variance in the interferogram, and in the worst case, the centroid has an error variance of approximately $(n \times \text{SNR}_{\mathcal{I}}^2)^{-1}$, where n is the number of data points above the threshold $\text{SNR}_{\mathcal{I}}$. The conversion to a phase leads to a phase error variance equal to $[\sigma_{\Phi}^2(\sigma)]_{\text{direct}} \sim 2 \times (2\pi)^2 \sigma^2 / \sigma_0^2 / (n \times \text{SNR}_{\mathcal{I}}^2)$. This indicates that when the SNR is high enough, this direct estimate of the phase can become better than the estimate coming from an indirect OPD estimator with corresponding phase error variance $[\sigma_{\Phi}^2(\sigma)]_{\text{indirect}}$, like the attitude estimator used on BETTII.

In Chapter IV, Fig. IV.4, we use Eq. IV.20 and a total phase error variance which is a combination of the phase noise from the direct and indirect methods, to ensure continuity:

$$\sigma_{\Phi}^2(\sigma) = \left(\frac{1}{[\sigma_{\Phi}^2(\sigma)]_{\text{direct}}} + \frac{1}{[\sigma_{\Phi}^2(\sigma)]_{\text{indirect}}} \right)^{-1}. \quad (\text{A.18})$$

On BETTII, the bulk of the phase noise comes from the uncertainties in co-adding consecutive scans (timescale 3), as the estimator uses an indirect method and never really measures the absolute phase for low-SNR targets. For high-SNR targets, the method described above can serve as a fringe tracker that not only is useful for calibration, but can also substantially improve the phase estimator's stability over long periods of time by preventing drifts.

Appendix B

Attitude representation in three dimensions

There are three common representations of the orientation, or *attitude*, of an object in a 3-dimensional Euclidian reference frame: in the following we will discuss the Tait-Bryan angles (which are very similar to, and sometimes confused with proper Euler angles), rotation matrices, and quaternions. All of them can be understood as a rotation of the initial reference frame $I = \{\mathbf{I}, \mathbf{J}, \mathbf{K}\}$ into the object's local reference frame $L = \{\mathbf{i}, \mathbf{j}, \mathbf{k}\}$.

The reference frame I is assumed to be fixed while L is allowed to move. We can write each unit vector as follows: $\mathbf{I} = {}^I[1, 0, 0]^T$, $\mathbf{J} = {}^I[0, 1, 0]^T$, $\mathbf{K} = {}^I[0, 0, 1]^T$, and $\mathbf{i} = {}^L[1, 0, 0]^T$, $\mathbf{j} = {}^L[0, 1, 0]^T$, $\mathbf{k} = {}^L[0, 0, 1]^T$. $\{\mathbf{I}, \mathbf{J}, \mathbf{K}\}$ and $\{\mathbf{i}, \mathbf{j}, \mathbf{k}\}$ are orthonormal bases to I and L , respectively. The subscript before the vector indicates in which reference frame the vector is expressed, and the T after the vector indicates the transpose operation. We will keep this formalism for all vectors and matrices in this work.

B.1 Tait-Bryan/Euler angles

The Tait-Bryan formalism corresponds to a sequence of three angles, each corresponding to a rotation about one of the object's main axes: these are also called "intrinsic" rotations. They differ from "extrinsic" rotation, sometimes called "Euler angles", which correspond to a rotation about one of the axes of the global (fixed) reference frame. In the following, we will focus on using exclusively intrinsic rotations, as they are more intuitive. Note that sometimes people call this formalism "Euler angles" as well, so it is important to understand how this works. With this formalism, we start in the global reference frame and rotate the reference frame three times to end up in the *body* reference frame, which describes the final orientation of an object. We will most often choose a well-known sequence of rotation such as the $z - y' - x''$ order, which corresponds to the angles used to describe the heading, elevation and bank of an aircraft with respect to a reference frame attached to the Earth, for example the North-East-Down reference frame. The first rotation about **k** will transform I into L' . The second rotation, about the **j** axis of the rotated frame L' , transforms L' into L'' . The third and last rotation, about the **i** axis of L'' , will transform L'' into the final orientation, L , of the object (see Fig. B.4).

This sequence of rotation can be used to represent the rotation matrix that describes the attitude of an image of the sky. Celestial coordinates are usually given in terms of right ascension, declination. To fully describe the image of a patch of sky, we need another degree of freedom, which is the roll of the image about the boresight. When given these three angles: RA, DEC, and ROLL, one can reconstruct the attitude using the Tait-Bryan angles in the $z - y' - x''$ order, where the first, second and third elementary rotations correspond to the rotations in right ascension, declination and roll, respectively.

B.2 Rotation matrices

Perhaps the most common way to express the orientation of an object within a given reference frame is to use the matrix that describes the rotation from one reference frame to the other. Since rotations are linear transformations of \mathcal{R}^3 , there always exists a matrix to represent it. If we choose an orthonormal basis to \mathcal{R}^3 , matrices representing rotations are 3×3 orthogonal matrices. When given the traditional matrix multiplication operation, 3×3 orthogonal matrices with determinant of +1 form a group which is an isomorphism of the group of all 3-D rotations of Euclidian space (subsequently called SO(3) for "special orthogonal group"): it means that each rotation can always be represented by exactly one 3×3 orthogonal matrix. This theorem is the mathematical translation of the sometimes obvious intuition that rotation matrices always exist, are unique for a given rotation, and that the composition of two rotations is still a rotation. It also expresses the requirement that the corresponding rotation matrices have a determinant of +1, which can be useful when we consider numerical implementations of these matrices, as rounding errors might require a periodic normalization of the matrices to ensure they stay in this group. Note that the group of rotation is a cyclic group, since a rotation of an angle θ is the same as a rotation of $\theta + 2\pi$.

We are interested in matrices describing rotations of entire coordinate systems, which are also called *passive* rotations. This is different from matrices describing rotations of vectors within a given coordinate system (called *active* rotations), and an important distinction that can often lead to confusion. Let's suppose that we have an initial coordinate system I of basis $\{\mathbf{I}, \mathbf{J}, \mathbf{K}\}$, and a second coordinate system L of basis $\{\mathbf{i}, \mathbf{j}, \mathbf{k}\}$. For example, this applies when L is the body reference frame, and we want to understand its

orientation with respect to an initial reference frame, such as the inertial reference frame. The basis vectors of L can all be expressed by a linear combination of the basis vector of I . This transformation can be described using the *direction cosine matrix*, which has the following expression:

$${}^I_L \mathcal{R} = \begin{bmatrix} \mathbf{i} \cdot \mathbf{i} & \mathbf{j} \cdot \mathbf{i} & \mathbf{k} \cdot \mathbf{i} \\ \mathbf{i} \cdot \mathbf{j} & \mathbf{j} \cdot \mathbf{j} & \mathbf{k} \cdot \mathbf{j} \\ \mathbf{i} \cdot \mathbf{k} & \mathbf{j} \cdot \mathbf{k} & \mathbf{k} \cdot \mathbf{k} \end{bmatrix}. \quad (\text{B.1})$$

The columns of this matrix correspond to the expression of the basis vectors of I expressed in the basis of L . This is what we call the *rotation matrix* between I and L , and transforms vectors expressed in I into their representation in L . With this convention, the matrix pre-multiplies the vector. For example, if we have some vector ${}^I \mathbf{u}$ expressed in the initial reference frame I , its expression in the reference frame L will be ${}^L \mathbf{u} = {}^I_L \mathcal{R} {}^I \mathbf{u}$.

Note that the rotation matrix ${}^I_L \mathcal{R}$ is an orthogonal matrix of determinant +1: each columns are orthogonal with each other and of unit norm. Hence, the inverse of this matrix is its transpose, which also corresponds to the rotation of a vector from frame I to frame L : $({}^I_L \mathcal{R})^{-1} = ({}^I_L \mathcal{R})^T = {}^L_I \mathcal{R}$.

Let's take an example and consider the unit vector ${}^I \mathbf{u} = {}^I(1, 0, 0)$, expressed in I originally. Now, let's rotate the coordinate frame I by an angle θ with respect to the axis \mathbf{k} . The new reference frame is $L' = \{\mathbf{i}', \mathbf{j}', \mathbf{k}'\}$. For simplification, let's consider that $\theta = +90$ degrees. It is clear that the vector \mathbf{i} is now equal to $-\mathbf{j}'$, and ${}^{L'} \mathbf{i} = {}^{L'}(0, -1, 0)$.

In the more general case, let's suppose that the local reference frame L' is rotated by an angle θ about the \mathbf{k} axis (Fig. B.2) with respect to the reference frame I . The

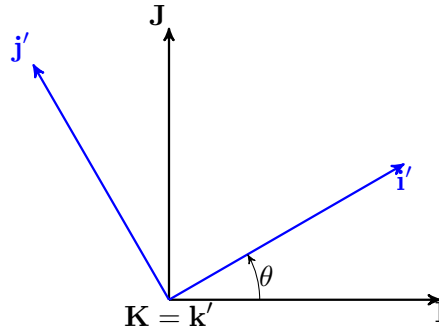


FIGURE B.1: The $\{i', j', k'\}$ reference frame (in blue) is rotated with respect to $\{I, J, K\}$ (in black). The rotation is about the axis K by an angle $\theta = 30$ degrees.

convention we adopt sets the rotation matrix for this transformation as being:

$${}_I^{L'} \mathcal{R} = \mathcal{R}_k(\theta) = \begin{bmatrix} \cos \theta & \sin \theta & 0 \\ -\sin \theta & \cos \theta & 0 \\ 0 & 0 & 1 \end{bmatrix}, \quad (\text{B.2})$$

where k indicates the third axis of the current basis (i and j represent the first and second axes, respectively). This will transform vectors from I to L' . Suppose now that we further rotate our reference frame by an angle ϕ about the newly-rotated j' axis. The rotation for this elementary transformation is:

$${}_{L'}^{L''} \mathcal{R} = \mathcal{R}_j(\phi) = \begin{bmatrix} \cos \phi & 0 & -\sin \phi \\ 0 & 1 & 0 \\ \sin \phi & 0 & \cos \phi \end{bmatrix}. \quad (\text{B.3})$$

And let's do one last rotation about i'' , of an angle ψ , for which the transformation matrix is:

$${}_{L''}^L \mathcal{R} = \mathcal{R}_i(\psi) = \begin{bmatrix} 1 & 0 & 0 \\ 0 & \cos \psi & \sin \psi \\ 0 & -\sin \psi & \cos \psi \end{bmatrix}. \quad (\text{B.4})$$

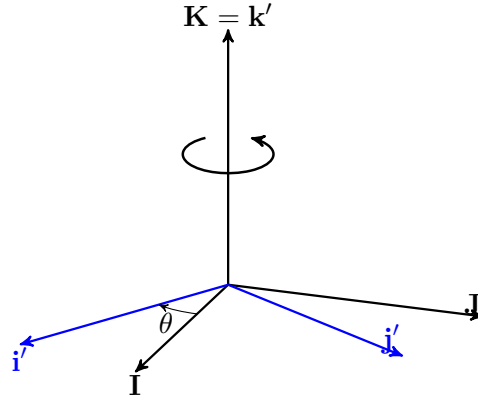


FIGURE B.2: The $\{i', j', k'\}$ reference frame (in blue) is rotated with respect to $\{I, J, K\}$ (in black). The rotation is about the axis K by an angle $\theta = -30$ degrees.

The matrix that corresponds to the active transformation of I to L will multiply vectors expressed in I and express them in L . Hence, this matrix can be written:

$${}_I^L \mathcal{R} = {}_{L''}^L \mathcal{R}_{L'}^{L''} \mathcal{R}_I^{L'} \mathcal{R} = \mathcal{R}_i(\psi) \mathcal{R}_j(\phi) \mathcal{R}_k(\theta), \quad (\text{B.5})$$

where we pre-multiply the matrix for each consecutive rotation of reference frames. This corresponds to the "natural order" of rotations (Shuster, 1993), and is especially relevant when related to quaternions. While the first axis of rotation, k , is defined in the initial reference frame, it is important to realize that the axes corresponding to the second and third rotations are defined in the intermediate frames L' and L'' , respectively. We can understand this by thinking that the transformations follow the *body*, as each rotation is done in the body reference frame, and is a particularly useful approach to our problem.

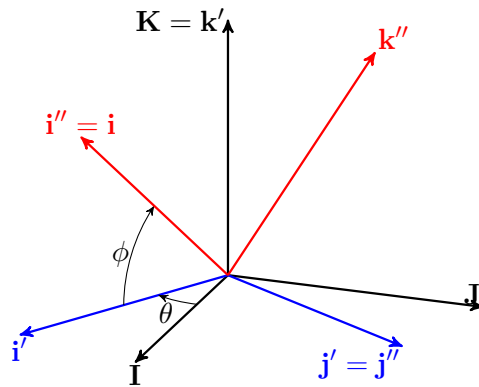


FIGURE B.3: The $\{i'', j'', k''\}$ reference frame (in red) is rotated with respect to $\{i', j', k'\}$ (in blue). The rotation is about the axis j' by an angle $\phi = -45$ degrees.

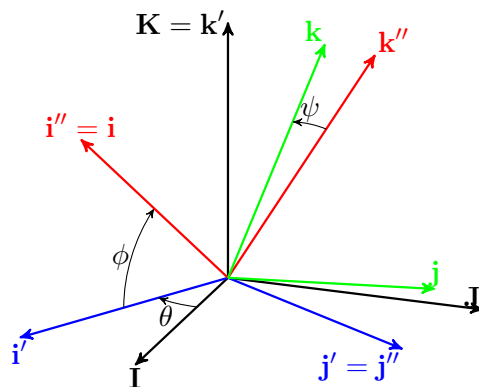


FIGURE B.4: The $\{i, j, k\}$ reference frame (in green) is rotated with respect to $\{i'', j'', k''\}$ (in red). The rotation is about the axis i'' by an angle $\psi = 15$ degrees.

B.3 Quaternions

Quaternions are a more modern way to describe the orientation of a reference frame with respect to another, and are today widely used to describe spacecraft orientation (e.g. Wertz, 2012). From a strictly mathematical point of view, quaternions form a normed algebra over the real numbers that is an extension of traditional complex numbers. The quaternion normed algebra has four dimensions, instead of just two for the complex numbers. At its fundamental level, the basis for the quaternion algebra consists of one real axis and three imaginary axes $\{1, \mathbf{i}, \mathbf{j}, \mathbf{k}\}$. Like complex numbers (which have a basis $\{1, \mathbf{i}\}$), there are fundamental relations between the basis elements that govern the multiplication operation, such as the well known identity $\mathbf{i}^2 = -1$, that we will discuss at length later in this section. In this document, we will write a quaternion using one of the following equivalent notations (Schmidt et al., 2001) :

$$\bar{q} = q_r \times 1 + q_i \mathbf{i} + q_j \mathbf{j} + q_k \mathbf{k} = q_r + \mathbf{q} = \begin{bmatrix} q_i \\ q_j \\ q_k \\ q_r \end{bmatrix} = \begin{bmatrix} \mathbf{q} \\ q_r \end{bmatrix} = \begin{bmatrix} \mathbf{q}^T & q_r \end{bmatrix}^T, \quad (\text{B.6})$$

where we make a clear distinction between the quaternion's real part q_r , and its 3-dimensional imaginary part that we choose to represent as a vector $\mathbf{q} = q_i \mathbf{i} + q_j \mathbf{j} + q_k \mathbf{k}$. Like complex numbers, quaternion have a conjugate operation, which negates the imaginary part:

$$\bar{q}^* = \begin{bmatrix} -\mathbf{q}^T & q_r \end{bmatrix}^T. \quad (\text{B.7})$$

Quaternions are interesting beyond their pure mathematical definition because the

subset of quaternions of unit norm can be used to represent a coordinate frame rotation in three dimensions. The Euler rotation theorem states that any coordinate frame rotation can be described by a rotation of an angle θ about an appropriately-chosen unit vector $\mathbf{u} = x\mathbf{i} + y\mathbf{j} + z\mathbf{k}$ (also called the "Euler axis" or "Euler vector"). This formalism has 3 degrees of freedom, the minimum needed to describe a rotation between two reference frames: two degrees of freedom in the vector (which is constrained to be of unit norm), and one in the rotation angle. If we encode this information in a quaternion using Euler's exponential notation for vectors [need references here], this precisely defines the quaternion:

$$\bar{q} = \exp \left[\frac{\theta}{2}(x\mathbf{i} + y\mathbf{j} + z\mathbf{k}) \right] = \cos \frac{\theta}{2} + (x\mathbf{i} + y\mathbf{j} + z\mathbf{k}) \sin \frac{\theta}{2}. \quad (\text{B.8})$$

This quaternion completely describes the rotation between the two reference frames and has unit norm. Conversely, every quaternion of unit norm can be decomposed like this and represent a rotation in three-dimensional Euclidian space. Like rotation matrices, the unit quaternions form a group under the quaternion multiplication operation, which is isomorphic to the special unitary group $SU(2)$ [reference]. It is known that $SU(2)$ is a surjective 2:1 homomorphism of $SO(3)$. This means that each element in $SO(3)$ can be described by exactly two elements in $SU(2)$, or equivalently, two distinct unit quaternions: the quaternion \bar{q} , and its opposite $-\bar{q}$.

Quaternions use 4 numbers to describe 3 degrees of freedom: an advantage over matrices (9 elements), but an apparent disadvantage over Tait-Bryan angles, which consist of an optimal number of 3 elements. However, Tait-Bryan angles can be shown to exhibit a phenomenon called *gimbal lock*, which leads to a degeneracy when describing the set of angles corresponding to rotations when the pitch angle (second rotation angle, about \mathbf{j}) is $\pm\pi/2$. This creates situations where some rotations and sequences of rotation would have

to be avoided by fear of creating numerical issues caused by gimbal lock. Quaternions, while needing an extra number to represent the rotation, are free of this concern. This is one of the main reasons that they were originally preferred to Tait-Bryan angles early in the spaceflight era (Wertz, 2012; Shuster, 1993).

B.3.1 Quaternion multiplication

In order to form the unit quaternion group, one has to define an appropriate multiplication operation. We warn that the formulation that we use and present in the next few paragraphs does not correspond to the commonly accepted rules for quaternion operations (also called "Hamilton notation", from W. R. Hamilton who is attributed the discovery of quaternions). We use a formalism that was popularized by Cayley (Cayley, 1963) and adopted in most of the aerospace community, mostly to describe the orientation of satellites in inertial space. Its main advantage is that consecutive transformations using quaternions consist of multiplying elementary quaternions in a "natural order", exactly in the same order as the corresponding rotation matrices.

To avoid confusion, we will not mention the original Hamilton rules in this work. Instead, we define the quaternion elementary multiplication rules as follows (Shuster, 1993):

$$\begin{aligned} \mathbf{i}^2 &= \mathbf{j}^2 = \mathbf{k}^2 = -1; \\ \mathbf{ji} &= -\mathbf{ij} = \mathbf{k}; \\ \mathbf{kj} &= -\mathbf{jk} = \mathbf{i}; \\ \mathbf{ik} &= -\mathbf{ki} = \mathbf{j}. \end{aligned} \tag{B.9}$$

Using the relations in Eq. B.9, we define the general quaternion multiplication operator \otimes :

$$\begin{aligned}
 \bar{p} \otimes \bar{q} &= (p_r + p_i\mathbf{i} + p_j\mathbf{j} + p_r\mathbf{k}) \times (q_r + q_i\mathbf{i} + q_j\mathbf{j} + q_r\mathbf{k}) \\
 &= (p_r q_r - p_i q_i - p_j q_j - p_k q_k) \\
 &\quad + (p_r q_i + p_i q_r - p_j q_k + p_k q_j)\mathbf{i} \\
 &\quad + (p_r q_j + p_j q_r - p_k q_i + p_i q_k)\mathbf{j} \\
 &\quad + (p_r q_k + p_k q_r - p_i q_j + p_j q_i)\mathbf{k}
 \end{aligned} \tag{B.10}$$

To express a vector ${}^I\mathbf{v} = {}^I(x, y, z)$ in the new frame L , we construct a purely imaginary quaternion from this vector: $\bar{q}_{\mathbf{v}} = 0 + x\mathbf{i} + y\mathbf{j} + z\mathbf{k}$, and we use the quaternion multiplication to obtain:

$$\begin{bmatrix} {}^L\mathbf{v} \\ 0 \end{bmatrix} = {}_I^L\bar{q} \otimes \bar{q}_{\mathbf{v}} \otimes {}_I^L\bar{q}^{-1}, \tag{B.11}$$

and extract the vector ${}^L\mathbf{v}$ from the resulting quaternion.

Note that the quaternion inverse operation for quaternions of unit norm is the same as the conjugate operation.

B.3.2 Relationship with matrices and elementary quaternions

Using this formalism, a quaternion is behaving in the same way as the corresponding *passive* transformation matrix to describe a reference frame rotation. This means that consecutive rotations are multiplying in the "natural order", which makes it more intuitive.

For example, let's consider the elementary rotation described in Fig B.2 that represents a rotation of the initial reference frame I into a reference frame L about \mathbf{k} . Using the "left-hand" rule, the angle θ of rotation about \mathbf{k} is now $\theta = +30$ degrees. This quaternion

is ${}^L_I \bar{q} = \bar{q}_{\mathbf{k}}(\theta) = \cos \frac{\theta}{2} + \sin \frac{\theta}{2} \mathbf{k}$, and represents the same rotation as the passive rotation matrix $\mathcal{R}_{\mathbf{k}}(\theta)$ discussed in Section ???. If the rotation of the reference frame is described by three consecutive rotations of angles θ , ϕ and ψ about \mathbf{k} , \mathbf{j}' , and \mathbf{i}'' , respectively [see some figure], we can write:

$$\begin{aligned} {}^L_I \bar{q} &= \bar{q}_{\mathbf{i}}(\psi) \bar{q}_{\mathbf{j}}(\phi) \bar{q}_{\mathbf{k}}(\theta) \\ &= \begin{bmatrix} 0 \\ \sin \frac{\psi}{2} \\ 0 \\ \cos \frac{\psi}{2} \end{bmatrix} \begin{bmatrix} 0 \\ 0 \\ \sin \frac{\phi}{2} \\ \cos \frac{\phi}{2} \end{bmatrix} \begin{bmatrix} 0 \\ 0 \\ \sin \frac{\theta}{2} \\ \cos \frac{\theta}{2} \end{bmatrix}, \end{aligned} \quad (\text{B.12})$$

which forms a quaternion that is equivalent to the rotation matrix multiplication $\mathcal{R}_{\mathbf{i}}(\psi)\mathcal{R}_{\mathbf{j}}(\phi)\mathcal{R}_{\mathbf{k}}(\theta)$. Note that the order of the quaternions is the same as the order of the matrices. This is one of the advantages of choosing this "natural order" convention (Shuster, 1993).

B.4 Quaternion derivative and integration

Properly defining the derivative and integral of quaternions is necessary for our purpose. We will need a derivative to describe our dynamic system as its orientation changes over time; and we will need to integrate (or *propagate*) those equations to find a numerical solution to the attitude estimation problem.

In the following, we consider the body reference frame $L(t)$ which evolves as a function of time with respect to a fixed, inertial reference frame I .

The mathematical derivations leading to those results can be found elsewhere (Trawny et al., 2005). Over an infinitesimal time step dt , the local frame is rotating by an angular

vector $\delta\theta$. The instantaneous angular velocity, expressed in the body reference frame $\mathbf{L}(t)$, is ${}^L(t)\boldsymbol{\omega}(t) = \lim_{dt \rightarrow 0} \frac{\delta\theta}{\delta t}$. It can be shown (Trawny et al., 2005) that with this formalism, the quaternion derivative is defined using either a quaternion multiplication, or an equivalent matrix multiplication:

$${}^L(t)\dot{\bar{q}}(t) = \frac{1}{2} \begin{bmatrix} \boldsymbol{\omega} \\ 0 \end{bmatrix} \otimes {}^L(t)\bar{q} = \frac{1}{2} \boldsymbol{\Omega}(\boldsymbol{\omega}) {}^L(t)\bar{q}, \quad (\text{B.13})$$

where the matrix

$$\boldsymbol{\Omega}(\boldsymbol{\omega}) = \begin{bmatrix} 0 & \omega_z & -\omega_y & \omega_x \\ -\omega_z & 0 & \omega_x & \omega_y \\ \omega_y & -\omega_x & 0 & \omega_z \\ -\omega_x & -\omega_y & -\omega_z & 0 \end{bmatrix} \quad (\text{B.14})$$

is going to play an important role in the later sections.

The integrator formulas are derived in [1]. The problem is to find a matrix $\boldsymbol{\Theta}$ to integrate a quaternion ${}^L(t)\bar{q}(t)$, and estimate attitude at time $t + \Delta t$, knowing the instantaneous angular velocity $\boldsymbol{\omega}(t)$:

$$\bar{q}(t + \Delta t) = \boldsymbol{\Theta}(t, t + \Delta t) \bar{q}(t) \quad (\text{B.15})$$

A zeroth-order solution assumes that the angular velocity $\boldsymbol{\omega}$ is a constant over the timestep Δt , an important special case since it describes the typical discrete representation that we will use in our software. The solution can be expressed as:

$$\boldsymbol{\Theta}(t, t + \Delta t) \equiv \boldsymbol{\Theta}(\Delta t) = \exp \left(\frac{1}{2} \boldsymbol{\Omega}(\boldsymbol{\omega}) \Delta t \right), \quad (\text{B.16})$$

where the matrix exponential is defined using a Taylor expansion [give reference for that].

A first-order solution is given in Trawny et al. (2005) and uses knowledge of two previous ω values to estimate the integral.

B.5 Covariance matrices in different reference frames

In the following, we will be describing our attitude using quaternions or rotation matrices in a Kalman filter with a state-space representation. This means that we will be make estimates of physical quantities, as well as estimates of our estimation error. These errors are represented using covariance matrices.

Covariance matrices contain information about the cross-correlation of the variables in the state vector. The diagonal elements represent the auto-covariance of a given variable, while the terms off the diagonal indicate the degree of covariance (or correlation) between the different variables. For example, we will have three gyroscopes which will be mounted orthogonally from each other, each measuring the angular velocity about three different axes. In the ideal case, all gyroscopes are independent and the covariance matrix associated to the set of three angular velocities is diagonal, with the variances of each gyroscope on the diagonal.

If we rotate the gyroscopes' frame with a rotation matrix \mathbf{C} , the new covariance matrix \mathbf{Q} needs to be rotated as well: $\mathbf{Q}' = \mathbf{C}\mathbf{Q}\mathbf{C}^T$.

B.5.1 Small angle approximation

Quaternions become more intuitive in the small angle approximation. Indeed, when all angles are small with respect to π , we can write:

$$\overset{L}{I}\bar{q} \approx \begin{bmatrix} \frac{1}{2}\delta\boldsymbol{\theta} \\ 1 \end{bmatrix}, \quad (\text{B.17})$$

where $\frac{1}{2}\delta\boldsymbol{\theta} = \frac{1}{2}[\delta\theta_i, \delta\theta_j, \delta\theta_k]^T$ corresponds to three small rotations about all the three axes of the initial reference frame. Because we are in the small angle approximation, the order of the rotations does not matter. Hence, if the imaginary part of a quaternion has small values q_i, q_j, q_k , and if $q_r \approx 1$, this quaternion represents a rotation of the reference frame by an angle $\delta\theta_i = 2q_i$, then by an angle $\delta\theta_j = 2q_j$, and finally by an angle $\delta\theta_k = 2q_k$, where all the angles are expressed in radians.

More simplifications can also be found. For example, in the limit where $\boldsymbol{\omega} \rightarrow \mathbf{0}$, the matrix exponential defined in Eq. B.16 simplifies into:

$$\boldsymbol{\Theta}(\Delta t) \xrightarrow{\boldsymbol{\omega} \rightarrow \mathbf{0}} \mathbf{I}_{4 \times 4} + \frac{\Delta t}{2} \boldsymbol{\Omega}(\boldsymbol{\omega}). \quad (\text{B.18})$$

Appendix C

The PID control loop

Before we elaborate on the control architecture of the entire system, let's first discuss the elementary controls block: the PID.

A Proportional-Integral-Derivative (PID) control loop is one of the most basic, yet most used method to build systems with active control. The problem that these systems try to solve is simply to make an object reach a desired state: a sensor is used to measure the current state, and the difference between the desired state and the current state is fed to an apparatus capable of changing the state. Most commonly, this uses motors and either position or velocity sensors, but it can also be used for example for temperature control in a cryogenic environment, where heaters are used to change the temperature. For simplicity, in the rest of this work, we will always consider a loop with sensors and actuators.

In its most simple expression, the PID can be reduced to a simple proportional loop, where the command is proportional to the error between the desired and measured state. The value of this proportional coefficient usually sets the dynamics of the response, as a large proportional gain K_p will mean that even a small deviation from our desired state will trigger a large response. Sometimes, a purely proportional system can lack stability.

A proportional-derivative loop adds the information of the speed at which the error varies. If the error is growing quickly, we can increase our command. If the error is being reduced quickly, it is time to slow down the command to avoid overshooting our target. This uses the time derivative of the error that multiplies a gain, K_d , and has the effect to damp the motion. A PD loop usually will help with the system's stability.

But even then, a proportional-derivative loop help stabilize the dynamics of the system; it does not guarantee that you will reach your desired state. We then complete the PID loop with an integral gain K_i , which multiplies the integral of the error over some length of time. While the K_p and K_d gains mostly control the dynamics of the response, the integral term will control the steady-state error and ensure it converges to zero. This term needs to be considered with precaution, as some situations can lead to a diverging response.

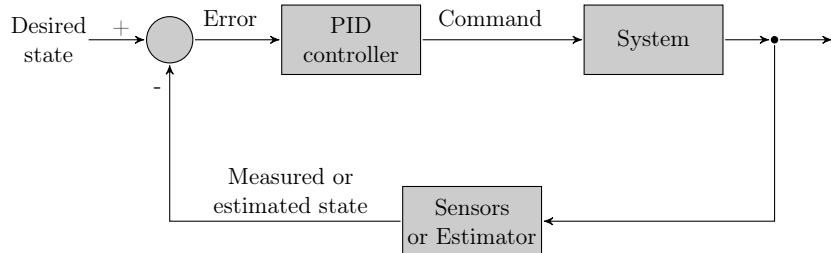


FIGURE C.1: Diagram of a PID loop.

A simple PID loop diagram is shown in Fig C.1, with the desired input state at the entrance of the loop and the real state at the output of the loop. It is often the case that the state cannot be directly measured: this require the use of an *estimator* or *observer*, in which various indirect measurements will feed a mathematical model of the system to estimate its parameters. The relevant example for us is a scenario where we only measure a velocity measurement, while we want to close the loop on the position. Simply put, we know that the position has an integral relationship with the velocity, and the observer's

role is to estimate the integration constants.

The estimator is also used to realize *sensor fusion*. This consists of combining various types of measurements to provide the best estimate of the state to feed back to the control loop. The various measurements often happen at different discrete rates, with different lag times, which can lead to rather complex implementations. One of the most well-known estimation algorithms is the Kalman filter, which we will discuss at length in Chapter V.

For BETTII, each subsystem has its own PID control loop. Each PID loop structure consists of 7 variables: the K_p , K_d , K_i gains, and overall scaling factor, an upper and a lower limit on the command, and a boolean value that is used to reset the content of the integral term used to multiply K_i .

The traditional PID loop can be enhanced many ways to increase various of its properties, such as its robustness or noise-rejection properties. We implement two key enhancements which are used in most of our PID loops. The first is a low-pass filtering of the derivative error, which helps avoid velocity noise (such as the structure's resonant mode at 25 Hz) from being injected into the command. The second is called a deadband, and is critical to the success of the azimuth loop. Indeed, as the target is reached and the angular velocity has roughly a zero average, the velocity changes sign often due to its inherent noise. Since the proportional contribution is often small, this can cause the gimbal actuator to change direction very fast, which in turn excites vibrations, and contributes to wear on the stepper motor shaft. The deadband solves this problem by only using the derivative contribution if it is outside of a band about zero. On BETTII, while this makes the loop non-linear, its benefits far outweigh its drawbacks, especially since the deadband is typically kept at small values such as $\pm 2''\text{s}^{-1}$.

Appendix D

FORCAST fit results

TABLE D.1: Fitted parameters for the 84 sources in our 42 SOFIA fields.

SOFIA Name	Coordinates (J2000)	Type	R37	α	R	M_{env} (M_{\odot})	Calc. M_{env} (M_{\odot})	L_{mod} (L_{\odot})	L_{bol} (L_{\odot})	i (°)	A_V (mag)
CepA.1	22h56m06.9s +62d04m34.0s	Isolated	1.16	-0.75	0.66	0.015 ± 0.006	—	39.9 ± 6.0	6.1	19	7
CepA.2	22h56m03.0s +62d02m58.0s	Extended	1.71	1.86	0.79	0.114 ± 0.027	—	163.2 ± 21.3	25.0	19	14
CepA.3	22h56m14.0s +62d02m17.3s	Isolated	1.42	1.89	0.29	0.171 ± 0.075	—	17.5 ± 3.6	3.8	19	14
CepA.4	22h56m19.0s +62d01m54.4s	Extended	2.61	2.40	9.92	22.17 ± 1.776	—	374.4 ± 0.0	2004.0	0	14
CepC.1	23h05m45.8s +62d30m21.4s	Isolated	0.88	1.38	1.06	1.95 ± 0.944	—	5.6 ± 1.1	5.5	0	11
CepC.2	23h05m47.9s +62d30m38.6s	Isolated	0.00	1.67	0.79	4.38 ± 0.869	—	134.4 ± 44.5	0.7	27	14
CepC.3	23h05m40.0s +62d29m16.2s	Isolated	1.04	-0.30	1.89	0.001 ± 0.000	—	111.1 ± 21.3	7.3	51	12
CepC.4	23h05m49.7s +62d30m00.8s	Extended	1.54	0.19	2.07	0.01 ± 0.003	—	11.9 ± 22.3	15.3	0	8
IRAS20050.1	20h07m06.6s +27d28m48.0s	Clustered	—	0.07	0.74	0.004 ± 0	—	128.0 ± 15.3	14.9	65	9
IRAS20050.2	20h07m06.2s +27d28m49.1s	Clustered	2.28	1.64	0.76	0.577 ± 0.217	—	26.6 ± 6.0	8.0	19	14
IRAS20050.3	20h07m06.3s +27d28m56.6s	Clustered	2.00	1.13	0.73	0.256 ± 0.114	—	48.5 ± 6.3	12.8	27	5
IRAS20050.4	20h07m05.9s +27d28m59.2s	Clustered	2.09	1.70	0.24	0.577 ± 0.217	19.174	48.5 ± 8.7	14.9	47	5
IRAS20050.5	20h07m06.6s +27d28m53.1s	Clustered	2.07	0.54	0.78	0.01 ± 0.003	—	49.4 ± 6.2	5.8	43	14
IRAS20050.6	20h07m02.2s +27d30m26.0s	Isolated	1.40	-0.34	2.22	0.004 ± 0	—	201.6 ± 32.1	19.3	81	14
IRAS20050.7	20h07m07.9s +27d27m15.8s	Isolated	—	1.23	1.42	0.015 ± 0.040	3.196	3.5 ± 3.2	3.0	19	14
NGC1333.1	03h29m07.7s +31d21m57.0s	Isolated	0.75	0.29	3.40	0.004 ± 0.005	0.972	32.5 ± 7.8	8.4	51	14
NGC1333.2	03h29m10.3s +31d21m55.5s	Extended	2.23	1.24	1.77	22.168 ± 9.901	—	7.7 ± 1.1	27.8	0	2
NGC1333.3	03h29m01.5s +31d20m20.5s	Isolated	0.90	0.71	3.39	0.004 ± 0.027	1.122	3.5 ± 2.1	8.1	0	14
NGC1333.4	03h29m11.1s +31d18m30.8s	Isolated	1.10	2.00	0.83	2.919 ± 0.447	1.496	2.3 ± 0.4	3.1	19	11
NGC1333.5	03h29m10.6s +31d18m19.6s	Isolated	1.62	1.78	0.77	1.297 ± 0.327	1.496	1.3 ± 0.3	2.8	19	14
NGC1333.6	03h29m13.0s +31d18m13.8s	Isolated	0.95	0.87	1.21	0.001 ± 0.001	0.471	7.5 ± 1.2	1.5	27	14
NGC1333.7	03h28m43.4s +31d17m34.8s	Isolated	1.19	0.93	1.83	0.001 ± 0.001	—	9.6 ± 1.8	1.4	58	0
NGC1333.8	03h29m03.7s +31d16m03.9s	Isolated	0.77	1.15	1.06	1.946 ± 0.746	2.020	17.0 ± 2.4	35.1	0	13
NGC1333.9	03h28m55.6s +31d14m36.6s	Isolated	0.80	2.88	2.62	2.919 ± 0.354	1.721	17.0 ± 2.4	24.3	19	14
NGC1333.10	03h28m57.4s +31d14m15.0s	Isolated	0.80	1.79	1.16	0.256 ± 0.178	0.449	5.6 ± 0.9	4.8	19	14
NGC1333.11	03h28m37.1s +31d13m30.0s	Isolated	1.02	1.67	0.99	0.577 ± 0.133	0.269	7.7 ± 0.7	7.5	19	14
NGC2071.1	05h47m04.8s +00d21m43.1s	Isolated	1.17	2.31	2.83	22.168 ± 2.597	13.521	43.7 ± 3.3	297.2	0	14
NGC2071.2	05h47m04.7s +00d21m48.2s	Isolated	2.13	2.21	1.28	22.168 ± 14.238	20.464	74.1 ± 20.7	199.9	19	14
NGC2071.3	05h47m05.4s +00d21m50.3s	Isolated	—	1.01	1.51	0.171 ± 0.317	6.212	28.8 ± 7.9	113.7	19	14
NGC2071.4	05h47m04.0s +00d22m10.5s	Isolated	0.96	1.01	1.31	0.001 ± 0.001	—	39.9 ± 6.1	21.4	38	14
NGC2071.5	05h47m10.7s +00d21m14.0s	Isolated	1.11	0.32	0.96	0.002 ± 0.001	—	39.9 ± 5.1	14.9	27	14
NGC2264.1	06h41m04.5s +09d36m20.5s	Isolated	0.88	1.86	0.45	1.297 ± 0.286	—	43.7 ± 3.9	8.9	19	11
NGC2264.2	06h40m59.1s +09d35m50.5s	Isolated	1.13	1.72	0.93	0.01 ± 0.004	—	49.4 ± 13.6	6.7	0	5
NGC2264.3	06h41m06.5s +09d35m54.2s	Isolated	1.61	1.76	1.01	1.95 ± 0.331	—	14.5 ± 1.7	1.9	19	3
NGC2264.4	06h41m09.9s +09d35m40.5s	Isolated	1.07	2.15	0.98	2.93 ± 0.515	—	32.3 ± 3.8	2.9	19	12
NGC2264.5	06h41m06.7s +09d34m45.9s	Isolated	1.23	0.10	0.79	0.007 ± 0.002	—	59.5 ± 7.3	16.7	0	7
NGC2264.6	06h41m11.9s +09d35m33.8s	Isolated	1.40	1.37	0.42	0.022 ± 0.010	—	11.0 ± 4.3	2.4	0	14
NGC2264.7	06h41m05.7s +09d34m06.9s	Isolated	1.70	1.32	0.47	0.114 ± 0.268	—	11.9 ± 5.3	1.9	27	13
NGC2264.8	06h41m06.1s +09d34m08.5s	Isolated	1.87	1.37	0.58	6.568 ± 2.243	—	163.2 ± 52.9	1.4	27	2
NGC2264.9	06h41m05.8s +09d35m29.8s	Isolated	1.80	0.29	0.47	0.004 ± 0	—	65.5 ± 6.8	7.2	27	13
NGC2264.10	06h41m08.6s +09d35m42.1s	Isolated	1.30	2.23	1.87	2.92 ± 0.475	—	9.2 ± 1.9	1.4	19	14
NGC2264.11	06h41m11.3s +09d29m05.6s	Isolated	1.07	1.72	0.04	0.171 ± 0.098	—	26.6 ± 2.0	3.3	19	11
NGC2264.12	06h40m59.1s +09d33m23.9s	Isolated	—	1.37	0.21	0.022 ± 0.010	—	3.3 ± 7.4	2.3	0	14
NGC2264.13	06h41m08.9s +09d29m44.9s	Isolated	1.26	1.35	0.59	0.114 ± 0.021	—	147.2 ± 13.9	19.9	72	13
NGC2264.14	06h41m10.2s +09d29m33.3s	Isolated	1.05	0.41	1.57	14.78 ± 1.908	—	374.4 ± 0.0	1856.1	0	0
NGC2264.15	06h41m12.7s +09d29m04.5s	Isolated	1.03	0.72	1.77	0.015 ± 0.004	—	374.4 ± 31.3	86.3	27	13
NGC2264.16	06h41m02.8s +09d36m14.7s	Extended	2.12	0.41	1.03	0.022 ± 0.007	—	166.4 ± 27.8	37.8	51	9
NGC2264.17	06h41m06.8s +09d33m31.5s	Isolated	0.98	1.39	1.25	2.919 ± 0.880	—	10.4 ± 2.0	1.2	19	14
NGC2264.18	06h41m04.3s +09d34m59.3s	Isolated	1.38	0.80	0.51	0.004 ± 0.001	—	38.0 ± 7.1	2.9	43	14
NGC2264.19	06h41m01.8s +09d34m33.7s	Isolated	1.55	0.44	0.39	0.007 ± 0.002	—	26.6 ± 3.6	4.0	55	14
NGC2264.20	06h41m06.3s +09d33m50.4s	Isolated	1.49	0.99	0.67	22.17 ± 16.130	—	374.4 ± 267.4	1.4	19	0
NGC2264.21	06h41m09.3s +09d30m25.8s	Isolated	1.10	0.89	0.93	0.004 ± 0.002	—	26.6 ± 4.1	3.9	0	14

Continued on next page

Table (continued)

SOFIA Name	Coordinates (J2000)	Type	R37	α	R	M_{env} (M_{\odot})	Calc. M_{env} (M_{\odot})	L_{mod} (L_{\odot})	L_{bol} (L_{\odot})	i ($^{\circ}$)	A_V (mag)
NGC7129.1	21h43m06.4s +66d06m55.4s	Extended	–	0.28	1.54	0.05 ± 0.014	–	249.6 ± 31.1	126.3	38	0
NGC7129.2	21h43m01.8s +66d07m08.7s	Extended	1.60	1.19	0.64	6.568 ± 3.028	–	72.3 ± 9.0	62.7	0	14
NGC7129.3	21h42m59.7s +66d06m11.3s	Extended	2.57	2.20	0.38	0.384 ± 0.153	–	331.2 ± 28.1	60.4	19	14
NGC7129.4	21h42m50.2s +66d06m36.1s	Extended	1.63	0.50	1.20	0.022 ± 0.014	–	128.0 ± 29.0	27.6	90	0
NGC7129.5	21h43m06.9s +66d06m42.1s	Isolated	–	-0.13	1.32	0.007 ± 0.003	–	201.6 ± 28.6	12.4	68	14
Oph.1	16h27m10.3s -24d19m12.9s	Isolated	0.92	0.28	0.67	0.01 ± 0.002	0.040	7.9 ± 1.3	3.6	78	3
Oph.2	16h26m44.2s -24d34m48.2s	Isolated	0.93	0.82	1.97	0.004 ± 0	0.051	8.0 ± 1.2	1.2	75	14
Oph.3	16h27m09.4s -24d37m18.3s	Isolated	0.99	0.54	1.54	0.004 ± 0.002	0.040	85.0 ± 19.7	13.4	0	14
Oph.4	16h27m02.5s -24d37m27.6s	Extended	1.80	0.19	2.22	$0.004 \pm 4E-04$	0.066	14.3 ± 2.7	4.5	38	14
Oph.5	16h27m06.8s -24d38m15.4s	Isolated	1.31	0.35	1.36	0.001 ± 0	0.032	4.3 ± 0.5	0.5	81	14
Oph.6	16h27m15.7s -24d38m45.8s	Isolated	1.29	2.36	0.90	0.001 ± 0.001	0.020	26.6 ± 6.6	0.8	90	13
Oph.7	16h27m28.0s -24d39m33.8s	Isolated	0.97	1.35	1.39	0.015 ± 0.002	0.026	26.6 ± 3.5	6.5	72	14
Oph.8	16h27m37.2s -24d30m34.8s	Isolated	1.02	0.55	1.13	0.007 ± 0.002	0.026	17.7 ± 3.4	5.0	78	12
Oph.9	16h27m21.8s -24d29m53.7s	Isolated	–	-0.49	2.08	0.001 ± 0	0.009	11.8 ± 1.2	1.0	81	14
Oph.10	16h27m17.5s -24d28m55.0s	Isolated	1.26	0.45	1.31	0.002 ± 0.001	0.004	2.9 ± 0.3	0.6	81	14
Oph.11	16h26m59.2s -24d35m00.2s	Extended	2.60	2.04	0.74	0.034 ± 0.010	–	11.9 ± 1.9	4.0	78	14
Oph.12	16h26m34.0s -24d23m40.7s	Extended	2.97	3.37	1.05	0.076 ± 0.025	–	39.9 ± 5.0	10.3	87	14
Oph.13	16h27m30.1s -24d27m43.3s	Isolated	–	-0.39	2.23	0.001 ± 0	0.009	17.7 ± 5.5	1.5	81	14
Oph.14	16h27m28.4s -24d27m21.1s	Isolated	1.89	-0.15	1.00	0.001 ± 0.001	0.021	4.3 ± 0.6	1.0	81	14
Oph.15	16h27m29.4s -24d39m16.6s	Isolated	1.25	0.02	1.12	0.004 ± 0.001	0.019	3.3 ± 0.4	0.6	27	14
Oph.16	16h26m24.1s -24d24m48.3s	Isolated	1.80	-0.74	1.87	0.001 ± 0	–	17.7 ± 2.9	2.2	78	10
Oph.17	16h26m23.6s -24d24m39.4s	Isolated	0.96	-0.10	1.21	0.001 ± 0	–	5.3 ± 0.6	1.3	81	14
Oph.18	16h26m17.2s -24d23m45.1s	Isolated	1.18	0.56	1.15	0.003 ± 0.002	0.036	2.8 ± 1.0	0.3	81	14
Oph.19	16h26m30.5s -24d22m59.9s	Isolated	2.51	0.43	0.84	0.001 ± 0.001	0.009	5.3 ± 1.0	1.2	72	14
S140.1	22h19m32.7s +63d19m24.4s	Isolated	0.91	1.82	1.25	4.38 ± 2.347	–	25.0 ± 3.6	22.9	0	14
S140.2	22h19m20.9s +63d18m28.8s	Isolated	–	1.20	0.11	0.015 ± 0.038	–	8.0 ± 9.4	6.6	0	14
S140.3	22h19m19.8s +63d18m49.6s	Clustered	3.02	1.68	1.97	14.78 ± 2.345	–	331.2 ± 27.3	631.6	0	13
S140.4	22h19m18.2s +63d19m03.9s	Clustered	2.24	3.56	3.77	14.78 ± 1.946	–	331.2 ± 24.9	455.8	0	13
S140.5	22h19m18.1s +63d18m47.0s	Extended	1.13	1.48	7.28	22.17 ± 1.639	–	374.4 ± 0.0	4129.7	0	0
S140.6	22h19m22.4s +63d18m04.5s	Isolated	1.04	1.50	0.15	0.076 ± 0.040	–	10.4 ± 3.1	2.0	19	14
S140.7	22h19m14.7s +63d19m00.0s	Isolated	–	-1.49	0.07	0.384 ± 0.321	–	26.6 ± 10.5	2.4	19	10
S171.1	00h03m59.8s +68d35m05.8s	Isolated	1.03	0.45	2.56	0.004 ± 0	–	201.6 ± 35.8	23.5	78	14
S171.2	00h04m02.0s +68d34m33.3s	Isolated	–	-0.77	0.60	$0.001 \pm 4E-04$	–	48.4 ± 5.6	7.8	43	6

Bibliography

- Allamandola, L J, A G G M Tielens, and J R Barker (1985). “Polycyclic aromatic hydrocarbons and the unidentified infrared emission bands - Auto exhaust along the Milky Way”. In: *Astrophysical Journal* 290, pp. L25–L28.
- Allen, Christine A et al. (2006). “Far infrared through millimeter backshort-under-grid arrays”. In: *Millimeter and Submillimeter Detectors and Instrumentation for Astronomy III*. Edited by Zmuidzinas 6275, 62750B–62750B–8.
- Allen, L et al. (2007). “The Structure and Evolution of Young Stellar Clusters”. In: *Protostars and Planets V*, p. 361.
- André, P et al. (2014). “From Filamentary Networks to Dense Cores in Molecular Clouds: Toward a New Paradigm for Star Formation”. In: *Protostars and Planets VI*, pp. 27–51.
- André, Ph et al. (2010). “From filamentary clouds to prestellar cores to the stellar IMF: Initial highlights from the Herschel Gould Belt Survey”. In: *Astronomy and Astrophysics* 518, p. L102.
- Anglada, Guillem et al. (1998). “On the Exciting Sources of the L723 and IRAS 20050+2720 Quadrupolar Molecular Outflows”. In: *Star Formation with the Infrared Space Observatory* 132, p. 303.
- Astropy Collaboration et al. (2013). “Astropy: A community Python package for astronomy”. In: A&A 558, A33, A33. doi: 10.1051/0004-6361/201322068. arXiv: 1307.6212 [astro-ph.IM].

- Bachiller, R, A Fuente, and M Tafalla (1995). “An extremely high velocity multipolar outflow around IRAS 20050 + 2720”. In: *Astrophysical Journal* 445, pp. L51–L54.
- Bachiller, Rafael (1996). “Bipolar Molecular Outflows from Young Stars and Protostars”. In: *Annual Review of Astronomy and Astrophysics* 34.1, pp. 111–154.
- Beltrán, M T et al. (2008). “On the nature of outflows in intermediate-mass protostars: a case study of IRAS 20050+2720”. In: *Astronomy and Astrophysics* 481.1, pp. 93–105.
- Benford, Dominic J (2008). “Transition Edge Sensor Bolometers for CMB Polarimetry”. In: *Workshop on Technology Development for a CMB Probe of Inflation*.
- Bevington, Philip Raymond and D Keith Robinson (2003). *Data Reduction and Error Analysis for the Physical Sciences*. McGraw-Hill.
- Blind, N et al. (2011). “Optimized fringe sensors for the VLTI next generation instruments”. In: *Astronomy and Astrophysics* 530, p. 121.
- Bonnell, I A et al. (1997). “Accretion and the stellar mass spectrum in small clusters”. In: *Monthly Notices of the Royal Astronomical Society* 285, p. 201.
- Bonnell, Ian A and Matthew R Bate (2002). “Accretion in stellar clusters and the collisional formation of massive stars”. In: *Monthly Notice of the Royal Astronomical Society* 336.2, pp. 659–669.
- (2006). “Star formation through gravitational collapse and competitive accretion”. In: *Monthly Notices of the Royal Astronomical Society* 370.1, pp. 488–494.
- Bracco, A et al. (2011). “Herschel-ATLAS: statistical properties of Galactic cirrus in the GAMA-9 Hour Science Demonstration Phase Field”. In: *Monthly Notices of the Royal Astronomical Society* 412.2, pp. 1151–1161.

- Cardelli, Jason A, Geoffrey C Clayton, and John S Mathis (1989). “The relationship between infrared, optical, and ultraviolet extinction”. In: *Astrophysical Journal* 345, pp. 245–256.
- Cayley, Arthur (1963). *The Collected Mathematical Papers of Arthur Cayley*.
- Chen, H et al. (1997). “IRAS 20050+2720: An Embedded Young Cluster Associated with a Multipolar Outflow”. In: *The Astrophysical Journal* 475.1, pp. 163–172.
- Chini, R et al. (2001). “Mm/Submm images of Herbig-Haro energy sources and candidate protostars”. In: *Astronomy and Astrophysics* 369.1, pp. 155–169.
- Clauzet, Aaron, Cosma Rohilla Shalizi, and M E J Newman (2007). “Power-law distributions in empirical data”. In: *arXiv.org* 4, pp. 661–703. arXiv: 0706.1062v2 [physics.data-an].
- Collaboration, Planck et al. (2016). “Planck intermediate results. XXIX. All-sky dust modelling with Planck, IRAS, and WISE observations”. In: *Astronomy and Astrophysics* 586, A132.
- Crassidis, John L and John L Junkins (2011). *Optimal Estimation of Dynamic Systems, Second Edition*. CRC Press.
- Davis, Sumner P, Mark C Abrams, and James W Brault (2001). “Fourier transform spectrometry”. In: *Fourier transform spectrometry by Sumner P. Davis et al. San Diego*.
- De Buizer, James M et al. (2012). “First Science Observations with SOFIA/FORCAST: 6-37 μm Imaging of Orion BN/KL”. In: *The Astrophysical Journal Letters* 749.2, p. L23.
- Draine, Bruce T (2011). “Physics of the Interstellar and Intergalactic Medium”. In: *Physics of the Interstellar and Intergalactic Medium by Bruce T. Draine. Princeton University Press*.

- Dunham, Michael M et al. (2010). “Evolutionary Signatures in the Formation of Low-Mass Protostars. II. Toward Reconciling Models and Observations”. In: *The Astrophysical Journal* 710.1, pp. 470–502.
- El Badaoui, Noad et al. (2014). “Towards a solid-state ring laser gyroscope”. In: *Comptes Rendus Physique* 15.10, pp. 841–850.
- Elias, Nicholas M et al. (2007). “The Mathematics of Double-Fourier Interferometers”. In: *The Astrophysical Journal* 657.2, pp. 1178–1200.
- Enoch, Melissa L et al. (2009). “Properties of the Youngest Protostars in Perseus, Serpens, and Ophiuchus”. In: *The Astrophysical Journal* 692.2, pp. 973–997.
- Evans, Neal J et al. (2009). “The Spitzer c2d Legacy Results: Star-Formation Rates and Efficiencies; Evolution and Lifetimes”. In: *The Astrophysical Journal Supplement* 181.2, pp. 321–350.
- Evans, Neal J II (1999). “Physical Conditions in Regions of Star Formation”. In: *Annual Review of Astronomy and Astrophysics* 37.1, pp. 311–362.
- Fischer, William J et al. (2012). “Multiwavelength Observations of V2775 Ori, an Outbursting Protostar in L 1641: Exploring the Edge of the FU Orionis Regime”. In: *The Astrophysical Journal* 756.1, p. 99.
- Fixsen, D J et al. (1996a). “A Balloon-borne Millimeter-Wave Telescope for Cosmic Microwave Background Anisotropy Measurements”. In: *Astrophysical Journal v.470* 470, p. 63.
- Fixsen, D J et al. (1996b). “The Cosmic Microwave Background Spectrum from the Full COBE FIRAS Data Set”. In: *Astrophysical Journal v.473* 473.2, pp. 576–587.

- Fixsen, D J et al. (1998). "The Spectrum of the Extragalactic Far-Infrared Background from the COBE FIRAS Observations". In: *The Astrophysical Journal* 508.1, pp. 123–128.
- Fixsen, D J and J C Mather (2002a). "The Spectral Results of the Far-Infrared Absolute Spectrophotometer Instrument on COBE". In: *The Astrophysical Journal* 581.2, pp. 817–822.
- Fixsen, D J and Eli Dwek (2002b). "The Zodiacal Emission Spectrum as Determined by COBE and Its Implications". In: *The Astrophysical Journal* 578.2, pp. 1009–1014.
- Fontani, F, R Cesaroni, and R S Furuya (2010). "Class I and Class II methanol masers in high-mass star-forming regions". In: *Astronomy and Astrophysics* 517, A56.
- Forman, Michael L, W Howard Steel, and George A Vanasse (1966). "Correction of Asymmetric Interferograms Obtained in Fourier Spectroscopy". In: *Journal of the Optical Society of America* 56, p. 59.
- Furlan, E et al. (2016). "The Herschel Orion Protostar Survey: Spectral Energy Distributions and Fits Using a Grid of Protostellar Models". In: *The Astrophysical Journal Supplement Series* 224.1, p. 5.
- Gillessen, S et al. (2010). "GRAVITY: a four-telescope beam combiner instrument for the VLTI". In: *Proceedings of the SPIE*. Max-Planck-Institut für extraterrestrische Physik, Germany. SPIE, 77340Y–77340Y–20.
- Gillett, F C, W J Forrest, and K M Merrill (1973). "8 - 13-micron spectra of NGC 7027, BD +30 3639, and NGC 6572." In: *Astrophysical Journal* 183, pp. 87–93.
- Glindemann, Andreas (2011). "Principles of Stellar Interferometry". In: *Principles of Stellar Interferometry:*

- Glindemann, Andreas et al. (2000). “The VLT Interferometer: a unique instrument for high-resolution astronomy”. In: *Proc. SPIE Vol. 4006* 4006, pp. 2–12.
- Grainger, William F et al. (2012). “Demonstration of spectral and spatial interferometry at THz frequencies”. In: *Applied Optics* 51.12, pp. 2202–2211.
- Greene, Thomas (2001). “Protostars”. In: *American Scientist* 89.4, pp. 316–.
- Griffiths, Peter R and James A De Haseth (2007). *Fourier Transform Infrared Spectrometry*. John Wiley & Sons.
- Günther, H M et al. (2012). “IRAS 20050+2720: Anatomy of a Young Stellar Cluster”. In: *The Astronomical Journal* 144.4, p. 101.
- Gutermuth, R A et al. (2009). “A Spitzer Survey of Young Stellar Clusters Within One Kiloparsec of the Sun: Cluster Core Extraction and Basic Structural Analysis”. In: *The Astrophysical Journal Supplement* 184.1, pp. 18–83.
- Gutermuth, R A et al. (2011). “A Correlation between Surface Densities of Young Stellar Objects and Gas in Eight Nearby Molecular Clouds”. In: *The Astrophysical Journal* 739.2, p. 84.
- Gutermuth, Robert A et al. (2005). “The Initial Configuration of Young Stellar Clusters: A K-Band Number Counts Analysis of the Surface Density of Stars”. In: *The Astrophysical Journal* 632.1, pp. 397–420.
- Harman, Richard R (2005). *Wilkinson Microwave Anisotropy Probe (WMAP) Attitude Estimation Filter Comparison*.
- Harries, J E (1980). “Atmospheric radiometry at submillimeter wavelengths”. In: *Applied Optics* 19.18, p. 3075.
- Hartmann, Lee and Scott J Kenyon (1996). “The FU Orionis Phenomenon”. In: *Annual Review of Astronomy and Astrophysics* 34.1, pp. 207–240.

- Harvey, Paul M et al. (2012). “First Science Results from SOFIA/FORCAST: Super-resolution Imaging of the S140 Cluster at $37\ \mu\text{m}$ ”. In: *The Astrophysical Journal Letters* 749.2, p. L20.
- Harwit, Martin, David Leisawitz, and Stephen Rinehart (2006). “A far-infrared/submillimeter kilometer-baseline interferometer in space”. In: *New Astronomy Reviews* 50.1-3, pp. 228–234.
- Helmich, Frank P and R J Ivison (2009). “FIRI—A far-infrared interferometer”. In: *Experimental Astronomy* 23.1, pp. 245–276.
- Hennebelle, Patrick and Edith Falgarone (2012). “Turbulent molecular clouds”. In: *The Astronomy and Astrophysics Review* 20.1, p. 55.
- Herter, T L et al. (2012). “First Science Observations with SOFIA/FORCAST: The FORCAST Mid-infrared Camera”. In: *The Astrophysical Journal Letters* 749.2, p. L18.
- Herter, T L et al. (2013). “Data Reduction and Early Science Calibration for FORCAST, A Mid-Infrared Camera for SOFIA”. In: *Publications of the Astronomical Society of the Pacific* 125.933, pp. 1393–1404.
- Heyer, Mark and T M Dame (2015). “Molecular Clouds in the Milky Way”. In: *Annual Review of Astronomy and Astrophysics* 53.1, pp. 583–629.
- Hudgins, D M and L J Allamandola (2004). “Polycyclic Aromatic Hydrocarbons and Infrared Astrophysics: The State of the PAH Model and a Possible Tracer of Nitrogen in Carbon-rich Dust.” In: *Astrophysics of Dust* 309, pp. 665–.
- Jørgensen, Jes K et al. (2008). “Current Star Formation in the Ophiuchus and Perseus Molecular Clouds: Constraints and Comparisons from Unbiased Submillimeter and Mid-Infrared Surveys. II.” In: *The Astrophysical Journal* 683.2, pp. 822–843.

- Juanola-Parramon, Roser (2016). A Far-infrared Spectro-spatial Space Interferometer: Instrument Simulator and Testbed Implementation. Springer.
- Kalman, R E (1960). “A New Approach to Linear Filtering and Prediction Problems”. In: *Journal of Basic Engineering* 82.1, pp. 35–45.
- Kato, Eri et al. (2010). “Far-Infrared Interferometric Telescope Experiment : I. Interferometer Optics”. In: *Transactions of Space Technology Japan* 7.ists26, pp. 47–53.
- Kempen, T A van et al. (2009). “The nature of the Class I population in Ophiuchus as revealed through gas and dust mapping”. In: *Astronomy and Astrophysics* 498.1, pp. 167–194.
- Kempen, T A van et al. (2012). “The Small-scale Physical Structure and Fragmentation Difference of Two Embedded Intermediate-mass Protostars in Orion”. In: *The Astrophysical Journal* 751.2, p. 137.
- Kennicutt, R. C. and N. J. Evans (2012). “Star Formation in the Milky Way and Nearby Galaxies”. In: *ARA&A* 50, pp. 531–608. DOI: 10.1146/annurev-astro-081811-125610. arXiv: 1204.3552.
- Kennicutt, Robert C and Neal J Evans (2012). “Star Formation in the Milky Way and Nearby Galaxies”. In: *Annual Review of Astronomy and Astrophysics* 50.1, pp. 531–608.
- Kessler, M F et al. (1996). “The Infrared Space Observatory (ISO) mission.” In: *Astronomy and Astrophysics* 315, pp. L27–L31.
- Kim, Sang-Hee, P G Martin, and Paul D Hendry (1994). “The size distribution of interstellar dust particles as determined from extinction”. In: *Astrophysical Journal* 422, pp. 164–175.

- Korte, Piet A J de et al. (2003). "Time-division superconducting quantum interference device multiplexer for transition-edge sensors". In: *Review of Scientific Instruments* 687.8, pp. 3807–3815.
- Lawson, Peter R (2000). "Principles of Long Baseline Stellar Interferometry". In: *Principles of Long Baseline Stellar Interferometry. Course notes from the 1999 Michelson Summer School.*
- Leach, Robert W and John Denune (1994). "Noise and readout performance of a multiple-readout CCD controller". In: *Proc. SPIE Vol. 2198* 2198, pp. 821–828.
- Lefferts, E J, F L Markley, and M D Shuster (1982). "Kalman Filtering for Spacecraft Attitude Estimation". In: *Journal of Guidance* 5.5, pp. 417–429.
- Leisawitz, David et al. (2007). "The space infrared interferometric telescope (SPIRIT): High-resolution imaging and spectroscopy in the far-infrared". In: *Advances in Space Research* 40.5, pp. 689–703.
- Leisawitz, David et al. (2012). "Developing wide-field spatio-spectral interferometry for far-infrared space applications". In: *Optical and Infrared Interferometry III. Proceedings of the SPIE*. Ed. by Françoise Delplancke, Jayadev K Rajagopal, and Fabien Malbet. NASA Goddard Space Flight Ctr. (United States). SPIE, 84450A.
- Mariotti, J-M and S T Ridgway (1988). "Double Fourier spatio-spectral interferometry - Combining high spectral and high spatial resolution in the near infrared". In: *Astronomy and Astrophysics (ISSN 0004-6361)* 195, p. 350.
- Markley, F Landis and John L Crassidis (2014). *Fundamentals of Spacecraft Attitude Determination and Control*. New York, NY: Springer.
- Mathis, J S, W Rumpl, and K H Nordsieck (1977). "The size distribution of interstellar grains". In: *Astrophysical Journal* 217, pp. 425–433.

- Mathis, John S (1990). "Interstellar dust and extinction". In: *IN: Annual review of astronomy and astrophysics. Vol. 28 (A91-28201 10-90)*. Palo Alto 28.1, pp. 37–70.
- Matsumoto, T, S Matsuura, and M Noda (1994). "2.4 micrometer sky brightness at balloon altitude". In: *Astronomical Society of the Pacific* 106, p. 1217.
- Maybeck, Peter S (1982). *Stochastic Models, Estimation, and Control*. Academic Press.
- McKee, Christopher F and Jonathan C Tan (2003). "The Formation of Massive Stars from Turbulent Cores". In: *The Astrophysical Journal* 585.2, pp. 850–871.
- McKee, Christopher F and Eve C Ostriker (2007). "Theory of Star Formation". In: *Annual Review of Astronomy and Astrophysics* 45.1, pp. 565–687.
- Megeath, S T et al. (2012). "The Spitzer Space Telescope Survey of the Orion A and B Molecular Clouds. I. A Census of Dusty Young Stellar Objects and a Study of Their Mid-infrared Variability". In: *The Astronomical Journal* 144.6, p. 192.
- Mendillo, Christopher B et al. (2012). "Flight demonstration of a milliarcsecond pointing system for direct exoplanet imaging". In: *Applied Optics* 51.29, p. 7069.
- Meynart, Roland (1992). "Sampling jitter in Fourier-transform spectrometers - Spectral broadening and noise effects". In: *Applied Optics (ISSN 0003-6935)* 31.30, p. 6383.
- Michelson, Albert A and Edward W Morley (1887). "On the Relative Motion of the Earth and of the Luminiferous Ether". In: *Sidereal Messenger* 6, pp. 306–310.
- Mighell, Kenneth J (2005). "Stellar photometry and astrometry with discrete point spread functions". In: *Monthly Notices of the Royal Astronomical Society* 361.3, pp. 861–878.
- Molinari, S et al. (1996). "A search for precursors of ultracompact HII regions in a sample of luminous IRAS sources. I. Association with ammonia cores." In: *Astronomy and Astrophysics* 308, pp. 573–587.

- Monnier, John D et al. (2004). “The Michigan Infrared Combiner (MIRC): IR imaging with the CHARA Array”. In: *New Frontiers in Stellar Interferometry* 5491, pp. 1370–.
- Murakami, H et al. (2007). “The Infrared Astronomical Mission AKARI”. In: *Publications of the Astronomical Society of Japan* 59.sp2, 369–S376.
- Myers, P C and E F Ladd (1993). “Bolometric temperatures of young stellar objects”. In: *Astrophysical Journal* 413, pp. L47–L50.
- Myers, Philip C (2011). “Star Formation in Dense Clusters”. In: *The Astrophysical Journal* 743.1, p. 98.
- Neugebauer, G et al. (1984). “The Infrared Astronomical Satellite (IRAS) mission”. In: *Astrophysical Journal* 278, pp. L1–L6.
- Noriega-Crespo, Alberto et al. (2004). “A New Look at Stellar Outflows: Spitzer Observations of the HH 46/47 System”. In: *The Astrophysical Journal Supplement Series* 154.1, pp. 352–358.
- Offner, Stella S R and Christopher F McKee (2011). “The Protostellar Luminosity Function”. In: *The Astrophysical Journal* 736.1, p. 53.
- Ossenkopf, V and Th Henning (1994). “Dust opacities for protostellar cores”. In: *Astronomy and Astrophysics (ISSN 0004-6361)* 291, pp. 943–959.
- Oxley, Paul et al. (2004). “The EBEX experiment”. In: *Infrared Spaceborne Remote Sensing XII. Edited by Strojnik* 5543, pp. 320–331.
- Palla, F et al. (1991). “Water masers associated with dense molecular clouds and ultracompact H II regions”. In: *Astronomy and Astrophysics (ISSN 0004-6361)* 246, pp. 249–263.
- Peltier, JCA (1834). *Investigation of the heat developed by electric currents in homogeneous materials and at the junction of two different conductors*. Ann. Chim. Phys.

- Pilbratt, G L et al. (2010). "Herschel Space Observatory. An ESA facility for far-infrared and submillimetre astronomy". In: *Astronomy and Astrophysics* 518, p. L1.
- Poppenhaeger, K et al. (2015). "YSOVAR: Mid-infrared Variability of Young Stellar Objects and Their Disks in the Cluster IRAS 20050+2720". In: *The Astronomical Journal* 150.4, p. 118.
- Porras, Alicia et al. (2003). "A Catalog of Young Stellar Groups and Clusters within 1 Kiloparsec of the Sun". In: *The Astronomical Journal* 126.4, pp. 1916–1924.
- Portegies Zwart, Simon F, Stephen L W McMillan, and Mark Gieles (2010). "Young Massive Star Clusters". In: *Annual Review of Astronomy and Astrophysics* 48.1, pp. 431–493.
- Press, William H et al. (1992). "Numerical recipes in C. The art of scientific computing". In: *Cambridge: University Press*.
- Rebull, L M et al. (2014). "Young Stellar Object VARIability (YSOVAR): Long Timescale Variations in the Mid-infrared". In: *The Astronomical Journal* 148.5, p. 92.
- Richards, M A (2003). "Coherent integration loss due to white gaussian phase noise". In: *IEEE Signal Processing Letters* 10.7, pp. 208–210.
- Rinehart, S A et al. (2014). "The Balloon Experimental Twin Telescope for Infrared Interferometry (BETTII): An Experiment for High Angular Resolution in the Far-Infrared". In: *Publications of the Astronomical Society of the Pacific* 126, pp. 660–673.
- Rizzo, Maxime J et al. (2012). "Tracking near-infrared fringes on BETTII: a balloon-borne, 8m-baseline interferometer". In: *Optical and Infrared Interferometry III. Proceedings of the SPIE* 8445, 84451T.
- Rizzo, Maxime J et al. (2014). "Building an interferometer at the edge of space: pointing and phase control system for BETTII". In: *Proceedings of the SPIE*. Ed. by Jacobus

- M Oschmann et al. Univ. of Maryland, College Park (United States). SPIE, 91433H–91433H–12.
- Rizzo, Maxime J et al. (2015). “Far-Infrared Double-Fourier Interferometers and their Spectral Sensitivity”. In: *Publications of the Astronomical Society of Pacific* 127.9, pp. 1045–1060.
- Robitaille, T P (2011). “HYPERION: an open-source parallelized three-dimensional dust continuum radiative transfer code”. In: *Astronomy and Astrophysics* 536, A79.
- Robitaille, Thomas P et al. (2006). “Interpreting Spectral Energy Distributions from Young Stellar Objects. I. A Grid of 200,000 YSO Model SEDs”. In: *The Astrophysical Journal Supplement Series* 167.2, pp. 256–285.
- Robitaille, Thomas P et al. (2007). “Interpreting Spectral Energy Distributions from Young Stellar Objects. II. Fitting Observed SEDs Using a Large Grid of Precomputed Models”. In: *The Astrophysical Journal Supplement Series* 169.2, pp. 328–352.
- Schmidt, J and H Niemann (2001). “Using Quaternions for Parametrizing 3-D Rotations in Unconstrained Nonlinear Optimization.” In: *VMV*.
- Sellgren, K (1994). “Tiny Grains, Large Molecules, and the Infrared Cirrus”. In: *The First Symposium on the Infrared Cirrus and Diffuse Interstellar Clouds. ASP Conference Series* 58, pp. 243–.
- Shimizu, T Taro et al. (2016). “Herschel far-infrared photometry of the Swift Burst Alert Telescope active galactic nuclei sample of the local universe - II. SPIRE observations”. In: *Monthly Notices of the Royal Astronomical Society* 456.3, pp. 3335–3353.
- Shirley, Yancy L et al. (2000). “Tracing the Mass during Low-Mass Star Formation. I. Submillimeter Continuum Observations”. In: *The Astrophysical Journal Supplement Series* 131.1, pp. 249–271.

- Shuster, Malcolm D (1993). "Survey of attitude representations". In: *Journal of the Astronautical Sciences (ISSN 0021-9142)* 41, pp. 439–517.
- Sromovsky, Lawrence A (2003). "Radiometric Errors in Complex Fourier Transform Spectrometry". In: *Applied Optics OT* 42.10, p. 1779.
- Staguhn, Johannes et al. (2014a). "Design and Expected Performance of GISMO-2, a Two Color Millimeter Camera for the IRAM 30 m Telescope". In: *Journal of Low Temperature Physics* 176.5, pp. 829–834.
- Staguhn, Johannes G et al. (2014b). "The GISMO Two-millimeter Deep Field in GOODS-N". In: *The Astrophysical Journal* 790.1, p. 77.
- Stecher, T P and B Donn (1965). "On Graphite and Interstellar Extinction". In: *Astrophysical Journal* 142, pp. 1681–.
- Tan, J C et al. (2014). "Massive Star Formation". In: *Protostars and Planets VI*, pp. 149–172.
- Terebey, S, F H Shu, and P Cassen (1984). "The collapse of the cores of slowly rotating isothermal clouds". In: *Astrophysical Journal* 286, pp. 529–551.
- Thompson, A Richard, James M Moran, and Jr George W Swenson (2008). *Interferometry and Synthesis in Radio Astronomy*. John Wiley & Sons.
- Trawny, N and S I Roumeliotis (2005). "Indirect Kalman filter for 3D attitude estimation". In:
- Ulrich, R K (1976). "An infall model for the T Tauri phenomenon". In: *Astrophysical Journal* 210, pp. 377–391.
- Weingartner, Joseph C and B T Draine (2001). "Dust Grain-Size Distributions and Extinction in the Milky Way, Large Magellanic Cloud, and Small Magellanic Cloud". In: *The Astrophysical Journal* 548.1, pp. 296–309.

- Werner, M W et al. (2004). “The Spitzer Space Telescope Mission”. In: *The Astrophysical Journal Supplement Series* 154.1, pp. 1–9.
- Wertz, James R (2012). *Spacecraft Attitude Determination and Control*. Ed. by James R Wertz. Vol. 73. Astrophysics and Space Science Library. Dordrecht: Springer Science & Business Media.
- Whitney, B A et al. (2013). “Three-dimensional Radiation Transfer in Young Stellar Objects”. In: *The Astrophysical Journal Supplement* 207.2, p. 30.
- Whitney, Barbara A et al. (2003a). “2-D Radiative Transfer in Protostellar Envelopes: I. Effects of Geometry on Class I Sources”. In: *arXiv.org* 2, pp. 1049–1063. arXiv: astro-ph/0303479v1 [astro-ph].
- Whitney, Barbara A et al. (2003b). “Two-dimensional Radiative Transfer in Protostellar Envelopes. II. An Evolutionary Sequence”. In: *The Astrophysical Journal* 598.2, pp. 1079–1099.
- Wilking, B A et al. (1989). “A millimeter-wave spectral-line and continuum survey of cold IRAS sources”. In: *Astrophysical Journal* 345, pp. 257–264.
- Williams, J P, L Blitz, and C F McKee (2000). “The Structure and Evolution of Molecular Clouds: from Clumps to Cores to the IMF”. In: *Protostars and Planets IV (Book - Tucson: University of Arizona Press; eds Mannings,* pp. 97–.
- Wolfire, Mark G and Joseph P Cassinelli (1986). “The temperature structure in accretion flows onto massive protostars”. In: *Astrophysical Journal* 310, pp. 207–221.
- Wright, Edward L et al. (2010). “The Wide-field Infrared Survey Explorer (WISE): Mission Description and Initial On-orbit Performance”. In: *The Astronomical Journal* 140.6, pp. 1868–1881.

- Zernike, F (1938). "The concept of degree of coherence and its application to optical problems". In: *Physica* 5.8, pp. 785–795.